Cardiff University

School of Engineering

The Influence of Inter-device Spacing on the Performance of a Tidal Stream Turbine

Robert Ellis

A Thesis submitted to Cardiff University for the Degree of
Doctor of Philosophy

Submission Date: 10th March 2020

Acknowledgements

The author acknowledges financial support from SuperGen UK Centre for Marine Energy (EPSRC: EP/N020782/1), MaRINET II Transnational Access Program and Cardiff University. In addition, the experimental testing carried out at IFREMER and the Kelvin Hydrodynamics Laboratory was funded by the EPSRC Impact Acceleration Account (IAA) and the DyLoTTA project respectively. The author would like to thank the staff at both IFREMER and the Kelvin Hydrodynamics Laboratory for their help throughout the experimental test campaigns.

This research was performed using the supercomputing facilities at Cardiff University operated by Advanced Research Computing at Cardiff (ARCCA) on behalf of the Cardiff Supercomputing Facility and the HPC Wales and Supercomputing Wales (SCW) projects. The author acknowledges the support of the latter, which is part-funded by the European Regional Development Fund (ERDF) via the Welsh Government.

The author would especially like to thank his supervisors, Prof. Tim O'Doherty and Dr. Allan Mason-Jones for their continued guidance and support throughout the work completed in this thesis. Thanks also to Dr. Matthew Allmark for his advice throughout on all things experimental.

Abstract

The focus of this thesis was to investigate how the wake of an upstream horizontal axis tidal turbine influenced the performance of a downstream device. The upstream device used a 0.5m diameter rotor while the downstream device was 0.9m diameter rotor. This was achieved using the commercial CFD software ANSYS CFX and experimental testing for a 1/20th scale, 0.9 m diameter device.

The design and characterisation of the HATT is established using two numerical methods: the blade element momentum theory and ANSYS CFX. The numerical models are validated using experimental testing at the Kelvin Hydrodynamics Laboratory and the IFREMER flume and are within 4 % and 6 % at peak power for the C_P and C_T respectively. The influence of Reynolds number on device performance is studied and for all testing conducted throughout this thesis the device was independent of the Reynolds number.

The stress blended eddy simulation turbulence model, a hybrid RANS-LES turbulence model was used, giving a trade-off between turbulence resolution and computational time, for the wake and device interaction modelling.

The results show that an increased level of ambient turbulence in the flow improved the wake recovery in both the near and far wake for comparable values of C_T. The stress blended eddy simulation turbulence model provides a good prediction, within 6 % between 4-11D downstream for the recovery of a wake for low turbulence when compared to experimental data using a volumetrically averaged approach. There is a greater difference between the experimental and numerical results when the inlet turbulence is increased.

The discretisation scheme selection has a large impact on the prediction of wake recovery but causes minimal changes to the performance of the device. The bounded central difference scheme was found to be the preferred discretisation scheme. When using the high resolution scheme an upwind scheme was still dominant leading to greater smearing in flow variables and gave an under prediction of wake recovery.

The work conducted throughout this thesis shows that the positioning of a turbine within the bypass flow can lead to an increase in the performance of the individual device when operating at peak power due to the acceleration of the flow between upstream devices. The unsteady loading seen by the fluctuation in the mean characteristics as characterised as a percentage of the mean were also reduced when located in the bypass flow.

Contents

List of Figures

List of Tables

Nomenclature

$\bar{u}$	Mean flow velocity / $\mathrm{m\,s^{-1}}$
β_m	Discretisation scheme blending function
δ_{max}	Maximum cell edge length / m
ϵ	Turbulence dissipation / $\mathrm{m^2\,s^{-3}}$
λ	Tip speed ratio
μ	Dynamic viscosity / $\mathrm{kg\,m^{-1}\,s^{-1}}$
μ_b	Bias uncertainty
μ_p	Precision uncertainty
μ_{tot}	Total uncertainty
ω	Turbulence dissipation rate / $\mathrm{s^{-1}}$
ω_t	Angular velocity / $\mathrm{rad\,s^{-1}}$
Φ	Mean component of convected flow variable
ϕ	Convected flow variable
ϕ'	Fluctuating component of convected flow variable
π	Pi
ρ	Density / $\mathrm{kg\,m^{-3}}$
σ	Standard deviation
C_D	Coefficient of drag
C_L	Coefficient of lift
C_P	Coefficient of power
C_Q	Coefficient of torque
C_T	Coefficient of thrust
C_{BM}	Out-of-plane bending moment coefficient
C_{DES}	Calibration constant (0.61)

f	Frequency / Hz
F_t	Rotor thrust / N
l	Characteristic length / m
L_t	Turbulence length scale / m
M_{xy}	Out-of-plane bending moment / Nm
Q_t	Rotor torque / Nm
u'	Fluctuating velocity component / $\mathrm{m\,s^{-1}}$
u_∞	Far upstream velocity / $\mathrm{m\,s^{-1}}$
v	Characteristic velocity / $\mathrm{m\,s^{-1}}$
$\mathbf{C}$	Adjacent upstream node
$\mathbf{D}$	Far downstream node
$\mathbf{f}$	Node at the cell face
$\mathbf{U}$	Far upstream node
$\mathbf{x}$	Position vector (x,y,z)
k	Turbulence kinetic energy / $\mathrm{m^2\,s^{-2}}$
A	Turbine swept area / m^2
a	Blade in wake angle / °
D	Diameter / m^2
R	Radius / m
r	Local radius / m
Re	Reynolds number
y+	Distance to first node from boundary

Acronyms and abbreviations

ADCP Acoustic Doppler Current Profiler

ADV Acoustic Doppler Velocimeter

AoA Angle of Attack

BCD Bounded Central Difference

BEMT Blade Element Momentum Theory

CAD Computer Aided Design

CBC Convection Boundedness Criterion

CD Central Differencing

CEL CFX Expression Language

CFD Computational Fluid Dynamics

D Turbine diameter

DDES Delayed Detached Eddy Simulation

DES Detached Eddy Simulation

DNS direct numerical simulation

EMEC European Marine Energy Centre

GIS Grid Induces Separation

HATT Horizontal Axis Tidal Turbine

HR High Resolution

IFREMER Institut Français de Recherche pour l'Exploitation de la Mer

INSEAN Istituto Nazionale Per Studi Ed Esperienze Di Architettura Navale

IPCC Intergovernmental Panel on Climate Change

KHL Kelvin Hydrodynamics Laboratory

LDA Laser Doppler Anemometer

LES Large Eddy Simulation

LUD Linear Upwind Differencing

MCT Marine Current Turbines

MFR Moving Frame of Reference

NREL National Renewable Energy Laboratory

NVA Normalised Variable Approach

NVD Normalised Variable Diagram

ORE Offshore Renewable Energy

PMSM Permanent Magnet Synchronous Motor

RANS Reynolds-Averaged Navier-Stokes

RMS Root Mean Square

RSM Reynolds Stress Model

SBES Stress Blended Eddy Simulation

SBF Specified Blend Factor

SDES Shielded Detached Eddy Simulation

SGS Sub-Grid Scale

SME Sustainable Marine Energy

SST Shear Stress Transport

T_{DOWN} Downstream turbine

TI Turbulence Intensity

TIGER Tidal Stream Industry Energiser Project

TKE Turbulence Kinetic Energy

TSR Tip-Speed Ratio

T_{UP} Upstream turbine

TI Turbulence Intensity

UD Upwind Differencing

VATT Vertical Axis Tidal Turbine

Chapter 1

Introduction

1.1 Renewable energy drivers

It is estimated by the Intergovernmental Panel on Climate Change (IPCC) that through the contributions of human activity there has been a global warming of approximately 1 °C since pre-industrial levels [1]. Within the report it was stated that the levels of CO_2, CH_4 and N_2O have never been higher within the last 800,000 years. The warming effect is largely associated with the introduction of these greenhouse gas emission into the atmosphere, predominantly as by products of fuel consumption. Fossil fuels such as coal and oil are huge carbon reserves, which when burnt is released into the atmosphere.

The ramifications of 1 °C of warming may still be unobservable to a large number of the global population at present. However, based on the current trajectory warming will reach and surpass 1 °C. If the warming effect reaches a level of 1.5 °C or 2 °C then the theoretical knock on effects are many. A rise in global sea levels, an increase in average temperatures of inhabited land regions, greater precipitation in regions, the probability of droughts in larger regions and a rise in the salinity and temperature of the oceans are all possible outcomes, to name but a few [1]. While it is accepted the full effect of global warming is not yet fully understood, it is globally agreed that the impacts will have a largely negative affect on human and natural systems alike.

The Paris Agreement [2] aims to limit the global temperature rise below 2 °C within the next century. One of the ways to achieve this goal is to reduce the reliance of fossil fuels as a means of energy generation. The UK Renewable Energy Roadmap [3] highlights the UK's pathway to reducing its impact on global warming. The UK's aim is to generate 15 % of all energy used from fully renewable sources by the year 2020, moving away from the burning of coal and oil. At the time the report was written back in 2011 only 3.8 % of the UK's total energy supply came from renewable sources. There are also economic drivers, with the perceived reformation of the energy market in the coming years, the UK could see huge investment estimated to be around £100-110 billion [3].

Fast forward to today, and the increase in renewable energy both in terms of installed capacity and energy generation is increasing year on year. If the same quarter from 2018 and 2019 are compared then a number of positive comparisons can be made. Figure 1.1 shows the production of energy within the UK based on quarter 2 for 2018 and 2019. It shows that not only was energy from coal at a record low but the contribution from renewable sources increased. The main driver for the increase in renewable energy is the increased installed capacity around the UK [4]. The breakdown of renewable sources in Figure 1.2 highlight the importance that wind energy is having in mixing up the UK energy market.

Wind energy has gained large amounts of traction within the UK as of late. At the time of writing the UK has the largest installed capacity in the world for offshore wind and as such the cost of energy generated has dropped by at much as 5 % since 2015, making it a cheaper alternative than both gas and nuclear [5]. The UK has recently finished the largest installed offshore wind farm comprising of 147 turbines. Off the back of this a second offshore wind farm is being developed off the Yorkshire coastline which is proposed to have a greater capacity [6].

This continued investment into the renewable energy sector will only drives costs down, making them more viable alternatives for energy generation in the UK. While the drive to develop and be at the forefront of offshore wind is good, several other technologies are possibly being left behind, and are not receiving the investment required to make them commercially viable yet. One of the areas that has huge potential but is yet to reach commercial viability is marine renewable energy.

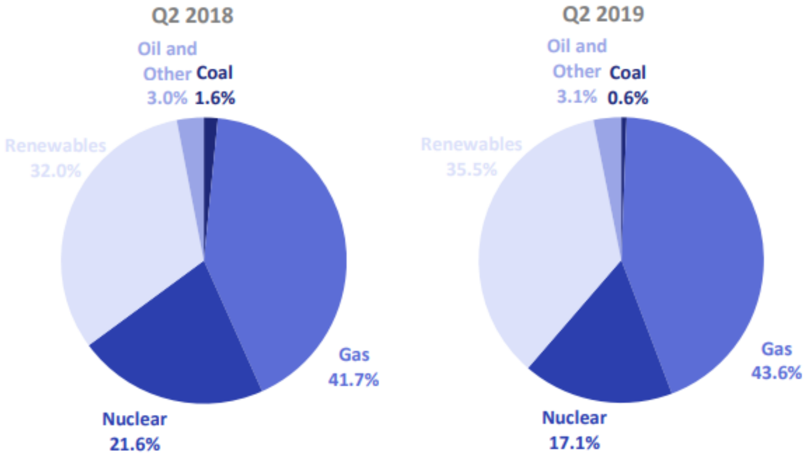

Figure 1.1: Sources for the production of energy in the UK for Q2 in 2018 and 2019 [4].

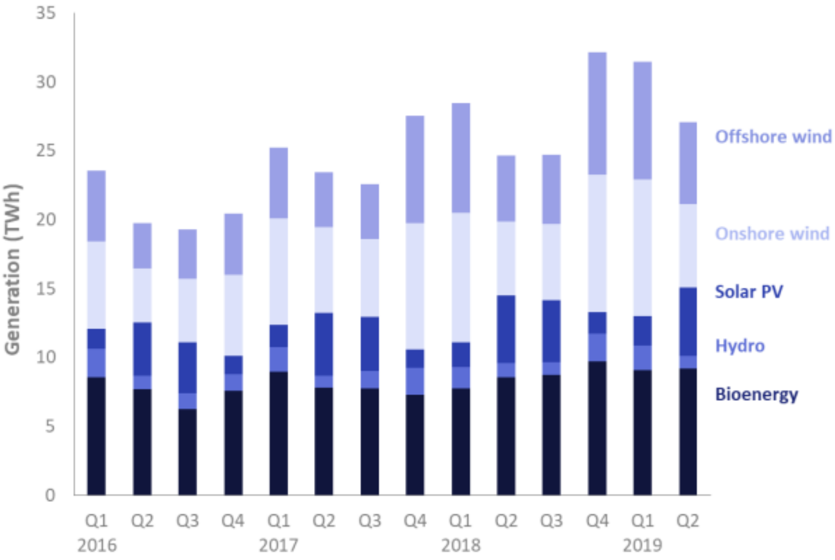

Figure 1.2: Breakdown of renewable energy sources within the UK since 2016 [4].

1.2 Marine renewable energy

Marine renewable energy is used to describe the energy that is available from the sea. The UK has the benefit of access to extensive reaches of coastline that are suitable for marine energy extraction through one of three ways; wave energy, tidal range and tidal stream. Wave energy is in essence a form of wind energy. The interaction of the wind blowing over the sea for long stretches causes the formation of waves through the energy transfer from the wind to the sea. Most of this energy is found at or near the surface of the sea. The engineering challenges faced by designers trying to harness wave energy are not to be underestimated. Devices must operate and extract energy in a highly energetic region of the sea. The unpredictable nature of the wind means that wave energy is also an unpredictable energy resource.

While wave energy offers a strong potential energy resource around the UK, both tidal range and tidal stream are more predictable, and operate in regions that are less energetic, simplifying the engineering challenges.

It is estimated that the theoretical UK resource for marine renewable energy is in the region of 285 TW h, of which 216 TW h could be supplied from both tidal range and tidal stream [7]. These figures are based on large scale deployment of marine technology to maximise the vast potential within the oceans around the UK coastline. It is estimated that if both tidal range and tidal stream resources were exploited then approximately 10 % of the UK's energy requirements could be fulfilled [8] based on the technology at this time.

1.2.1 Tidal range

Tidal range works using barrages or lagoons to control the flow of water as required. A barrage is usually positioned at an estuary and spans the width of the estuary mouth. A lagoon on the other hand is a self-contained area that is completely artificial and is generally constructed in a region of shallow water that has a high tidal range [8]. Both use turbines housed within the structure to generate energy as flow passes through. It works by exploiting the gravitational potential energy that is generated by creating a head on one side of the wall. When the gravitational potential is at its maximum the water is released through the turbines. Due to the periodic nature of the tidal cycle there are either one or two low and high tides per lunar day. The larger the tidal range at a location, the greater the energy potential.

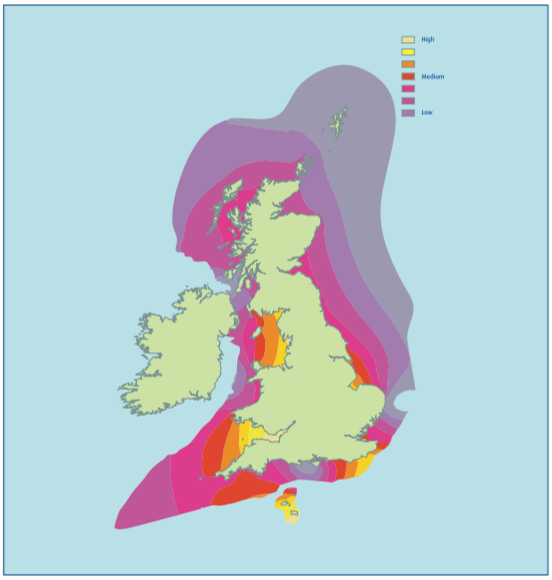

Figure 1.3: The tidal range resource around the UK coastline [8].

This form of marine energy extraction is very predictable due to both the cyclic nature of the tides and that the tidal range is well characterised for many sites globally, during both the spring and neap tides. The turbines housed within the barrage are subject to a less harsh environment than at open sea and so do not suffer from the same maintenance requirements. The design, production and completion of the barrage is a huge engineering undertaking. The expected capital costs are high, and the required project time makes tidal range a less attractive method. Not only this but there are environmental impacts that are associated with 'blocking' estuary mouths or even large regions of coastline [8].

One area of active interest in the UK is the Severn Estuary. It has one of the highest tidal ranges in the world with a tidal range of 14 m [9], and the highest anywhere around the UK, as shown in Figure 1.3. Several variations for how best to capture this resource have been proposed however none have gained any major traction yet. Beyond the installation there are wide reaching concerns over the impact a barrage might have on the mean water level at high and low tide, sediment transport, salinity gradients and the effects on ecology, habitats, birds and fish.

One example of a barrage is the La Rance barrage in northern France. It was completed in 1966 and is located on the estuary of the Rance River, Brittany, France. The barrage houses 24 turbines and has a total capacity of 240 MW [10]. There was a very large impact on the local marine ecosystems during the construction of the barrage due to the disrustion of habitat and changes to the salinaity gradeint in the estuary, but within 10 years the marine life was as diverse as before. The successful development of such a barrage highlights the potential for tidal range technology, however only a handful of projects have been successfully completed since then in Canada, China, Russia and Korea [8, 11].

While a brief overview of tidal range has been given, the associated engineering and financial difficulties and the consideration of the disruption of to the local marine habitat make it less appealing as a means of marine renewable energy and so it is not the focus of this thesis and is not discussed any further.

1.2.2 Tidal stream

Tidal stream energy extraction utilises the kinetic energy of the tidal current to generate electrical energy as water flows through a turbine rotor. The devices are located at regions that have a high tidal flow velocity to maximise potential power extraction. The fundamental technology is heavily based on the wind industry.

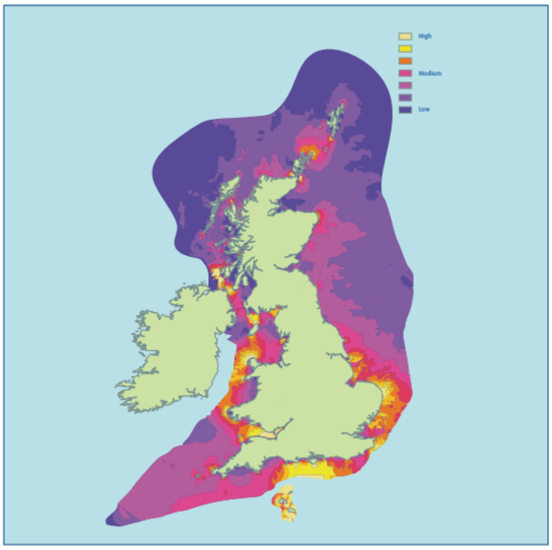

Figure 1.4: The tidal stream resource around the UK coastline [8].

While the principles of energy generation remain similar to the wind industry, there are unique difficulties for both tidal stream and tidal range technologies. The marine environment is harsh, and no devices have been subject to extended submerged periods to fully understand the impacts on device life. Developers must not only consider the marine habitat and ecosystems that may be disrupted, but also design for saltwater corrosion and biofouling. Devices are usually located on the seabed or suspended within the water column. The associated environmental impact during installation and operation of a device is smaller when compared to tidal range options. It remains to be seen what impact full scale arrays may have on the marine ecosystem [12].

Figure 1.4 shows the flow velocity for sites around the UK. Deployment in regions with the highest tidal flows are preferred. Recently the Tidal Stream Industry Energiser Project (TIGER) received €46.8 million and aims to focus on improving the tidal stream sector [13]. The project aims to install 8 MW of tidal capacity in The Channel, between the UK and France. To achieve this capacity multiple devices will be installed from different developers. The hope is that by using economies of scale, the cost can be brought down, making TIGER a perfect platform to show that energy generation from tidal sites can be cost-effective, ultimately acting as a springboard for future tidal development. The project involves 19 partners from across the UK and France and is led by the UK's Offshore Renewable Energy (ORE) Catapult.

1.3 Other projects

The work conducted throughout this thesis was done in conjunction with the dynamic loading of tidal turbine arrays (DyLoTTA) project (EP/N020782/1). The DyLoTTA project focussed on studying the loading and performance of different configurations of tidal stream turbine arrays using numerical modelling and model scaled experiments. Part of the work proposed involved the the design and testing of the lab scale device as well as the numerical modelling of the devices. Therefore the work in this thesis was conducted alongside the project and any design work or experimental testing described in the following thesis was conducted by the author. The work in this thesis also built on previous findings of work conducted at Cardiff University by Ebdon [14].

1.4 Thesis aims and objectives

To compliment the proposals of the DyLoTTA project the aim of the work in this thesis was to investigate the performance characteristics of both single and multiple tidal devices using computational fluid dynamics and experimental testing. This was achieved via the following objectives:

- The development, characterisation and validation of a new rotor geometry using experimental and numerical methods.
- Investigation of the impact that the turbulence model and discretisation scheme had

on the rotor performance and the wake prediction.

- A study using computational fluid dynamics to assess the performance characteristics of a downstream device based on the inter-device spacing.
- Undertaking experimental test campaigns to provide validation for the numerical models, looking at wake recovery and device interaction.

1.5 Thesis layout

Chapter 1 introduces the thesis and the drivers for renewable energy, with a focus on marine renewable energy and specifically tidal energy. It contains the thesis aims and objectives and the thesis layout.

Chapter 2 presents a literature review describing the technology, current state of marine energy research and resource estimations. This explains the importance of and requirement for the modelling of device interaction and the impact of turbulence on a device. It reviews previous research to show the current industry progress and shows the suitability of CFD modelling to the desired task in relation to previous works.

Chapter 3 details the applicable theory used for the modelling and analysis of tidal stream turbines within this work.

Chapter 4 presents the methodology and results for the design of a new blade that is modelled as part of the work in this thesis. A comparison is made between the new blade design and the existing design used in the past.

Chapter 5 provides a comparison between the discretisation schemes available in ANSYS CFX and their suitability to the modelling of turbine wakes and prediction of device performance.

Chapter 6 studies the performance of a downstream device in three locations downstream of a first generation device; directly in the wake, partially in the wake and fully out of the wake.

Chapter 7 provides the conclusions from the thesis and recommendations for further work.

Chapter 2

Literature review

This review gives an introduction to tidal energy. Examples of devices currently under development and testing are given. Following this a more in-depth review on numerical and experimental methods and their use to the marine industry are discussed. Work on lab scale devices is presented when used for characterising turbine performance. Following this a review of studies looking at the influence of grid generated, and device generated turbulence on rotors in the flow and as part of arrays. The influence of array spacing, turbulence intensity and length scale on blade fatigue is discussed. This is not an in depth study on blade fatigue, but highlights the loads that can lead to fatigue issues. Finally, the suitability of ocean scale models used for array layout and resource estimation is examined.

2.1 Tidal stream devices

Despite the increasing interest in tidal stream energy generation over both that of wave and tidal range the industry has not reached a level of commercial readiness that lends itself to large-scale deployment. There are currently several companies independently testing and developing tidal devices and there are a couple of projects currently in progress around the UK coastline and the European Marine Energy Centre (EMEC) has provided a great foundation upon which to develop and test potential tidal devices. Table 2.1 gives an overview of active examples of tidal stream technology.

Several devices now exist and the majority fall into one of three categories; horizontal axis, vertical axis or oscillating devices. The main area of active research in the industry is focussed around the first two categories. A select number of the devices in Table 2.1 will be discussed in greater detail throughout the following chapter.

Table 2.1: Summary of active development and testing of tidal stream technology.

Developer	Technology type	Device name	Rotor diameter, *m*	Total rated capacity, *MW*	Status
SIMEC Atlantis [15]	HATT - 3 blades	AR1500	18	1.5	2016 - Grid connected
	HATT - 3 blades	AR2000	20-24	2	Under construction
Orbital marine Power [16]	2 x 2 bladed HATT - Floating platform	SR2000	16	2	2018 - Removed for Orbital 02
	2 x 2 bladed HATT - Floating platform	Orbital 02	20	2	2020 - deployment @ EMEC
Sabella [17]	HATT - 6 blades	D03-30	3	0.03	2016 - 2009 - Removed
	HATT - 6 blades	D10-1000	10	1	2016 - 2016 - Removed
	HATT - 6 blades	ICE D10-1000	10	1	2019 - Deployed
	2 x HATT - 5 blades	PHARES D12-500	12	1	2019 - Under construction
Sustainable Marine Energy [18]	4 x 3 bladed HATT - Floating platform	PLAT-I: SIT250 turbines	4 - 6.3	0.28	2018 - Deployed
	Submerged platform	PLAT-O: SIT250 turbines	4 - 6.3	-	Under development
Minesto [19]	Tidal kite	Deep Green	1.5	0.5	2018 - Deployed
Nautricity [20]	Contra-rotating - 3 and 4 bladed device	CoRMat	10	0.5	2018 - Recovered for future deployment
EEL Energy [21]	Flexible Membrane	-	-	1	Under development
Verdant Power [22]	3 x 3 bladed HATT - Tri frame	KHPS	5	0.135	2020 - deployment @ New York City East River
Andritz Hydro Hammerfest [23]	HATT - 3 blades	HS1000	18	1.5	2016 - Grid connected
Magallanes Renovables [24]	Floating platform	ATIR Ocean 2G	19	2	2019 - Grid connected @ EMEC

2.1.1 Horizontal axis tidal turbines

Horizontal axis tidal turbines (HATT) are most closely related to the common wind turbine in both design and operation. The rotational axis of the device is aligned with the direction of the free stream flow. However, several differences remain, most notably the rotor diameter and the proposed operating environment. The higher fluid density in tidal flows increases the structural loading on the blades and support structure, limiting the size of the device. The devices are designed to be fully submerged so the rotor radius must be small enough so as not to interfere with shipping traffic at low tide.

The marine environment offers many challenges. The harsh surface conditions limit the safe operating windows for installation, maintenance and removal of tidal devices [25]. Under the surface not only must the devices be watertight, but the highly corrosive nature of saltwater requires devices to be engineered so that their life expectancy makes the project cost effective. Marine biofouling can also impact the life expectancy and performance of the device [26]. Several devices have used bed mounted gravity bases, so the bathymetry plays a large part in dictating the potential location of device installations.

The focus of this thesis is on both single and multiple HATT devices and so a few examples of existing devices have been given, most of which are the focus of active projects.

SeaGen

The SeaGen device was the first commercial scale, grid connected tidal stream project and was deployed by Marine Current Turbines (MCT) in the Strangford Lough, Northern Ireland between 2008 - 2019 [27]. The device consisted of two, two-bladed, 600 kW, 16 m rotors [25] at a rated flow speed of $2.25\,\mathrm{m\,s^{-1}}$. The rotors could be removed from the water for maintenance, and the device is displayed in Figure 2.1. The blades had active pitch control allowing the blade pitch to be changed depending on if it were an ebb or flood tide. MCT were acquired by Atlantis in 2015 and the project was completely decommissioned in 2019 [27]. During this time over 11.6 GW h of power was exported to the grid.

One of the main benefits of the SeaGen device was the accessibility of the rotors. Due to the crossbeam support structure the ability to raise the rotors out of the water reduced maintenance costs. There was no reliance on specialist vessels to remove the device during short windows of slack tide, a large associated cost for certain devices [25]. The mono-pile was surface piercing so the device would not be suitable for use near shipping lanes.

Figure 2.1: The SeaGen device that was in Strangford Lough between 2008 - 2019 [28].

SIMEC Atlantis Resources

SIMEC Atlantis use a three-bladed device, which most closely highlights the impact of the wind industry on HATT design. The first of the Atlantis devices is the AR1500, Figure 2.2. It has a rated power of 1.5 MW for an 18 m diameter device [29]. The turbine uses a gravity base to secure the device to the seabed. Two AR1500 devices are currently deployed in the Pentland Firth, Scotland, as part of the MeyGen project [15]. Phase 1A of the project has now been completed where 4 devices were grid connected exporting 17 GW h to the grid. The turbine has yaw control allowing the turbine rotor to turn into the oncoming flow. Unlike pitch control this allows the rotor to always be upstream of the stanchion and nacelle. If the nacelle is upstream of the stanchion, then the performance decreases while the amplitude of the load fluctuations increases [30].

More recently Atlantis have begun development of the AR2000 device which will be used for phase 1B of the MeyGen project which has recently been given the go ahead [15].

Sustainable Marine Energy

Sustainable Marine Energy (SME) have partnered with the propulsion team at Schottel to develop PLAT-I, seen in Figure 2.3. PLAT-I is a floating platform that houses an array of 4 Schottel SIT250 devices. The devices have a diameter of 4 - 6.3 m with a rated power of 54 - 70 kW [32]. The rotor uses composite blades and has no active pitch mechanism. As PLAT-I is a floating platform it is designed for use in more sheltered locations, and is currently deployed in the Grand passage, Nova Scotia [18]. Each of the 4 devices can

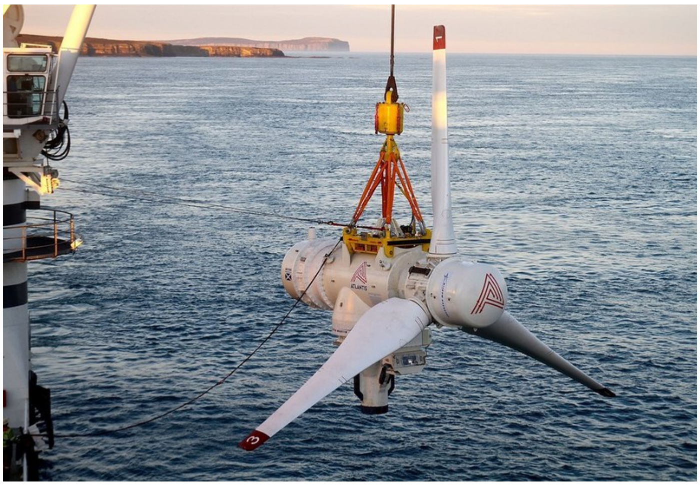

Figure 2.2: The AR1500 device from Atlantis that is currently deployed in the Pentland Firth [31].

be individually removed from the water to allow for easy maintenance, again reducing the dependency of specialised vessels.

Figure 2.3: The PLAT-I platform using 4 of the Schottel SIT250 devices [33].

Rough sea conditions make for a hostile environment to deploy surface-based arrays and so SME and Schottel are developing PLAT-O, shown in Figure 2.4. This is for use in open sea and is a bed mounted platform that aims to reduce the impact associated with extracting energy from the higher regions of the water column [34].

Nautricity

The CoRMaT HATT developed and tested by Nautricity uses two contra rotating rotors, a 3 bladed rotor that sits directly upstream of a 4 bladed rotor, see Figure 2.5. The two

Figure 2.4: The PLAT-O platform using 4 of the Schottel SIT250 devices [34].

contra-rotating rotors mean that no gearbox is required as the turbine drives the contra-rotating generator. The torque is therefore split between the two rotors eliminating the reactive torque that is usually supplied by the rigid support structure. For this reason, the device can be moored, rather than fixed and enables a greater range of operating depths between 8 - 500 m [20]. The 10 m diameter 500 kW device was deployed at the EMEC's Fall of Warness test site in 2017 and was recovered in 2018 to determine the impact of extended deployment on the device [35]. The other benefit of such a mooring system is that the device does not suffer from blade-stanchion interaction.

Figure 2.5: The contra-rotating CoRMat device developed by Nautricity [36].

2.1.2 Vertical axis tidal turbines

The difference between a HATT and a vertical axis tidal turbines (VATT) is the orientation of the rotational axis in relation to the flow direction. For a VATT the rotational axis is perpendicular to the stream wise flow direction. The benefit of this is that the orientation of the blades and turbine rotor need not be changed to capture the ebb and flood of the tide [37]. The blades themselves are either straight or helical and usually take the appearance of an extruded aerofoil. The simplicity of both the blade design and the lack of active pitch or yaw control can substantially reduce the cost of the devices. A selection of example devices can be seen in Figure 2.6.

Due to the nature of the rotation the vortices shed from the upstream blade will affect the performance and loading on the downstream blades. Not only that but the relative pitch angle will change throughout the rotation heavily affecting the torque generation throughout the cycle. This can lead to lower performance coefficients, compared to HATT's [38]. For a comprehensive list of vertical axis tidal developers the reader is directed to [39].

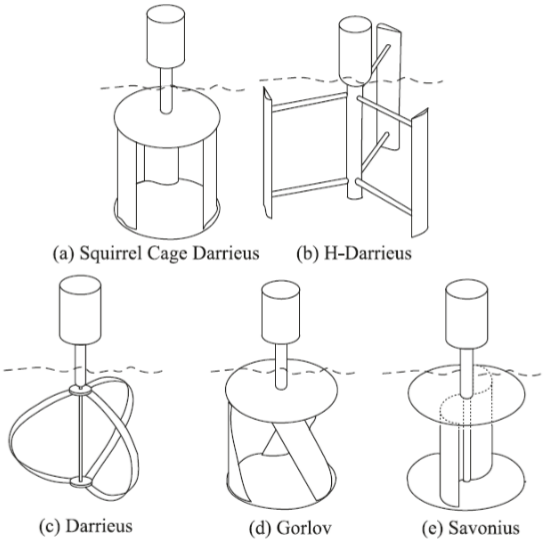

Figure 2.6: Example of vertical axis tidal turbines [40].

2.1.3 Oscillating devices

Oscillating devices generally fall into two categories; either a fixed hydrofoil or a flexible membrane. For the fixed hydrofoil, the hydrofoil acts as a wing using the tidal current to generate the lift required to drive the device. The hydrofoil is then connected to a hydraulic system which in turn converts the motion of the hydrofoil into electricity [41]. The other alternative uses a flexible membrane that is held by tensioned cables keeping the membrane curved. The pressure changes over the membrane due to the fluid motion cause the membrane to continuously undulate. The membrane undulation is converted into electricity by an electromechanical system that runs the length of the membrane [21].

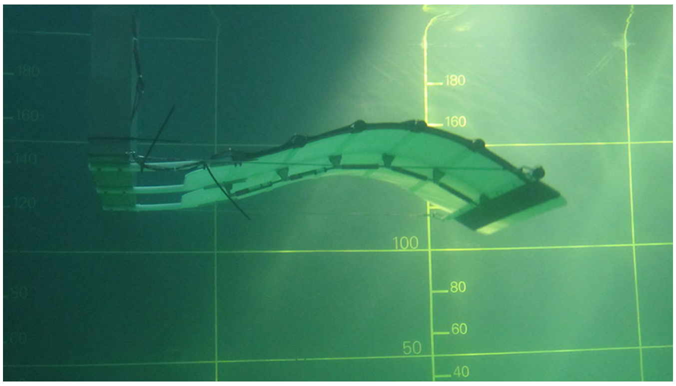

Figure 2.7: The oscillating tidal device from EEL Energy undergoing testing at IFREMER [42].

An example of a flexible membrane is the one developed by EEL Energy, shown in Figure 2.7. It has been subject to scale testing at the Institut Français de Recherche pour l'Exploitation de la Mer (IFREMER) flume in Boulogne-Sur-Mer, France, as well as two sets of sea trials on the 1:6 scale device. The development of a larger device is currently taking place, and EEL Energy are looking for a maximum of €7 million to aid development. The aim is to develop larger 30 kW and 100 kW devices that are suitable for the lower velocities seen in rivers, before expanding to a 1 MW device for the marine environment [43].

2.1.4 Other tidal devices

There are a few devices that do not fit into the previously mentioned technologies categories. An example of one of these devices is the Minesto 'Deep Green', which is currently undergoing development and testing, shown in Figure 2.8. The device has a 1.5 m diameter, 0.5 MW, rotor fixed beneath a 12 m wing. The interaction of the tide with the wing generates a lift force that is used, along with a rudder and servo, to drive the wing in a figure 8 motion. The device is tethered to the seabed. The turbine rotor is estimated to see flow velocities several times greater than that of the actual free stream flow velocity due to the acceleration of the device in the water based on the lift generation of the wing [19]. The design of the device makes it both smaller and lighter than other commercial designs, making installation and removal easier, ultimately driving down the cost per MW. However, the reliance on the control algorithms to ensure the wing flows in a smooth pattern to optimise power extraction means that the system must be very finely tuned and robust.

Minesto are currently undertaking commissioning tests in Holyhead, UK, and aim to deploy a tidal array with a potential power capacity of 80 MW [44].

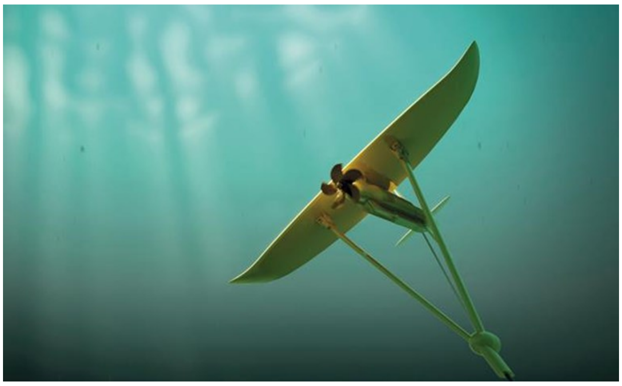

Figure 2.8: The 'Deep Green' device by Minesto [19].

An overview has been give of the different types of devices that are currently under development however HATT's are the most commonly developed and tested device to date. Going forward the focus of the literature review and the remainder of the work in this thesis will focus solely on HATT's.

2.2 Resource assessment and estimation

There has been significant work on the potential tidal resource assessment around the UK coastline [45, 46, 47]. While not the main area of interest for this thesis it is necessary to understand the basic environmental conditions that a device will be subject to when deployed.

Acoustic doppler velocimeter (ADV) and acoustic Doppler current profiler (ADCP) measurements have been used to provide information on proposed sites to inform developers as to the expected flow characteristics [48]. To gain the most from these studies the ADV's must be deployed for a prolonged period. The IEC 62600-200 standard proposes a standardised method for evaluating the power performance of a tidal turbine. It proposes ADCP regions upstream of the device that could be used when trying to determine the onset flow to the device however further information on resource assessment is found in IEC 62600-201. The swept area of the rotor is split into a number of segments and ADCP measurements are taken at each segment for ten minutes [49].

This does mean that a large number of data points must be captured for a considerate total length of time if the onset flow to the rotor is to be characterised using the proposed standard, which is not always possible during lab scale testing. Studies by both Blackmore et al. [50] and Mycek et al. [51] took a grid of LDV measurements over the swept area of the rotor. However the time taken to map the flow is significant and so a number of other studies [52, 30, 14] have used single point measurement upstream.

The turbulence characterisitcs at the proposed site must also be taken into consideration. Milne et al. [53] obtained a set of time histories for the flow velocity at a location and found that 5 m from the seabed the turbulence intensity was approximately 12-13 % in the streamwise direction. This was in keeping with other literature that recorded values between 8.4-13 % [54, 55, 56, 57]. However the value for TI is not contanst between sites and can vary at individual sites with the ebb and flood tide as found by Gooch et al. [58] when characterisitng sites near Marrowstone Island, Puget Sound. It is thererfore likely that flow characteristics will be site specific [53], however most proposed tidal sites will be turbulent in nature.

Based on the work of [59] the proposed channels for device deployment have the potential to produce 10-1000's of MW of electricity. While not all this resource will be realised at all tidal sites it shows the suitability of tidal energy for helping deliver alternative sources on energy. The number of devices installed, and the size of the devices, will change the resource available in the channel. The estimation of resources and how best to optimise energy extraction is not as simple as assuming a total installed capacity based on a set number of devices. The changing resource and device interaction must be considered to give an informed and realistic estimation for a site.

O'Hara Murray and Gallego [60] found that with maximum extraction in the Pentland Firth there were huge changes to the volume transport in the region as well as a drop in the tidal speed and water elevation in local areas. The associated environmental impacts of this are unknown but expected to be high. This was based on extracting the theoretical maximum amount of energy from the flow, the actual amount extracted will be much less. It highlights the importance of understanding and simulating more realistic scenarios that are more representative of the scale of deployment that is proposed by the industry.

To try and capture a more realistic estimation Lewis et al. [47] used a model of the Irish sea to estimate the resource available based on a minimum operating velocity of $2.5\,\mathrm{m\,s^{-1}}$ and a maximum depth of 25 m, the proposed requirements for 1st generation devices [61]. The total feasible area which fit the specifications was limited, reducing the total resource dramatically. However, if installation depth was increased and devices were optimised for a flow velocity of 2 m/s then the resource estimations became more favourable.

This understanding of the expected flow can be used to improve the prediction of ocean scales models and resource estimations as well as the order of magnitude required for experimental and numerical simulations.

2.3 Tidal stream research

The ability to model and test tidal devices under numerous conditions increases the understanding of how device performance will change given a certain scenario. This progression will help drive the tidal energy sector to a position of commercial viability while simultaneously building the base for more in depth studies. Numerical modelling techniques and experimental test campaigns have been used in tandem to accelerate the rate at which data is now gathered, broadening the understanding of tidal stream energy. There are numerous studies that use numerical and/or experimental methods, and cover everything from characterising lab-scale devices to the optimisation of array layout in current locations of interest. The following work aims to highlight these studies and give an overview of the current state of tidal stream research.

2.3.1 Numerical modelling of tidal stream turbines

At present it is difficult to quickly and cheaply physically design, develop and manufacture a tidal stream turbine, meaning other methods are required when estimating device performance and behaviour. Numerical modelling techniques have improved in recent years and lend themselves to the problem of characterising device development and performance. Several numerical methods now exist for, but not limited to, simulating aerofoil design, device performance, cavitation, estimating turbine wakes, device interaction, wave-current interaction and the optimisation of full-scale arrays based on site information [52, 14, 62, 63]. There are limitations. Most obvious and important is the compromise that is made between the accuracy of the model and the solution run time

[64]. In an ideal world each model would directly simulate all aspects of a tidal device, from the performance to the wake, resolving all aspects of the flow to the smallest length scale. With the current computing power this is not possible, and so several methods now exist that aim to simplify the problem, while still providing adequate levels of detail for the desired set of testing.

This section will review the methods of numerical models utilised for device development. The description of modelling methods begins with the comparatively simple actuator disk theory before progressing in complexity and finishing with blade-resolved methods.

Actuator Disk Theory

Actuator disk theory or momentum theory uses an infinitely thin disk to represent the swept area of a turbine [65]. Mass conservation is assumed throughout the system and the disk is surrounded by a stream tube that increases in size downstream of the turbine. There is no knowledge of the turbine geometry within the model. The turbine is represented via a thrust force that is exerted on the fluid. The flow characteristics seen downstream and just upstream of the device are sensitive to small changes in the thrust force.

The flow velocity cannot be reduced to zero downstream of the actuator disk otherwise there would be no flow passing through the rotor, therefore implying there is a limit to the total power extraction. No-flow through a turbine rotor would occur for an axial induction factor of 0.5 whereas the peak power coefficient is for an axial induction factor of 1/3. The Betz model showed this limit to be when the power coefficient $C_P = 0.593$ [65]. In application the efficiency of most devices is well below this limit. It is possible to exceed the Betz limit when a turbine is placed in a tidal farm due to the increased turbine blockage in a channel [66]. However the flow is reduced in a tidal array due to the extraction of power by the devices. Therefore exceeding Betz limit does not mean more power is necessarily being extracted by a turbine from the flow as the flow is reduced in a tidal farm.

Blade Element Momentum Theory

The Blade Element Momentum Theory (BEMT) is a combination of the blade element and momentum theories [67]. It was developed initially for use in the wind industry to aid in the performance prediction of rotor designs [68] however it has more recently been used in the tidal industry for the same reasons. One benefit is that it requires very little computational time and power to produce a solution. An overview of the basic principles of BEMT have been given in Chapter 3.

BEMT offers a 2D approach to characterising the performance of a turbine based on the blade element and momentum theories. The quick computational time and relative simplicity with which a basic version can be executed makes it popular for modelling blade design and device performance. It has been used for a number of applications including; blade design at different scales, blade loading, wake recovery for coupled simulations and array modelling, modelling wind and tidal devices and with uniform and profiled flow for both vertical and horizontal axis devices [69, 70, 71].

Computational Fluid Dynamics

Computational fluid dynamics (CFD), while generally considered more computationally expensive, allows for the resolution of the entire flow field rather than just the lift and drag forces on the rotor. It is widely used to model anything from chemical reactions to weather prediction and more relevant to this work the marine environment [30, 52]. CFD codes aim to resolve the Navier-Stokes equations [64], discussed in greater detail in Chapter 3, under given boundary conditions. One of the most common methods of doing this, and most applicable to this work, uses the Reynolds averaged Navier-Stokes (RANS) equations.

Lower fidelity CFD methods can still incorporate elements of BEMT or actuator disk theory in order to simplify the simulation. Coupled BEMT-CFD simulations use elements of both BEMT and CFD. The norm is to represent the turbine or device by means of an actuator disk in the flow. However rather than assuming the disk to impart a uniform thrust on the oncoming flow field it takes information from BEMT. The thrust and power coefficients from BEMT are assumed to act on the disk and so the thrust force acting on the flow changes with respect to disk radius. By superimposing the rotor characteristics on to the disk there is a better prediction of the thrust exerted on the flow by the disk. A CFD package is then used to model the flow around the disk.

The more complex, higher fidelity, modelling approaches allows the user the ability to model the full rotor using blade-resolved models and allows the flow physics to be captured in 3 dimensions around the blade. Coupled with a transient simulation, the rotational components imparted by the blade on the flow can be modelled. This modelling leads to a more realistic representation of the flow as it interacts with a device. The turbulence models used in the CFD codes play a large role in dictating the level of resolved detail that is achieved in the model, and further detail on common turbulence models and the implementation of them is given in Chapter 3.

There are several CFD packages that are either commercially available, open source, or in-house codes. Examples of popular CFD packages include; ANSYS CFX, ANSYS Fluent, Star-CCM+, OpenFOAM. As CFD in general is pushed forward by advances in computing resources the differences between what each of these models can achieve is reduced. The repeatability of results between CFD packages will help improve confidence in CFD modelling.

2.3.2 Design of tidal stream turbines

As yet no single design has been settled on within the industry, with companies preferring to design and develop individual devices [15, 16, 17, 20]. While most of the current technology uses a three bladed rotor, all use different rotor geometries. The ability of tools such as BEMT and CFD models to aid in the design process has the potential to reduce design cost. While they are not without their shortcomings many studies have used a combination of numerical methods, validated against experimental data, as a method for the design and testing of new devices.

Prediction of lift and drag coefficients

BEMT has already been touched upon as a method for predicting the turbine performance and more information can be found in Chapter 3. However the accuracy of the predictions from BEMT are dependent upon the prediction of the lift, C_L, and drag, C_D, coefficients which are used when determining the performance of the aerofoil at each radial section. A lookup table is required that contains the C_L and C_D values for a range of angle of attacks (AoA). A couple of methods can be used to generate the C_L and C_D; 2D CFD, experimental testing of aerofoil profiles or 2D panel methods. While 2D CFD is not strictly a 2D analysis, the thickness is assumed to be one cell with a size considerably less than the chord length. Aerofoil profiles can be tested in wind tunnels or flumes, however matching the Reynolds number, if the testing has not determined the point of Reynolds independence, is important if the results are to be compared.

An example of a panel method is XFoil. It was proposed by Drela [72] and suggests a new method for aerofoil design which uses a 2D panel method to perform analysis for viscous, inviscid or inverse analysis calculations. The aerofoil is broken up into several panels, which can be unevenly distributed around the blade profile to capture leading and trailing edge regions in more detail. The pressure distribution is then resolved for the aerofoil allowing the lift and drag coefficients to be determined.

Molland et al. [73] compared experimental values for the lift and drag with XFoil for a selection of NACA profiles. The angle of attack was varied between -10 and 20° focussing on a flow speed of $4\,\mathrm{m\,s^{-1}}$. The tests found good agreement between XFoil and the experimental data when predicting the lift coefficients. For the drag coefficients the prediction was not as accurate at low AoA's and considerably under predicted for AoA's greater than 7 degrees. This under prediction is likely to be caused by the fact that XFoil is a 2D method and so the numerical prediction of stall and separation are not resolved adequately. Batten et al. [74] also found similar agreement between experimental and XFoil predictions for C_L and C_D.

A study by Goundar et al. [75] combined XFoil and 2D CFD. The study found good agreement, at the same Reynolds number, between XFoil and experimental tests for the pressure distribution and the lift coefficient. While CFD gave good predictions for the pressure distribution, the lift coefficient was under predicted. Similar results were found by Jo and Lee [76] who found that the characteristics of the NREL S814 aerofoil were different for the CFD when compared to the experimental data. Morgado et al. [77] compared XFoil to two different CFD packages, Fluent and OpenFOAM, for a chord based Reynolds number of $2x10^5$ when looking at a propeller. Reynolds number is discussed in greater detail in Chapter 3. The results showed that XFoil gave better predictions when compared to the experimental results than both CFD packages, especially for a low angle of attack. It was also found to be much easier to use and implement than the more complex CFD packages.

The computational time to run 2D CFD models is high, compared to XFoil, as the boundary layer needs to be resolved very accurately requiring very high mesh resolution for a complex geometry. The studies show that XFoil allows for a rapid and accurate method for predicting aerofoil characteristics, thus allowing designers to quickly test new aerofoils.

Blade design

The optimisation of a HATT blade is important to maximise energy extraction. Emphasis is therefore placed on ensuring HATT blades have a high power coefficient, C_P. However, a trade-off must be made between power capture and thrust loading on the blades. High thrust coefficient, C_T, values for a blade will lead to high thrust loads during operation and a shorter life expectancy. Several factors influence the performance of a blade; chord length, aerofoil, pitch angle and twist being of high importance. Consideration must be given to all elements in the design process and in particular to the environment that they will be operating in. Numerical methods such as BEMT and CFD are useful tools that can be exploited by developers to help optimise new blade designs.

Lee at al. [78] compared CFD and BEMT. The C_P curves for BEMT and CFD exhibited similar estimates for the trend of the curve and the peak tip-speed ratio (TSR). Small differences were observed for TSR < 4 and TSR > 8. These were outside of the perceived operating region and deemed non-trivial, showing that BEMT is a useful tool when it comes to the initial work for blade design. It is worth noting that only one blade was modelled in the CFD simulation with the assumption of rotational symmetry.

A study by Lawson et al. [79] used the HARP_opt code that is freely available from National Renewable Energy Laboratory (NREL) [80]. It uses a genetic optimization algorithm coupled with BEMT to improve the performance of the aerofoil. At each radial section of the blade it manipulates the shape of the aerofoil and finds the optimum blade characteristics. The BEMT under predicted the results for the hydrodynamic forces on the blade when compared to the CFD modelling. However, there was reasonable agreement overall between the CFD and the BEMT based HARP_Opt results giving confidence in both numerical methods as a means for designing a HATT blade. Neither of the numerical results were compared to experimental data.

Batten et al. [81] used the experimental data from Bahaj et al. [82] to validate the use of BEMT for the design of a HATT blade. BEMT was shown to provide satisfactory agreement when compared to the experimental data when used for the prediction of the device performance.

However, limitations of BEMT exist and one of them is that it only works with flows that are considered in the same plane as the aerofoil. No spanwise flow is considered, which is present in 3D flows, especially with rotating surfaces [65, 78]. The lack of spanwise flow impacts the modelling of flow separation over the blade, affecting the prediction of the lift and drag forces [83]. The flow behaviour over the blade is complex at high and low TSR values and the inability to model spanwise flow can subsequently affect the predicted performance. It does however provide a quick and easy method for designers when looking at optimising blade characteristics.

BEMT is one of the preferred numerical tools when looking at the performance of turbines despite having limitations. Studies ranging from 1/20th scale rotors [76] to full-scale rotors [75, 79, 81] have used BEMT to provide an initial blade design which is subsequently used for further CFD or experimental testing.

2.3.3 Performance of individual tidal devices

The prediction of device performance is of obvious importance if there is to be an accurate representation of array power output. A fully characterised device under different flow conditions will shed light on the expected behaviour of the device and several studies have started to address this [84, 85, 86, 87]. This understanding can help inform the manufacture and design of devices. The impact of scaling is considered an issue as many experimental tests are conducted at lab-scale [88]. Little data is readily available for full scale devices currently deployed. One alternative approach is the use of numerical modelling for device prediction. Lab-scale testing can be used to validate numerical models, which in turn can be used for the estimation of full-scale devices.

Experimental testing

Bahaj et al. [82] studied the performance of an 800 mm diameter, three-bladed HATT in both a cavitation tunnel and a tow tank. A strain gauge dynamometer placed directly behind the rotor was used to measure the torque and thrust. The rotor was well characterised under several flow conditions. The data has since been used by several studies as a means of validation for numerical models [78, 81, 89, 90]. Similar experimental tests were conducted by Mason-Jones [52] at the University of Liverpool recirculating flume using a 500 mm diameter prototype HATT. A comprehensive test campaign was conducted and used as validation for CFD models. This same device was used for further testing at IFREMER [14] and the Istituto Nazionale Per Studi Ed Esperienze Di Architettura Navale, Italy (INSEAN) [85].

The relationship with Reynolds number must be carefully observed for lab scale devices and is discussed in greater detail in Chapter 3. Mason-Jones et al. [91] found that for the devices tested, a 0.5 m diameter device, the non-dimensional performance parameters became independent of a rotor based Reynolds number in excess of $5x10^5$. In another study Doman et al. [92] tested a 1/20th scale device in the Kelvin Hydrodynamics Laboratory (KHL) tow tank looking at device performance. The study performed extensive testing over a full operational range to obtain the power and thrust coefficients. It showed the dependency on Reynolds number during the tests, hence why it is important to use a variety of flow speeds to ensure Reynolds independence has been reached.

In a similar study Jo et al. [76] also tested a 1/20th scale physical model, this time in a circulating water channel at Inha University. The results were used to validate a CFD model.

Numerical modelling

A number of CFD studies have been carried out at Cardiff University [30, 52, 93, 94] looking at the influence of high shear flows, flow direction, stanchion positioning, solidity and swirl on the performance and characteristics of tidal devices. This wide range of studies shows the suitability and capability of CFD modelling to assist in the characterisation of tidal devices.

A study by Bai et al. [95] modelled a coupled BEMT-CFD simulation. Good agreement was found between the experimental and numerical data sets when predicting the C_P of the device. Bahaj et al. [89] used two different BEMT codes to determine the characteristics of a three bladed device. The data was compared to the experimental data obtained in a cavitation tunnel and tow tank by [82]. Good agreement was found between the BEMT codes and the experimental data.

McSherry et al. [90] performed a transient simulation for a blade-resolved device based on the experimental testing performed by [82]. The commercial code ANSYS CFX was used. The numerical and experimental data for the thrust and power coefficient showed good agreement, especially for TSR values around the desired operating region (peak power). O'Doherty et al. [84] also saw good agreement between CFD simulations and experimental data, with the C_P within 2 % of the experimental results for the TSR corresponding to peak power.

Several studies [30, 52, 90, 95] used RANS models, more information will be given in Chapter 3. To capture the full flow physics around the rotor it is important to model blade resolved transient simulations, crucial for looking at the interaction of devices as discussed in Section 2.3.8.

2.3.4 Impact of turbulence on device performance

Throughout the previous studies looking at device performance, little work was undertaken to try and understand the influence that turbulence has on the performance of a tidal device. Also the ability to generate difference turbulence intensities (TI) at test facilitates is not necessarily straight forward.

Blackmore et al. [50] studied the influence of grid generated turbulence on device loading and performance for an 800 mm diameter HATT in the IFREMER flume. A range of TI values between 4.6 - 25.2 % were used. The performance of the device was presented via the non-dimensional performance coefficients, C_P and C_T. More information on the performance coefficients can be found in Chapter 3. The flow velocity was calculated in three ways to highlight the variation seen in the coefficients; time averaged for a point measurement, time averaged over the rotor swept area and the final option performs the squaring and cubing prior to the time averaging.

The study [50] found that an increase in the TI led to an increase in the thrust load on the blade, in some instances, this increase could be as much as 5-fold. A similar outcome was seen when the length scale was increased. While both the TI and the length scale seemed to have an impact on the device performance, the length scale had a larger impact on the device loading compared to the TI. Maganga and Uihlein [96] also found that there were greater fluctuations in the loadings seen on a tidal device during testing when the ambient turbulence in the flow field was increased.

The fluctuations in the torque and thrust appeared to be correlated and large fluctuations in one ultimately led to larger fluctuations in the other. This correlation highlights the relationship between the generation of lift and drag for an aerofoil. Variations in the power and thrust of up to 10 % where seen for the range of turbulence intensities tested. Whereas an increase in the length scale increased the power and thrust coefficients by over 10 % [50].

Mycek et al. [51] used two turbulence intensity values, 3 % and 15 %, for a similar set of testing. In this case the flow velocity was changed while the TI was kept constant. For a TI of 3 % the C_P results were independent of Reynolds number for flow velocities greater than $0.4\,\mathrm{m\,s^{-1}}$. This flow velocity corresponded to a rotor based Reynolds number of 2.8

x 10^5 However, for the higher TI value of 15 % the C_P prediction is below 0.4 for almost all flow velocities. Not only that but the predicted C_P changed for all flow velocities considered. So despite being Reynolds independent above $0.4\,\mathrm{m\,s^{-1}}$, the high TI in the flow was having a larger impact on the mean performance. A similar finding could be drawn for the thrust coefficients.

When choosing locations for device deployment the ability to maintain a constant power output is desirable. One of the main points noted by [51] was that the change in TI had a minor affect on the mean performance values. It did however, have significant effect on the standard deviations of these performance values. This agreement in the mean values indicates that similar devices can be placed in regions with different TI values and in regions where the flow velocity and TI can change on a more local scale over the flood and ebb cycles, but the fluctuations can be an issue.

2.3.5 Simulating ambient turbulence

As described in Section 2.2 the regions of interest for proposed device deployment are likely to be turbulent in nature. Similarly ifthe performance of turbulence on a device is to be understood through the use of CFD models the implementation of turbulence in the model is important. Another possibility is to use the flow data from a precursor simulation as the inlet condition however this is very problem specific as the inlet conditions have to match the flow regime desired.

If this is to be avoided it becomes desirable to be able to represent the turbulence at the inlet in another way. most commonly done using either spectral or synthetic models. One commonly used spectral model is the Von Kármán model which is used in the DNV GL Tidal Bladed software [97]. The method is parametrised by the length scale, mean velocity and the turbulence intensity. It is these parameters that govern the shape of the power spectral densities.

A new synthetic eddy method was proposed by Jarrin et al. [98] which generated synthetic eddies at the inlet that were represented by a shape function. This shape function is used to describe the spatial and temporal characteristic of the flow. The study was able to reproduce specific first and second order one point statistics as well as autocorrelation functions.

Zonal LES can be implemented in ANSYS CFX. It allows the user to predetermine regions that will be either RANS or LES. If the inlet is defined with a small LES region then harmonic functions are used to generate synthetic turbulence at the inlet, however this is currently a beta feature [99] and so limited information is available on this.

2.3.6 Turbulence models

The selection of the turbulence model can vary the computational run time and the accuracy of the results. RANS models have shown their strength for wall modelled flows and mean performance values can be obtained that match experimental data [30, 52, 93]. Bardina et al. [100] compared four turbulence models for several flow conditions; the one equation Spalart-Allmaras model [101], $k-\epsilon$ [102], $k-\omega$ [103] and the SST $k-\omega$ models [104]. These four models are commonly used to close the RANS equations. For simple flows the predictions between all four models were similar. The SST k-omega model was considered the best for complex flows that involved separation but required improvement when modelling a wake. None of the models listed did well modelling the recovery of a flow, however reasons for this are not discussed by the author.

The Large eddy simulation (LES) solves for the largest energy containing eddies in free shear flow. It is preferred for the modelling of wakes, but in the boundary region the length scales can be related to the boundary layer thickness making LES a poor choice for wall bounded flows [99]. Afgan [105] compared a blade-resolved model of a HATT, modelled using the SST $k-\omega$ and LES turbulence models. The study found that the power and thrust coefficients in the operation region where within 3 % for both models. While the mean predictions are the same only LES captured the blade tip vortices and the influence of the support structure on the flow. Work by Ebdon et al. [106] looked at the wake behind a HATT. The study found that RANS under predicted the wake recovery and resolved very few of the complex flow characteristics associated with the wake. It showed that a hybrid RANS-LES model gave a better prediction for the wake of the device and showed good agreement with experimental data for several turbulence intensities over a range of TSR values.

The selection of the turbulence model is objective to the desired outcome of the model. For wall bounded flows it has been shown that RANS is suitable however the inability to capture the wake and tip vortices make it less suitable when modelling the wake of a device. Hybrid models offer a middle ground that is a compromise between turbulence resoltuion and computational time and can lead to a realistic representation of the flow [14].

2.3.7 Wake of a tidal device

Understanding the wake of tidal device is important if large numbers of turbines are to be placed in arrays. The characterisation of a wake can help inform developers as to the flow conditions that could be expected for a downstream device. A typical parameter measured in experiments or reported in CFD analysis is the centreline wake deficit or wake reovery [14].

Experimental testing

The centreline velocity in a wake does not always give a fair representation as to the full influence of the turbine on the total velocity deficit. Mycek et al. [51] also looked at the volumetric averaged wake recovery based on the swept area of the turbine to determine the recovery behind a device for two turbulence intensities, 3 % and 15 %. The higher ambient turbulence had a greater influence on the TI and flow velocity in the wake. The flow velocity at 6 diameters (D) was mostly recovered for an ambient turbulence of 15 %, however it was closer to 10D for the lower TI value, and the peak TI in the wake occurred around 5-7D behind the device.

Myers and Bahaj [107] tested the variation of thrust extraction on the wake via porous disks. The study found a strong relationship between an increase in the thrust exerted on the flow by the disk and a reduction in the flow velocity in the near wake up to 6D. The far wake however showed similar properties for all thrust values by 10D downstream. The work also considered the proximity of the disk to the seabed and the seabed roughness. It showed that when the device was placed closer to the tank bed, within 1/3 of the non-dimensional tank depth, the wake took longer to recover. The slower recovery was due to the lack of flow acceleration underneath the disk and therefore reduced mass flow rate, promoting stagnant regions of flow. The flow acceleration leads to higher turbulence in the flow and therefore the greater mixing between the wake region and the ambient flow.

Another study by Myers and Bahaj [108] used wake mapping to determine the influence of the support structure on the near wake for a 1/20th scale device. The findings showed that the shape and size of the support structure had a large impact upon the near wake flow field. Such impacts included greater turbulence and velocity reduction. The proximity and profile of the stanchion, while affecting the performance of a device [30, 109], may also lead to increased velocity reduction in the wake due to the blockage effect.

Maganga et al. [96] tested a 3 bladed HATT in the IFREMER flume. As expected, the wake recovery increased relative to the increased turbulence and the wake was also narrower. After 5D for the high TI value the wake deficit was less than 10 %. Whereas for the 8 % TI value the deficit was still noticeable beyond 10D.

Numerical modelling

Actuator disk based CFD models have been used for predicting the wake of a tidal turbine due to the reduced complexity and computational power required when compared to blade-resolved models. It is however a more simplistic approach and some of the limitations include: the estimation of the device impact on the flow based on the BEMT results, the disk does not rotate and therefore induces no rotation into the flow, the interaction of the blade geometry and therefore vortices are not captured.

Modelling by Batten et al. [110] aimed to predict the wake of a lab scale device using an actuator disk based CFD model. Two methods were used to represent the turbine. The first assumed a uniform and constant thrust applied to the fluid from the disk whereas the second was a RANS-BEMT model. Overall both methods showed reasonable agreement for the time averaged prediction of the centreline velocity and turbulence intensity of a turbine wake when compared to experimental data recorded by [108].

Another similar study by Harrison et al. [111] compared numerical results with the experimental results of [107] which measured wakes behind porous disks. The SST k-ω turbulence model within ANSYS CFX was used. The model was found to deviate from the experimental data for prediction of the near wake but showed that there was a trend between an increase in C_T and an increase in velocity deficit.

Pinon et al. [112] implemented the vortex method to model two different devices. In the vortex method, regions behind the turbine are denoted as vortical zones which are represented by vorticity-carrying particles. The first device was developed by [89] and the second was tested by [96]. While the numerical method gave good approximations for the C_P and C_T for the lower TSR region there was an inability of the code to model flow separation and for TSR > 3.5 the numerical and experimental results diverged rapidly. The study found that the velocity maps and profiles were in good agreement with the experimental testing up to 10D downstream of the device. However, it was noted that the turbulence implementation needed to be improved, a range of TI values needed to be tested and the code needed to be corrected to model the full range of TSR values.

Ebdon et al. [106] compared the SST k-ω turbulence model to the detached eddy simulation (DES), a hybrid RANS-LES, model for a blade resolved model using ANSYS Fluent. The numerical results were compared to data measured from testing at the IFREMER flume tank on a 0.5 m diameter device. The DES model gave a better prediction for both the wake length and the size of the turbulent perturbations than the SST k-ω turbulence model when compared to experimental data. This was because the use of LES within the wake region allowed the large scale turbulence to be directly resolved, something that does not occur in RANS models.

The inclusion of blade resolved models allows for a more accurate representation of the flow physics around the rotor region and therefore in the wake. Similarly, the choice of turbulence model can drastically affect the prediction of wake recovery. The numerical studies discussed up to this point have used the SST k-ω turbulence model to close the RANS equations. While this model is suitable for the prediction of device performance [30, 52, 93] it does not capture the wake behind a tidal device as well [14].

2.3.8 Device interaction for small numbers of devices

It is expected that, to fully maximise the energy potential at a tidal site, many devices will be deployed in an array. Unlike the wind industry, the location of these devices is more constrained by water depth, bathymetry and flow velocities. There is potential for a higher interaction between devices within the array for a tidal site than there is for a wind site. To help reduce the interaction between multiple devices careful consideration must be applied to the region these devices are deployed and the array layout.

Developers looking at array configurations should not only consider what is feasible for a site but also how to optimise the deployment of multiple devices. The optimisation of the array layout could lead to larger theoretical power outputs based on inter device interaction [113]. From a design point of view the understanding of inter-device interaction can help drive the optimisation process. Namely, the lateral and longitudinal spacing will influence the amount of power available for downstream devices and the possible fluctuations due to the levels of turbulence.

Lateral spacing - numerical modelling

The influence of the upstream row of turbines on the downstream flow is important to capture and plays a big part in how the remainder of an array may function.

Work by Malki et al. [71] looked at the impact of lateral spacing on a 10 m diameter device using a coupled BEMT-CFD model. The study concluded that for a spacing of less than 2D the blockage caused by the devices can not only reduce the velocity between the rotors but also increase the downstream turbulence. If the spacing is increased beyond 2D then it is possible that the flow velocity in between the two rotors is accelerated. If a spacing of 4D was used, then the flow velocity between the two rotors was 4 % higher than the far upstream flow.

Studies by Nuernberg and Tao [114] and Bai et al. [115] found similar results using a blade resolved CFD model and a coupled BEMT-CFD model respectively. The results for both studies showed good agreement with experimental data.

Lateral spacing - experimental testing

Only a small amount of research has focussed on the experimental testing of array configurations. One of the limiting factors associated with work of this kind is that the facility used must have a large enough cross-sectional area so that the blockage ratio is minimised. A way to mitigate the blockage is to use a smaller diameter rotor for the testing. However, [88] found that for rotor diameters less than 0.8 m problems are introduced due to disparate scaling laws. A rotor based Reynolds number is dependent upon the diameter of the device. The larger the diameter of the device the lower the flow speed required to reach Reynolds independence. Although some of these problems are solved by using actuator disks in the flow.

Actuator disks are the most commonly used method for small array testing due to the relative ease with which they can be installed and tested. One study by Stallard et al. [116] investigated how the wake behind a device changed depending on whether it was placed in the flume as a single device or as part of an array. The test used 3-bladed 270 mm diameter rotors. For a single device the wake width was estimated to expand to 1.5-2D up to 4D downstream of the device. It was found that for small lateral spacings the wakes merged downstream. In this region where the wakes of the array merged, there was a higher velocity deficit, up to 10 %, and higher turbulence intensity compared to centreline values for a single device. On increasing the lateral spacing to 3D each wake remained independent. For three devices the wake behind the middle device recovered more quickly due to the increased turbulence between wakes.

Another study by Myers and Bahaj [117] found that if the lateral spacing between disks was optimised then the flow was accelerated between the devices increasing the potential kinetic energy in the flow by 22 %, ultimately improving the power capture for the downstream devices. As the lateral spacing was reduced below 1D the trust loading on each of the disks was increased by almost 20 %. The near wake of the two devices merged and one larger wake was seen which extended further downstream when compared to a larger lateral spacing. At 1D the wakes merged at 7D downstream, at 1.5D the wakes did not merge. The flow was also accelerated when the lateral spacing was 1.5D.

A third study by Nuernberg and Tao [114] tested three-bladed 0.28 m diameter rotors. It also found that when close lateral spacing was used the wake recovery was slow and the velocity deficit was high due to the combination of the wakes. As the distance between devices increased the flow acceleration around the devices and the ambient flow in the tank led to improved wake recovery. The vortices shed by the blades begin to breakdown downstream of the turbine structure but before the wake is deemed fully expanded. The vortices and support structure led to an increased wake width downstream of the device.

One of the shortcomings in these studies is the assumption of straight flow. Frost et al. [118] combined velocity data measured in the Ramsey Sound, UK, with CFD modelling to assess the impact of yawed flow on a turbines performance. From the site data it was found that flow misalignment was within ± 20°. Based on the CFD models it was found that with a misaligned flow of 20° the power and thrust coefficients dropped by over 20 % compared to straight flow. It also found that the out-of-plane bending moment coefficient about the drive shaft increased up to 9-fold.

Results from all studies show that the lateral spacing can be optimised to accelerate the flow, potentially increasing the power output of downstream devices. However, if the spacing is too close, both the upstream device due to blockage and the downstream device due to increased turbulence can result in increased loading [116, 117]. The loading needs to be characterised and understood to maximise the life expectancy of devices in an array.

Longitudinal spacing

The study of wake recovery behind a single device has already shed some light on the proposed longitudinal spacing based on velocity recovery [51, 108, 112]. To maximise the space available for deployment a staggered configuration would be preferred due to the interaction of axially aligned devices. Liu et al. [119] found that for aligned devices, with a 8D between each device, the power output of the downstream device was less than 50 %

of the upstream device based on actuator disk model, while [115] suggested the greatest possible longitudinal length should be used for device spacing.

The issue of longitudinal spacing was particularly noticeable for axially aligned devices. Malki et al. [71] found using a BEMT-CFD model that for a second device axially aligned, 10D downstream, the power output was only 29 % of the upstream device whereas 40D downstream the power was 83 % of the upstream device.

Another study by O'Doherty et al. [120] used ANSYS Fluent to model contra-rotating blades that shared the same nacelle. The modelling used a scaled up 10 m diameter device. The CFD had been validated at lab-scale prior to the scaling. The axial spacing between the rotors was varied between 1D and 3D. The study found that the power generation was higher for the contra-rotating rotors than for the singular device. However, there was a large increase in the axial thrust loading on the contra-rotating blades.

All these numerical studies have used a coupled BEMT-CFD model with the RANS equations. Ebdon [14, 106] showed that the modelling of wakes using the RANS method under predicts the wake recovery due to a lack of turbulence resolution and so higher order turbulence models are required to get a better understanding of device interaction.

2.3.9 Blade loading

From several studies looking at device interaction and wake recovery it has been constantly found that there is greater turbulence intensity behind a device [117, 116]. While the mean values for thrust at power were not necessarily affected over a long enough time frame these elevated levels of turbulence intensity can cause the standard deviation of the measurements to increase [121, 51]. The irregular nature of the fluctuations adds to the complexity of device design because of the potential for fatigue. Hydrodynamic loads due to increased turbulence or wave-current interaction has the potential to have a big impact on the life expectancy of a marine device.

A study by Gaurier et al. [122] wanted to assess the blade loading on a 900 mm diameter tidal device for current and wave-current situations. The flow velocity and ambient turbulence in the flume was considered low (5 %) when compared to what might be seen at proposed tidal sites. While the mean of the strain on the blades for both cases was similar, the standard deviation for the current and wave-current case was very different, in the order of 2-3 times larger for the wave-current case.

Two studies by Milne et al. [123, 124] looked at the in- and out-of-plane bending moments for a lab scale HATT. Perturbations were added upstream of the device in the tow tank. The unsteady blade loads increased by up to 15 % when compared with measurements taken in steady flow conditions. Payne et al. [125] conducted similar tests in a flume with two inlet turbulence intensities. The load frequencies below the rotational frequency were correlated to the spectral density in the ambient flow while load frequencies above the rotational frequency were affected by the operational conditions of the turbine. A comparative study by Wang [126] showed good agreement between CFD modelling and experimental testing conducted in a tow tank when predicting the out-of-plane bending moments. There was zero turbulence in both the tow tank tests and the CFD modelling.

Apsley et al. [63] used a rotating actuator line CFD model, validated for a single device against data from Bahaj et al. [82], to study the performance of devices in arrays. Three scenarios for the interaction of two turbines were considered; fully in wake, partially in wake and fully out of wake. The second device was located 5D downstream. For the fully in wake case the load coefficients were reduced however the unrealistic turbulence levels lead to a discrepancy in the modelling of the wake size and recovery. For the partial wake case the loading on the blades was correlated to rotational position. Large fluctuations were observed as the blade moved in and out of the wake. Fully out of wake case led to higher power and thrust than the upstream turbine as the device was in the accelerated bypass flow region.

A few lab scale devices under different flow conditions have tried to characterise the loading on a device. However, it is desirable to be able to predict how a full-scale device will behave. Ahmed et al. [127] used both a RANS and an LES simulation to model the behaviour of an 18 m diameter device under both low and high turbulence conditions. For the low turbulence case both RANS and LES predicted similar mean values for blade loads. With a turbulent inlet only the LES model resolved the turbulence and gave a better representation of realistic frequencies seen in the flow.

2.3.10 Ocean scale array modelling

Funke et al. [113] tried to optimise the layout of tidal arrays using a 2D finite element method to predict the flow field and the performance of a device so that the power extracted based on turbine position can be computed. The study found that in each of the test cases a ‘fence’ of densely packed devices was created. The model was used to model up to 256 devices in the Inner Sound of the Pentland Firth, UK. A similar layout was proposed as was found in the initial tests for a smaller number of devices and can be seen in Figure 2.9.

The first few rows of fences had a large longitudinal distance between them to reduce the inter device interaction. The final fence consisted of two rows, with minimal longitudinal spacing. The devices are staggered to reduce the impact of the wake interaction. Using the optimisation tool, the proposed power output of the whole array was increased by 33 % when compared to a having uniform spacing between all the devices. The author noted that the shortcomings include; the lack of bathymetric data, the modelled domain needed extending to account for the surrounding flow regions, it used a fixed inflow rather than making use of a forced head loss to show the impact the devices have on the ambient flow velocity and a better turbulence model was required to more accurately model the wake and therefore the device interaction.

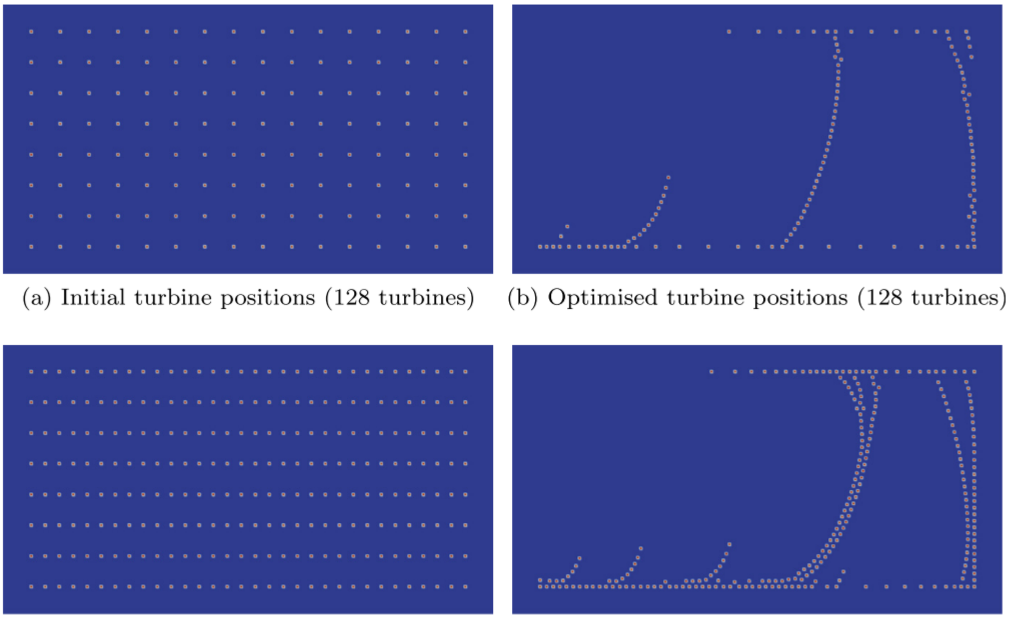
(a) Initial turbine positions (128 turbines)
(b) Optimised turbine positions (128 turbines)
(c) Initial turbine positions (256 turbines)
(d) Optimised turbine positions (256 turbines)

Figure 2.9: Initial and optimised turbine positions for the Pentland Firth example taken from [113]. In each case the flow is from left to right.

2.3.11 Installation and maintenance

The associated cost and complexity of installation and maintenance for tidal devices and arrays varies from site to site and developer to developer. A lack of uniformity in the design of devices means that no one solution is best for all. One of the key decisions that must be made involves the fixing method used to hold the device in place. The installation method used is subject to the depth of the water, the bathymetry and the proposed region of the flow where the turbine will operate [128]. Installation methods can involve gravity bases, mono-piles, tethered devices and floating platforms. One of the biggest associated problems are the high axial thrust loads that the device and support structure encounter. To make deployment of a device economically viable the life expectancy of the project should be in the region of 20-30 years [129].

The methods for deployment currently require the use of specialised vessels and the price to hire such vessels is enormous [25]. The benefit of PLAT-I [33] and SeaGen is that the removal from the sea for maintenance requires no specialist vessels reducing operational costs through the life cycle of the projects [25]. The weather windows for the installation and extraction of devices can be very short [130]. High tidal flow speeds mean that bed mounted devices can only be moved during slack water. These problems are not only true for the deployment of the device but also the cabling required to connect back to shore.

To mitigate the cost of the cabling the MeyGen project is looking to develop a sub-sea hub [29]. Each of the devices will connect to the hub and only one export cable will be required. This not only reduces the cost of the total cabling required but also reduces the installation cost due to reduced cable laying time and maintenance costs. The use of wet mate connectors allows the export cable connection to be made sub-sea reducing the required operational window for turbine installation on to the gravity base. The cost reduction in using a wet mate connector was 65 % for the MeyGen project [29]. These are very site- and project-specific factors, but it begins to highlight some of the methods for cost reduction that can be taken during the installation and maintenance of a tidal array, important if tidal energy is to become commercially viable.

2.4 Summary of literature review

The previous literature review has provided information on the current state of tidal technology and described a selection of the devices currently under development and testing. A review of previous research highlighted many studies aimed at progressing the understanding of HATT technology. A number of modelling methods such as XFoil, BEMT and CFD have been shown to agree well with experimental models when used for the initial design and prediction of a turbine blade and calculating the performance of a tidal turbine.

Several studies have looked at modelling the wake of a device most of the studies looked at either used a simplified geometry or a RANS based model which has been shown not to capture the wake as well as other available models. The computational requirements in creating blade-resolved models and directly resolving the turbulence is not to be underestimated however. Fluctuations in the blade loading were found to be correlated to the turbulence intensity and length scale, a big factor when estimating life expectancy during the design process given the proposed locations for device deployment likely to be turbulent.

This becomes even more important when estimating the interaction of devices within an array, which is the proposed method of deployment to make tidal stream energy generation a commercially viable option. While CFD has been shown to provide a good estimation for device performance the literature has highlighted the importance of using an LES based turbulence model to directly resolve the largest turbulent length scales within CFD models if the performance of a second downstream device is to be captured.

The work in this thesis will add to the literature by providing extensive experimental testing for a new device. It will also target a gap in the modelling of the wake of a tidal turbine, specifically by looking at the influence that the turbulence model and discretisation scheme have on the modelling of a turbine wake. This thesis will also focus on the performance prediction and loading of a secondary device placed downstream using a validated CFD model. A hybrid RANS-LES model using blade-resolved geometry, along with experimental measurements will be used to study the influence of the location on the performance of downstream device.

Chapter 3

Theory

The following chapter details the relevant theory applied to the modelling and characterisation of a tidal stream turbine. Firstly, the blade design tool, BEMT, is described, followed by an overview of the fundamental governing equations for fluid flows used for the computational modelling. The turbulence models and discretisation schemes used to close the governing equations are presented. The equations for the non-dimensional power, thrust, torque and bending moment are presented are used when characterising the turbine performance. Finally, the influence of flow velocity on the performance of the device is considered and the uncertainty associated with the turbine performance.

3.1 Blade element momentum theory

BEMT has been well documented and explained in a number of texts [65, 67, 131]. A brief synopsis is presented here. Within one dimensional momentum theory the turbine is modelled using a simple ideal permeable disk [131], or actuator disk, which is placed in a stream tube that is considered independent from the surrounding flow, Figure 3.1. By considering the conservation on momentum either side of the disk, equations for the two unknown induction factors can be derived. However, the momentum theory contains no information about the rotor geometry in question and so it must be coupled with the blade element theory.

The blade element theory aims to resolve the forces on the blades, as shown in Figure 3.2. To do this each blade is broken down into several independent radial elements, Figure 3.3. The lift and drag coefficients must be known for the aerofoil in question. Once the lift and drag for the aerofoil has been found then, via an iterative method, the distribution of

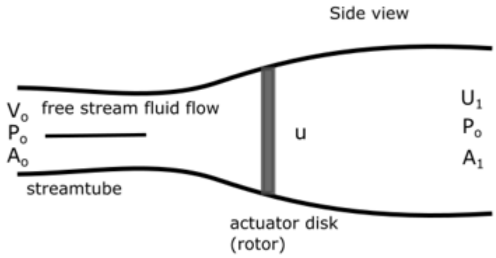

Figure 3.1: Stream tube used for momentum theory [131].

forces along the length of the blade can be found in relation to the induction factors [65]. By combining these sets of equations from the momentum and blade element theories the performance of the rotor can be found as long as; the lift and drag coefficients for the aerofoil, twist distribution from root to tip, chord lengths and the radial increments are known.

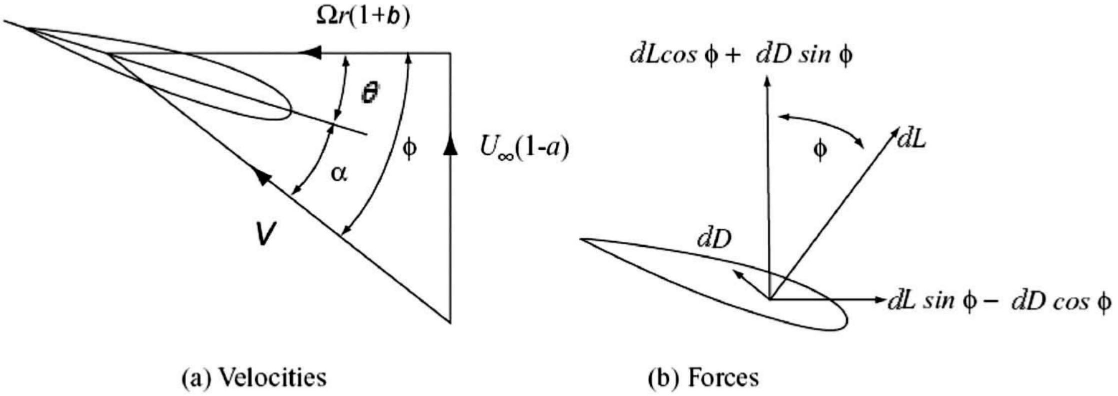

(a) Velocities

(b) Forces

Figure 3.2: The forces and velocities acting on an aerofoil in a flow [131].

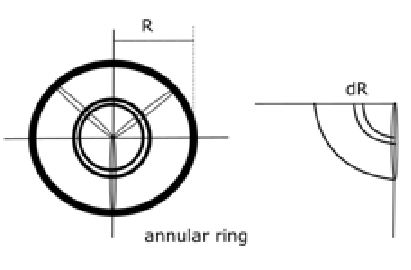

Figure 3.3: Stream tube broken into angular rings [131].

Both steady and unsteady BEMT codes can be used, but in this work only a steady code was used [70]. Unsteady conditions are more representative of real-life examples due to the influence of turbulence on the flow and therefore the performance prediction however because of the random and chaotic nature of turbulence computational tools such as BEMT become more complex.

3.2 Reynolds number

The Reynolds number is used to describe whether or not the flow regime is laminar or turbulent and is given by,

$$Re = \frac{\rho v l}{\mu} \tag{3.1}$$

where v is the characteristic flow velocity, l is the characteristic length of the geometry, ρ is the density and μ is the dynamic viscosity. The Reynolds number is a function of both the fluid velocity and the geometry so as they increase so does the Reynolds number. The Reynolds number is used to infer whether the flow is laminar or turbulent in nature.

Two approaches can be taken when representing the Reynolds number. A chord based Reynolds number uses the chord length at a point on the blade, usually the outer section where the blade loading is greater, to determine the Reynolds number. The second approach uses the onset flow Reynolds number and uses the rotor diameter as the characteristic length as well as the upstream flow velocity.

The lift and drag generated by an aerofoil changes as the Reynolds number is increased or decreased. For a low Reynolds number flow separation occurs prematurely causing an increase in the drag and decrease in the lift [132]. As the Reynolds number increases the maximum lift coefficient also increase while the minimum drag decreases [133].

A device can be considered to be independent of Reynolds number if the performance remains unchanged as the fluid velocity is increased at a specific tip-speed ratio. At this point the non-dimensional performance of the device is governed by the blade design, surface roughness and the operating parameters, not the Reynolds number. Both the chord based or rotor based Reynolds number are governed by the device in question, and the independence of the performance for different devices will occur at different Reynolds numbers. A comparison of geometrically scaled devices can be made once the point of Reynolds independence has been found, as long as the geometry is directly scaled and is not edited [91]. The Reynolds number used during lab-scale testing will be smaller than for full scale devices due to the change in the characteristic length making it important to determine if the rotor has reached Reynolds independence at the smaller scale before making a comparison.

3.3 Turbulence

Turbulence is a feature of fluid flows rather than fluids themselves and is present within all fluid flows above a certain scale [134]. At a certain Reynolds number the flow regime moves from being laminar to turbulent as it becomes gradually more unstable or random. The complexity of a flow therefore increases with the introduction of turbulence. The influence of turbulence can be visualised via the fluctuations around the mean value in the flow variables.

The turbulence spectrum gives information on the magnitude of the fluctuations. The integral length scales contain the largest energy containing eddies in the flow and it is these that have the largest fluctuation of flow velocity. The size of the integral length scale is usually governed by the characteristic length of the geometry in question. Energy is transferred from the integral length scale to the smallest length scales, the Kolmogorov length scale by means of an energy cascade where it is dissipated due to the viscous forces.

It is then the fluctuations in the flow variables that are of most interest to the work presented here. It is highly likely that proposed tidal sites will have flow regimes that are turbulent in nature [53]. Therefore the purpose of this work is not to resolve and understand the turbulence itself but to use it as a tool to determine the influence that a turbulent flow has on the performance of a HATT. Further reading on turbulence can be found from Tennekes and Lumley [134].

As well as comparing the instantaneous fluctuations in the flow field to the mean the flow the turbulence intensity metric can be used. The turbulence intensity, most commonly given as a percentage, is used to relate the fluctuation, u' in the flow to the mean flow, $\bar{u}$. For this work only 1-dimensional turbulence intensity has been considered when discussing the results and can be given by the Root Mean Square (RMS) of the velocity divided by the mean velocity.

$$TI = \frac{\sqrt{\overline{u'^2}}}{\bar{u}} \tag{3.2}$$

3.4 Turbulence models in ANSYS CFX

The governing equations for fluid motion, or Navier-Stokes equations, are derived from Newtons conservation laws of physics. By considering the smallest possible particle whose macroscopic properties are unaffected by the individual molecules of the fluid then the equations for the conservation for mass, energy and momentum can be derived. The energy equation is of less importance throughout this work and so only the continuity and momentum equations are of interest. The work done as part of this thesis assumes that the fluid domain in question is incompressible, and so only the incompressible version of the continuity and momentum equations have been used.

3.4.1 Reynolds averaged Navier-Stokes

A time averaged solution is desirable for many of the flows of interest within engineering applications, and so the instantaneous fluctuations within the flow field are less important. The resolution of the fluctuations within an unsteady flow increases the computational resources required. The RANS equations have been developed to provide a time-averaged solution.

To generate the RANS equations Reynolds decomposition must be applied to the instantaneous Navier-Stokes equations. During Reynolds decomposition a given flow variable, ϕ, that is a function of time and space, is broken down so that it can be expressed as a sum of the mean and fluctuating components [64],

$$\phi(\mathbf{x}, t) = \Phi(\mathbf{x}, t) + \phi'(\mathbf{x}, t) \tag{3.3}$$

Where Φ is the mean component, ϕ' is the fluctuating part and $\mathbf{x} = (x, y, z)$ is the position vector. If each instantaneous variable is decomposed and then introduced back into the incompressible Navier-Stokes equations then we are left with the time averaged, or Reynolds averaged equations for continuity and momentum. For more information and for the derivation of the full equations see [64].

An extra term is added due to the Reynolds decomposition, referred to as the Reynolds or turbulent stresses. The modelling of the Reynolds stresses is important if the RANS equations are to be closed. The Boussinesq approximation is used to simplify the problem of the Reynold stresses. It assumes that the turbulent shear stress is analogous to the viscous shear stress by introducing a term for the eddy viscosity. This assumption then allows for the use of turbulence models to model the eddy viscosity and therefore the closure of the RANS equations.

There are several turbulence models available ranging from more simple mixing length models to the complex Reynolds Stress Model (RSM). However, in the following work only the two equation Shear Stress Transport (SST) $k-\omega$ model was used when modelling the RANS equations and so a brief overview has been given. More information on many of the other common turbulence models used to the close the RANS equations can be found in [64].

3.4.1.1 SST k-ω

The most common turbulence models are two equation turbulence models which are used to represent the turbulent properties of the flow by means of introducing extra transport equations. Generally, they will include a term for the turbulence kinetic energy, k and either the turbulence dissipation, ϵ, or the turbulence dissipation rate.

One of the first k-ϵ models was developed by Jones and Launder [135]. It has since been subject to several iterations by different authors however the fundamentals remain the same. It was found to be good for predicting free stream flows however when it came to predictions of the viscous sub layers it was found that it would delay or completely prevent separation [136] as it lacked sensitivity to adverse pressure gradients in simulations.

The k-ω model was originally developed by Wilcox [137] and was better suited in adverse pressure gradients, leading to a better prediction for boundary layer flows. It was however very sensitive to the turbulence frequency outside of the shear layer [138] and it was found that changes in the free stream turbulence frequency could impact the results dramatically.

Menter's [104, 139] SST model was designed to address the shortcomings in both the k-ϵ and the k-ω. It looked at incorporating a blending function to transition between the two models when solving for either the free stream or the boundary layer thus using the strengths of both models [104]. The model required no input from the user as the blending was automatic. CFX uses the SST model developed in [139] albeit with a few small changes that can be found in [140].

3.4.2 Large eddy simulation

More complicated turbulence models exist that try to resolve the turbulence spectrum in the flow to differing degrees. The most complicated is direct numerical simulation (DNS) which tries to resolve the turbulence for all scales throughout the domain. The mesh and timestep requirements make the size of the computational resources required impractical. The inclusion of complex geometry in the simulation only compounds this issue. With the problems of DNS in mind other methods have been proposed [64], one of which LES.

LES looks at resolving only the largest energy containing eddies in the flow which are assumed to be governed by any geometry in the model. For LES the Navier-Stokes equations are filtered in both the space and the time domain. Only the eddies which are larger than the filter width are resolved. The small-scale motions are modelled, rather than directly resolved, by the solver as they are assumed to be of a similar nature to one another and so a more simplistic approach can be taken. In CFX a sub-grid scale (SGS) model is used.

While more computationally expensive than RANS, there are associated advantages to LES modelling. Unlike RANS modelling where the Boussinesq approximation is used to model the effect of the turbulence on the flow, LES directly resolves the turbulence for the larger scales giving a more realistic representation of turbulent flows. Therefore, the fluctuations in the flow are resolved in LES. However, the mesh requirements for an LES model are much greater than that of RANS especially in the boundary layer region. As only the small-scale eddies are to be treated with the SGS model, the mesh must be of an order that captures both the large and medium length scales, otherwise the use of LES is hard to justify.

This limitation in LES modelling gives rise to the use of hybrid RANS-LES models where wall flows are resolved using RANS and the free stream large scale eddies are resolved using LES.

3.4.3 Detached eddy simulation

Many flows do require the turbulence spectrum to be resolved to a certain degree, rather than just the average flow field, even if it is limited to a very specific region of the fluid domain. While RANS modelling has been the mainstay for CFD simulations for a number of years, the increase in computational power and resources has enabled the complexity of simulations to increase. LES has until recently been computationally expensive to run, especially for wall-bounded flows [141] as the mesh requirements to resolve the turbulence in this region are high due to the length scale at the wall being very small. RANS has proved successful for wall-bounded flows but offers the user little by means of representative resolution in the free shear flow [99].

Based on the shortcoming of both models several hybrid models have been developed that incorporate both RANS and LES. Most relevant to this work is the DES turbulence model, proposed by Strelets [142] which aims to use the RANS model in the near wall region and LES in free stream region where there is large separation [142]. The switch is based on the maximum edge length of a cell in either the *x, y* or *z* direction, Δ_{max}, in relation to the length scale, L_t,

$$C_{DES}\Delta_{max} > L_t \rightarrow RANS \tag{3.4}$$

$$C_{DES}\Delta_{max} < L_t \rightarrow LES \tag{3.5}$$

C_{DES} is the calibration constant and has a value of 0.61 and is specified by ANSYS [143]. Based on the switching method the mesh size in the LES region of the flow need to be of LES quality for the transition to occur. It reasons that if the mesh was suitably fine throughout the entire domain then the model would run in LES. This is not the desired outcome when selecting the DES model and so only the free stream regions of interest have a mesh that is of LES standard.

If the grid resolution within the boundary layer is already of LES quality, then the RANS modelling in this region is affected. It can lead to grid induced separation (GIS), separation at arbitrary points within the boundary layer, due to a reduced estimation of the eddy viscosity. To get around the problem of GIS the delayed detached eddy simulation (DDES) was proposed by Spalart et al [144]. DDES introduces a shielding term to protect the boundary layer from switching between RANS and LES. It allows the grid sizing to be 5 times smaller in the boundary layer than that of DES before a switch to LES will take place, protecting the RANS boundary layer even if he mesh is previously of LES quality. GIS is still possible if the mesh is reduced below this value.

3.4.4 Stress blended eddy simulation

The shielded detached eddy simulation (SDES) turbulence model takes this solution one step further and allows the grid sizing to be 25 times smaller in the boundary layer. This not only protects the RANS boundary layer region but also allows for a quick transition from RANS to LES as the mesh outside of the boundary layer is already of LES quality. The speed of the switch from RANS to LES allows for the resolution of the turbulence once out of the boundary layer, desirable for the modelling of wake scenarios. The stress blended eddy simulation (SBES) is based on the SDES however it adds a second shielding function so that it not only controls the switch from RANS to LES but also the 'switch between different turbulence model formulations' [99]. The SBES formulation is recommended by ANSYS for scale resolving simulations, such as those carried out as part of the work in this thesis [99].

3.5 Discretisation schemes

Discretisation schemes are used to provide a solution for the discrete version of the Navier-Stokes equations. CFX uses the element-based finite volume method [143], and as such the domain is broken down into many spatially discretised elements. CFX uses a vertex-centred approach and so the node, which contains the solution, is located at the vertex of each element. The discretisation scheme is then used to determine the value of the field at the face, ϕ_f, by means of a face interpolation, based on the values of the surrounding nodes shown in Figure 3.4. This is repeated throughout the entire domain, over every element, providing one final solution.

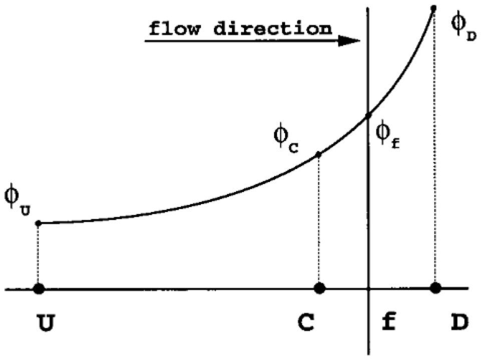

Figure 3.4: Variation of ϕ around the face, **f** [145].

U and **D** refer to the far upstream and downstream nodes respectively and **C** refers to the node directly upstream of the face, **f**.

With the use of any discretisation scheme the aim is to provide a accurate and converged solution while maintaining boundedness [145]. One of the main problems when it comes to providing an accurate, stable and bounded solution is the discretisation of the convection term. There are several well-known proposed schemes ranging from the first-order upwind scheme to the higher-order QUICK scheme [146]. For a solution to be bounded it must satisfy the convection boundedness criterion (CBC) for every point in the domain. This forms the basis of the normalised variable approach (NVA). The full method/derivation can be found in [147] however the criterion is given here and is as follows,

- For $0 \leq \widetilde{\phi}_c \geq 1$, $\widetilde{\phi}_c$ is bounded below by the function $\widetilde{\phi}_f = \widetilde{\phi}_c$ and above by unity, and passes through the points (0,0) and (1,1).
- For $\widetilde{\phi}_c < 0$ and $\widetilde{\phi}_c > 1$, $\widetilde{\phi}_f$ is equal to $\widetilde{\phi}_c$

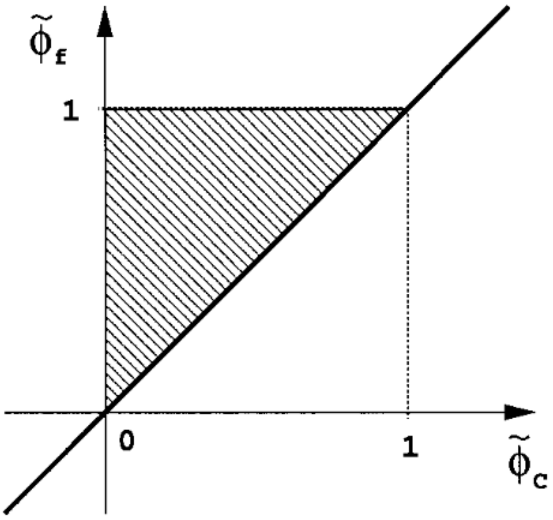

Figure 3.5: Representation of the CBC [147].

The CBC is diagrammatically expressed in Figure 3.5. The normalised variable diagram (NVD) for some more commonly used discretisation schemes can be seen in Figure 3.6. The schemes shown include the upwind differencing (UD), central differencing (CD), second-order linear upwind differencing (LUD) and the third-order QUICK scheme. When the chosen scheme does not satisfy the CBC, as is the case with the second-order schemes

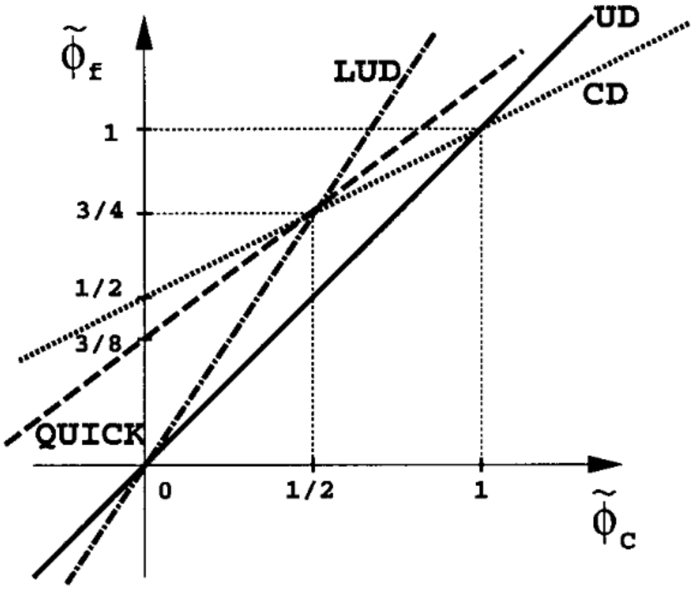

Figure 3.6: Common discretisation schemes [147].

shown in Figure 3.6, then instability can occur leading to non-physical oscillations in the flow field variables. It can be seen that only the UD scheme, a first-order scheme, satisfies the CBC. Alterations to the NVA have tried to incorporate ways to help determine areas of unboundedness so that an intervention can be applied if necessary [147], the most relevant of which is described in more detail in Section 3.5.5. A brief overview of the different schemes available in ANSYS CFX is given below.

3.5.1 Upwind differencing

The UD scheme is a first-order accurate discretisation scheme and is the only scheme to fully satisfy the CBC. It uses information from the upwind node to determine the value of the flux on a face. The value of a variable $\widetilde{\phi}_c$ at the node is taken to be the value of $\widetilde{\phi}_f$. The assumption of a constant variable value across the cell leads to the 'smearing' that is commonly associated with UD results.

It is used largely with RANS solvers or flow regions due to the stable nature of the scheme. The stability makes it useful to provide a solution for use as an initial condition when using higher-order schemes. The stability comes at the cost of numerical dissipation and as such the UD scheme is not as accurate as other high-order schemes.

3.5.2 Specified blend factor

The specified blend factor (SBF) allows the value of the blending function β_m to be varied between 0 and 1 based on the users input. A value of 0 will results in a first order upwind scheme and a value of 1 will results in an unbounded second order upwind scheme.

3.5.3 High Resolution

The high resolution (HR) scheme is the default option for DES models in ANSYS CFX [99]. In the RANS flow regions, it performs a switch between the first and second order upwind schemes based on the value of β_m. In the LES regions of the flow it uses the same approach as the bounded central difference scheme put forward by [147] and is discussed in Section 3.5.5. The flow conditions determine the point at which the switching occurs and can be influenced by the quality and size of the mesh in the unstable flow regions.

3.5.4 Central difference scheme

The CD scheme applies a linear interpolation between the two nodal points either side of the face to determine the values of the variables on the connecting face. It assumes a linear change or progression in a variable ϕ across the entire cell.

The scheme is second order accurate, however it is unbounded as it does not satisfy the CBC. The unboundedness can cause oscillations to develop when resolving for complex geometry with non-ideal grids [99] and so flow field variables may not behave as expected. The use of a pure CD scheme for DES can cause problems as the RANS regions of the flow are still treated with the second order CD scheme, when ideally, they would use a first or second order upwind scheme. It is generally used for LES or DNS simulations.

3.5.5 Bounded central difference scheme

The bounded central difference (BCD) scheme used by CFX uses the second-order central difference scheme wherever possible unless the CBC would not be satisfied. It is based on the gamma differencing scheme developed by Jasak [147]. The NVD can be seen in Figure 3.7 and incorporates a blending, through the use of β_m, between the first-order UD scheme and the second-order CD scheme to ensure the CBC remains satisfied for all points in the domain. The UD scheme is used predominantly for the RANS regions of the flow, and the CD scheme is used for the LES regions. The higher the value of β_m the greater the influence of the UD on the solution and so the greater the numerical dissipation

[147]. Ideally the value of β_m is kept as low as possible to ensure that the CD scheme is dominant.

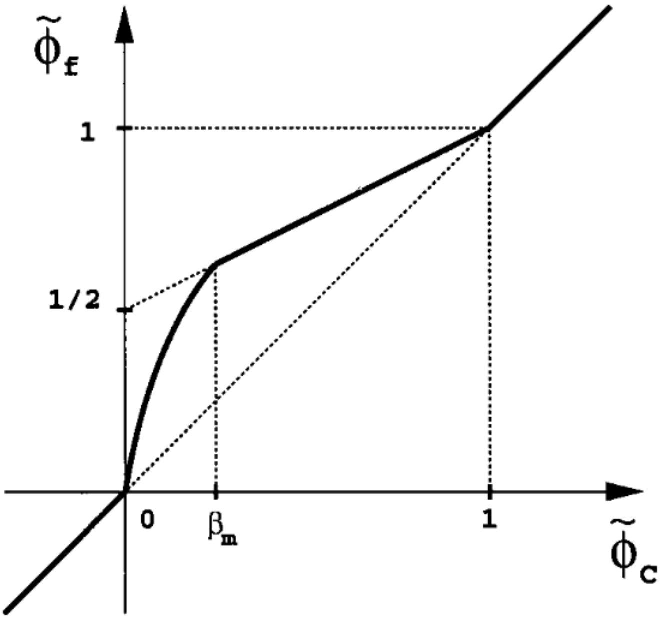

Figure 3.7: The NVD for the gamma differencing scheme, used as the basis for the BCD scheme in ANSYS CFX [147].

Due to the inclusion of the UD scheme a larger amount of numerical dissipation is seen, however compared to either the UD or the SB scheme it is comparatively small. The BCD scheme is deemed suitable for use with DES turbulence models as it has been shown to handle both the RANS and LES flow regions well [99].

3.6 Y plus

One metric used to determine the mesh resolution in the boundary layer is y+. The y+ gives an indication as to the distance from the boundary to the first node in the mesh. The smaller the y+ the greater the number of cells in the boundary layer and the more accurate the solution tends to be. A value of 11 is used to determine in CFX whether the boundary layer is directly resolved or modelled using wall functions. Above a y+ of 11 CFX uses wall functions. It was found that there was only a 2 % difference in the results for 2 < y+ < 100 when using the SST $k - \omega$ turbulence model [140].

3.7 Non-dimensional performance coefficients

The device characteristics for tidal devices are usually displayed by means of the non-dimensional performance coefficients. These coefficients are based on the momentum theory for actuator disks by Froude [65]. In using the non-dimensional performance characteristics geometrically different devices can be compared irrelevant of design, radius or flow speed. However, one assumption is that the flow in all cases is ideal, which often is not actually the case. During this work the non-dimensional performance coefficients have been used to give an indication as to the impact that different flow conditions have on device performance. To compare devices via the non-dimensional performance curves the performance coefficients at like values of tip-speed ratio, λ , need to be compared. The equation for λ is as follows,

$$\lambda = \frac{\omega_t R}{u} \tag{3.6}$$

where ω_t is the angular velocity of the turbine in *rad/s*, R is the radius of the turbine in m and u is the free stream flow velocity in *m/s.*

3.7.1 Power coefficient

The power coefficient is used to represent the amount of power generated by the turbine rotor, in relation to the total available power in the upstream flow over the swept area of the turbine.

$$C_P = \frac{Q_t \omega_t}{\frac{1}{2}\rho A u^3} \tag{3.7}$$

Where ρ is the density of water, $997\,\mathrm{kg\,m^{-3}}$, as given by the value used in the CFD code, A is the swept area of the turbine in m^2 and Q_t is the torque generated by the turbine in Nm.

3.7.2 Thrust coefficient

As with the power coefficient, the thrust coefficient expresses the thrust that is acting on the rotor, F_t, relative to the total thrust if the flow where to be acting on a disk with the same swept area as the rotor.

$$C_T = \frac{F_t}{\frac{1}{2}\rho A u^2} \tag{3.8}$$

3.7.3 Torque coefficient

Lastly the torque coefficient, C_Q, compares the torque generated by the rotor compared to the maximum theoretical torque that could be developed.

$$C_Q = \frac{Q_t}{\frac{1}{2}\rho A u^2 R} \tag{3.9}$$

3.7.4 Blade root bending moments

The blade root bending moments refer to the bending moment around the root of the blade caused by the thrust loading of the flow. It is the product of the point at which the force over the entire blade is perceived to act, the centre of pressure, and the distance from this point to the blade root. In this case the out-of-plane bending moment was calculated using,

$$C_Q = \frac{M_{xy}}{\frac{1}{2}\rho A u^2 R} \tag{3.10}$$

Where M_{xy} refers to the resultant out-of-plane bending moment in the x- and y-directions.

3.7.5 Impact of flow velocity on the performance coefficients

The fluid velocity used when calculating the non-dimensional performance coefficients can have a big impact of the recorded performance of the turbine. The cubed and squared terms in Equations 3.7 - 3.10 can artificially increase or decrease the final value if the velocity value chosen is not representative of the flow seen by the device.

One method that can be applied uses a point measurements upstream of the rotor. The mean velocity at this location is then used in Equations 3.7 - 3.10. The use of a single point upstream of the rotor is not a good representation of the flow over the rotor swept area however as the flow properties vary depending on the location in the water column. The proximity of the measured point to the rotor must also be considered as the effect of blockage, especially in lab scale test facilities, can cause the flow velocity upstream to reduce. To counter this, measurements can be taken far upstream of the device, so that the influence of the turbine is negligible, however in certain test facilities this is not possible due to the usable working area.

The volumetric average flow velocity over the swept area of the turbine can be used instead of a point measurement. To calcualte the volumetric average a greater number of data points across the diameter of the device must be measured upstream of the device. The more points taken the greater the accuracy of the estimation. The swept area is broken down into several annular rings and the flow velocity in each of the corresponding rings in used to provide an estimation of the mass flow rate. The total mass flow rate is found and divided by the swept area giving a volumetrically averaged flow velocity. The one assumption is that the flow is rotationally symmetrical therefore allowing a point measurement to be used to provide an estimate for the annular section. This method was found to give a better estimation of the velocity available to a downstream device [52, 14, 51].

The difficulties with the flow velocity selection are compounded when considering the performance of a device within an array. The flow downstream of a device is highly turbulent. The use of a point measurement then becomes almost obsolete unless downstream devices are so far apart that the flow can be assumed to have the same characteristics as the ambient flow field far upstream of the array. With that in mind a single value far upstream of the array could be used to provide a global estimate for the array performance, however the estimations for individual devices will provide little insight into how they are performing as only the first row of devices is likely to see that flow velocity.

The length of time available for experimental testing is finite and so usually a compromise is made. The number of points measured upstream over the rotor area is usually reduced to ensure that at each point the data sample is long enough to provide a reliable mean value. As mentioned before the flow velocity used to calculate the non-dimensional performance coefficients can end up theoretically breaking the Betz limit. If the measured flow velocity upstream of the device is lower than the velocity seen by the device the C_P value will be theoretically greater. Therefore, it is important to try and capture the flow field in as much detail as possible prior to presenting the turbine performance.

The problem is a little less complex for CFD modelling as an almost infinite number of monitor points can be included into the fluid domain without any additional computational time or power. However, as the CFD models are using the experimental data for validation then it seems prudent that at the first instance only the points within the experimental testing that were measured should be used for the CFD, allowing for a like for like comparison.

3.8 Uncertainty analysis

Measurements taken during experimental test campaigns are, in an ideal world, accurate and precise. The accuracy of a measurement denotes how close the measured value is to the true variable value and is dependent upon the measurement system in use. The bias uncertainty is used to give an indication as to the errors associated with the accuracy of a measured value. The precision or repeatability of a measurement indicates how tightly grouped a data series will be. The precision uncertainty is used to highlight the repeatability of a measurement. During experimental testing measured values will have an associated bias, μ_b and precision uncertainty, μ_p. These uncertainties can be combined to give the total standard uncertainty, μ_{tot} for a measured value,

$$\mu_{tot} = \sqrt{(\mu_b)^2 + (\mu_p)^2} \tag{3.11}$$

Within a calculation there can be multiple variables that contain measurement uncertainties, such as the variables found in the equations for the performance coefficients. Rules govern how the measured variables are used to give an estimate of the total uncertainty of a calculation. For example, to find the certainty in a quantity Q which is dependent on a number of variables, a and b etc. then the following rules apply,

For addition or subtraction if,

$$Q = a + b + ... - y - z \tag{3.12}$$

then

$$\mu Q = \sqrt{(\mu_{tot}a)^2 + (\mu_{tot}b)^2 + ... - (\mu_{tot}y)^2 - (\mu_{tot}z)^2} \tag{3.13}$$

For multiplication or division if,

$$Q = ab/yz \tag{3.14}$$

then

$$\mu Q = |Q|\sqrt{(\frac{(\mu_{tot}a)}{a})^2 + (\frac{(\mu_{tot}b)}{b})^2 + ... - (\frac{(\mu_{tot}y)}{y})^2 - (\frac{(\mu_{tot}z)}{z})^2} \tag{3.15}$$

For multiplication of a variable by a known number (e.g. A = π) if

$$Q = Az \tag{3.16}$$

then

$$\mu Q = |A|\mu_{tot}z \tag{3.17}$$

Coverage Factor

The coverage factor is used to re-scale the combined standard uncertainty. Depending on the level of confidence required in the results the following can be applied,

$$U = k\mu \tag{3.18}$$

where k is the coverage factor. The overall uncertainty is scaled by the value of k. There are associated levels of confidence depending on the value of k, and the most commonly used is a value of 1.96 which gives a confidence value of 95 percent.

Chapter 4

Blade design and CFD validation

The Cardiff Marine Energy Research Group, Cardiff University, have been using the same blade design for a number of years now that has been subject to extensive experimental testing and numerical modelling [30, 52, 84, 93, 106, 148, 149]. Several iterations of turbine design have come and gone, while the basic blade design has remined the same. The original blade was developed, tested and validated by Egarr [148] and was based on the Wortmann FX63-137 aerofoil. Figure 4.1 shows the Wortmann aerofoil used for the experimental geometry and so the trailing edge has been truncated for manufacturing purposes.

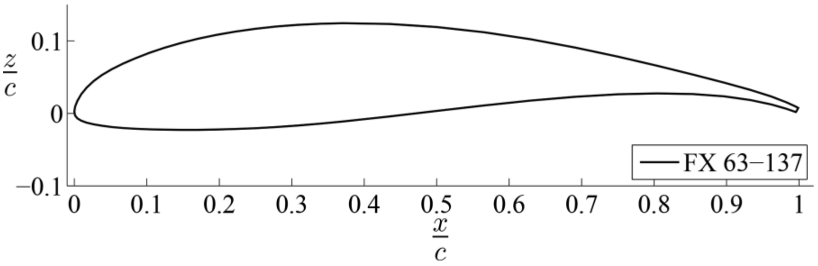

Figure 4.1: Wortmann FX63-137 aerofoil.

The blade characteristics of the blade can be seen in Table 4.1. The large twist and chord length were used as the turbine was initially designed to have a self-starting capability when placed in the flow. The Wortmann aerofoil was chosen as it offers high lift and low stall characteristics [150]. The peak pitch angle was found to be 6 degrees and the peak TSR to be 3.65 which gave a C_P of 0.39 and C_T of 0.86 [52].

Development of a new turbine within the Cardiff Marine Energy Research Group led to a redesign of the blade, based on the Wortmann aerofoil. The diameter of the new turbine was increased from 500 mm to 900 mm so the blade length increased from 190 mm to 384.5 mm. The design objectives were as follows and were focussed on the TSR that corresponded to peak power;

- The twist distribution from root to tip
- The chord length for each section
- The pitch angle
- Increasing the C_P compared to the existing blade design.

The following chapter describes the process followed to select a radial variation of pitch and chord, an overview of the experimental testing with the new turbine and finally a comparison between the numerical and experimental results. The BEMT code was used as the initial numerical tool to determine the blade characteristics so that a 3D model could be simulated using CFD.

Table 4.1: Old blade characteristics from Mason-Jones [52].

r/R	Twist (deg)	Chord Length (mm)
0.229	33.89	75.0
0.305	26.01	75.5
0.382	19.86	74.5
0.459	15.29	70.0
0.536	11.6	63.5
0.615	8.41	56.0
0.692	5.52	45.25
0.768	3.19	39.04
0.845	1.25	35.0
0.922	0.25	31.65
1.00	0.0	29.5

4.1 Blade element momentum theory

BEMT was used as one the design tools when designing the new blade. The fundamentals of BEMT were described in Chapter 3. The BEMT code used in this work was developed by [70]. Other than the flow velocity and the rotor geometry in question nothing was changed in the code and so no more detail about the code is given. The full code used and details about it can be found in [70]. The code has been previously validated through the use in other work [70, 151]

Table 4.2: Blade characteristics comparison.

r/R	Design 1 chord (mm)	Design 2 chord (mm)	Design 3 chord (mm)
0.146	72.5	72.5	72.5
0.229	87.8	82.8	87.8
0.305	103.1	97.6	103.1
0.382	109.6	106.8	109.6
0.459	109.5	106.2	109.5
0.536	105.1	105.1	105.1
0.615	93.1	93.1	93.1
0.692	83.6	83.6	83.6
0.768	73.6	74.3	74.3
0.845	67.6	68.3	68.3
0.922	62.8	64.1	64.1
1.00	58.9	60.2	60.2

A number of chord length distributions, twist distributions and pitch angles were modelled to find the optimum blade design. The twist distribution was varied between 15° and 25° in 1° increments. Pitches angles between 5° and 9° were tested. Three examples of the chord length distributions are shown in Table 4.2. Design 1 was the base case during the comparisons. Design 2 had a reduced chord length at the root of the blade and an increased chord length at the tip. Finally Design 3 had the same chord length at the root as Design 1 but the chord length at the tip was like that of Design 2.

As a steady BEMT code was used there was no turbulence in the flow and so when working out the forces and velocities over the aerofoil the value of $1\,\mathrm{m\,s^{-1}}$ was used. This corresponded to a chord based Reynolds number range of $6.6x10^4$ - $1.23x10^5$ over the full blade length of 384.5 mm. The BEMT code was executed using MATLAB. An iterative approach was taken so that each pitch angle was modelled for each of the twist distributions. This was then repeated for the 3 designs to see the influence of the chord length, twist and pitch angle on the performance. In total 132 designs were modelled to determine the best outcome. When discussing the results only a few examples of the designs with the best performance have been given.

4.2 Computational fluid dynamics

All the simulations run as part of the work in this thesis were modelled using the commercial CFD software ANSYS CFX 18.0. CFX uses the finite volume method. All simulations were run using the HPC facilities at Cardiff University due to the high computational cost of the CFD models. For all the CFD simulations the stream-wise flow is in the z-direction, the x-direction refers to cross-stream and the y-direction is the vertical direction.

4.2.1 Model geometry

The geometry used for the CFD modelling was created using the computer aided design (CAD) editor SOLIDWORKS 18.0. The rotor geometry and stanchion in the computational model, shown in Figure 4.2, are based on the device described in Section 4.3.

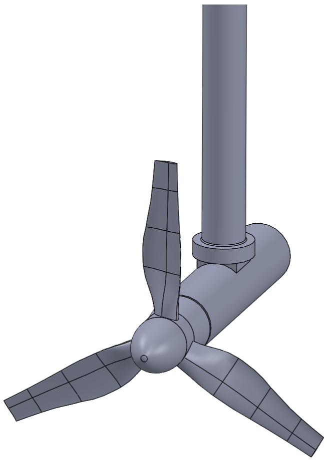

Figure 4.2: SOLIDWORKS drawing of the turbine and stanchion used for the CFD modelling.

Design modeller, the in-built ANSYS CAD editor, was used to create the fluid domains used for the simulations. The first domain consisted of a control volume that represented the tow tank used during the experimental testing. The details for the experimental testing can be found in Section 4.3. The cross-sectional area of the control volume, referred to as ‘flume’ from now in within the CFD section, was kept the same as the tow tank and so the rotor performance could be directly compared without the need for applying any blockage correction.

The second domain created was used to simulate the turbine rotation. A cylindrical body, from now on referred to as the moving frame of reference (MFR), encompassed the turbine rotor, hub and nose cone. The diameter of the MFR was 1.3 m and was deliberately made larger than the rotor diameter. This was done to avoid any boundary effects between the tip of the blade and the non-conformal interface between the rotating and stationary regions of the flow. The effect of MFR diameter on rotor performance can be seen in Table 4.3. The model run as part of the MFR study used a domain with a larger cross sectional area and did not have a stanchion. It is for this reason that the thrust values given in Table 4.4 are higher than stated here.

Table 4.3: Performance coefficients in relation to MFR diameter.

MRF Diameter (m)	Torque (Nm)	C_P	Thrust (N)	C_T
1	18.32	0.432	266.5	0.84
1.1	18.47	0.435	266.5	0.84
1.3	18.49	0.436	266.6	0.84
1.7	18.49	0.436	266.6	0.84
2.1	18.49	0.436	266.6	0.84

ANSYS CFX treats all volumes as fluid and so the turbine geometry was removed from the model. A boolean operator was used to subtract the turbine geometry from the two domains creating a void which represented the turbine. To achieve the void the turbine geometry was not preserved. The hashed regions in Figure 4.3 show the bodies that are treated as a fluid by the solver. The MFR was then subtracted from the flume, again using the boolean operator, however for the MFR the subtracted body was preserved leaving two independent bodies. The three faces that comprised the cylinder were left, and three more faces were generated in the flume where the cylinder had been subtracted. These faces were used to create the non-conformal interface later. The flume domain was then further broken up into blocks or bodies, shown in Figure 4.4 so that a more structured mesh could be applied to the model.

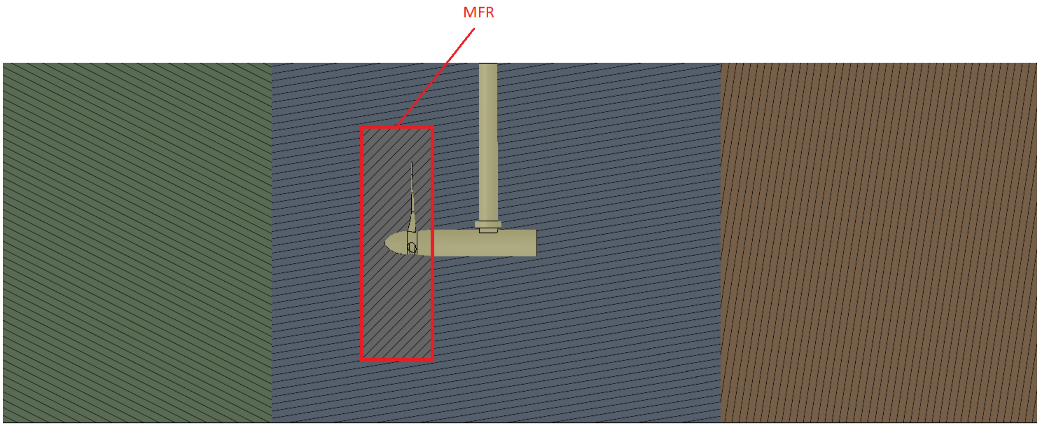

Figure 4.3: Void created by the boolean operator. The hashed regions show bodies that are treated as a fluid region.

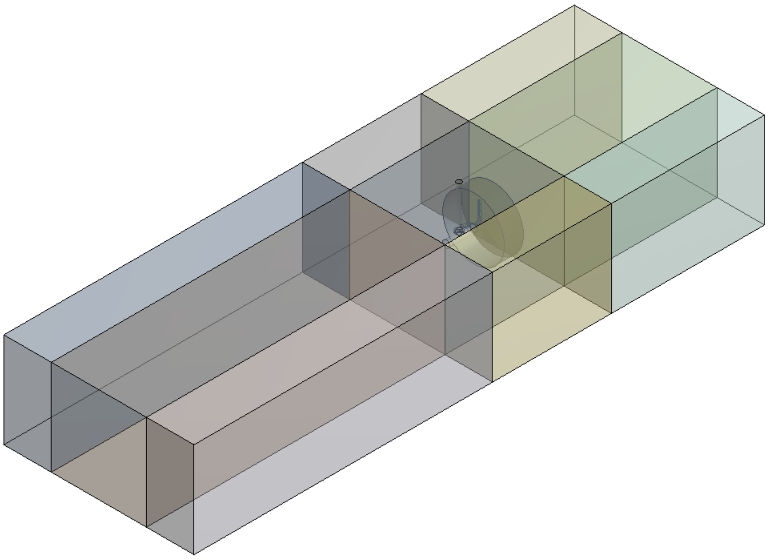

Figure 4.4: Blocking approach used to break up the model geometry.

4.2.2 Simulating turbine rotation

Two analysis methods are available within ANSYS CFX; steady state or transient. Both offer the user different controls over the model, most notably when modelling rotation. The rotation of the turbine is usually controlled by use of a MFR. The MFR is an independent sub-domain, seen in Figure 4.3, within the model that contains, in this case, the turbine rotor.

When using the steady state analysis method, a single final time independent solution is found. This is achieved by adding a rotational component to the flow as it enters the MFR. The flow is rotated around a stationary or 'frozen' rotor at the rotational velocity corresponding to the desired angular velocity for the turbine and is used to replicate the turbine rotation. One of the problems with steady analysis for a turbine rotor is that the turbine will only ever be in one location relative to the stanchion and nacelle. The periodic fluctuations associated with the blade passing the stanchion will not be observed as the rotor will not be moving during the simulation. If the blade was at top dead centre throughout the simulation then interaction with the stanchion could cause the C_P and C_T to be lower than expected.

The transient analysis uses a sliding mesh approach to simulate the rotation of the turbine. For transient simulations the MFR rotates with respect to time. In using a transient approach, the thrust and torque on the blades is resolved at each time step as the turbine rotates giving a more representative view of the rotor performance throughout the entire rotation of the turbine. This is particularly important when looking at the fluctuating loads associated with highly turbulent and unsteady flows. The instantaneous fluctuations in the flow will be represented via changes in the thrust and torque values seen in the results. The interaction of the stanchion on the turbine performance can also be seen.

Despite being more computationally expensive due to the use of a sliding mesh, transient simulations were used for all simulations to allow the dynamic behaviour of the device to be captured during this study, unless otherwise stated.

4.2.3 Domain interface

The two domains in the model needed to be connected to ensure the preservation of terms between the flume and MFR, as the domains were changing from stationary to rotating respectively. A ‘fluid-fluid’ domain interface was used and included the three faces for both the cylinder and the flume, as discussed in Section 4.2.1, so that the flow passing between the flume and MFR was uninterrupted.

4.2.4 Mesh controls

A control volume is created around the vertex in question from the central point of the surrounding elements. The Navier-Stokes equations are then resolved at the node to determine the properties of the flow field in this region. As CFX is vertex centred the number of elements and the number of nodes in the simulation are different. The larger the number of nodes in the model the greater the detail gathered about the flow field, however the longer the computational time.

The size, density and shape of these elements will influence the accuracy of the overall solution and the speed at which a converged solution is reached. The greater the number of cells in the unstable flow regions, the more accurate the result, however the longer the simulation will take [152, 153].

4.2.4.1 Global mesh controls

ANSYS meshing allows global controls to be set for the mesh in all the domains in the model. While there are a number of options that can be altered within the global mesh controls only those that were changed are mentioned and discussed here.

Due to the complex nature of the turbine geometry the global sizing function was set to *proximity and curvature* which refines the mesh in regions where geometric faces and/or edges are in close proximity to one another as well as areas where there is high curvature of either faces or edges so that the 'size will not violate the maximum size or the curvature normal angle' [152]. The *relevance centre* setting was also changed. The three options coarse, medium and fine can be chosen by the user and alter the density of the mesh throughout the domains. The *fine* option was selected to refine the mesh in regions where no local refinement was used.

Although not a setting that is manually changed by the user, information on the number of elements and nodes contained in the global mesh can be found within the global mesh tools.

4.2.4.2 Local mesh controls

Local mesh controls enable the user to select specific nodes, edges, faces or bodies where the mesh is to be refined. Unlike the global controls the refinement only occurs at the specified locations.

For the turbine rotor, hub, stanchion and nacelle the *face sizing* option was used to control the maximum face size applied to the selected surfaces. The interface between the MFR and the flume was refined so that both sides of the interface would have comparable face sizing to help with the preservation of terms. The face sizing on the blades was set to 0.0015m. The expansion rate was 1.2 from the boundary layer until the mesh size reached the value given to the MFR volume of 0.015m. Both sides of the interface mesh was also given a sizing of 0.015m.

The blocking approach used in Section 4.2.1 when making the geometry allowed a hexahedral mesh to be generated in large regions of the model. Hexahedral cells offer the advantage of producing a more structured mesh when compared to tetrahedral cells and can also reduce the element count in the model, important for keeping the computational time down. For each of these blocks an edge sizing was used to divide the model into a number of divisions in the global x-, y- and z-directions giving more control over the number of cells used in the total model. The block surrounding the stanchion and the MFR was left with a tetrahedral mesh due to the complex geometry and a max cell size was applied. An example of the hexahedral and tetrahedral meshes are shown in Figure 4.5.

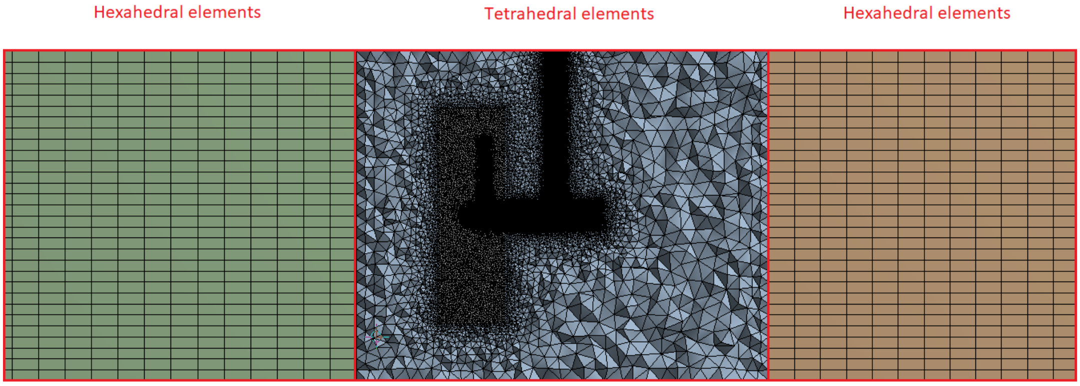

Figure 4.5: Structured hexahedral mesh used upstream and downstream of the turbine with an unstructured tetrahedral mesh around the MFR and stanchion.

4.2.5 Mesh independence

To ensure the CFD results were not being influenced by the mesh, a mesh convergence study was conducted. The mesh independence study has been split into two parts to simplify the impact of each region on the turbine performance; the flume and the MFR. The mesh independence study was conducted for the proposed turbine operating region, TSR 4.

Flume The mesh in the flume region was refined incrementally to see how the turbine performance changed. To determine the mesh for the flume a random mesh was generated for the turbine blades so the impact of changing the flume size could be seen. It was noticed early on that the far upstream and far downstream mesh had minimal impact on the turbine performance. The tetrahedral mesh region around the MFR and the stanchion had the largest impact on the torque and thrust prediction. Table 4.4 shows the results from the study. In each case the rotor was run at TSR 4, peak power, with a flow velocity of $1\,\mathrm{m\,s^{-1}}$.

Table 4.4: Impact of flume mesh density on torque and thrust prediction.

Mesh Number	Elements	Nodes	Torque, Nm	Thrust, N
1	2.92 x 10^6	5.59 x 10^5	18.55	329.82
2	3.44 x 10^6	7.01 x 10^5	18.01	323.79
3	3.79 x 10^6	7.71 x 10^5	17.78	323.47
4	5.08 x 10^6	9.94 x 10^5	17.73	321.25

The torque and thrust reduce as the mesh sizing is reduced and the node count increases. The percentage difference between mesh 1 and mesh 4 for the torque and thrust is ≈ 4 % and 3 % respectively. The percentage difference between mesh 3 and 4 is less than 1 %. The computational time increases as the element count increases so mesh 3 was chosen over mesh 4.

Moving frame of reference To help with the preservation of terms across the interface between the flume and the MFR a comparable mesh sizing was required. A ratio of 3:1 on the flume side and MFR side respectively is recommended [152]. Using a ratio of 3:1 would mean that one node is being used by 3 nodes on the other side of the interface and so to try and align the nodes on either side of the interface a ratio of 1:1 was used in this work. The size of the mesh used on the MFR faces however was determined by the max face size used as the volume mesh in the MFR.

The blade mesh was incrementally changed to determine the influence of the mesh structure and size on the performance of the device. The CFD results were compared to one of the sets of experimental data from [154]. All information on the testing and the data can be found in [154]. In total five different meshes were considered that decreased the face size on the pressure and suction sides of the blade. The torque and thrust values for each of the 5 meshes at TSR 4 for a flow speed of $1.1\,\mathrm{m\,s^{-1}}$ can be seen in Table 4.5. These values may differ from Tables 4.5 and 4.4 as during those studies the blade mesh had not been studied and so a generic mesh was used based on the global mesh settings.

Table 4.5: Impact of MFR mesh density on torque and thrust prediction.

Mesh Number	Elements	Nodes	Torque, Nm	Thrust, N	Max y+
1	2.79×10^6	5.13×10^5	17.48	346.27	150
2	2.78×10^6	5.10×10^5	17.48	346.24	160
3	3.34×10^6	6.10×10^5	18.13	352.50	130
4	5.30×10^6	9.68×10^5	18.46	357.73	125
5	5.38×10^6	9.88×10^5	18.40	356.41	120

There is only a 5 % difference in the thrust and torque values between meshes 1 and 5 despite almost doubling both the elements and the nodes around the blade surface. Even though the percentage difference in the torque and thrust predictions were small between all of the meshes, it was decide that one of the higher density meshes should be used to improve the capture of the boundary layer. The boundary layer region around the blade is complex due to both the flow and the geometry shape, and so increasing the number of nodes in the boundary would improve the quality of the resolution.

The change in the torque and thrust was less than 1 % for meshes 4 and 5 despite increasing the mesh density on the blades. The main difference between the meshes was the way the blade mesh was created. Mesh 4 used a more structured approach but with the same blade sizing as mesh 5. Due to the minimal change in the torque and thrust prediction of both meshes, mesh 4 was chosen going forward due to the lower element count.

4.2.6 Setup

The simulation was set up using CFX-Pre. Here the physical constraints on the model, the fluid properties, turbulence models and the settings required for the solver were set.

4.2.6.1 Domain and fluid properties

The relative pressure through the domain was set to 0 Pa as the fluid flow was not pressure driven. The fluid was selected as ‘liquid water’ and used the predefined properties from the CFX database for fresh water. The density was 997.0 $\mathrm{kg\,m^{-3}}$ with a dynamic viscosity of $8.8994 \times 10^{-4}\,\mathrm{kg\,m^{-1}\,s^{-1}}$.

The SST k-ω turbulence model was used to close the RANS equations. Each domain could be specified as rotating or stationary, the MFR was set to be rotating with the flume domain stationary. For the MFR an *if* statement was used to control the angular velocity. It meant the angular velocity was incrementally increased after a specified time based on the angular velocity of the turbine and therefore the number of rotations completed. The number of rotations was chosen to be high enough that convergence could be reached even at the highest TSR value, while still providing enough rotations to average the results over. This helped reduce the time taken for convergence between the rotational speeds as the changes between models were minimised.

4.2.6.2 Boundary conditions

Inlet The inlet boundary condition was used to define the region where the flow was entering the model upstream of the turbine. When modelling the tow tank simulations, the normal speed option was selected. The turbine saw almost zero turbulence during the experimental tow tank testing and so the inlet was given a low turbulence value of 1 %. In application the resolved turbulence will be close zero due to the averaging process in the RANS equations filtering out any fluctuations in the flow velocity [155].

Outlet The outlet boundary condition was used downstream of the turbine to denote where the flow was exiting the domain. The static pressure was set in accordance with the relative pressure over the domain, 0 Pa, which was then maintained over the outlet as a fixed value.

Walls The no slip wall condition was used for the tank, stanchion, blades and hub. The no slip condition assumes that there is no flow at the wall. For the top surface of the tank in the model the free slip wall condition was used, which sets the wall shear stress to zero and so the fluid near the wall is not affected by friction [153]. The walls were deemed to be outside the region of influence and therefore the mesh was left unrefined to reduce the element count.

Initial conditions For all transient simulations the domain was initialised for a time of t=0. The fluid velocity and turbulence options were set to match those at the inlet. A steady state model was run until converged with the same inlet and outlet boundary conditions and the results file was used as the initial conditions file for the transient simulation. In doing this any regions of stable flow that were determined in the steady state model were already resolved and so the transient model takes less computational time to converge for the first transient time step.

4.2.6.3 Expression monitoring and monitor points

CFX expression language (CEL) was used to monitor the thrust and torque on the blades. Not only does this allow the instantaneous values for thrust and torque to be seen at each time step throughout the transient simulation but it also offers another monitor for convergence. The following expression was used, to track a specified variable acting in a given coordinate direction on a named boundary.

$$variable\_z()@BoundaryName \tag{4.1}$$

In this instance the thrust loading on the blade in the z- direction was monitored at each time step. The torque in the x-, y- and z-directions was monitored so that the rotor torque and blade root bending moments could be found. Monitor points were put in 1 m upstream of the device on the horizontal place containing the rotational axis at cross-stream positions between $x = \pm 0.45$ at 0.05 m increments. These monitor points recoded the flow velocity in x-, y- and z-directions at each time step.

4.2.6.4 Solver settings

Discretisation scheme The high resolution scheme was used with the RANS model, which switches between either a first or second order upwind scheme depending on whether the boundedness criterion was satisfied.

Residual targets The aim of the residuals is to see how well the solution satisfies the RANS equations. CFX uses normalised residuals to judge the convergence of the model [143]. The value was set to $1e-4$ which is deemed suitable for many engineering applications [153]. The residual target affects the convergence of the simulation and so the impact of the residual target on the results was considered. To do this the target was changed first to $1e-5$ and then $1e-6$ for a number of iterations. The smaller residual targets made no difference to the results obtained from the model, however the computational time increased by a factor of 4 and 10 for the $1e-5$ and $1e-6$ targets respectively. Based on this the value of $1e-4$ was used.

Coefficient Loops Within each time step there are a predefined number of coefficient loops. The model aims to reach convergence during these coefficient loops before moving on to the next time step. 10 coefficients loops were used as an upper limit however convergence was normally reached within 3 or 4 loops.

4.3 Experimental testing

The device used during the experimental testing, which formed the basis for the computational model, was a 900 mm diameter lab-scale, 3 bladed horizontal axis tidal turbine. This was in line with a 1/20th scale device and can be seen in Figure 4.6. The blades were located on pins attached to the hub and each pin used two full-bridge strain gauge set-ups to measure the blade root bending moments. The blades were 384.5 mm in length and were grub screwed in place. The nose cone had a diameter of 130 mm which was stepped up to 150 mm behind the blades. The rotor loads were measured via an integrated torque and thrust transducer located behind the hub. A permanent magnet synchronous motor (PMSM) as used to control the turbine. It was located at the back of the nacelle to reduce electrical noise in the measurements from the front of the rotor. The stanchion diameter was 105 mm giving a gap of 3.5 stanchion diameters between the front of the stanchion and the back of the blades. Further detail about the device can be found in [154].

Experimental testing was conducted in the tow tank facility at the Kelvin Hydrodynamics Laboratory. The tank is 2 m (depth) x 4.6 m (width) x 76 m (length), and the turbine was fixed to the carriage with the rotational axis of the turbine 1 m below the surface. The turbine was controlled at set-point torque and speed control using the PMSM. As the angular velocity in CFX was set to a fixed value the comparison of results was done for speed control only.

Data was recorded for 60 s at each point on the curve. The sample rate for data acquisition was 2 kHz. The turbine was accelerated until it reached the desired angular velocity prior to the carriage moving so that the full length of the tow tank could be utilised. Table 4.6 details the test cases used for the experimental testing. The CFD simulations were set up to replicate the experimental tests.

Figure 4.6: Turbine in-situ during testing at the Kelvin Hydrodynamics Laboratory.

Table 4.6: KHL test cases.

Tow speed, $ms^{-}1$	λ
0.8	1.5, 2.5, 3 ,3.5, 4, 5, 6.5
1	1.5, 2.5, 3 ,3.5, 4, 5, 6.5
1.2	1.5, 2.5, 3 ,3.5, 4, 5, 6.5

4.3.1 Uncertainty in Turbine Performance

The bias and precisions errors associated with the measurement systems used to record the data contribute to the uncertainty analysis. Calibration of the measurement systems and quantification of the uncertainty is required. The thrust and torque transducer was supplied and calibrated by Applied Measurements prior to the delivery. The results from the calibration can be seen in Table 4.7. The hysteresis gives an indication to the difference between the values for a specific point when loading and unloading the transducer. The non-linearity refers to how linear the curve is for the fit of the calibration data. When loading the transducer, there is going to be an associated strain in the x, y and z directions even if the load is only to be applied in the x direction. The magnitude of the strains in the y and z directions are given by the cross-sensitivity.

Table 4.7: Calibration results for the torque and thrust transducer as provided by Applied Measurements Ltd.

	Value
Thrust Gradient, A/N	5.349E-4
Thrust non-linearity	±0.056 % FS
Thrust hysteresis	$<$ 0.098 % FS
Thrust cross-sensitivity	$<$ 0.45 % FS
Torque Gradient, A/Nm	8.01E-3
Torque non-linearity	±0.031 % FS
Torque hysteresis	$<$ 0.062 % FS
torque cross-sensitivity	$<$ 0.18 % FS

The out-of-plane bending moments were calibrated prior to the experimental testing. A hanging mass was incrementally increased and decreased to load and unload the transducers. The current in Amps was recorded at each point. The results from the calibration can be seen for each of the blades in Table 4.8. During the testing only the measurements from blade 2 were recorded due to water ingress and so when discussing any results for the out-of-plane bending moments later on it will be for to a single blade. The problem of water ingress was later identified as an ineffective seal at the nose cone due to the insufficient compression of an O-ring.

The sources of the uncertainties, shown in Table 4.9, are as follows. The torque and thrust transducer are traceable to the National Standards Certificate Number TD0242. The out-of-plane bending moment bias uncertainty was calculated based on the measured calibration results. The angular velocity was found using the time stamp frequency and the corresponding encoder position. For the water density the difference in the density

Table 4.8: Calibration results for the flap-wise blade root bending moment transducers.

	Blade 1	Blade 2	Blade 3
Gradient	1.60E-4	1.63E-4	1.62E-6
Fit Uncertainty (SEE), Nm	0.43	0.41	0.90
Bias Uncertainty	0.12	0.12	0.12
Total Uncertainty	0.55	0.53	1.02

of fresh water between 10 °C and 25 °C was found. The turbine radius is based on the manufacturing tolerances throughout the production of the turbine components and the human error associated with fixing the blades onto the hub. Finally the fluid velocity is based on the LDV manufacturer calibrations.

Table 4.9: Uncertainty in the variables used for the experimental turbine performance calculations.

	μ_b	μ_p	μ_{tot}
Torque transducer, N	0.2	0.61	0.64
Thrust transducer, Nm	7.1	5.9	9.24
Out-of-plane bending moment, Nm	0.12	0.6	0.61
Angular velocity, rad$s^{-}1$	0.0001	0.028	0.028
Water density, $kgm^{-}3$	2	-	2
Turbine radius, m	0.005	-	0.005
Flow Velocity, $ms^{-}1$	0.001	0.0011	0.0021

Based on knowing the total uncertainty for a measurement presented in Table 4.9, and knowing the mean values for each measurement at each TSR the total percentage uncertainty for the performance coefficients for each TSR can be found using the rules for error propagation presented previously. An example for the power coefficient is given in Eq. 4.2. The total uncertainty values from Table 4.9 are then used to find the total uncertainty based on the measurement systems for the power coefficient. This process is repeated for the remaining performance coefficients. The results for one example for each of the performance coefficients can be seen in Table 4.10.It used the data in Chapter 4 for the mesh independence study from TSR 4.

$$\mu C_P = |C_P|\sqrt{(\frac{\mu_{tot}Q_T}{Q_T})^2 + (\frac{\mu_{tot}\omega}{\omega})^2 - (\frac{(\mu_{tot}\rho)}{\rho})^2 - (2 * (\frac{(\mu_{tot}R)}{R})^2) - (3 * \sqrt{(\frac{\mu_{tot}u}{u})^2})} \tag{4.2}$$

The total uncertainty in the measurements is small, less than 3 %, for all the performance coefficients. The flows considered throughout this work are largely turbulent in

Table 4.10: Example case calculating the total uncertainty in the performance coefficients based on data from [154].

TSR	μC_P	μC_T	μC_Q
4	0.012	0.018	0.0028

nature. Therefore, the fluctuations seen in the measurements are not related to a large uncertainty in the measurement instruments but are a characteristic of the data being measured. Due to this the standard deviation, σ, is used rather than the uncertainty. The standard deviation is used to give information on how different readings in the data set are from the mean value. Plus and minus one standard deviation is included to give a 95 % confidence level. Any error bars in the figures themselves are therefore the standard deviation.

4.4 Results

The results from the BEMT were used to find the preferred blade design from the designs tested. Once tested in BEMT a 3D model was drawn in SOLIDWORKS 18.0 for use in the CFD model. The numerical models were compared to each other to see how well each of the numerical methods predicted the device performance. The results for the experimental and the numerical testing were compared to each other to see how well the numerical models matched the measured values for device performance and are discussed below.

4.4.1 BEMT

A range of chord lengths and twist distributions were looked at to find the optimum blade design. The optimum chord length distribution was found to be that of Design 1 in Table 4.2. The results from the four twist distributions that gave the highest C_P are shown in Figure 4.7. It was found that the power coefficient for the 19 degree twist case gave the highest value when compared to the full range that was tested. The curve at the peak C_P value was also the flattest giving a wider operating range. BEMT found the peak C_P to be just over 0.45 at a TSR of 3.5. The C_T values for the same twist distributions are plotted in Figure 4.8. Despite the 19 degree case having the highest thrust coefficient it is still within the initial design remit of keeping the new C_T value within 10 % of the old blade. Based on the findings from the BEMT the chord lengths from Design 1 were used. The twist distribution of 19 degrees was also used and the value of the twist and the chord length at each radial position can be seen in Table 4.11.

Table 4.11: Blade characteristics for the revised blade design.

r/R	Twist, *deg*	Chord Length, *mm*
0.146	19	72.5
0.229	19	87.8
0.305	14.58	103.1
0.382	11.13	109.6
0.459	8.57	109.5
0.536	6.50	105.1
0.615	4.71	93.1
0.692	3.09	83.6
0.768	1.79	73.6
0.845	0.70	67.6
0.922	0.14	62.8
1.00	0	58.9

The pitch angle of the new blade was also determined using BEMT. The region that was focussed on was between 5-8 degrees and was chosen because the pitch angle for the old blade design was 6°. As such the pitch angle for the new blade was expected to be of a similar value. Figures 4.9 and 4.10 show the impact that changing the pitch angle has on the performance of the new rotor design. The pitch angle of 8° degrees was found to not only have the highest C_P value of ≈ 0.45 but also the smallest value of C_T or ≈ 0.88 at the TSR value for peak power. A pitch angle of 9° was also run however it sits on top of the 8° case and was left off from Figures 4.9 and 4.10 to improve clarity.

4.4.2 Numerical comparison

The two numerical methods, BEMT and CFD, were compared to each other when used to predict the performance of a tidal device. BEMT however does not include a stanchion when estimating device performance and so two CFD models were made: one that included the stanchion and one that did not. The cross section of the domain was chosen such that the blockage ratio was less than 1 % for both CFD models.

For the CFD model without the stanchion a steady state analysis was done to reduce the computational time as there was no interaction of the blades with the stanchion. The model that contained the stanchion was run using the transient analysis method and the results were averaged over several revolutions once convergence was reached. As previously mentioned the stanchion was 105mm, giving a spacing of ≈ 3 stanchion diameters from the back of the blade to the front of the stanchion. The thrust force acting on the stanchion

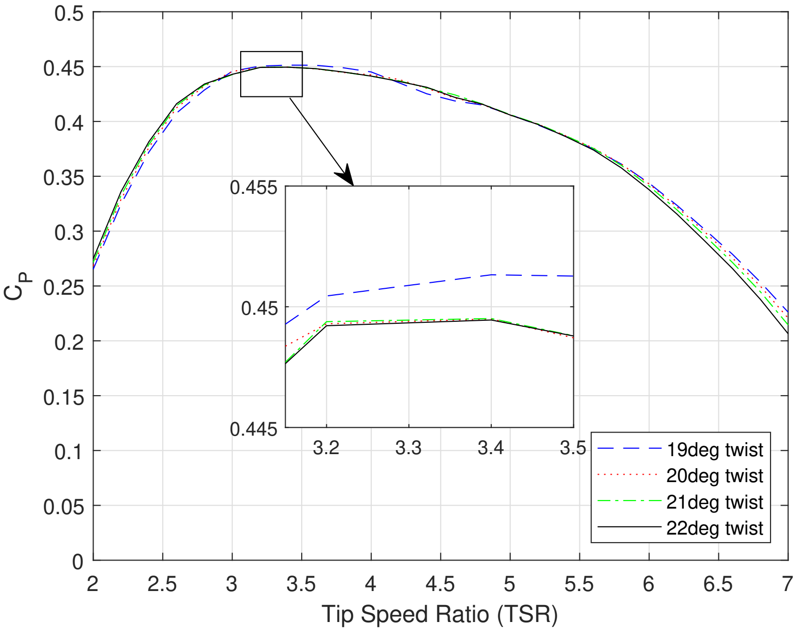

Figure 4.7: Comparison of the BEMT C_P prediction for twist distributions between 19-22 degrees

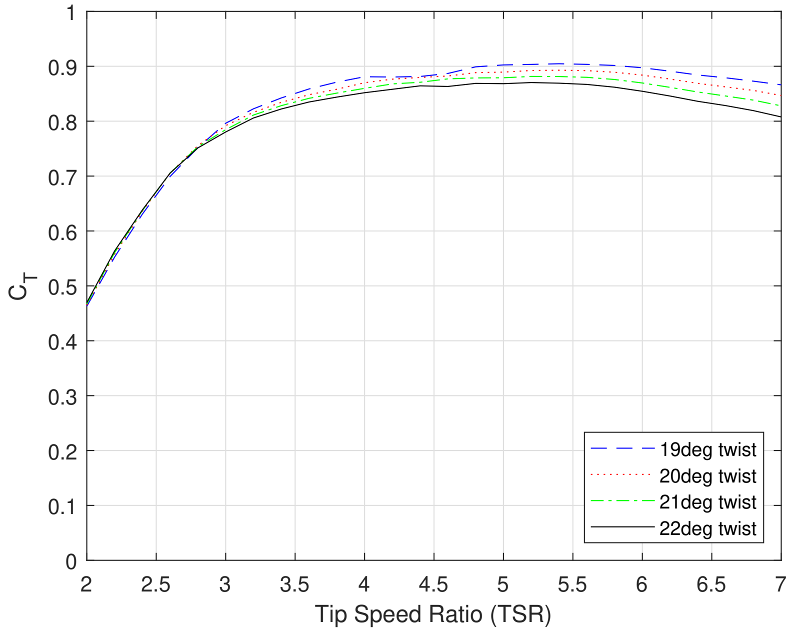

Figure 4.8: Comparison of the BEMT C_T predictions for twist distributions between 19-22 degrees

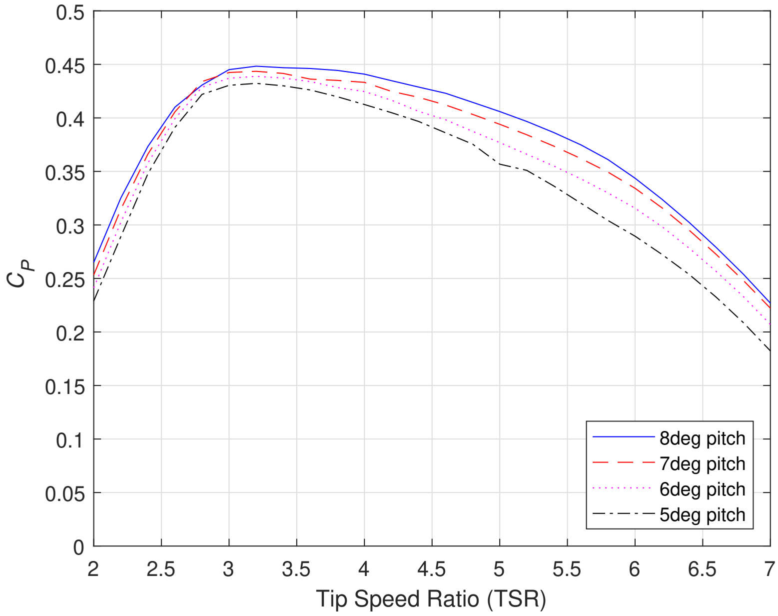

Figure 4.9: Comparison of the BEMT C_P predictions for pitch angles of 5-8 degrees with a twist distribution of 19 degrees.

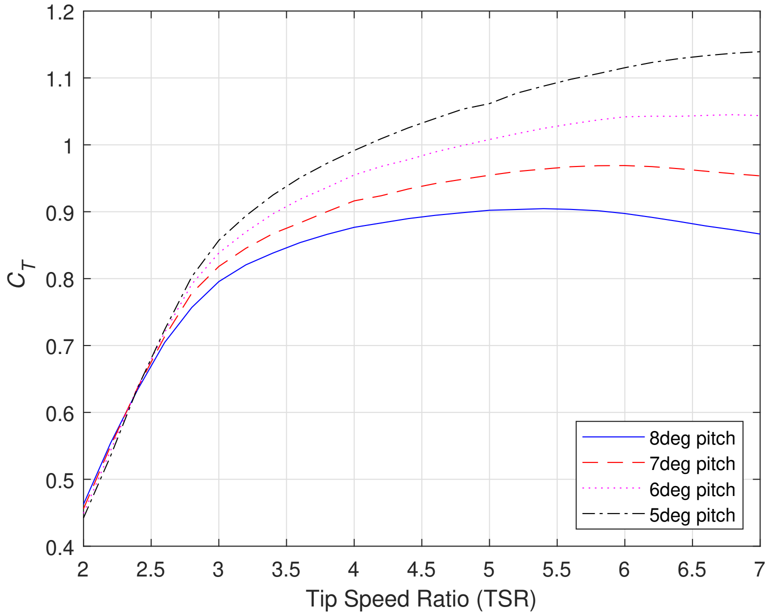

Figure 4.10: Comparison of the BEMT C_T predictions for pitch angles of 5-8 degrees with a twist distribution of 19 degrees.

is $\approx$ 10N.

Figures 4.11 and 4.12 compare the power and thrust coefficients for the three numerical models. The BEMT results for values of TSR < 2 have been ignored. BEMT only solves for a 2D aerofoil profile at different radial points up the blade and so no 3D, or spanwise, flow is accounted for. This can lead to stall delay which can introduce inaccuracies when predicting device performance at low TSR values [83, 156].

There are two comparisons to make; the CFD model that includes the stanchion against the BEMT and the CFD without the stanchion against BEMT.

CFD with stanchion v BEMT By looking at the curves in both Figures 4.11 and 4.12 you can see that the BEMT over predicts for both the power and thrust coefficient when compared to the CFD model. The stanchion causes a blockage effect on the flow directly behind the turbine rotor. A region of slower flow velocity develops here and attaches to the back of the blade, seen in Figure 4.13 ultimately reducing the torque and force generated by the turbine. As BEMT does not take the stanchion into consideration the values predicted will be higher, as seen.

CFD without stanchion v BEMT There is a close comparison between BEMT and the CFD model in this case. As the stanchion has been removed there is no impact of the region of slow flow velocity generated by the blockage from the stanchion and so the force and torque on the blades does not fluctuate in the cyclic nature that is associated with the blade passing the stanchion. The peak values for both C_P and C_T are in the same order of magnitude for BEMT and CFD however the peak TSR values change, with CFD giving a peak TSR at 4 and BEMT is close to 3.5. However, all the values in this region at the peak of the C_P curve seem to be ≈ 0.45 showing good agreement between the numerical methods.

The discrepancy in the methods is highlighted at the lower and higher TSR regions. For reasons already mentioned the lower TSR region for BEMT has been ignored. In the region for TSR > 5 the CFD model the C_P drops off quite rapidly. Possible reasons for the drop in C_P are discussed in Section 4.4.3.

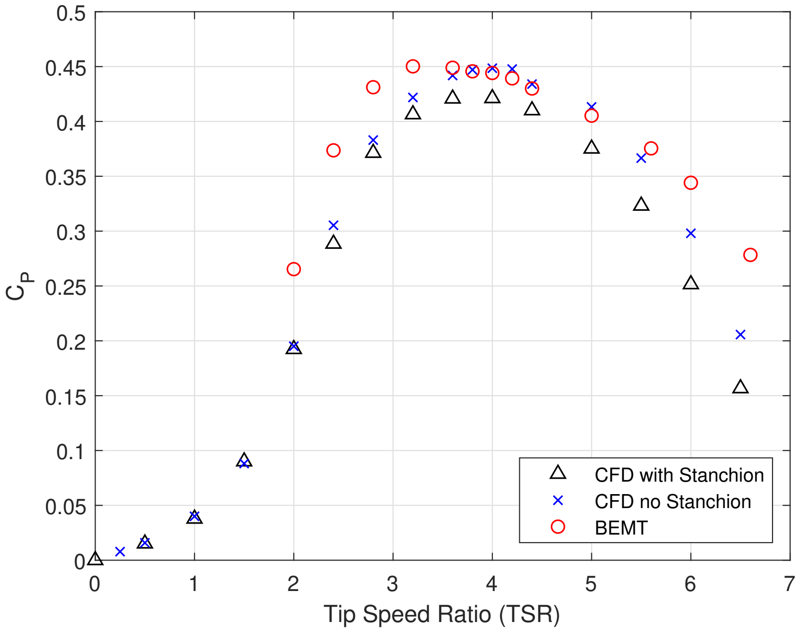

Figure 4.11: Comparison of C_P for BEMT and CFD, both with and without a stanchion.

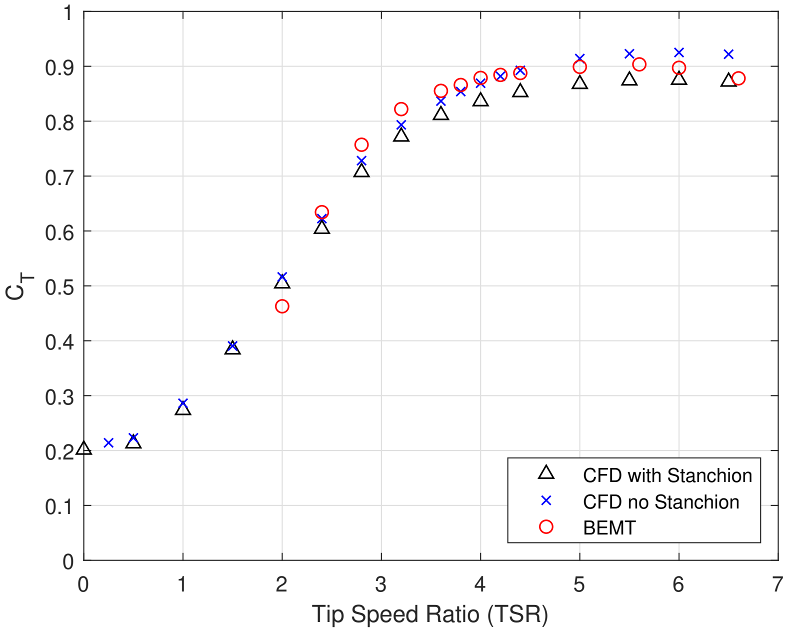

Figure 4.12: Comparison of C_T for BEMT and CFD, both with and without a stanchion.

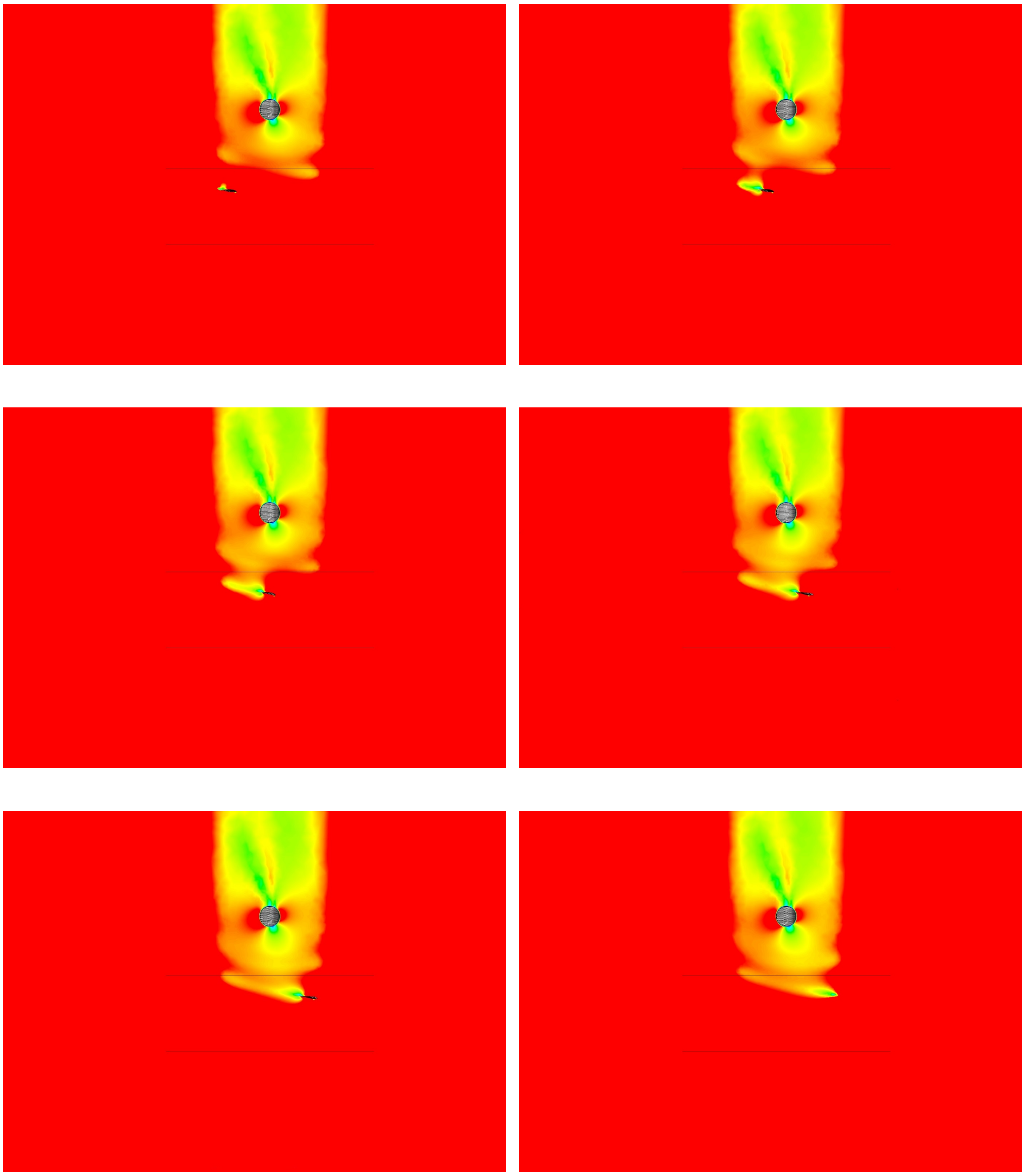

Figure 4.13: Region of slow flow velocity attaching to the blade due to the blockage effect from the stanchion. The plane showing fluid velocity is at r/R = 0.7.

4.4.3 Numerical validation

The experimental work was carried out at the KHL tow tank as discussed in Section 4.3. The CFD model was set up to directly replicate the tank geometry, water depth at the time of testing and the location of the turbine in relation to the tank surface. The length of the CFD domain was shorter than that of the tow tank as the wake was not being studied as part of the CFD modelling. Also, the extra computational time to model the full 180 m of the tow tank would be substantial.

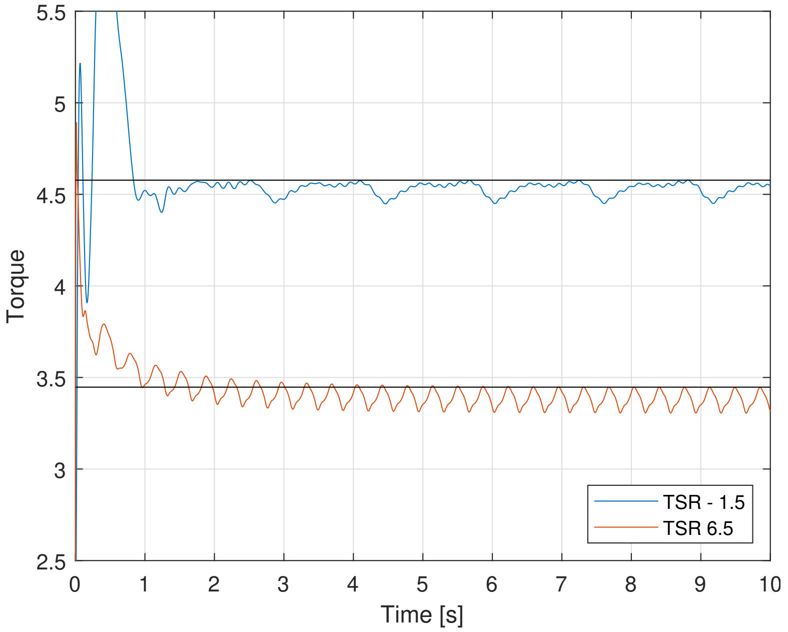

Figure 4.14: Convergence of the torque for one blade at TSR 1.5 and 6.5.

Each model was run for a minimum of 20 rotations. This meant the time for each was dependent on the angular velocity. It was assumed that at the higher angular velocities the model would take longer to converge and so by running for 20 rotations there would still be a suitable number of rotations to average the values over. It can be seen in Figure 4.14 that for a TSR 6.5 the torque takes $\approx$ 6 s to reach a converged state for one of the blades. For TSR 1.5 convergence is reached more quickly, $\approx$ 3 s. This time difference is not as drastic as thought prior to running but this could be more severe if the models were not run consecutively. For the following results a minimum of 10 rotations were used for the averaging of the results to ensure the turbine characteristics were captured. Only once the model was deemed converged by monitoring the residual targets were 10 rotations then used.

The performance coefficients for each of the three flow velocities are plotted in Figures 4.15, 4.16 and 4.17. Error bars have been included in the experimental results. The error bars are +/- the standard deviation, which show the fluctuation around the mean in the measure value rather than a quote on the uncertainty. This gives a confidence level greater than 95 %. The error bars have not been included in this instance for the CFD results as they are no wider than the points plotted.

To establish the dependence of performance and loading on Reynolds number, experiments were conducted with three onset velocities. As mentioned previously there is a relationship between the non-dimensional performance coefficients and the Reynolds number. Table 4.12 shows the values for the performance coefficients for the experimental and CFD cases at the peak power, TSR 4. The largest percentage difference is seen between the C_T cases at $\approx$ 6 %. The performance coefficients for the experimental for all three flow velocities fall within the error bars highlight that the performance of this device is independent of the Reynolds number. This is also seen in the CFD results which again sit on top of one another. The importance of being Reynolds independent is that the non-dimensional performance coefficients are independent of the flow velocity. They are only affected by a change in the angular velocity of the device.

Table 4.12: Comparison of performance coefficients at peak power, TSR 4.

Flow Velocity, ms^-1	Method	C_P	C_T	C_Q
0.8	Experimental	0.48	0.97	0.121
	CFD	0.50	1.04	0.125
1	Experimental	0.48	0.97	0.12
	CFD	0.50	1.04	0.125
1.2	Experimental	0.48	0.95	0.121
	CFD	0.50	1.04	0.126

The performance curves were generated from the rotor thrust and torque. As the CFD model used the same cross-sectional area as the tow tank no blockage correction was required as a like for like comparison was made. The blockage may explain the artificially high values of C_P, close to 0.49, but the aim of the validation was to compare the CFD to the experimental under the same conditions rather than correcting for blockage and comparing to an arbitrary CFD domain.

Good agreement is seen close to peak C_P for the experimental and numerical results. The CFD predictions for TSR 3-5 fall within the error bars. At TSR 2.5 and 6.5 the CFD under predicts the power generated by the turbine. As expected the C_Q and C_P curve

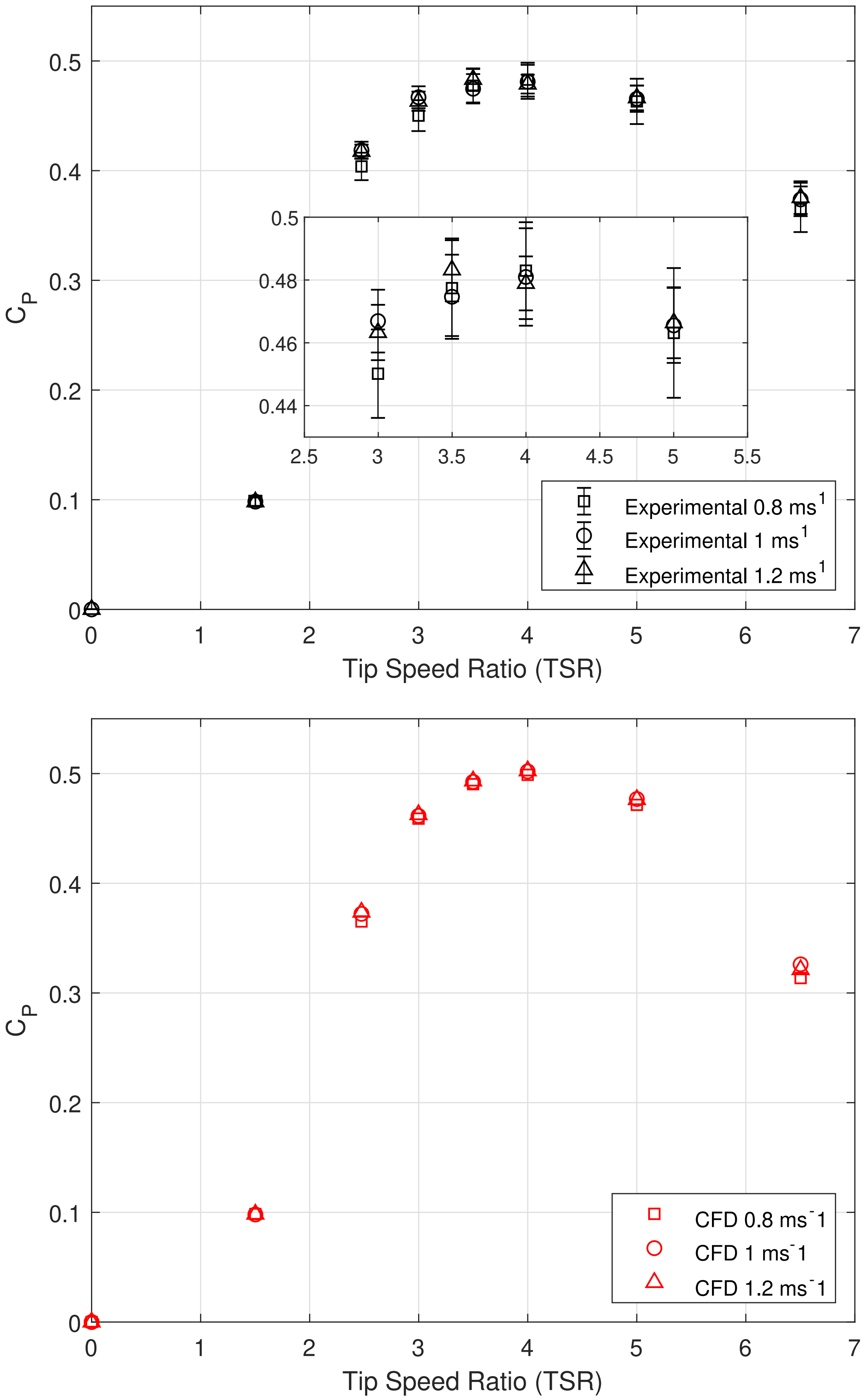

Figure 4.15: Performance curve comparisons for the C_P.

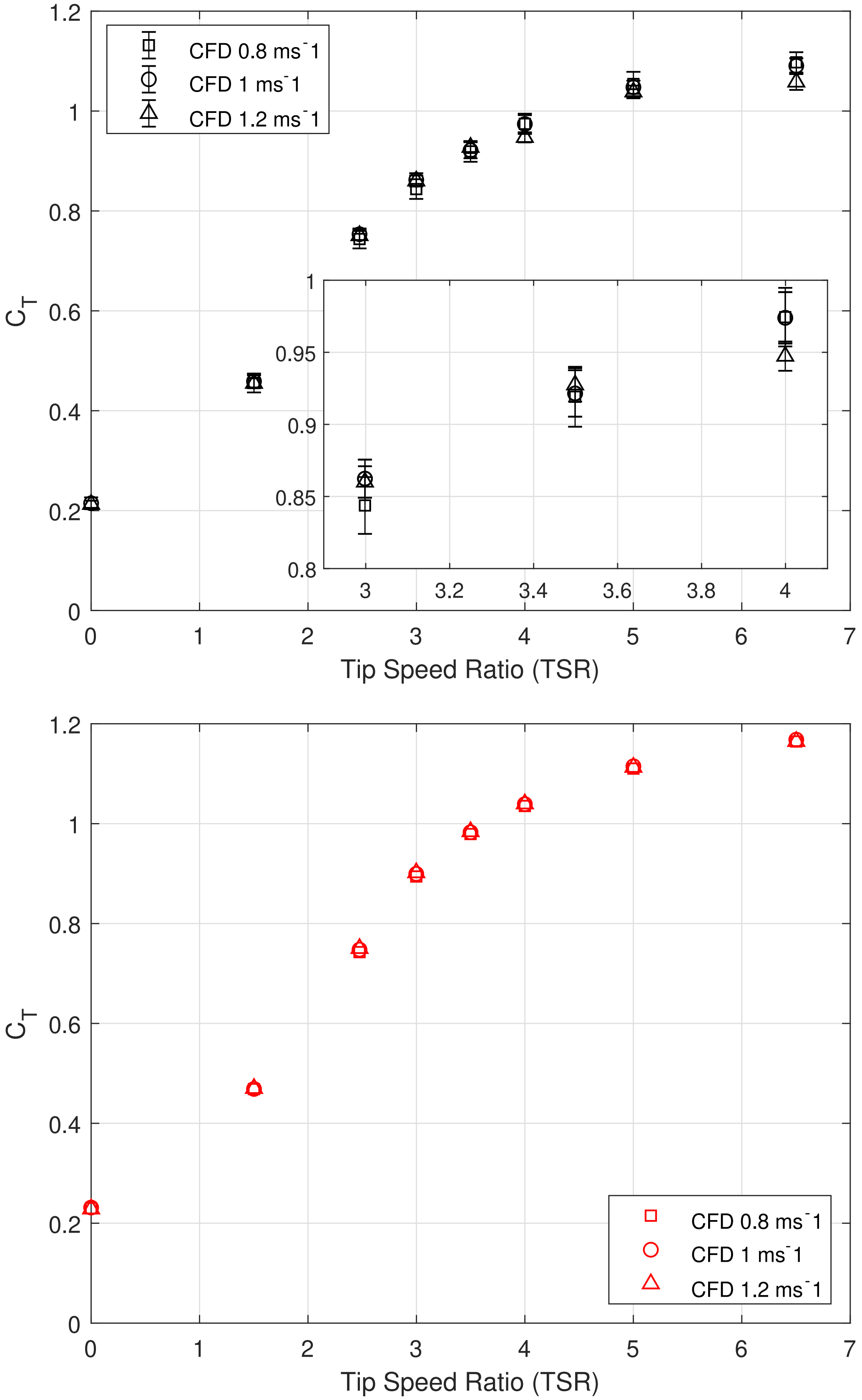

Figure 4.16: Performance curve comparisons for the C_T.

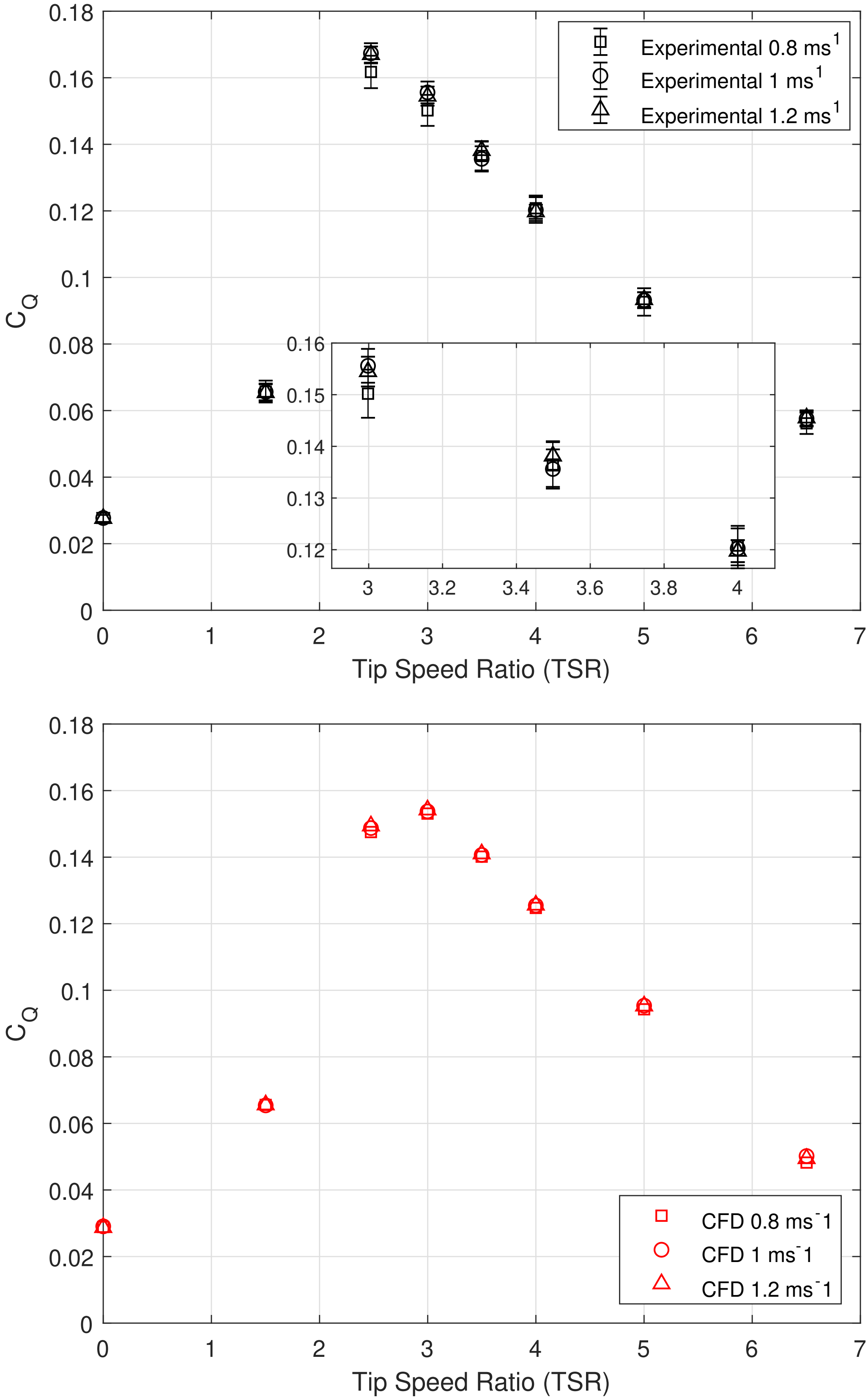

Figure 4.17: Performance curve comparisons for the C_Q.

follow the same trend with an under prediction of the torque at the lower and higher TSR.

The value for C_T is over predicted throughout the entire curve and so the drag force is being over predicted while the lift force in certain regions is under predicted. While an over prediction is not the desired outcome it does mean that when looking at the loading on the blade, there will be an overestimate of the loads that the device might be subject to. This over prediction of the C_P and the under prediction of the C_T points to an issue with the mesh. Specifically, in the boundary layer region as the lift and drag are being incorrectly calculated.

In this model the y+, discussed previously in Chapter [**theoryChapter**] at peak power was close to 100 on the pressure side at the tip of the blade and near 140 on the suction side at the tip of the blade. These values are very localised, and most of the blade has a much lower value of $30 < y+ < 70$. Therefore throughout these models the boundary layer is not directly resolved and wall functions are used. It is expected that as the local fluid velocity increases the y+. The local chord based Reynolds number is then changing for each radial element of the blade and as the flow velocity changes hence the variation in the y+ along the blade, with a peak at the tip of the blade where the local fluid velocity is the highest.

Figures 4.18, 4.19 and 4.20 show the y+ on the pressure and suction side of the blades for a TSR of 3, 4 and 5 respectively for a flow velocity of $1\,\mathrm{m\,s^{-1}}$. As the angular velocity increases higher up the TSR range the y+ on the blade increases, especially at the tip of the blade. The boundary layer becomes more complex as the velocity increases.

Producing one mesh for all points on the curve may not be the most suitable method when producing a full performance curve as the y+ between models is different. In an ideal world you would match the y+ between models so that the same approach was being taken in the wall regions for all angular velocities. However, this would require mesh optimisation for every point you wanted to run which is highly time consuming. The change in the y+ values maybe begin to answer why the drop-off in prediction occurs in the higher TSR region as the lift force is being under predicted due to an insufficiently refined mesh. The region of peak power is of most interest as this is where the turbine would be operating in a real-world application. In this case there is good agreement for TSR 3-5 between the CFD and experimental results, which is the expected turbine operating region. Due to this the mesh used for the modelling is suitably accurate to be capturing the peak power

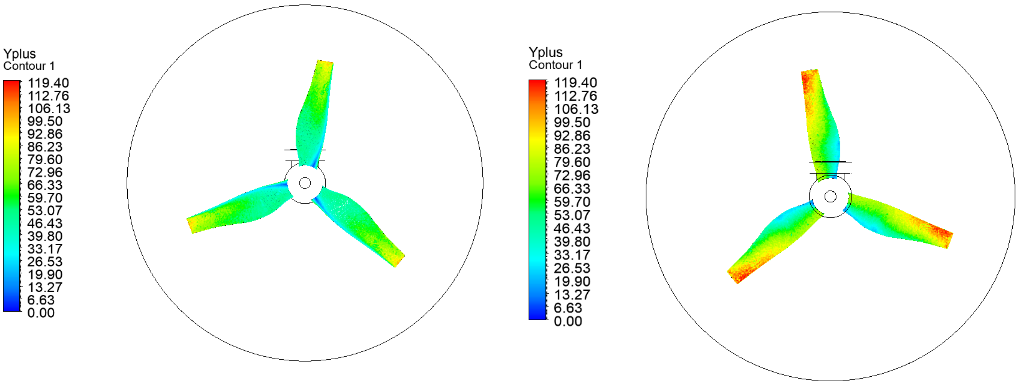

Figure 4.18: y+ values on the pressure (left) and suction (right) sides of the blade for TSR 3.

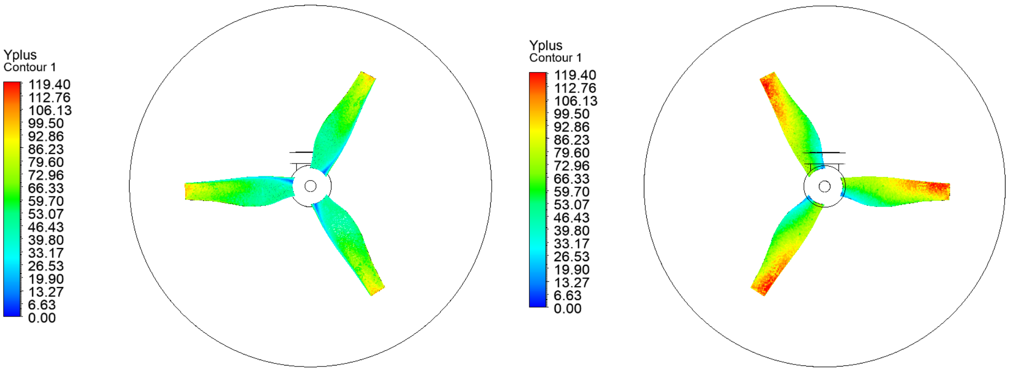

Figure 4.19: y+ values on the pressure (left) and suction (right) sides of the blade for TSR 4.

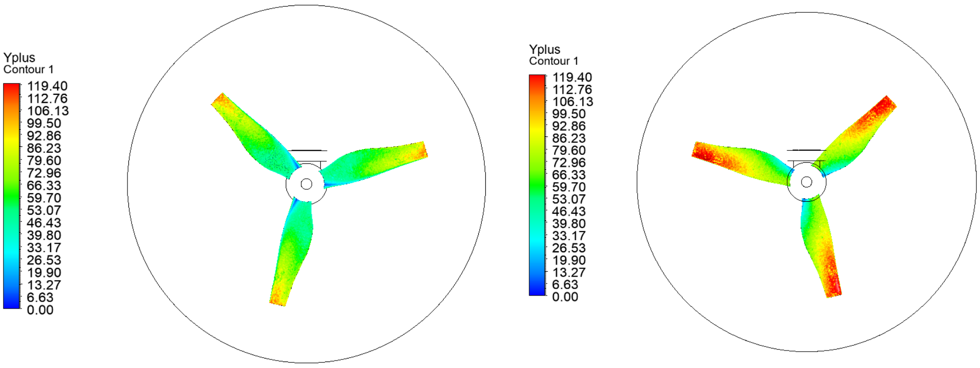

Figure 4.20: y+ values on the pressure (left) and suction (right) sides of the blade for TSR 5.

region, which is where the remainder of the modelling of this device will focus throughout the rest of this thesis.

The secondary objective of this chapter was to improve the C_P of the new design while not overly increasing the C_T compared to the previous turbine that has been used at Cardiff University. Both devices were tested during seperate experiemtnal test campaigns at the INSEAN town tank facility in Rome. The new device was tested by the auother and details of this work can be found in [157], however it has not been included as part of the work in this thesis. The old device was tested by [30]. As the diameter of the devices is different the blockage is not a perfect match however in both cases the blockage was less than 2 % and so no corrections were made [158]. The C_P for the new design was found to be 0.41 based on the experimental testing, whereas previously it was 0.39. The C_T was largely unchanged going from 0.84 to 0.87 for the new design. The new and old blade designs can be seen in Figure 4.21.

Figure 4.21: Comparison of the old blade (left) and the new blade (right).

4.5 Summary of new blade design

The new blade was 384.5 mm from root to tip used on a device with a rotor diameter of 900 mm. The chord length and twist distribution at each radial segment are the same as those shown in Table 4.2. Despite finding the optimum pitch angle to be 8° from the design process, during the experimental testing the pitch angle was set from the blade face rather than the chord as shown in Figure 4.22. The angle between the chord and the blade face was not accounted for. This meant that when the pitch angle was actually set it was only set at 6.24° as the angle between the face and the chord was not taken into consideration.

Therefore all the experimental data presented as part of this work was conducted with the pitch angle of the blade set to 6.24° as the pitch angle in the modelling was set from the chord. The data presented in Figures 4.15, 4.16 and 4.17 all used a pitch angle of 6.24° in keeping with the experimental. All further models and experimental tests discussed in this work also used a pitch angle of 6.24°.

Based on the numerical validation provided by the experimental testing the mesh for the new device, referred to from this point as T_{DOWN}, is the same as that used during Chapter 6.

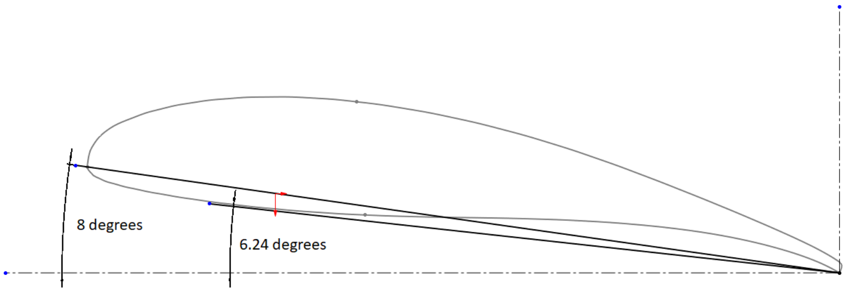

Figure 4.22: Representation of the error when setting pith angle as it was measured from the blade face and not the chord during the experimental set up.

Chapter 5

Comparison of CFD methods for turbine wake modelling

The study of turbine wakes is an area of active interest both experimentally and numerically [51, 110, 112]. The ability to accurately represent the wake of a device can help the development and installation of second-generation devices in tidal arrays. Numerical models and, particularly relevant to this work, CFD are being used more frequently to help understand the flow behind a device. Ebdon [14] experimentally and numerically tested a HATT device to characterise the wake and understand the impact of turbulence on wake recovery.

In the following chapter the device that was modelled and tested by [14], and not the device that was designed and developed in Chapter 4, is studied. This is done so that the wake modelling capabilities of CFX can be validated for use in Chapter 6 to study the performance of a second downstream turbine.

The following chapter details the experimental testing, CFD methodology used for the simulations and finally discusses the impact that the discretisation scheme has on the performance and wake prediction of a tidal device.

5.1 Experimental testing

The device used during the experimental testing, and that formed the basis for the computational model in the following chapter, was a 500 mm diameter lab-scale, 3 bladed horizontal axis tidal turbine. This device is referred to as T_{UP} from now on. The blades used the Wortmann FX63-137 aerofoil and had a twist from root to tip of 35°. The blade has a pin at the root which fits into the hub and fixed using grub screws. The instrumentation and motor power cabling were contained within the hydraulic hose shown in Figure 5.1 protruded from the downstream face of the nacelle. The turbine can be operated in fixed point speed or torque control using a synchronous torque motor however the fixed-point speed control option was used for the following testing. The torque generating current was used to provide the torque prediction for the rotor. No instrumentation was located upstream of the motor and so any losses in the system had to be quantified after testing to determine the rotor torque. The only thrust measurement was taken from strain gauges on the stanchion. The thrust value therefore includes the thrust from the rotor, hub and stanchion and so a direcet comparison with the CFD for rotor thrust cannot be made. A sample rate of 200 Hz was used to maximise the data capture time due to limited buffer size. Further detail about the turbine can be found in [52, 93, 14].

A Laser Doppler Anemometer (LDA) was used to take two-axis measurements of the flow field. As the testing was conducted as part of a wider test campaign the LDA measured the flow in the axial and cross-stream directions. LDA measurements were taken downstream of the turbine rotor. Measurements were taken at $x/D = \pm1.6, \pm1.2, \pm0.9, \pm0.6, \pm0.3$ and 0 for downstream positions of $z/D = 4, 5, 6, 7$ and 9 to characterise the wake. The LDA does not have a fixed data rate, but the rate was in the regin of 150-200Hz. The distance from the end of the LDA to the measurement location was 0.5m, meaning the LDA tower was outside the rotor swept area.

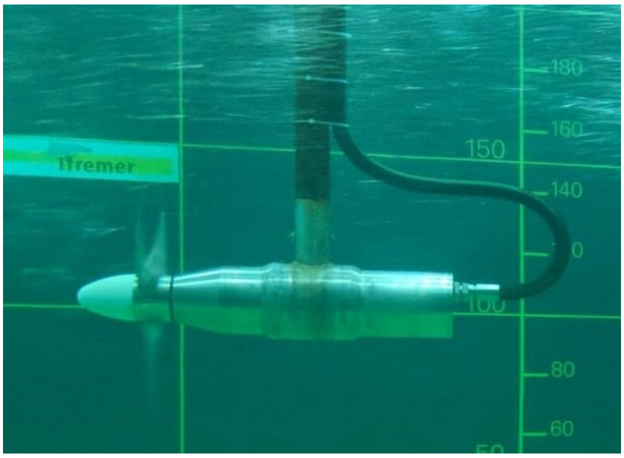

Figure 5.1: T_{UP} in-situ during experimental testing at IFREMER.

Experimental testing was conducted in the flume tank facility at IFREMER, France. A schematic of the flume is shown in Figure 5.2. The flume working section was 2 m (depth) x 4 m (width) x 18 m (length), and the turbine was fixed to a supporting beam with the rotational axis of the turbine 1 m below the surface.

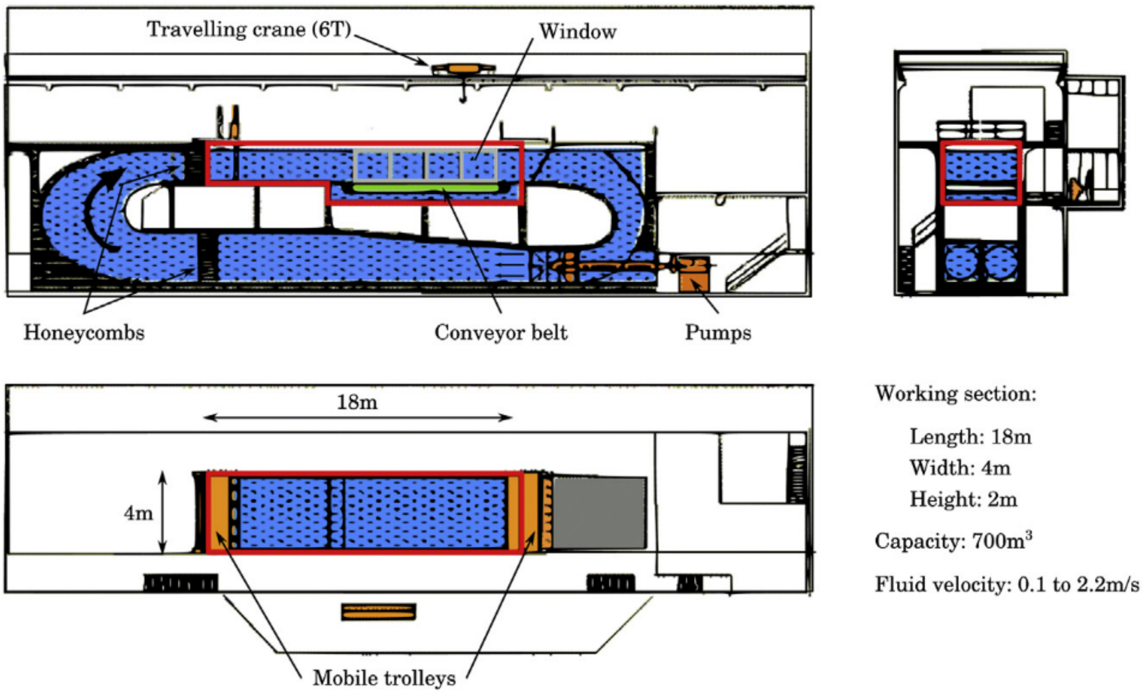

Figure 5.2: Schematic of the IFREMER recirculating flume [51].

The flume was characterised prior to testing to determine the ambient flow conditions. For each flow measurement data was recorded for 1000 s at the cross-sectional centre of the tank downstream of the inlet. The low turbulence testing utilised the flow-smoothing capabilities giving an ambient turbulence intensity of 1.75 %. A grid was installed to generate the 11.7 % turbulence intensity for the second set of testing. The grid consisted of a metal frame blocked with plywood boards. The dimensions of the grid were based on the work by [50].

5.2 Computational fluid dynamics

The CFD modelling approach detailed in Section 4.2 applies to the work presented in this chapter. Additional details that are applied to this, such as geometry and mesh are presented here. Any areas of the CFD methodology that have not been mentioned in the following chapter will be assumed to use the same methodology as that of Chapter 4. As with Chapter 4 the stream-wise flow is in the z-direction, the x-direction refers to cross-stream and the y-direction is the vertical direction.

The work in the following Chapter is built on the findings of Ebdon [14]. The mesh and setup have been replicated using CFX and aim to be as similar as possible to that of [14], but any changes are discussed.

5.2.1 Model geometry

Two approaches were taken when creating the model geometry. The first was based on the work of [14] and had a body of influence surrounding the stanchion and a cylindrical body extending down the length of the domain behind the turbine rotor and the MFR. The cylindrical body had a diameter of 0.75 m, larger than both the swept area of the turbine and the MFR. The cylindrical body allowed the mesh sweeping tool to produce a refined and structured mesh in the proposed wake region. The geometry was re-created within ANSYS CFX 18.0 using the same dimensions and can be seen in Figure 5.3.

The second approach built on the principles used during Chapter 4, breaking up the geometry into several blocks. Instead of creating a cylindrical region behind the turbine a rectangular domain was created that would be used to capture the wake. Secondly the region surrounding the turbine was extended to include the MFR, so that the inlet could be broken down into several rectangular blocks. The rectangular blocks meant a hexahedral mesh could be applied to all regions except those that were interacting with the turbine. A cross section of the new geometry can be seen in Figure 5.4.

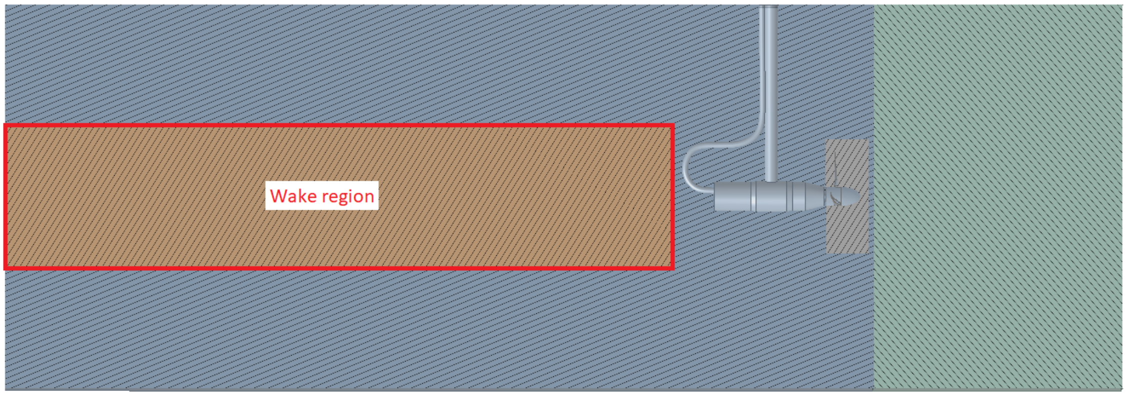

Figure 5.3: Cross-section of the CFD geometry broken down into its respective regions to refine the wake mesh.

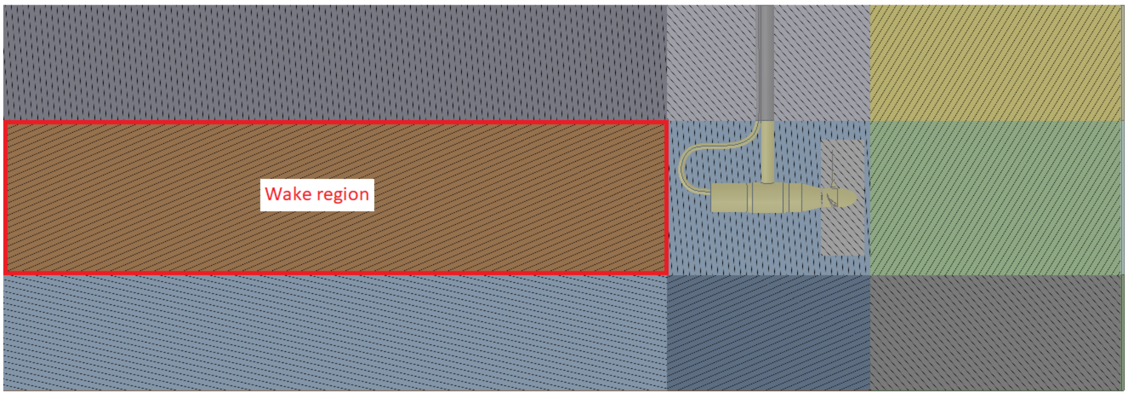

Figure 5.4: Cross-section of the CFD geometry broken down into a greater number of blocks to help improve the mesh structure.

5.2.2 Mesh independence

5.2.2.1 Turbine rotor

The turbine geometry modelled here has been the subject of many numerical and experimental test campaigns and as such the performance of the rotor has been well characterised [30, 52, 93, 149]. As such the mesh on the blades, hub, stanchion and within the MFR were based on the previous numerical studies and were unchanged for this work.

5.2.2.2 Wake region

The mesh for the wake region was initially based on the work by [14], referred to as Mesh 1. It used an unstructured tetrahedral mesh around the turbine and stanchion to encompass the complex geometry. A swept mesh approach was used to produce a structured mesh in the cylindrical body downstream of the turbine to capture the wake region. The remainder of the control volume was left largely unrefined and used a tetrahedral mesh to keep the element count down and therefore the computational time. It was assumed that the regions of the domain outside of the refined wake region were not modelled using LES, based on Equation 3.4. The impact that the RANS region would have on the wake recovery would be minimal and so it was left largely unrefined. The mesh used by [14] was replicated in CFX using the same sizing controls for this work and can be seen in Figure 5.5.

A second approach was used to create the geometry allowing for a more structured and uniform hexahedral mesh that could be applied over the majority of the domain, referred to as Mesh 2, and is shown in Figure 5.6. As in Chapter 4 the immediate region surrounding

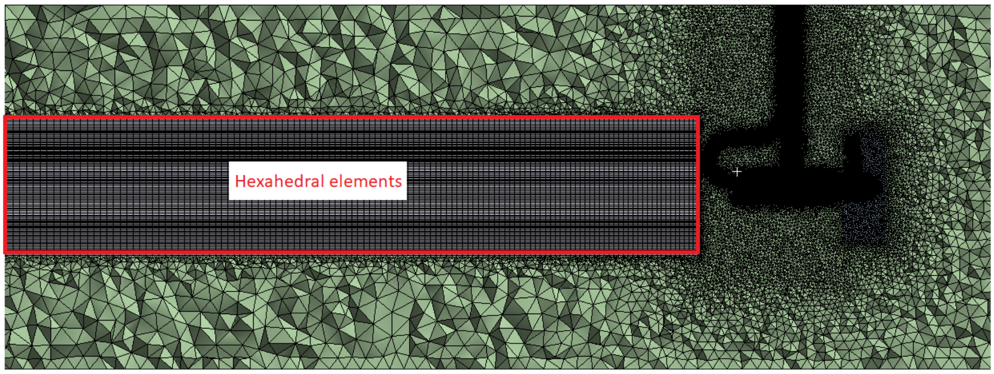

Figure 5.5: Cross-section of Mesh 1 which uses a largely unstructured tetrahedral except for the wake region.

the turbine used a tetrahedral mesh due to the complex geometry of the turbine. Both Mesh 1 and 2 have similar element counts, however they have different mesh formulations. The inlet and ambient flow regions use a more refined structure in Mesh 2.

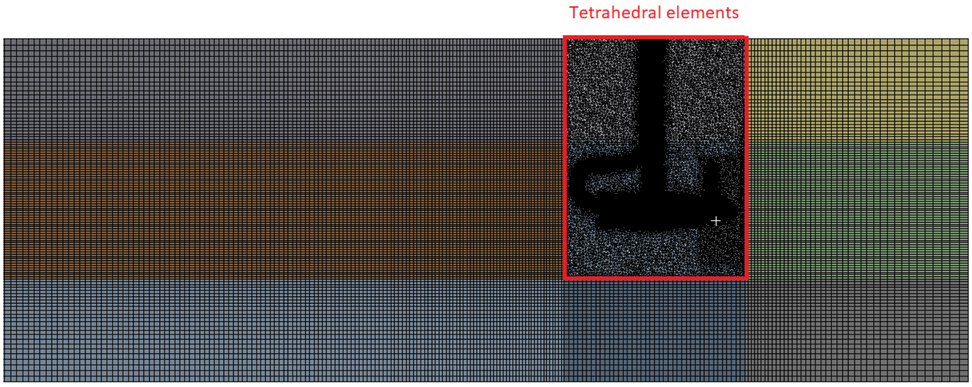

Figure 5.6: Cross-section of Mesh 2 which uses structured hexahedral elements where possible.

A third approach, Mesh 3, refined the wake and turbine mesh regions further. The near wake is defined as the region directly behind the rotor to the point downstream where by the tip vortices break down, after which the wake recovery is driven by mixing with the ambient flow. As the near wake mesh has a large impact on the resolved turbulence and therefore the far wake the tetrahedral mesh regions around the MFR and stanchion were refined. The number of elements in the x-, y- and z-directions were increased in the wake region. The outcome was a mesh that had double the number of elements when compared to Mesh 2. All these elements were added to regions that were running as LES, based on the results from Mesh 2 simulations. A figure of Mesh 3 has not been included as Figure 5.6 gives an indication as to how the mesh is structured.

Table 5.1: Number of elements and nodes in Mesh 1, 2 and 3.

Mesh Number	Elements	Nodes
1	$7.96x10^6$	$2.49x10^6$
2	$8.91x10^6$	$5.57x10^6$
3	$18.91x10^6$	$9.30x10^6$

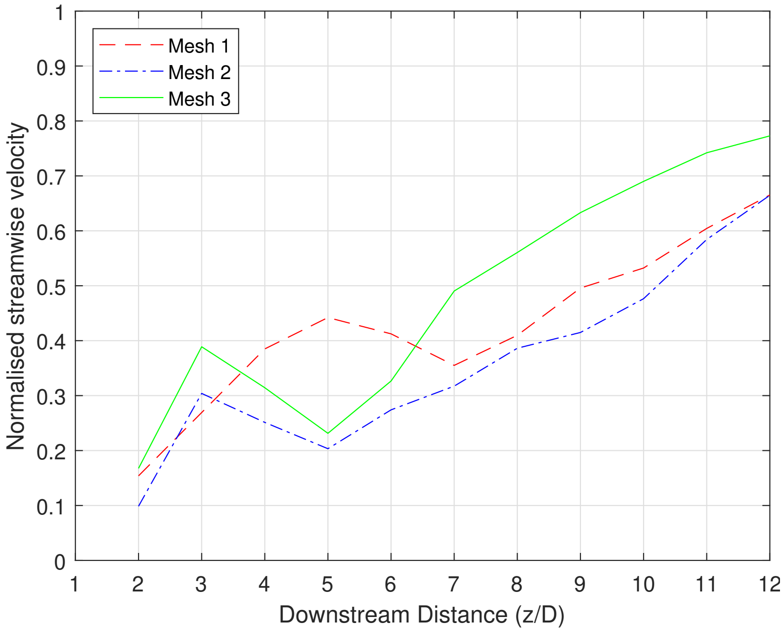

Figure 5.7: Comparison of meshes 1, 2 and 3 for the prediction of the centreline velocity recovery using the high-resolution discretisation scheme.

Each of the simulations in Figure 5.7 used the DES turbulence model with the high-resolution discretisation scheme. In each situation only the mesh was changed. There appears to be little to no convergence between each of the mesh options. Mesh 1 and 2 provide similar predictions for the far wake however with the refinement in the wake region the prediction changes drastically. As mentioned previously the HR scheme uses the BCD scheme in the LES region and so while the meshes themselves seem to offer little by the way of a converged solution the impact of the discretisation scheme needs to be looked at also. Table 5.2 shows the time taken for 12000 iterations for each of the models in Figure 5.7. Mesh 1 has been used as the base example to be compared to. Mesh 2 takes ≈ 10 %

less CPU time to run, whereas mesh 3 takes ≈ 20 % more CPU time to run. As Mesh 1 took in the region of 4 weeks to complete the run any, and all, time saving measures are vital to help reduce the total time.

The models were run on the Super Computing Wales cluster which allows for 72 hours run time per job. Each job used 120 cores. Multiple jobs can be submitted to run in sequence however each time a 72-hour job is completed it must go back into the queue before running. This extra time can have a big impact on the total time for the model to complete. Using Mesh 3 over Mesh 1 or 2 could mean that the total time taken for the simulation could be up to 2 weeks longer. To minimise the computational time Mesh 2 was used to compare the impact of the discretisation scheme on the wake prediction.

Table 5.2: CPU time taken for 12000 iterations in relation to the time taken for Mesh 1.

Mesh Number	CPU Time
1	t
2	$0.88t$
3	$1.18t$

Figure 5.8 shows a comparison between the HR and BCD scheme for Mesh 2, the differences between the schems have been discussed previously is Chapter 3. The use of the BCD scheme gave a better prediction for the downstream velocity recovery. Based on the recommendations by ANSYS [99] the SBES turbulence model was tested using the BCD scheme. Figure 5.9 shows that there is very little difference in the centreline velocity recovery prediction for the SBES and DES turbulence models, however due to the recommendation by ANSYS the SBES model was chosen going forward as the switch from RANS to LES was improved outside of the boundary layer. The computational time is also reduced when using the SBES turbulence model as shown in Table 5.3.

Table 5.3: Non-dimensional CPU time taken for 12000 iterations for Mesh 2.

Turbulence Model	Discretisation Scheme	CPU Time
DES	HR	$1.1t$
DES	HR	$1.25t$
SBES	BCD	t

Finally, the mesh selection was looked at again. Based on the previous findings the SBES turbulence model was used with the BCD discretisation scheme. As seen in Figure 5.10 there is almost no difference in the centreline velocity for the downstream wake. Due to the increased computational time the wake region was shortened for Mesh 3 however the

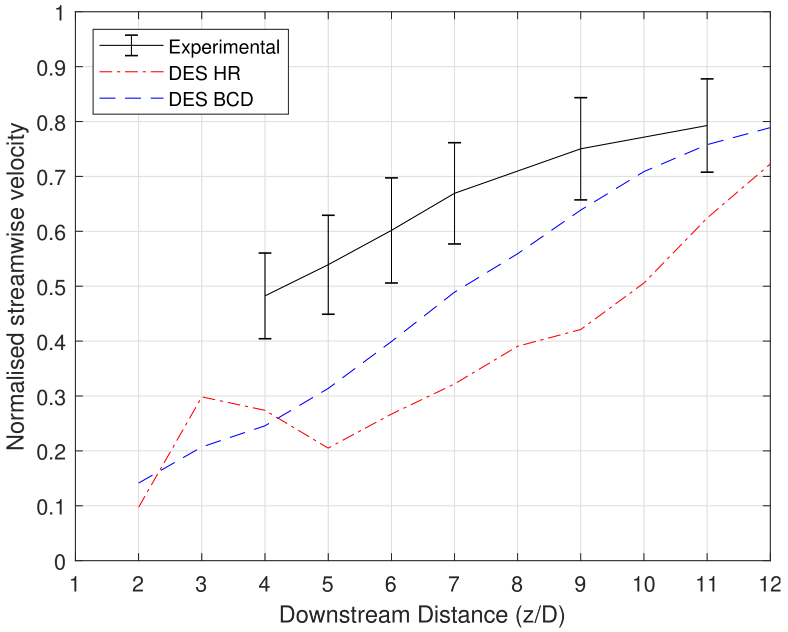

Figure 5.8: Centreline recovery for the HR and BCD scheme with the DES turbulence model using mesh 2.

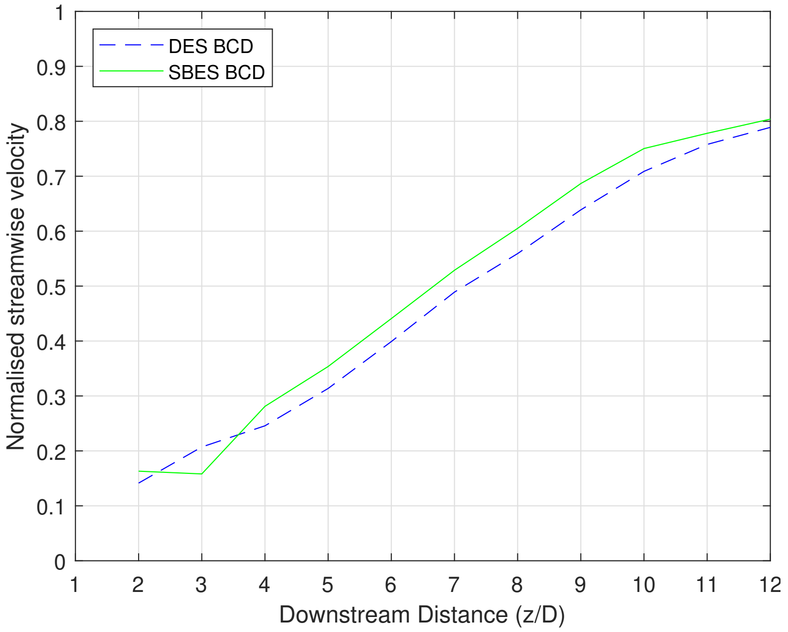

Figure 5.9: Centreline recovery with the DES and SBES turbulence models using the BCD scheme for mesh 2.

trend in both curves is very similar. Mesh 2 was selected for all future models due to the decreased run time. The SBES turbulence model and the BCD discretisation scheme were also selected based on the recommendations by ANSYS and the wake recovery predictions.

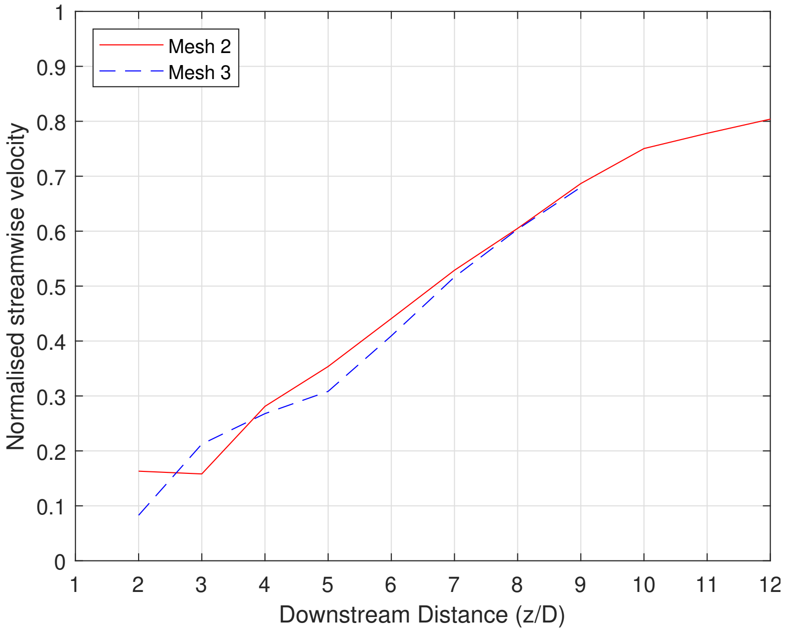

Figure 5.10: Centreline recovery with the SBES turbulence model for Mesh 2 and 3.

5.2.3 Model setup

5.2.3.1 Domain and fluid properties

During the modelling two turbulence models were considered for the hybrid RANS-LES simulations; DDES, within CFX this is just referred to as the DES, and SBES, which is based on the SDES. Both models are based on the underlying RANS model [159]. Further information on the models has been given in Chapter 3.

5.2.3.2 Boundary conditions

Inlet The ‘Cartesian velocity components’ setting was used at the inlet to specify the fluid flow upstream of the turbine. The turbulence was specified at the inlet. The ‘intensity and length scale’ option was used to initiate the desired turbulence at the inlet. The intensity and length scale values were based on the flume characterisation done before the experimental testing was conducted. Values for k and ϵ are found based on the intensity and length scale values. The values of k and ϵ are used to represent the turbulence throughout the domain.

One of the big issues with turbulence modelling however is the implementation of consistent inlet turbulence [159]. In this case the turbulence intensity at the inlet is sufficiently small for the low turbulence case of 1.75 % when compared to the turbulence downstream of the turbine and so the generation of the turbulence of the inlet should have little impact on the wake recovery.

Initial conditions The DES and SBES models are based on the underlying RANS model. A transient RANS model was run to allow the flow field to converge before using the final transient results file as the initial conditions for the hybrid RANS-LES simulations as suggested by ANSYS [159].

5.2.3.3 Solver settings

Discretisation scheme Both the HR and the BCD schemes were used during the work in this Chapter. Both have been discussed in more detail in Chapter 3.

5.2.4 Time step selection

The timestep of 0.005 s was chosen to be in-keeping with the sampling frequency of the experimental data, 200 Hz. It was also the same value used by [14] when studying the wake recovery. A second time step value of 0.001 s was considered. The smaller value was chosen to reduce the distance moved by the tip of the blade during each time step. The smaller the tip movement the less change between preceding time steps in what is a very complex region of the flow.

There was less than a 0.3 % change in the rotor performance when using the smaller time step value for either Mesh 2 or 3. The computational time increased $\approx$ 5-fold. Due to the lack of change in the results and the increased time making it highly impractical for future modelling the larger value of 0.005 s was kept as the time step.

5.2.4.1 Expression monitoring and monitor points

The thrust and torque in the x-, y- and z-directions were monitored at each time step. The monitor points used to characterise the wake were based on the LDV locations during the experimental testing.

5.2.5 Summary of CFD models

The following is aimed to give an overview of the different turbulence models and discretisation schemes used to make the comparison later on more simple. When discussing the results, the corresponding run number will be used. Table 5.4 shows CFD models that are compared in the following analysis.

Table 5.4: Summary of the CFD models run for the work in this Chapter.

Run Number	Mesh Number	Turbulence Model	Discretisation Scheme
1	1	DES	High Resolution
2	2	DES	High Resolution
3	3	DES	High Resolution
4	2	DES	Bounded Central Difference
5	3	DES	Bounded Central Difference
6	2	SBES	Bounded Central Difference
7	3	SBES	Bounded Central Difference
8	3	SST k-ω	High Resolution

5.3 Results

5.3.1 Impact of discretisation schemes on turbine performance

As mentioned in Section 5.2.2.1 the mesh for the rotor was based on the previous work by [30, 52, 93, 149]. Each of the three meshes used for the CFD models had the same mesh applied to the turbine rotor. This being the case, the difference between models was limited to the turbulence model and the discretisation scheme. Both DES and SBES use the SST $k - \omega$ turbulence model in the RANS regions of the flow and so the selection of the turbulence model was predicted to have less impact on the performance.

The non-dimensional performance coefficients were calculated using Equations 3.7, 3.8 and 3.9. The results for the performance coefficients for each of the models are shown in Table 5.5. Within each CFD model a monitor point was placed 1 m upstream of the device. The mean fluid velocity for this single point location upstream of the device was used when calculating the performance coefficients.

Table 5.5: Performance coefficient comparison for the CFD models.

Run Number	C_P	C_T	C_Q
1	0.445	0.843	0.121
2	0.447	0.843	0.122
3	0.442	0.838	0.121
4	0.452	0.825	0.124
5	0.451	0.824	0.123
6	0.452	0.823	0.123
7	0.451	0.822	0.123
8	0.446	0.843	0.122

The BCD scheme results (Runs 4-7) show good agreement with each other irrespective of which of the meshes were used. There is a slight variation in the performance coefficients, which is likely due to the unsteady and random nature of turbulence, however the difference between the results is less than 1 %. The BCD scheme was run using both the DES and SBES turbulence models.

The most notable difference in the rotor performance can be seen when the advection scheme is changed between the HR and BCD schemes. Within the RANS region of the flow an upwind scheme is used for both as discussed in Section 3. Figure 5.11 shows a plot of the beta function for velocity. This beta function does not actually show the velocity value of the fluid. Instead it shows the user which regions are being treated by either a first or second order scheme. For a value of 1 the second order upwind scheme is being used, whereas a value of 0 uses a first order scheme. For the HR scheme the upwind scheme is either first or second order depending on the boundedness of the solution. As can be seen in Figure 5.11 the rotor region is clearly operating with a second order scheme. Small regions can be seen where it is in between, and the flow is transitioning between first and second order depending on whether the CBC remains satisfied. The aim is to use the second order scheme for as much of the flow region as possible to reduce the smearing effects of the first order scheme.

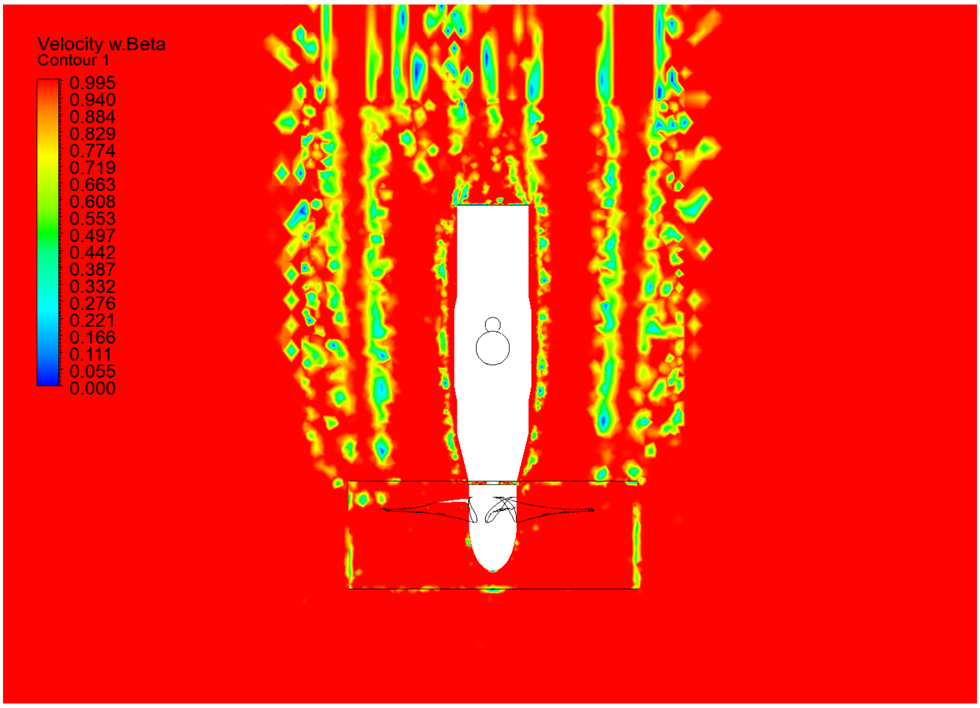

Figure 5.11: Contour plot highlighting which regions of the flow are treated by either a first or second order scheme, with a value of 0 and 1 respectively, for Mesh 2 with the HR simulation.

The BCD scheme uses only a first order upwind scheme within the RANS region and so the accuracy in the boundary layer region is reduced affecting the performance prediction of the device. It is hypothesized that the difference in the performance prediction for the HR and BCD schemes is associated with the smearing of the flow variables due to the use of a first order scheme.

The work by [14] used ANSYS Fluent which uses a cell centred approach in the solver, so the node is located at the centre of the cell. For this work CFX was used which uses a vertex centred approach. As the blade mesh sizing was the same across all simulations the y+ value for the CFX simulation was almost double that of Fluent due to how the nodes within the domain are determined. The y+ at the tip of the blade was ≈ 100. The y+ denoted the distance from the boundary to the fist node in the mesh. As Fluent uses a cell-centred approach to determine the nodes this distance will be the equivalent of half an element thickness. For CFX the first node in the boundary layer will be at distance equivalent of the element thickness. The work by [14] had a y+ values of ≈ 50. The value of 100 for the CFX model with the same mesh can be explained by the way the node locations are determined.

The percentage difference found by comparing the CFD results to the CFD values found by [14] are shown in Table 5.6. For the lowest prediction of the power and thrust coefficient the maximum percentage differences are less than 5 %. While the discretisation scheme appears to have an impact on the performance of the rotor it is not significant enough to completely rule out a specific scheme. The focal point of the work in this Chapter was on the wake modelling capabilities of the discretisation schemes rather than device performance, but it was important to ascertain whether there were any large differences observed in the ability to predict rotor performance. All of simulations compared here will also be compared in the following section looking at wake modelling.

Table 5.6: Absolute percentage difference in performance coefficients compared to CFD results from Ebdon [14].

Run Number	C_P	C_T	C_Q
1	1.07 %	2.3 %	0.53 %
2	1.58 %	2.29 %	1.18 %
3	0.46 %	2.90 %	0.94 %
4	2.71 %	4.48 %	2.32 %
5	2.39 %	4.71 %	2.04 %
6	2.61 %	4.77 %	2.22 %
7	2.38 %	4.89 %	2.04 %
8	1.35 %	2.27 %	1.00 %

5.3.2 Impact of discretisation schemes on wake recovery

The centreline velocity is a key metric used to show the recovery of the flow downstream of the turbine rotor. Monitor points were placed in the CFD models every turbine diameter downstream until the end of the domain. At each monitor point the flow velocity was recorded.

The velocity was averaged over an increasing quantity of time in order to see whether the velocity converged despite the random nature of the turbulence. Figure 5.12 shows the converge of the downstream centreline flow velocity for Mesh 2 using the SBES turbulence model. The initial fluctuations in the centreline velocity converged around a final value as the sampling time was increased. The convergence of the centreline velocity was seen for all the CFD models and so only one example has been given. The convergence for all the other CFD models can be found in Appendix A.1.

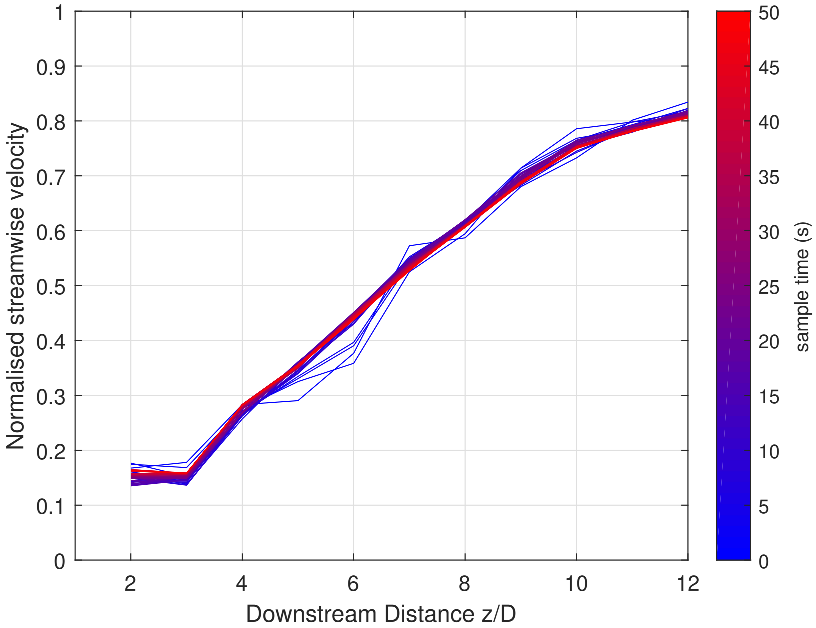

Figure 5.12: The effect of sampling time on the centreline velocity recovery downstream of the turbine rotor for Run 6.

The experimental case, shown in Figure 5.13, also shows good convergence when averaged over the full testing time of 100 s.

Figure 5.14 shows the centreline velocity recovery for all the CFD models based on a sample time of 50 seconds. The experimental data was averaged over the full data set, 100 seconds. Due to the variable data capture speeds for the experimental data, linear interpolation was used to organise the data prior to the averaging process. The error bars

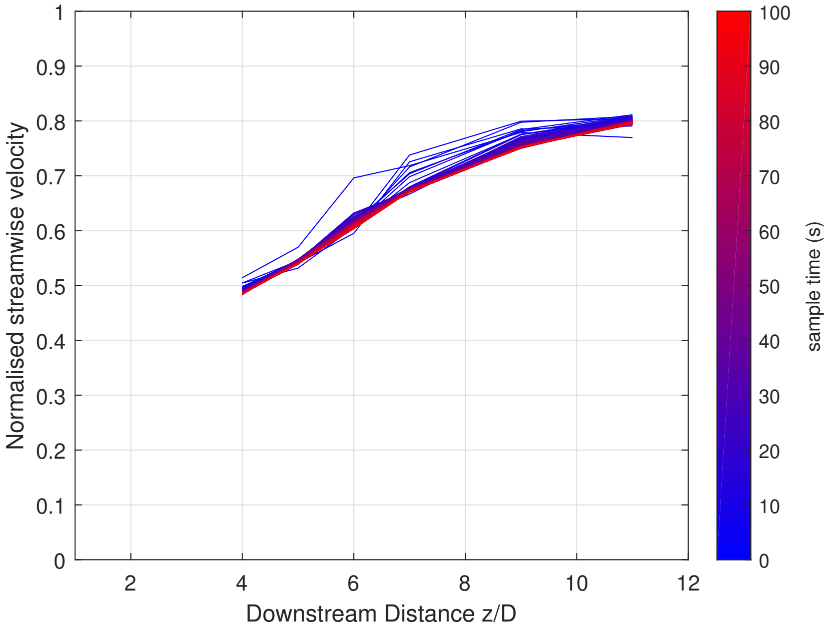

Figure 5.13: The effect of sampling time on the centreline velocity recovery downstream of the turbine rotor for the experimental testing.

added to the experimental data show +/- the standard deviation. No error bars were included as part of the CFD models for clarity however the standard deviation can be seen in Figure 5.15.

All the schemes under predict the velocity in the near wake region when compared to the experimental data. This is a complex and unsteady region of the flow that is difficult to accurately capture and define. Wake recovery in the far wake region is predominantly due to the interaction of the ambient flow with the wake. The higher the ambient turbulence in the flow the quicker the 'mixing' of the wake and ambient flow, speeding up the wake recovery [14].

The under prediction of centreline wake recovery in the near wake region could be due to a couple of different things. Figure 5.16 shows an iso-surface for velocities of $0.5\,\mathrm{m\,s^{-1}}$ throughout the domain. This value highlights the wake core. It can be seen in the CFD model that the wake core does not meander away from the rotational axis of the turbine in the near wake region. This distinct low velocity wake core is why the CFD models give such a slow recovery for the wake using the centreline recovery. It is unknown if the wake meanders during the experimental testing. The centreline recovery based on the experimental testing may be greater than the CFD models if the wake core were to be misaligned with the rotational axis of the turbine.

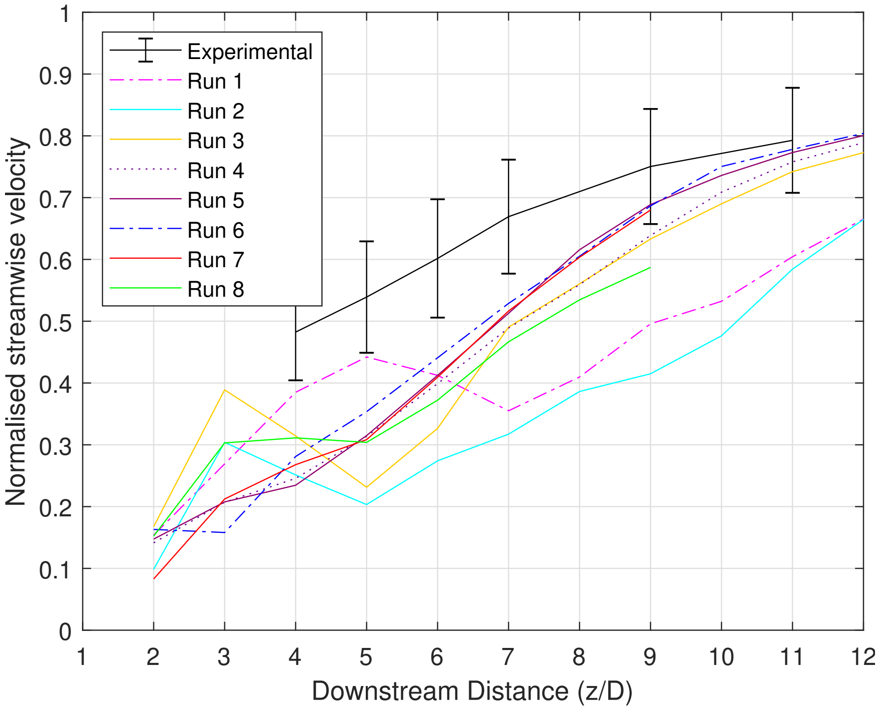

Figure 5.14: Comparison of centreline line velocity recovery for each of the CFD models run using different mesh, turbulence and discretisation scheme options.

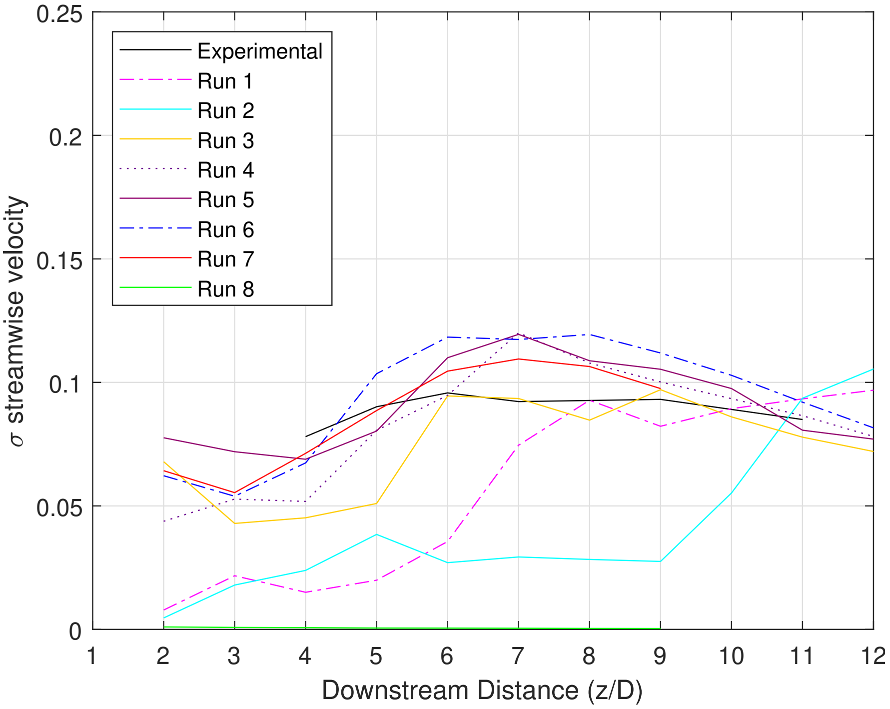

Figure 5.15: Comparison of the standard deviation for the centreline line velocity recovery for each of the CFD models run using different mesh, turbulence and discretisation scheme options.

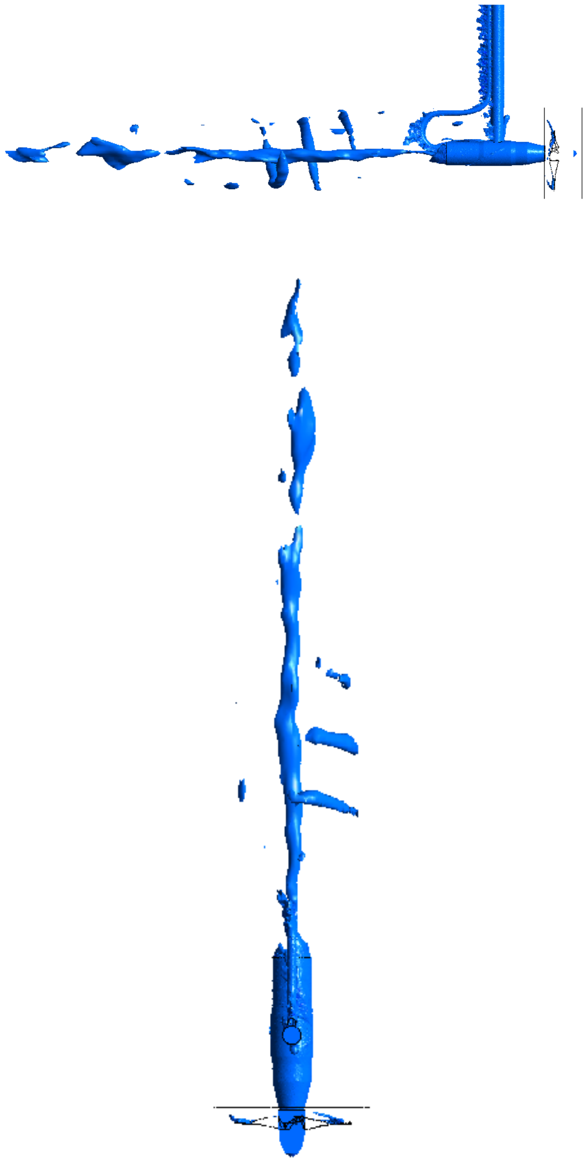

Figure 5.16: Iso-surface of the flow velocity for $0.5\,\mathrm{m\,s^{-1}}$.

The width of the wake downstream for the experimental testing and CFD modelling can be seen in Figures 5.17 and 5.18 respectively. Again, the centreline shows a large velocity deficit in the CFD compared to the experimental. Moving away from the centreline the flow velocity for the CFD and experimental results begin to agree at ≈ +/- 0.3 m. The CFD wake is narrower than the experimental. This is believed to be due to the switch back to RANS outside of the high turbulence region and so the full width of the wake is possibly under estimated by the CFD.

Another factor is how the turbulence kinetic energy (TKE) is carried downstream. There are two things that must be made clear when talking about the TKE. There is a distinct difference between the resolved and unresolved TKE in a CFD model. In the RANS regions it is expected that the resolved TKE value will be very low, if not zero as the averaging used in the Reynolds decomposition all but eliminates the turbulence. However, the unresolved TKE will steadily be decaying as it propagates downstream through numerical dissipation. Only when it reaches the region of the flow being treated by LES will the resolved TKE be more representative of what is seen, as the fluctuations generated by the flow instability will dominate. In this model the upstream ambient turbulence is very low and so the recovery of the near wake may be being under predicted, but similarly the transport of the TKE from the inlet may be affecting the wake recovery. The impact that the inlet turbulence has on the wake prediction can be seen in Section 5.3.3.

The resolved turbulence in the flow is heavily dependent upon the turbulence model so the point at which the switch from RANS to LES occurs is important. The boundary layer is treated by RANS for all the models however the SBES model was designed to switch more quickly between RANS and LES [99] as the mesh in the boundary layer region can be of LES quality without grid induced separation being a problem. The importance of this in the rotor region is that the vortices shed from the device may be being damped by the advection schemes used in the RANS regions.

The switch from RANS to LES can be visualised in all the CFD models. This way it is possible to see where in the domain the transition is occurring. The way in which the switch is visualised depends on the turbulence model and the discretisation scheme, discussed next.

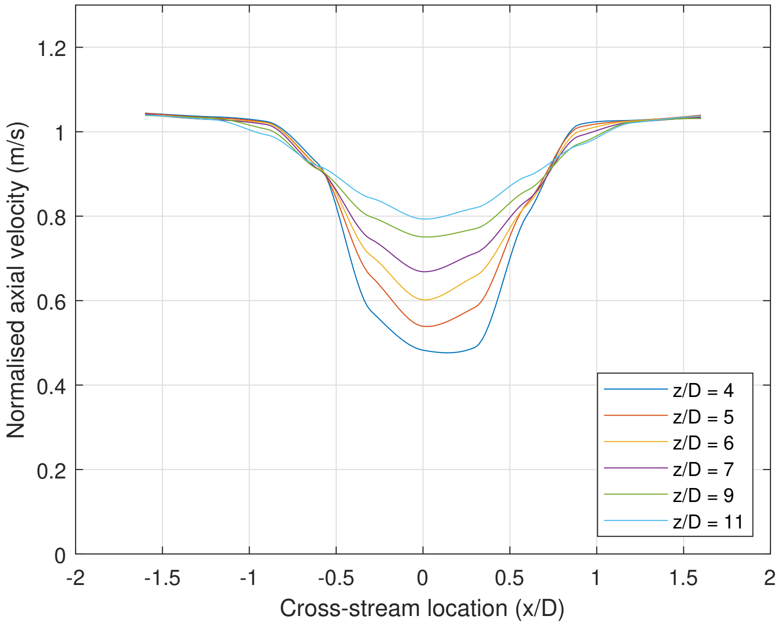

Figure 5.17: Experimental wake profile for TI = 1.75 %.

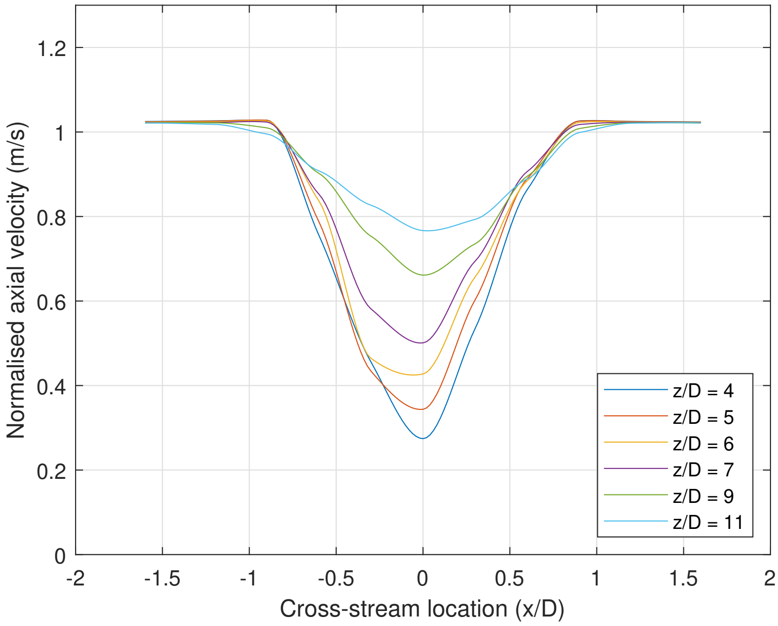

Figure 5.18: CFD wake profile for TI = 1.75 %.

DES When using the DES turbulence with the HR scheme the ‘Blending Function for DES mode’ can be plotted in CFD-Post as a contour. It shows the point at which the model switches from a first to a second order discretisation scheme. This does not necessarily mean the switch from RANS to LES has occurred and so it can be misleading. However, when using the BCD scheme this is not an option as BCD uses a second order dominated scheme unless the CBC is not satisfied at which point it switches to a first order scheme.

Therefore, to visualise the switch from RANS to LES when using the DES turbulence model the best method is to create an expression within CFD-Post for the DES function, F_{DES}. This is the function used to switch from RANS to LES based on the size of the turbulent length scale compared to the maximum local mesh spacing [143]. The function is as follows, and is based on a switch proposed by [142],

$$F_{DES} = max(\frac{L_t}{C_{DES}\Delta}, 1) \tag{5.1}$$

By plotting the value of $1/F_{DES}$ then a value of 1 will show a RANS region, 0 will show LES and regions in-between are where transition is occurring. This function can be visually represented using a contour plot over the domain, as seen in Figures 5.19a and 5.19b. The maximum local mesh spacing in the transition region is $\approx$ 0.025m.

SBES The SBES turbulence model uses a shielding function to explicitly switch between RANS and LES. In CFD-Post the ‘Shielding Function for SBES or SDES’ can be plotted as shown in Figure 5.19c.

Both Figures 5.19a and 5.19b show very similar transitions for the plot of $1/F_{DES}$. This is to be expected as both use the same turbulence model. However, in both models it is noted that a pure LES model, a value of 0, is never reached. It seems as though the DES turbulence model gives an ‘LES flavoured’ model rather than a full LES model.

The SBES model on the other hand shows a distinct transition from pure RANS in the boundary layer to pure LES as soon as it is outside the boundary layer. Not only is the transition quicker but it also uses a pure LES model. The mesh used for all three models is the same. And in both DES and LES the turbulent length scale is linked to the maximum local face size. Therefore, it seems this is less of a mesh problem and more of an issue with the formulation of the DES model, hence why ANSYS now recommends the use of the SBES turbulence model [99].

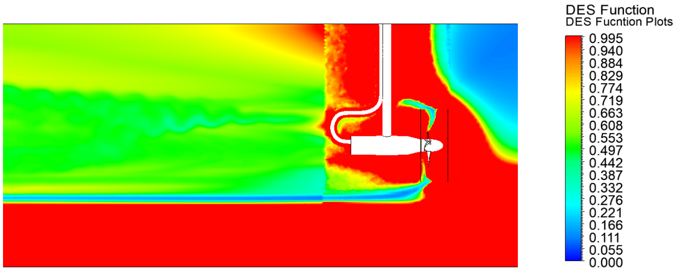

(a) Plot of F_{DES} limiter - HR scheme.

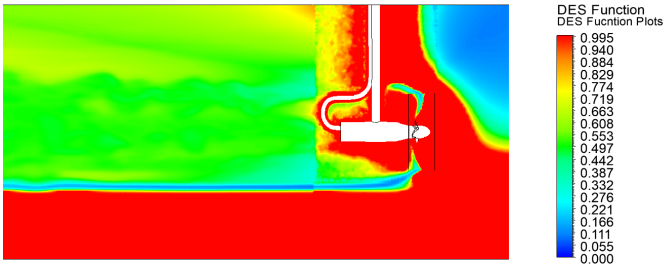

(b) Plot of F_{DES} limiter - BCD scheme.

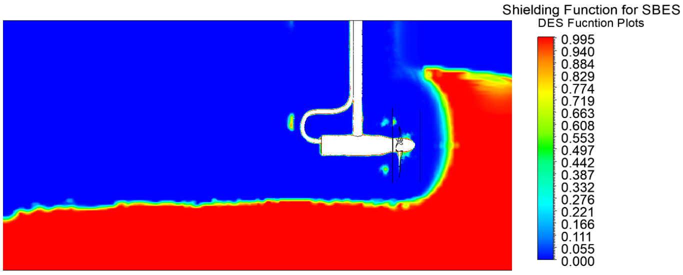

(c) Shielding function for SBES - SBES scheme.

Figure 5.19: Comparisons of transition from RANS to LES regions for the three discretisation schemes tested.

It is possible to visualise the relationship between the length scale and the maximum local face size for every element throughout the domain. This relationship is referred to, in this case, as the mesh ratio. ANSYS suggest that 'as a rule-of-thumb 8-10 cells per integral turbulence length scale are needed to resolve 80 % of the turbulence spectrum' which would give a mesh ratio in the order of 0.1. Figure 5.20 shows the mesh ratio for Meshes 1, 2 and 3.

From looking at Figure 5.20 it is clear that the structured hexahedral elements used upstream and around the wake region in Meshes 2 and 3 provide a better quality mesh than that of Mesh 1, based purely on the mesh ratio. However, as these regions are using RANS there is little impact on the wake recovery due to the lack of resolved turbulence in these regions.

Looking at the wake region the mesh ratio for all three meshes is ≈ 0.5. The similarity in the mesh ratio value was expected for Mesh 1 and 2 as the mesh density in the wake region was, were possible, the same. Mesh 3 uses a greater number of divisions in each of the x-, y- and z-directions. The global cell count was almost doubled from 10 to 20 million, however the mesh ratio in that region is unchanged. It seems that despite the reduction in the element sizing for Mesh 3 there has been little or no impact to the mesh ratio in the wake. This may go some way to explaining why the results shown from the mesh study in Section 5.2.2 show very minimal difference for Meshes 2 and 3.

The one area where a big difference is seen between Mesh 2 and Mesh 3 is in the unstructured tetrahedral region around the turbine rotor, stanchion and nacelle. The sizing was reduced by a factor of 2 and the mesh ratio subsequently dropped from 1 to 0.5. The mesh needs to be suitably refined in the near wake region, especially around the rotor to ensure the root and tip vortices are captured. If the root and tip vortices are not captured in the region directly behind the rotor then the impact that these vortices have on the wake will be lost. Despite the increase in the mesh density in the region surrounding the nacelle and stanchion the near wake is still being under predicted when compared to the experimental results.

The value of 0.5 in the wake and around the stanchion for Mesh 3 is still ≈ 5 times larger than the ratio of 0.1 recommended by ANSYS. To obtain a value of 0.1 the mesh must be dramatically refined in the wake region, ultimately increasing the total element count well beyond 20 million. Due to the computational and time resources available

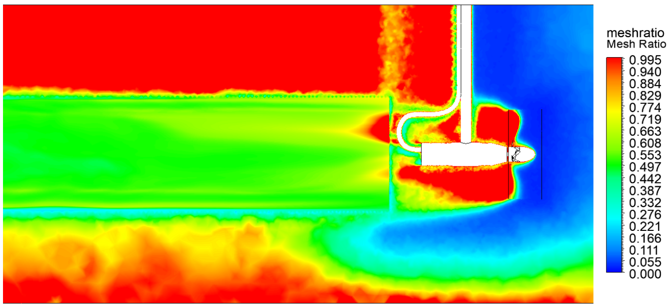

(a) Mesh ratio for Mesh 1.

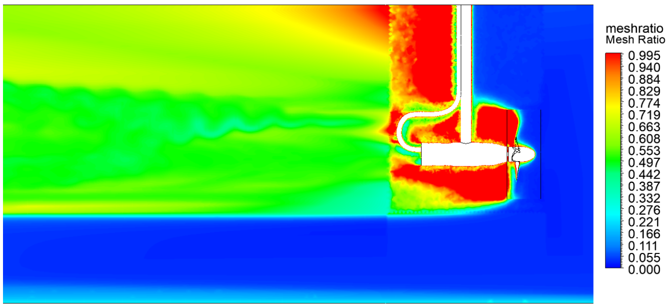

(b) Mesh ratio for Mesh 2.

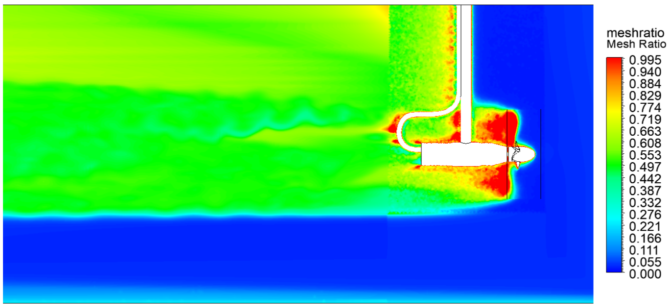

(c) Mesh ratio for Mesh 3.

Figure 5.20: Comparison of the mesh ratio for the three different meshes used for the wake modelling with the HR discretisation scheme.

during this work it was not possible to refine the mesh to such a level.

As shown the CFD wake core is aligned with the flow and the SBES turbulence model is clearly using a pure LES formulation in the wake. The use of the LES turbulence model does not seem to be breaking it up or causing it to deviate. As well as this the mesh ratio for all the meshes used are of a similar value highlighting again that there would not be a substantial benefit in using Mesh 3. The centreline velocity in a wake does not always give a fair representation as to the full influence of the turbine on the total velocity deficit. Therefore, a second method was used to determine the wake recovery downstream of the device. The volumetrically averaged flow velocity, described previously in Section 3.7.5, was used. The assumption of rotational symmetry is made when calculating the swept area average. This method has been used in stidies by Ebdon [14] and Mycek et al. [51] when characterising the wake downstream of a lab scale device for both numerical and experimental testing.

Two diameters were considered for the volumetric averaging. The first diameter was based on the upstream device, T_{UP} used during experimental testing. The second swept area was based on the diameter of the device used in Chapter 4, T_{DOWN}. The work done testing both devices in a flume is presented in Chapter 6 hence why the volumetric averaging was done for both swept areas.

The results from the volumetric averaging can be seen in Figures 5.21 and 5.22. Firstly, looking at the recovery based on swept area of T_{UP}, the predicted recovery is much closer for both the experimental and CFD. The flow velocity recovery is improved when compared to the centreline approach.

If the swept area of T_{DOWN} is used, then there is better agreement in the results. The curves are closer, especially for distances greater than $8D$. The recovery is again improved as a larger volume of the ambient flow is incorporated into the averaging process. The CFD and experimental results are much closer when using the volumetrically averaged flow velocity. Using information about more of the flow field over the swept area of a device gives more confidence in the velocity that a downstream device might be seeing.

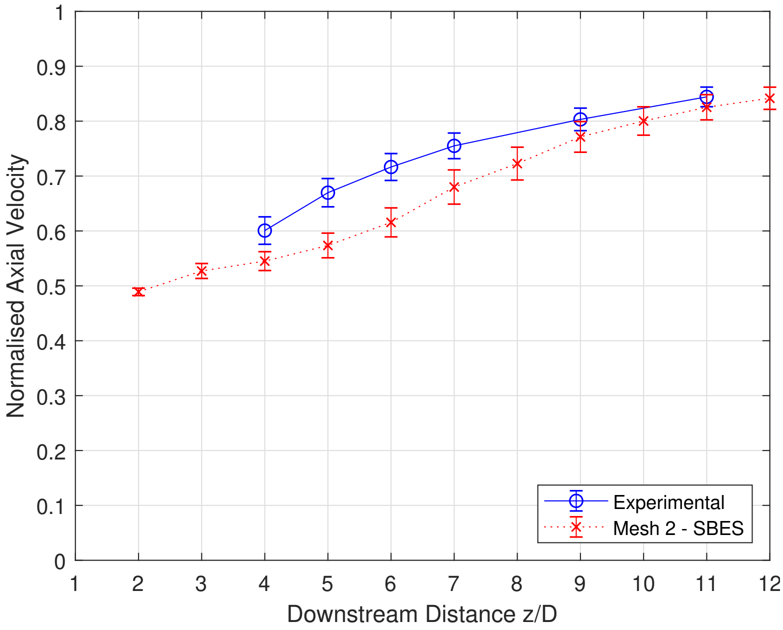

Figure 5.21: Volumetrically averaged wake recovery based on the swept area of T_{UP} with inlet turbulence of 1.75 %.

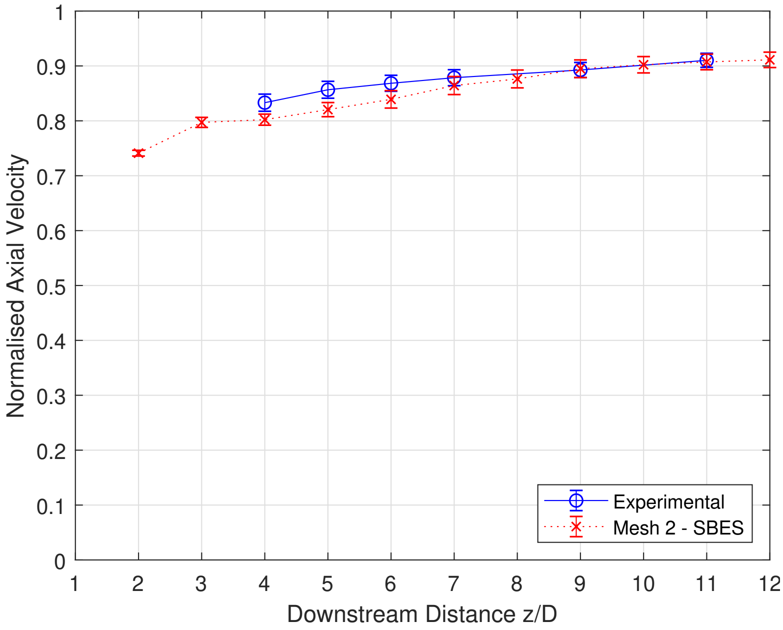

Figure 5.22: Volumetrically averaged wake recovery based on the swept area of T_{DOWN} with inlet turbulence of 1.75 %.

5.3.3 Impact of inlet turbulence on wake recovery

A second set of experimental tests and CFD models were conducted to study the influence of a higher inlet turbulence intensity on the recovery of the wake. A grid was installed, and the tank was characterised prior to device installation. The turbulence intensity was found to be 11.7 % at the rotor plane prior to turbine installation which was used as the inlet conditions for the CFD. The variation in the turbulence with downstream difference can be found in [14]. Based on the findings from the low turbulence analysis of the wake only the volumetrically averaging flow velocity method was used when looking at the wake recovery. The volumetric average showed better estimation between the experimental and CFD results. The area used for the volumetric average was again based on the diameters of T_{UP} and T_{DOWN}.

The normalised volumetric average flow velocity is shown in Figures 5.23 and 5.24. The mean flow velocity measured prior to the turbine installation, $1.02\,\mathrm{m\,s^{-1}}$, was used to normalise the results. Despite the increased inlet turbulence there seems to be little change in the wake recovery rate after 5D. The near wake wake recovery rate may be different for the two turbulence intensities however there is no data within 4D on the turbine for the low TI case. This is shown in both the experimental and the CFD results.

Figure 5.23 shows the wake recovery based on the area of T_{UP}. The experimental results show that the wake recovers close to 100 % by $12D$ downstream. There is $\approx 90\,\%$ recovery by $7D$ downstream. These results are in keeping with those of [51] when studying the impact of turbulence on wake recovery. The CFD model reached $\approx 90\,\%$ at $12D$, and at $7D$ it is closer to $\approx 70\,\%$. The trend of the recovery is the same for both methods.

The results based on the swept area of T_{DOWN}, shown in Figure 5.24 are similar. For the experimental case there is $\approx 100\,\%$ velocity recovery by $7D$ downstream. By $12D$ downstream the volumetric average is higher than the mean flow velocity used for the normalising. Figure 5.25 shows the downstream cross-sectional rake of the velocity. A line of $y = 1.02\,\mathrm{m\,s^{-1}}$ has been included. For all measured locations downstream the velocity at the edge of the tank is higher than this line. The blockage of the upstream device causes the flow to accelerate around the device. When averaging over the swept area of T_{DOWN} more of this accelerated region of low is included in the calculation. Therefore, the volumetric average is actually higher than the mean flow velocity used for the normalising, hence a value greater than 1. Measurements were not taken over the full width of the flume

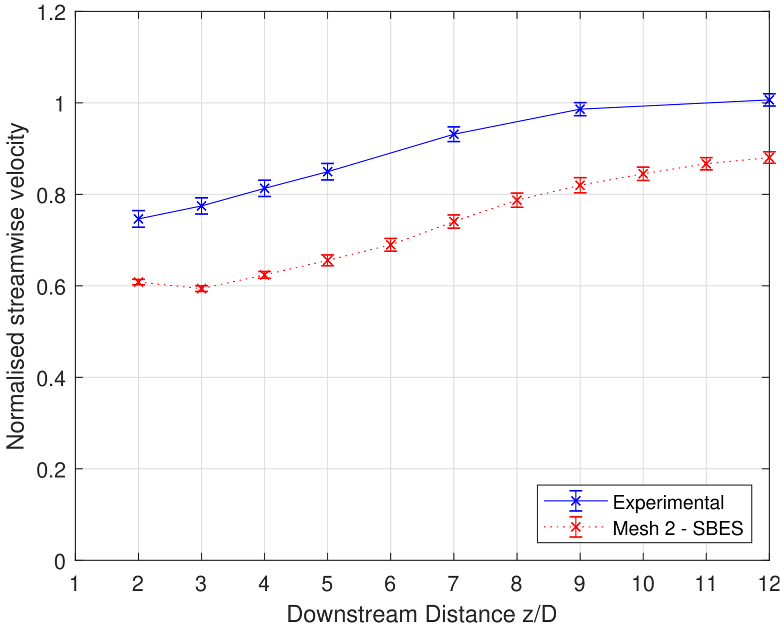

Figure 5.23: Volumetric average wake recovery based on the swept area of T_{UP} with an inlet turbulence intensity of 11.7 %.

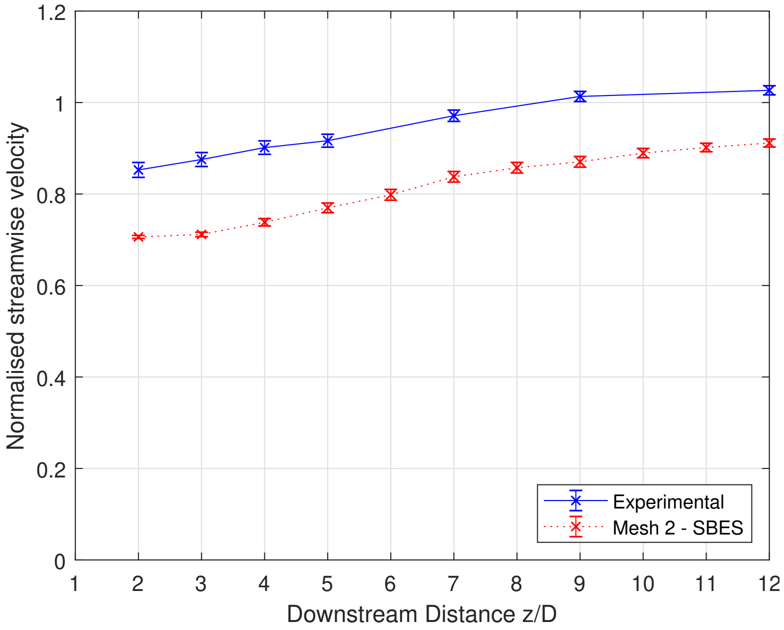

Figure 5.24: Volumetric average wake recovery based on the swept area of T_{DOWN} with an inlet turbulence intensity of 11.7 %.

so these results only capture a portion of the flow field. The normalising velocity was based on the characterisation of the flume prior to turbine installation and so any variation in this due to the increased levels of turbulence could cause a value higher than 1 as seen.

The CFD model recovers close to $\approx 90\,\%$ by $12D$ downstream and is $\approx 85\,\%$ $7D$ downstream. Again, the CFD model under predicts the wake recovery when compared to the experimental results. By looking at the downstream cross-sectional plots of the flow velocity the flow acceleration seen in the experimental data around the upstream device is not as prominent in the CFD, see Figure 5.26. While no value for C_T isd available from the set of experimental testing conducted here, the CFD results are with $2\,\%$ of the results obtained by [30]. The flow regions closer to the walls, whilst higher than the mean flow velocity are lower in the CFD than the experimental. Based on this, when averaging over the swept area of T_{DOWN} for the CFD models, the recovery is expected to be reduced compared to the experimental.

Figures 5.27 and 5.28 compare the high and low TI inlet values for both the experimental and the CFD models. It is clear in the experimental testing that an increase in the inlet TI causes an improved estimation for the wake recovery based on the volumetrically averaged flow. This is true when the swept area of both T_{DOWN} and T_{UP} are used. This is not the case for the CFD.

While there is an improved rate if wake recovery for the CFD model based on the swept area of T_{UP}, it is not of the same order of magnitude as the experimental. And when using the swept area of T_{DOWN} the high turbulence case the wake recovery is unchanged at $12D$ downstream and is lower for the near wake. Clearly for the larger swept area the higher TI at the inlet is having almost no effect on the recovery of the wake. As can be seen in the experimental results the ambient turbulence has a large impact on the far wake recovery.

This is not seen in the CFD modelling, so the implementation of TI in the models is clearly not giving a representative view of what is being seen in the experimental tests. While the predictions for wake recovery in the CFD models follows the same trend, it is consistently under predicting the recovery for the higher TI value. At $7D$ the estimation for the wake recovery for the CFD and experimental is within $10\,\%$. The use of full LES simulations may be required to accurately resolve the larger scale turbulence throughout the entire domain and promote a higher level of interaction with the ambient flow field. However, due to computational restrictions this was not possible to investigate.

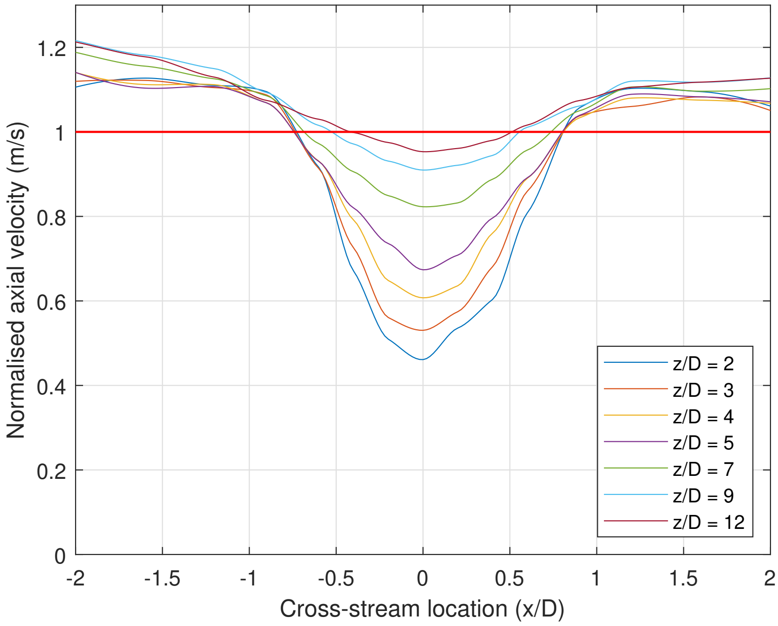

Figure 5.25: Cross-sectional rake behind T_{UP} with an inlet turbulence intensity of 11.7 % for the experimental testing.

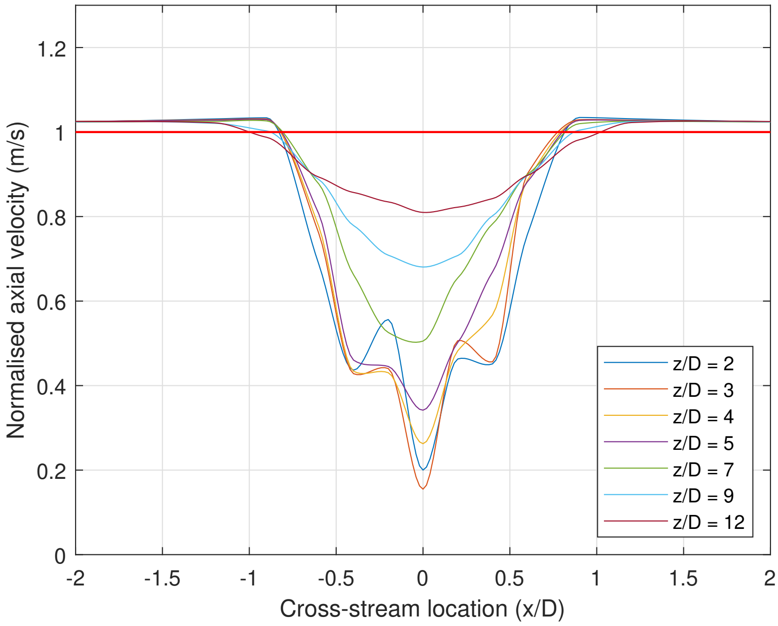

Figure 5.26: Cross-sectional rake behind T_{UP} with an inlet turbulence intensity of 11.7 % for the CFD model.

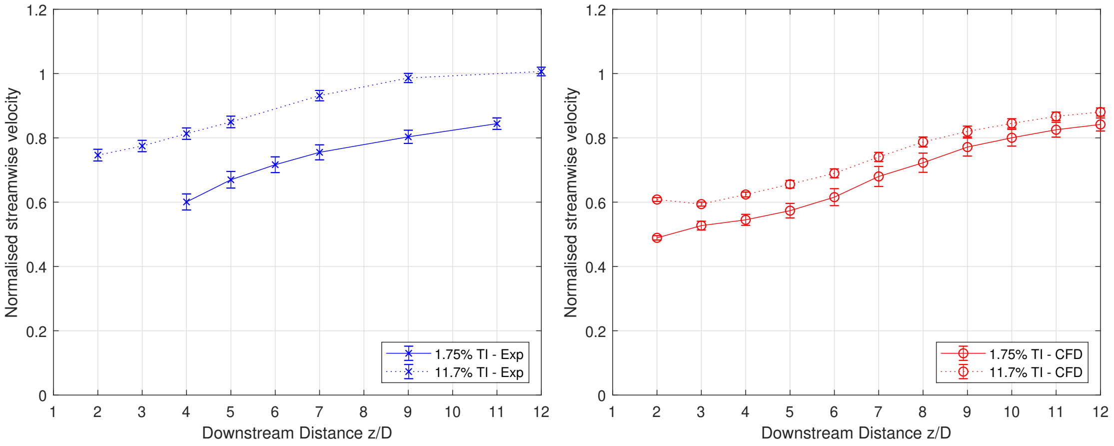

Figure 5.27: Influence of inlet turbulence on volumetric averaged wake recovery for experimental (left) and CFD (right) testing based on the swept area of T_{UP}.

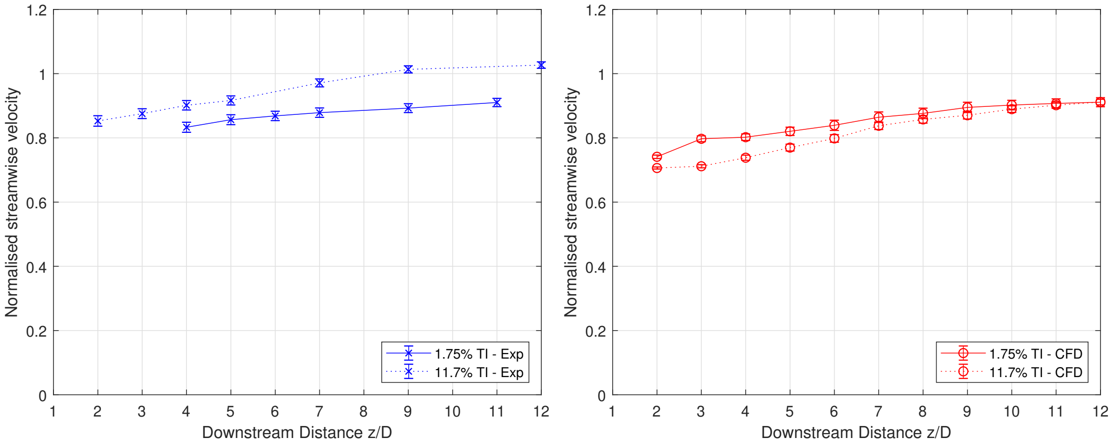

Figure 5.28: Influence of inlet turbulence on volumetric averaged wake recovery for experimental (left) and CFD (right) testing based on the swept area of T_{DOWN}.

5.4 Summary

The blocking method was used to break the domain into a larger number of divisions. This allowed for the more structured mesh to be applied over the domain. From the mesh study and looking at the mesh ratio later in the results there was little difference between mesh 2 and 3 when it came to the results. The computational time on the other hand was massively increased so Mesh 2 was chosen. The mesh needs to be further studied and refined however this was not possible as part of this work.

For the two timestep values tested there was no difference in the results for the rotor performance or the prediction of the wake recovery. Again, the computational time was massively increased for the smaller timestep.

The SBES turbulence model not only gave a better switch between RANS and LES but was suggested by ANSYS as the best method to use going forward due to the protection of the boundary layer allowing a more refined mesh. The BCD scheme was preferred to the HR scheme again due to the centreline velocity recovery. Also the HR scheme uses an upwind scheme over a larger region of the domain giving rise to the 'smearing' that is associated with upwind schemes. The suitability of the BCD scheme was backed up by the volumetrically averaged flow as it predicted the recovery of the wake well when compared to the experimental. The choice of turbulence model and discretisation scheme had a big influence on the prediction of the downstream centreline wake recovery.

The use of higher inlet turbulence resulted in an increased rate of wake recovery. The effect was less pronounced in the CFD but still present. The modelling of the inlet turbulence needs to be looked at in greater detail but for this work the turbulence was being used as a tool to change the device performance rather than being studied in detail. Going forward from this the use of full LES may be required to resolve turbulence throughout the domain. The volumetrically averaged flow velocity gave a much more realistic idea of what a downstream turbine would see compared to the centreline as the flow is considered over the full rotor area.

The mesh, timestep, turbulence model and discretisation scheme used for the final modelling the wake of a tidal turbine under two inlet turbulence intensities were the preferred options found from this work. The results for the CFD models were within 10 % of the experimental at $7D$ for the wake recovery at the high TI value. The modelling approach used in this Chapter was used going forward in Chapter 6.

Chapter 6

Performance of a turbine subject to an onset wake

The impact of the array layout on device performance and loading is of interest if full scale tidal arrays are to become commercial reality. The ability to determine the expected power output from an array, and understand the interaction between devices is an area of active research. The ability to capture wake features is fundamental to predicting array performance. Based on the work in the Chapter 5 the methodology and approach used gave reasonable agreement with the experimental results. Therefore, a study on the performance of a secondary, downstream, device was undertaken.

Three cases were considered to study the impact of the positioning of the downstream device in relation to the upstream turbine. Two of the cases used a combination of T_{UP} (referring to the upstream device) and T_{DOWN} (referring to the downstream device) for the testing, while one case used T_{DOWN} only. In the cases using both devices the stream-wise spacing was maintained at 3.5 m or 7D. The following chapter looks at the setup and implementation of both the CFD and experimental cases.

The CFD modelling in this chapter uses the findings from Chapters 4 and 5 as the basis for the CFD geometry, meshing and setup. Any differences in the modelling approach compared to Chapters 4 and 5 are discussed. As with all CFD simulations in this thesis the stream-wise flow is in the z-direction, the x-direction refers to cross-stream and the y-direction is the vertical direction. In the following work the co-ordinate axis used for the experimental testing was not the same as the CFD. The axis have therefore been included in the relevant figures when discussing the setup of the experimental work. T_{UP}, the device modelled in Chapter 5 is not studied in this part of the thesis. It is used purely to generate a wake to better understand the performance of a downstream device.

6.1 Experimental testing

The experimental testing in the following section is similar in execution as that detailed in Section 5.1. Both T_{DOWN} (0.9 m diameter) and T_{UP} (0.5 m diameter) were placed in the flume so that the effect of an upstream device could be monitored on the performance coefficients of the downstream device. The devices from Chapters 4 and 5 were used and so no more detail on the turbine design has been given here.

Three test cases were looked at and more detail is given below. In all cases only the TSR corresponding to peak power was tested and was based on the inlet flow velocity of $1.02\,\mathrm{m\,s^{-1}}$ found during flume characterisation prior to turbine installation. Flow measurements were taken at the proposed location for T_{DOWN} to give a better understanding of the flow in this region prior to device installation. This gave a TSR of 3.65 for T_{UP} and a TSR of 4 for T_{DOWN}. the corresponding angular velocity for T_UP and T_{DOWN} were $14.89\,\mathrm{rad\,s^{-1}}$ and $9/7\,\mathrm{rad\,s^{-1}}$ respectively. For the following testing the turbulence intensity was 11.7 %. More information of the flume characterisation has previously been given in Chapter 5. These points can be seen in Figures 6.1 and 6.2. An LDV was used to take flow measurements 1 m upstream of T_{DOWN} during all three cases. The devices were operated using fixed point speed control for all cases.

For the ambient case the prior flow measurements, shown in Figure 6.1, were not taken across the full width of the device. This was because the flume characterisation at this location was done for the diameter at T_{UP} initially. Due to time constraints in the testing a greater number of flow measurements could not be taken at this location. The configurations used for the in-wake and offset-wake cases were defined by the practical constraints of the tank dimensions.

Ambient case For the ambient case T_{DOWN} was placed 4 m downstream from the turbulence generating grid with the rotational axis 1 m below the water surface. The turbine was run under speed control. The setup is shown in Figure 6.3.

In-wake case During the in-wake case both T_{DOWN} and T_{UP} were used. T_{UP} was placed 4 m downstream from the turbulence generating grid. T_{DOWN} was placed 7.5 m

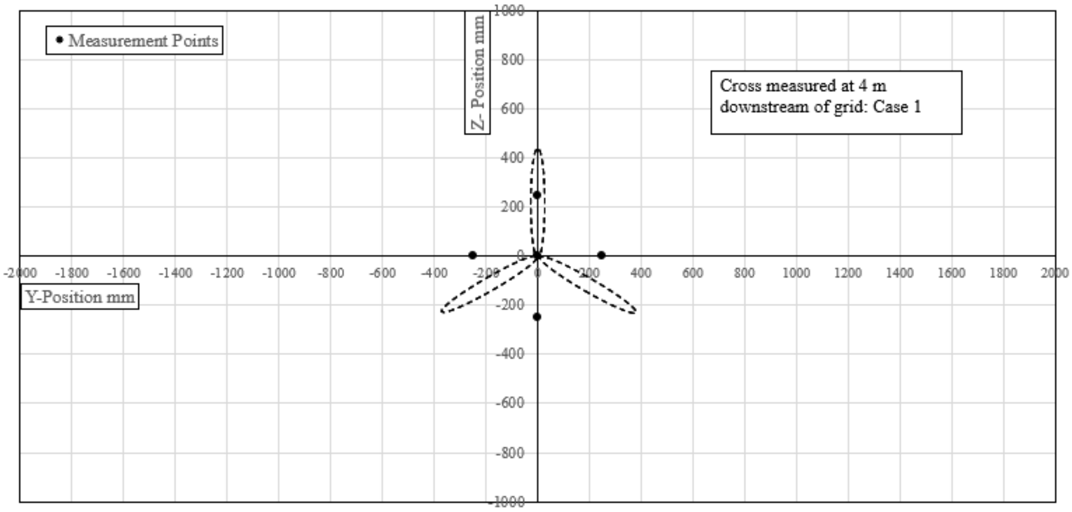

Figure 6.1: Location of LDV measurements taken prior to turbine installation for ambient case.

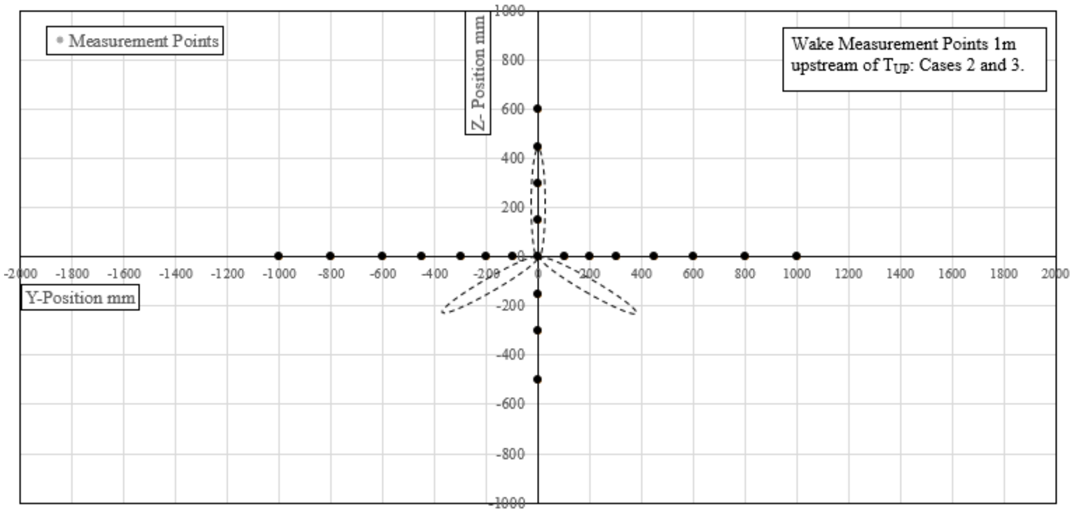

Figure 6.2: Location of LDV measurements taken prior to turbine installation for the in-wake and offset-wake cases.

downstream from the turbulence generating grid. The rotational axis for both devices was located half way through the water column, 1 m below the water surface. T_{DOWN} was placed directly in the wake of T_{UP} as both devices shared the same rotational axis and rotational direction. The setup is shown in Figure 6.4.

Offset-wake case During the offset-wake case both T_{DOWN} and T_{UP} were used. T_{UP} was placed 4 m downstream from the turbulence generating grid. T_{DOWN} was placed 7.5 m downstream from the turbulence generating grid. The rotational axis for both devices was located half way through the water column, 1 m below the water surface. T_{DOWN} was offset by 0.5 m so that the rotational axis were no longer aligned. This meant that during rotation one blade from T_{DOWN} was interacting with the wake behind T_{UP}. The setup is shown in Figure 6.5. The offset of 0.5 m was selected based on the diameter of T_{UP}.

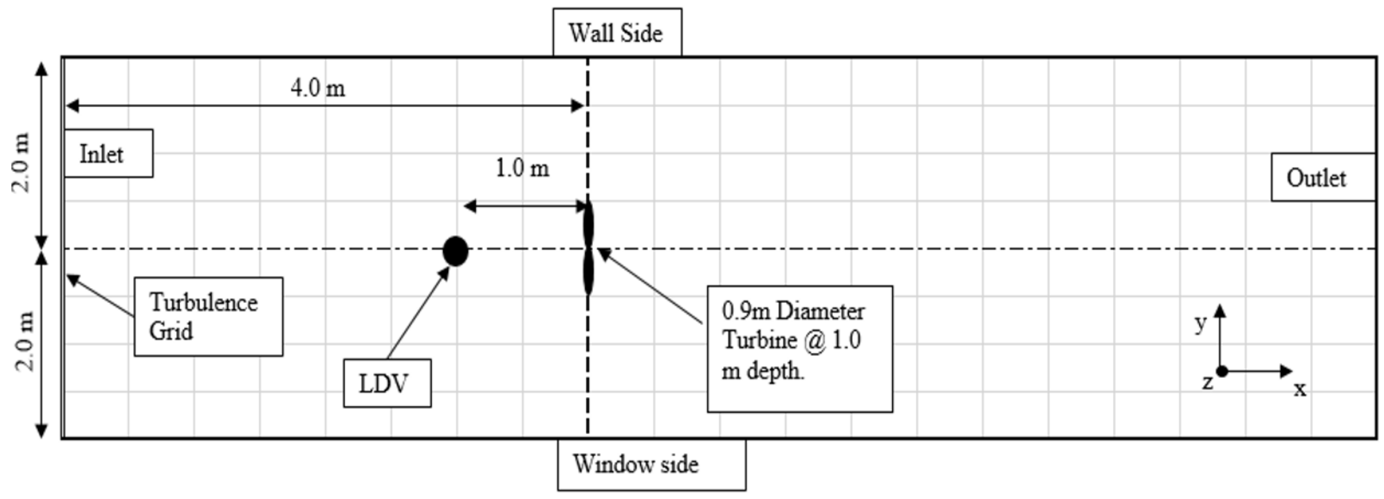

Figure 6.3: Representation of the testing conducted at the IFREMER flume tank for the ambient case.

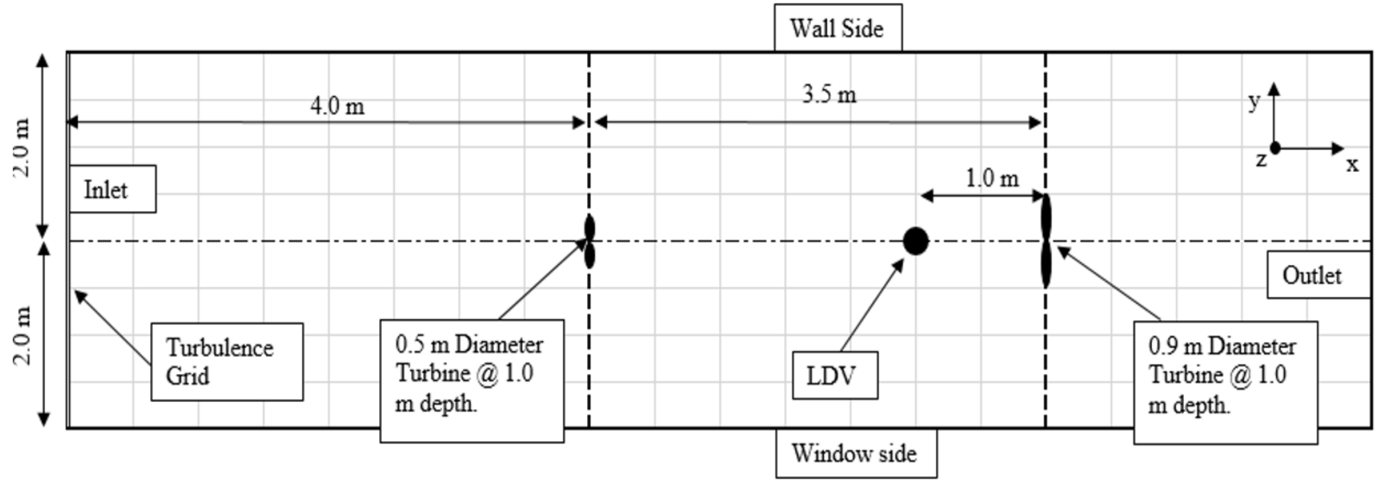

Figure 6.4: Representation of the testing conducted at the IFREMER flume tank for the in-wake case.

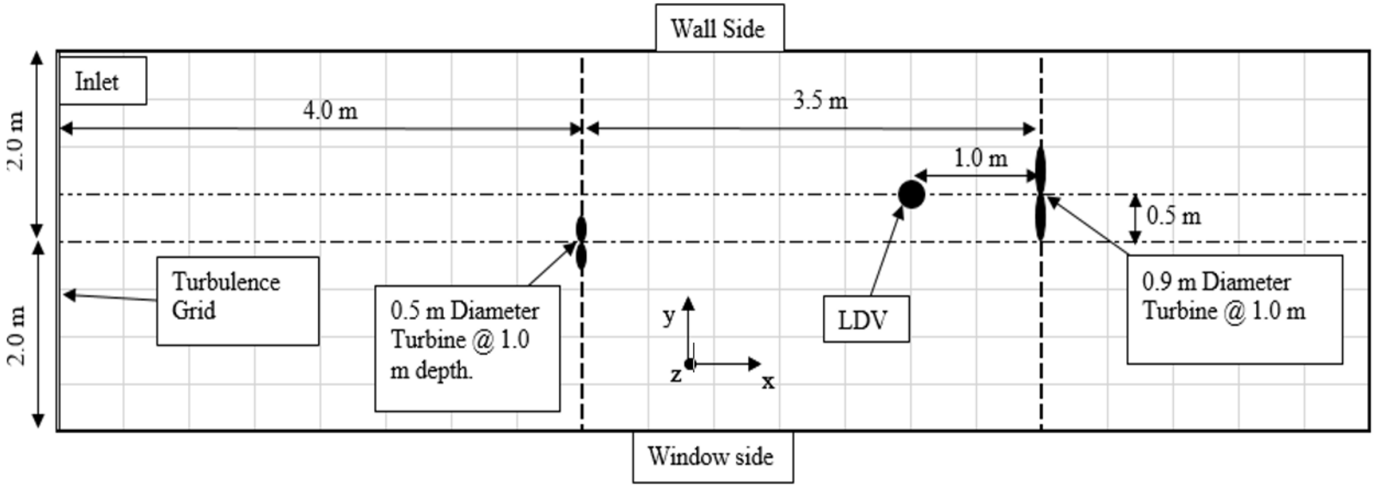

Figure 6.5: Representation of the testing conducted at the IFREMER flume tank for offset-wake case.

6.2 Computational fluid dynamics

The experimental testing was used as the basis for the following CFD models and the differences between the ambient, in-wake and offset-wake cases have been highlighted in the previous section. The approach taken for each of the cases was the same and they are discussed as one when talking about the geometry, mesh and setup. The CFD modelling approaches from Chapters 4 and 5 were used as so only a brief overview of the CFD model has been provided in this Chapter.

6.2.1 Model geometry

The CFD geometry was set up to replicate the experimental testing. As in Chapter 5 the domain inlet was shortened to keep the element count down in what was predominantly a RANS region. The grid used to generate the turbulence in the flume was not modelled. Instead the turbulence intensity, 11.7 %, and length scale, 0.5 m, based on the flume characterisation were specified at the inlet.

The geometry was divided using the blocking approach applied to the previous CFD modelling. For the ambient case the blocking approach was simple, however the in-wake and offset-wake cases were more complicated as two devices were being included in the model, shown in Figure 6.6. Due to the inclusion of a second device the complexity and the number of divisions required increased however the process was the same. The one notable difference are the dimensions used for the wake region. The wake region is larger than that used for the modelling in Chapter 5 due to the inclusion of the T_{DOWN}. The impact that this has on the mesh was negligible for reasons discussed in Section 6.2.2.

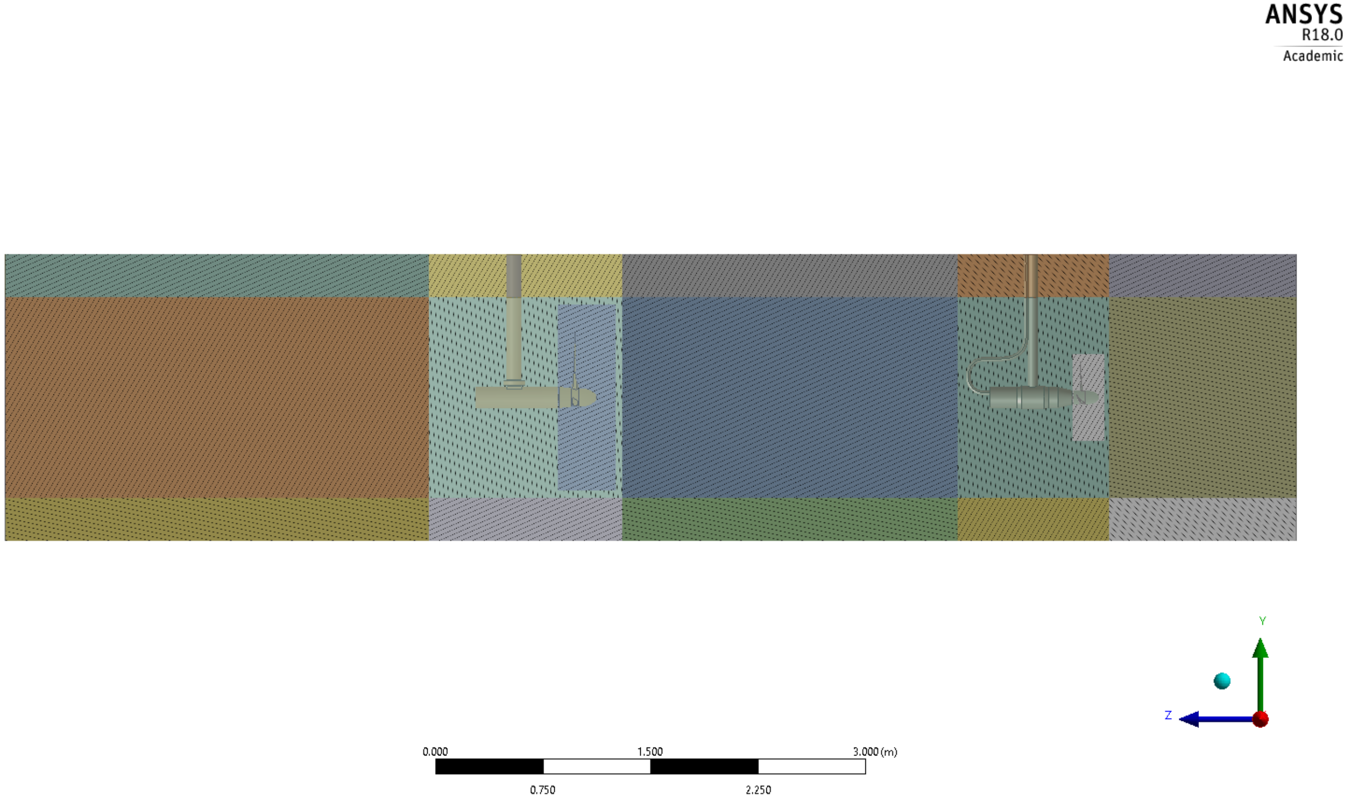

Figure 6.6: Blocking approach used for all three cases.

6.2.2 Mesh

The mesh studies conducted in Chapters 4 and 5 were used to produce the mesh used for the following CFD models as the results from both sets of work showed good agreement with the experimental data for both the performance prediction and wake prediction. Therefore no mesh study was carried out for this set of modelling.

Despite the more complicated approach taken to break up the geometry the mesh density in pre-determined regions were kept the same as the mesh density in Chapter 5. The ability to match the element count in the wake and rotor regions is one of the benefits of the blocking approach. In using the 'number of divisions' selection when generating the mesh throughout the domain it is possible to control the total number of the x, y and z directions. The element and node count for each of the cases can be seen in Table 6.1.

Table 6.1: Number of elements and nodes in the ambient, in-wake and offset-wake cases.

Case	Elements	Nodes
Ambient	$9.95x10^6$	$4.95x10^6$
In-wake	$17.65x10^6$	$7.06x10^6$
Offset-wake	$16.74x10^6$	$6.59x10^6$

T_{UP} **- upstream device**

The body used for the wake mesh was larger for the ambient case due to the inclusion of T_{DOWN} downstream. The ratio between edge length and number of divisions was found for Mesh 2 from Chapter 5. The new edge length for the wake region in the in-wake and offset-wake cases were then used to determine the number of cells required to achieve the same mesh density. By using this approach the number and size of the cells in the wake remained consistent throughout the models.

T_{DOWN} **- downstream device**

The mesh behind T_{DOWN} was left largely unrefined as the mesh behind the second device was not of interest to this study. In increasing the mesh sizing downstream of T_{DOWN} the total number of elements in the model was controlled to help reduce the computational time. The mesh used for the rotor region of T_{DOWN} was kept the same as that used in Chapter 4.

6.2.3 Model setup

The implementation of the CFD setup was unchanged compared to the high turbulence simulations run as part of Chapter 5. The SBES turbulence model was used with a time step of 0.005 s. Table 6.2 gives a summary of the operating conditions for each device and details which device was modelled for each case. The angular velocity for each device was calculated based on both devices operating at peak TSR with an inlet flow velocity of $1.02\,\mathrm{m\,s^{-1}}$. A converged transient simulation was used as the initial conditions file.

Table 6.2: Summary of the test cases.

Turbine	u_∞, ms^-1	Inlet TI, %	ω, $rads^-1$	λ	Diameter, m	Cases
T_{DOWN}	1.02	11.7	9.067	4	0.9	All
T_{UP}	1.02	11.7	14.89	3.65	0.5	In-wake and offset-wake

6.3 Results

6.3.1 Onset flow conditions

The performance of the device is most commonly expressed using the non dimensional performance coefficients. However, as mentioned throughout this work the selection of the velocity value can have a large impact on the non-dimensional performance coefficients. Given the complex nature of the flow for a downstream device, the way the flow velocity is expressed and calculated needs to be carefully considered.

When calculating the performance of T_{DOWN} in Section 6.3.5 five methods were used to determine the flow used in the equations for the performance coefficients. For each case the methods have been described below. In each of these cases the flow measurements are taken 1 m upstream of T_{DOWN}. Only method 5 was different between the cases, as the available data and location relative to the wake had to be taken into consideration. Therefore any changes to the approach taken when calculating the swept area average have been discussed for the relevant cases in the proceeding text.

Method 1 The mean value of the upstream flow velocity for the full time series is found.

Method 2 This method uses the flow velocity found when characterising the flume prior to device installation. It could also be likened to the far upstream flow velocity.

Method 3 The 2nd and 3rd moment of onset velocity for thrust and power respectively are calculated based on the measurement from the LDV 1m upstream of the device. Then the mean of the cubed and squared values are found. It is this mean value that is then used in the calculation. The cubed and squared terms can have a large impact on the final value as it can skew the results if the flow velocity seen by the device is not representative of the value used in the calculations.

Method 4 The performance coefficients are found for each of the recorded flow measurements. The mean value of all the performance coefficients is then used. The average value for the torque and thrust is used is this instance and so the phase shift between the torque/thrust and velocity is neglected.

Method 5 The volumetric average based on the swept area of T_{DOWN} using interpolation and makes assumption that flow is rotationally symmetric. This requires a larger number of data points to be measured as flow measurements across the face of the turbine are required. The assumption of rotational symmetry is made when finding the swept area average for method 5 as used by [14, 51].

6.3.1.1 Ambient case

Only T_{DOWN} is used for the ambient flow case. The turbulence is generated by means of a grid in the flume. The grid is 4m from the inlet. The turbulence dissipates downstream of the inlet as shown by [14, 50]. The values found prior to turbine installation at the proposed turbine location give a good estimation of the flow that the turbine is likely to see.

As the flow measurement locations did not span the full turbine diameter for the ambient case method 5 was not considered. Therefore, when calculating the performance curves for the ambient case for the experimental testing methods 1 - 4 have been used to find the flow velocity. The CFD models have used all 5 methods listed as a greater number of points could be easily measured in the simulations and so the performance curves for all methods have been presented.

6.3.1.2 In-wake case

To better understand the flow for the in-wake and offset wake cases the modelling from Chapter 5 can be used to give some insight into the expected onset flow. A contour plot of

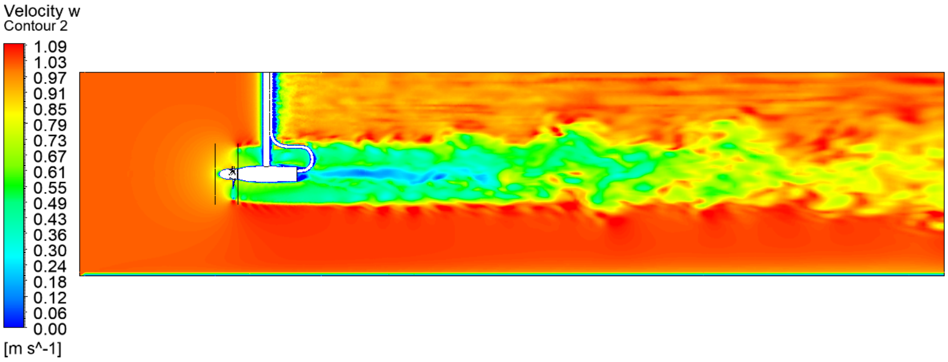

(a) Visualisation of the wake for a single time step.

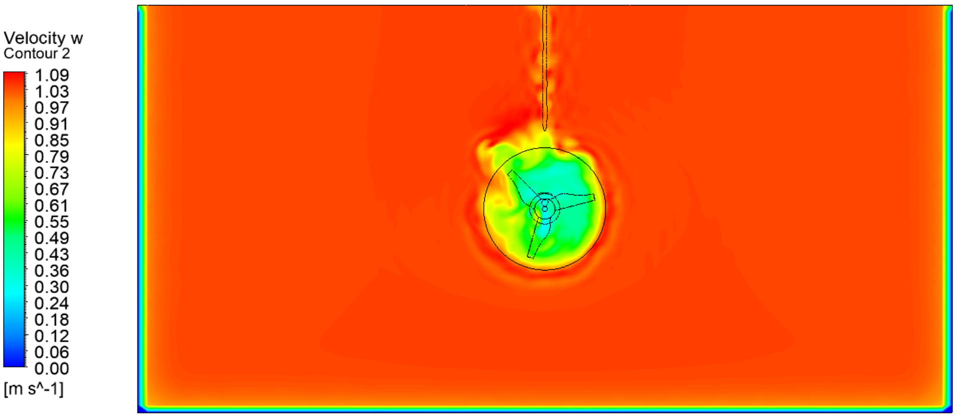

(b) Visualisation of the wake cross-section 5D downstream of T_UP for a single time step.

Figure 6.7: CFD contour plot for a single time step of the flow velocity from wake modelling from Chapter 5.

the velocity for a single time step can be seen in Figure 6.7. The contour plot is from the SBES CFD model. In the CFD model there is a clear wake region of slower flow velocity where LES is being used. Outside of this region the RANS model is dominant and so the flow velocity is similar to that of the inlet flow velocity.

Placing T_{DOWN} in the wake of the smaller diameter turbine, T_{UP} will mean that all but the tips of the rotor are in the wake.

The influence of the wake from T_{UP} can be better visualised in Figure 6.8. From Figures 6.9 and 6.10 it is suggested that the wake causes a flow deficit over a range of +/- 0.35m. This would leave the outer 0.1m of the blades exposed to the ambient flow. All but the tips of the blades of T_{DOWN} are encompassed by the wake. The tips of the blades will therefore be positioned in the bypass flow.

As only one point measurement was taken upstream of the device during the experimental testing the volumetric average (method 5) could only be found based on the flow

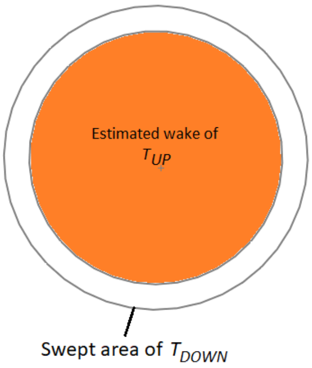

Figure 6.8: Representation of T_{UP} wake on compared to the swept area of T_{DOWN}.

measurements prior to turbine installation. This does not necessarily provide a realistic representation of the flow at this point once the turbine is in-situ.

6.3.1.3 Offset case

The onset flow for the offset-wake case can be visualised by looking at Figures 6.9 and 6.10. The offset is 0.5m and so the hub of T_{DOWN} will fall outside of the wake region. However during the rotation one of the blades will be passing through the wake. This interaction will mean the one blade is periodically exposed to a lower flow velocity and higher turbulence region, especially in the CFD model. This will cause the mean torque and thrust values to drop while the loading fluctuations associated with the turbulence could possibly increase in magnitude.

To determine the influence of the wake on the results it is important to understand the region of the wake that the blade passes through. An estimation of the wake diameter was required so that the angle, a, that the blade passes through the wake, shown in Figure 6.11 could be calculated. Figures 6.9 and 6.10 were used to give an estimation of the wake diameter prior to the installation of T_{DOWN}. The diameter of the wake was found based on the recovery of the flow velocity to $\approx 90\,\%$ of the upstream flow speed and was found to be $\approx 0.7\,\text{m}$ for the CFD and $\approx 0.6\,\text{m}$. Based on this wake diameter it was found that the blade passes through the wake of T_{UP} for ≈ 86 degrees during the CFD model and ≈ 75 degrees for the experimental testing. These values have been used later when calculating the flow velocity based on method 5 for Section 6.3.5. The interaction occurs at around 45 degrees, if the zero position is considered to be when the blade is at top dead centre. During this part of the rotation where the blade passes through the wake the performance

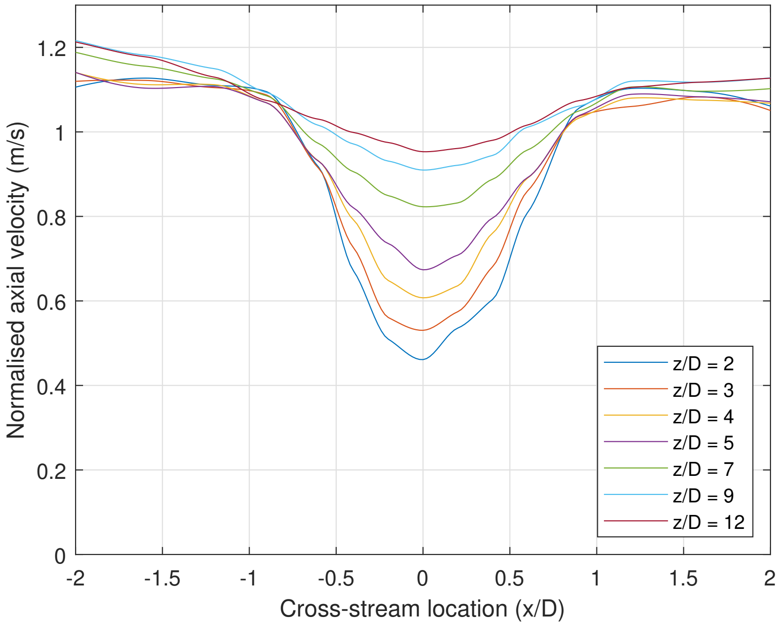

Figure 6.9: Cross-sectional rake behind T_{UP} with an inlet turbulence intensity of 11.7 % for the experimental testing.

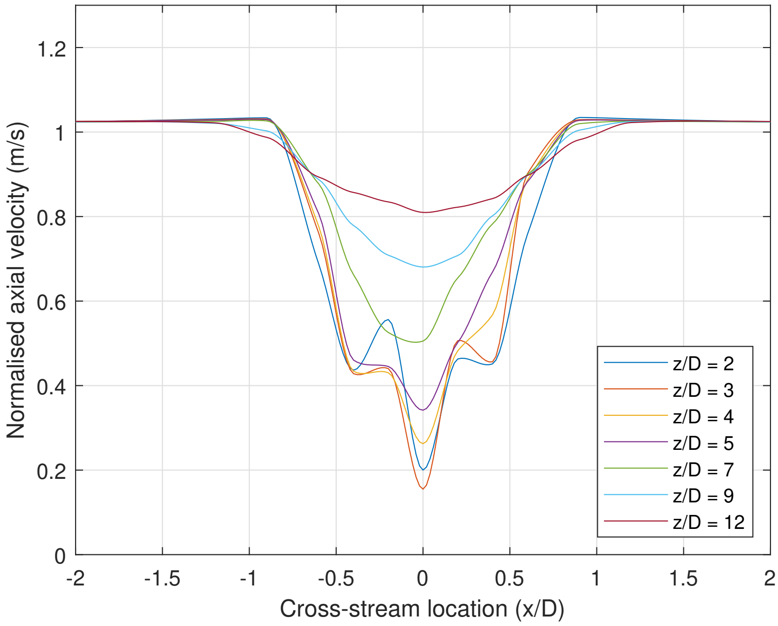

Figure 6.10: Cross-sectional rake behind T_{UP} with an inlet turbulence intensity of 11.7 % for the CFD model.

of the turbine is expected to be reduced due to the highly turbulent nature of the wake.

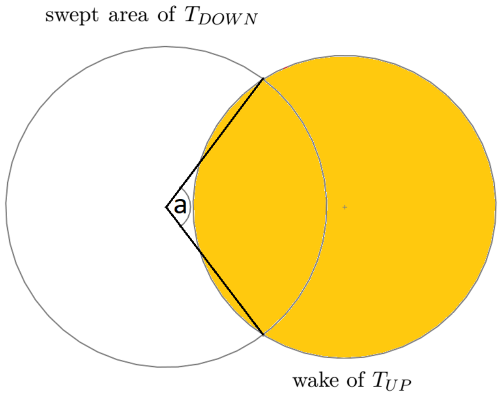

Figure 6.11: Representation of the angle, a, during which a blade passes through the wake of T_{UP}.

As only one point measurement was taken upstream of the device during the experimental testing the volumetric average could only be found based on the flow measurements prior to turbine installation. This does not necessarily provide a realistic representation of the flow at this point once the turbine is in-situ.

For the offset-wake case the blade of T_{DOWN} clips the wake of T_{UP} during the rotation. If rotational symmetry was assumed then the region of slow flow velocity would be over estimated. To avoid this the area of the wake that the blade passed through was found as shown in Figure 6.12. When the averaging was done the swept area was broken into two segments; out of wake and in wake. The purpose of this was to weight the volumetric average based on the whether the blade from T_{DOWN} passed through the wake area of T_{UP}.

6.3.2 Flow analysis

The flow measurements for each of the cases are presented. The sample times for the CFD are shorter than the experimental due to the computing resources required. The RANS model was run for 30 s and the data was averaged over the final 20 s. The results converged within this time frame. Using a longer run time for the RANS model would have resulted in no change in the results but an increased computational time. The SBES was run for 60 s and sampled over 50 s in keeping with the work done in Chapter 4. The experimental data was captured for 200 s for each of the cases.

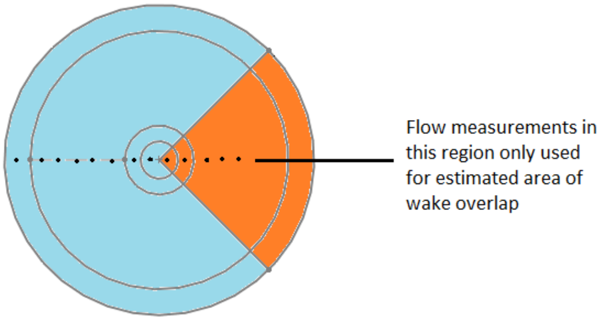

Figure 6.12: Representation of swept area calculation for the offset case. The area of overlap between the wake of T_{UP} and the rotor area of T_{DOWN}, shown in orange was found. The flow measurements in this region where used to find the swept area velocity for the overlap region. The flow measurements taken outside of the overlap region were used for the rest of the swept area velocity calculation.

6.3.2.1 Ambient case

A singular LDV measurement was taken 1 m upstream of the device. A sample of the time series can be seen in Figure 6.13. The fluctuations in the flow are obvious due to the grid induced turbulence upstream. The mean flow velocity, sampled over 200 s was $0.96\,\mathrm{m\,s^{-1}}$. This value was lower than the inlet velocity determined via characterisation prior to turbine installation. The blockage ratio is 8 % which causes an induction region. The fluctuations in the flow measurements show the flow was highly turbulent as seen in Figure 6.13. Based on Equation 3.2 the turbulence intensity was found to be 15.4 % 1 m upstream of the device. This is higher than the value found during the flume characterisation. The reason for this is assumed to be the proximity of the LDV to the grid. The value of 11.7 % was found based on an average of LDV measurements at the rotor plane. The single point LDV point measured during testing is very localised and closer to the grid.

The CFD model was run using both the RANS and SBES turbulence models to replicate the testing. Monitor points were included 1 m upstream to capture the flow during the simulation. There was no fluctuation in the flow velocity at the point measurement upstream of the device for the SBES model. At a point 1 m upstream of the device the RANS model is dominant as the transition to LES has not occurred. The RANS averaging process means that the resolved turbulence in the flow is below 0.1 % for both turbulence models. The turbulence at the inlet must still be included for the SBES model as the

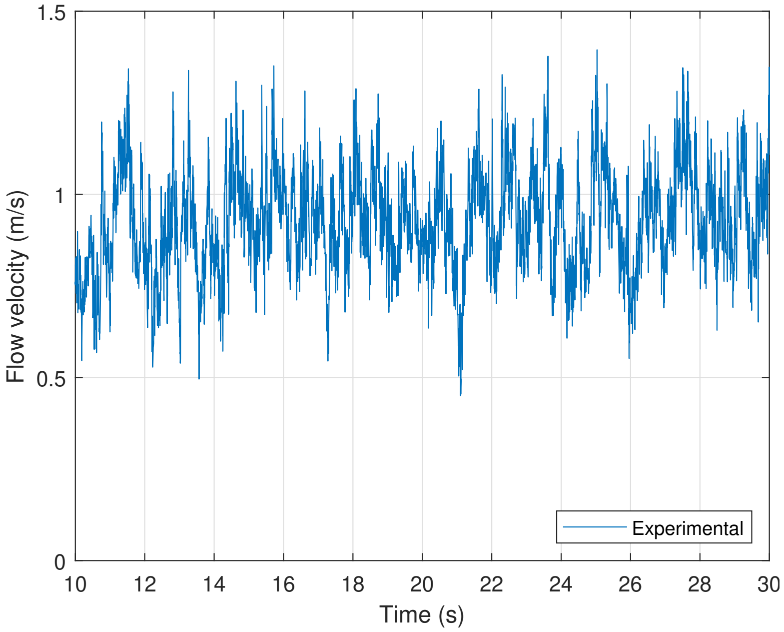

Figure 6.13: Flow velocity 1 m upstream of T_{DOWN} for the ambient case for the experimental testing.

unresolved turbulence is carried downstream until it reaches the LES region, at which point it is resolved.

The ease at which monitor points can be included in the CFD models meant that a cross-sectional rake upstream of the device was also captured. The mean flow in the CFD simulation across the diameter of the device is almost unchanged from the specified inlet velocity of $1.02\,\mathrm{m\,s^{-1}}$ despite the influence of the device.

The limitation in the hybrid turbulence model can be seen clearly when comparing the experimental flow to the simulated flow. There is a distinct lack of resolved turbulence due to the delayed switch to LES. The use of pure LES may be more suitable for determining flow characteristics for a single device in 'clean' flow, however, the mesh requirements and the computational costs are increased. A summary of the upstream flow conditions can be seen in Table 6.3.

The mean values for the flow velocity for both CFD and experimental show good agreement, and are within 4 %. The turbulence intensity is massively under predicted in the CFD models for a singular device when the monitor point is placed 1 m upstream of the device. Therefore, if wanting to study the performance of a single device in a turbulent flow it is likely that a LES simulation should be applied. For flows that have a large instability due to the influence of a body, such as the in-wake and offset-wake cases, full

LES is not necessarily required depending on the region of interest.

Table 6.3: Summary of the flow conditions 1 m upstream of T_{DOWN} for the ambient case.

Results	Mean Flow Velocity, $ms^{-}1$	TI, %	Sample Time ,s
Experimental	0.96	15.4	200
CFD - RANS	1.00	> 0.01	20
CFD - SBES	1.00	> 0.01	50

6.3.2.2 In-wake case

A singular LDV measurement was taken 1 m upstream of the device during the experimental testing. For the in-wake case this meant that the LDV measurement was in the wake, 2.5 m ($5D$ based on T_{UP} diameter) downstream of T_{UP}. A sample of the time series can be seen in Figure 6.14. The wake of T_{UP} is highly turbulent and fluctuations in the flow data are expected, as seen in Figure 6.14. The mean flow velocity, sampled over 200 s is 0.66 m s^{-1}. The flow velocity is well below the inlet velocity due to the influence of the upstream device. At $5D$ downstream the flow velocity has only reached 65 % recovery. By $7D$ this value could be higher as the flow recovers further downstream. However, as seen with the ambient case, the blockage of T_{DOWN} may cause the flow velocity upstream to slow down as the flow is accelerated around the device. This may mean that the flow velocity may not actually recover much above the value 65 %. The turbulence intensity was found to be 18.9 %.

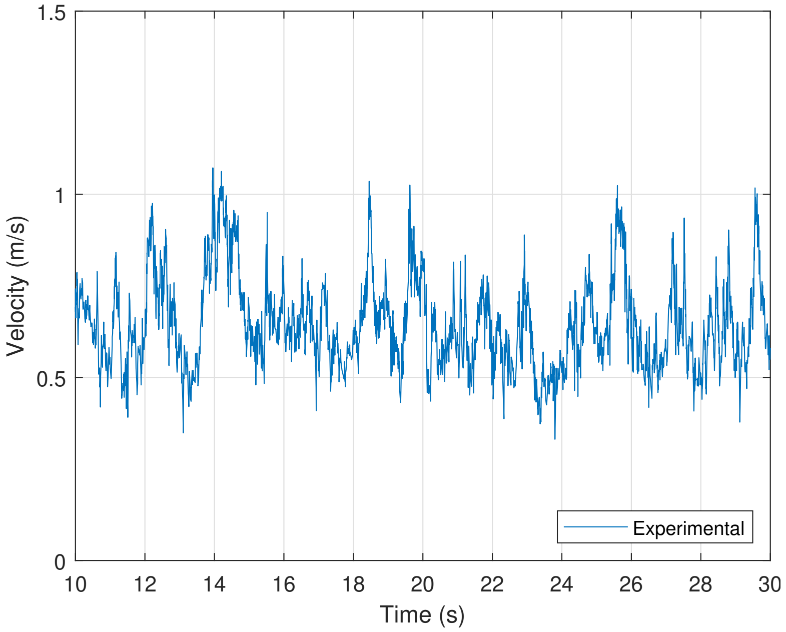

Figure 6.14: Flow velocity 1 m upstream of T_{DOWN} for the in-wake case for the experimental testing.

The flow velocity for the RANS and SBES models are shown in Figure 6.15. The RANS, as expected, contains no fluctuations. The TI is < 1 %. Given the location of the monitor point this is slightly surprising. It just highlights how effective the RANS model is at damping any fluctuations in the flow. For the SBES model the TI is close to 32 %, much higher than both the experimental testing and the value found during the flume

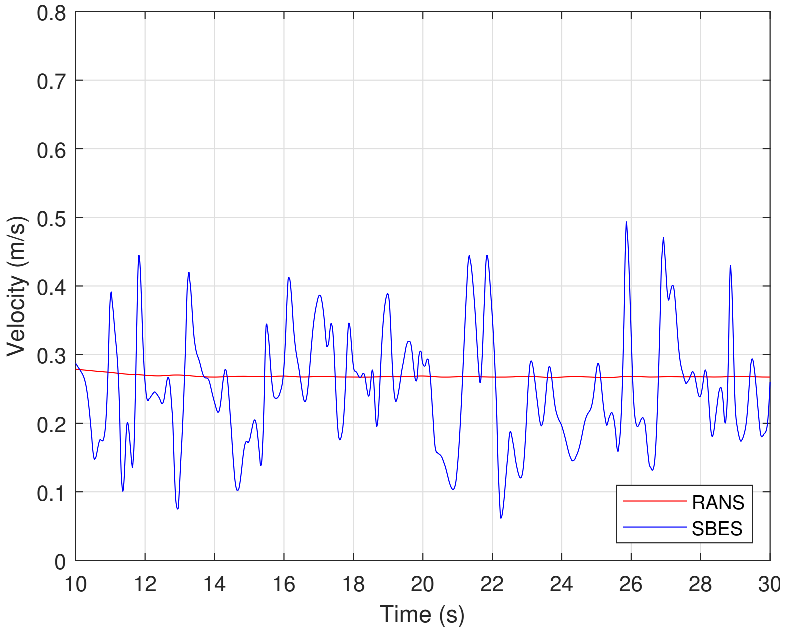

Figure 6.15: Flow velocity 1 m upstream of T_{DOWN} for the in-wake case for the CFD models

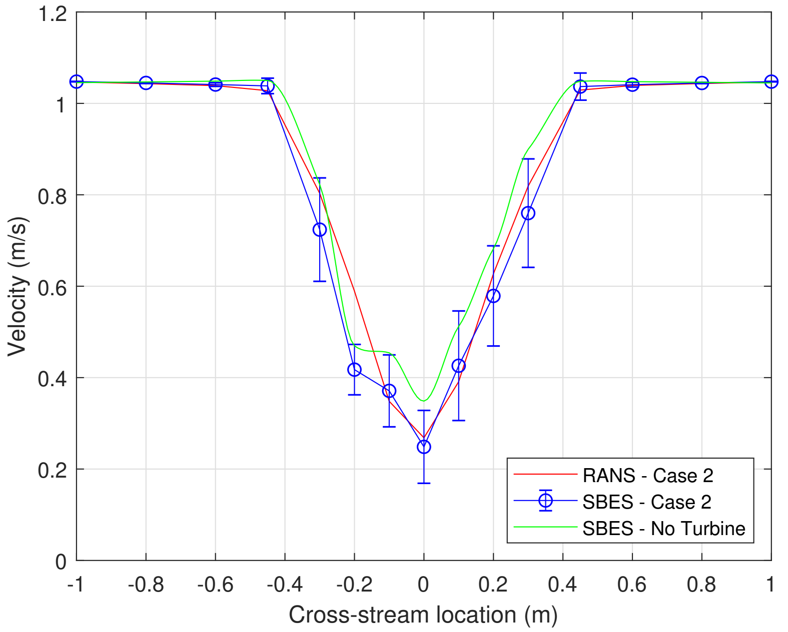

Figure 6.16: Cross-sectional flow velocity 1 m upstream of T_{DOWN} for the in-wake case for the CFD models compared to the cross-sectional rake before the turbine was placed in the flow.

characterisation. It is hypothesized that this was due to the lack of mixing between the ambient flow and the wake due to the hybrid turbulence model, as found in Chapter 5 when trying to model the near wake. This may also be the cause of the elevated turbulence intensity $5D$ downstream in the SBES model.

The mean flow velocity for both CFD models was similar, $0.27\,\mathrm{m\,s^{-1}}$ for the RANS model and $0.25\,\mathrm{m\,s^{-1}}$ for the SBES model. In both cases this value is below the experimental mean velocity of $0.66\,\mathrm{m\,s^{-1}}$. The inability to resolve the turbulence surrounding the wake causes a lower rate of mixing between the ambient flow and the wake in the CFD model have an impact on the wake recovery at $5D$ downstream.

A cross-sectional rake of the wake was also measured for the CFD models. A comparison has been made in Figure 6.16 between the CFD modes used for the in-wake case and the high turbulence CFD model from Chapter 5. The mean cross-sectional flow velocity for the SBES model in the in-wake case 1 m upstream of T_{DOWN} is lower than the flow velocity at the same cross-sectional location before T_{DOWN} is placed in the flume. The blockage of T_{DOWN} causes an induction region. A summary of the upstream flow conditions can be seen in Table 6.4.

The mean flow velocity for the CFD, both RANS and SBES is only 40 % of the experimental value. The TI for the SBES case is much higher than the experimental in the wake region based on 1D analysis.

Table 6.4: Summary of the flow conditions 1 m upstream of T_{DOWN} for the in-wake case.

Results	Mean Flow Velocity, $ms^{-}1$	TI, %	Sample Time ,s
Experimental	0.66	18.9	200
CFD - RANS	0.27	> 1	20
CFD - SBES	0.25	32.7	50

6.3.2.3 Offset-wake case

The LDV location for the offset-wake case fell outside of of the wake of T_{UP} due to the offset of the downstream device. Figure 6.17 shows an example of the time series for the LDV measurement. The mean flow velocity was 1.08 m s^{-1} with a TI of 9.2 %. The flow in this region was higher than the flow velocity found during the flume characterisation. Due to the blockage of T_{UP} the flow accelerates around the device causing the flow velocity in regions surrounding the wake to be higher.

The LDV location gives a good representation of the ambient turbulence intensity. The TI is lower than the value measured along the centreline of the flume during the flume characterisation. The turbulence dissipates gradually down the length of the domain as there is no geometry to induce greater turbulence on either side of the turbulence.

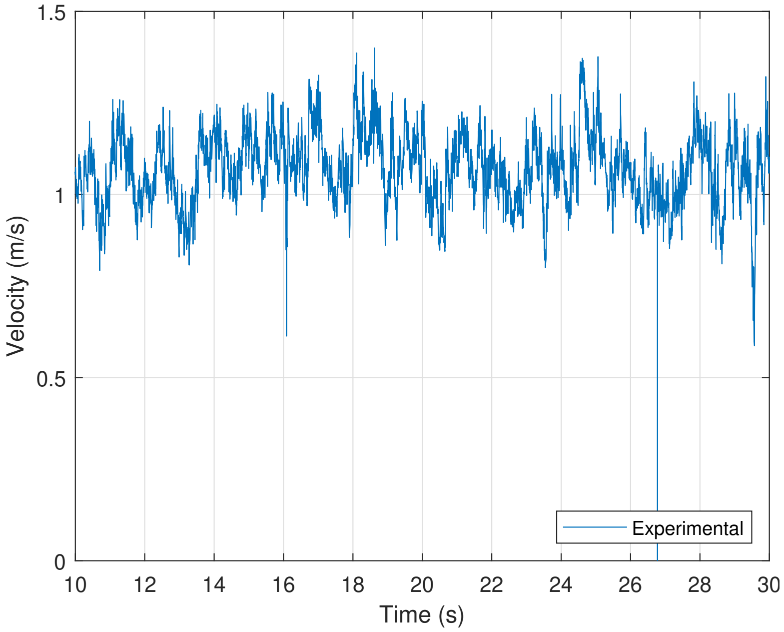

Figure 6.17: Flow velocity 1 m upstream of T_{DOWN} for the offset-wake case for the experimental testing.

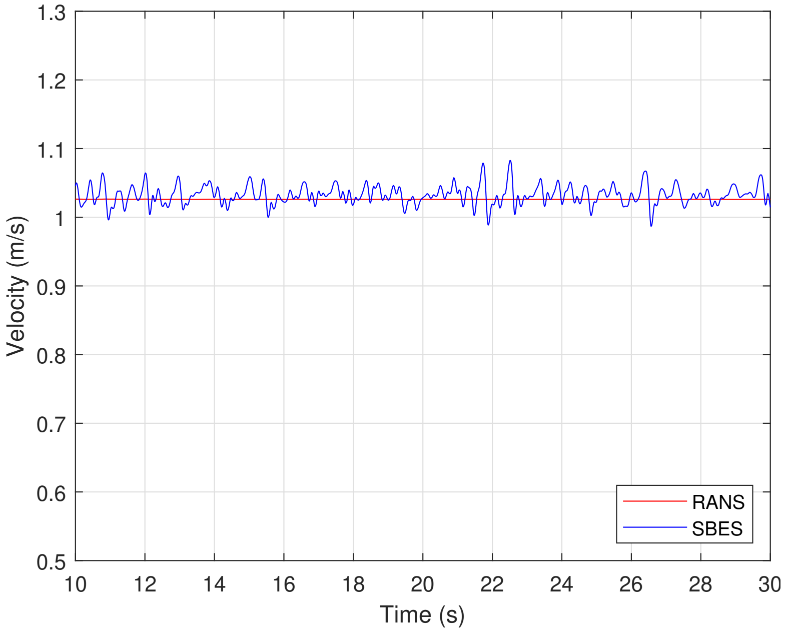

Figure 6.18: Flow velocity 1 m upstream of T_{DOWN} for the offset-wake case for the CFD models

Figure 6.18 presents the CFD flow data. The monitor point was located outside of the wake of T_{UP} and as with the ambient case there are no fluctuations in the flow velocity for regions modelled using RANS. Despite there being noticeable fluctuations in the SBES model due to the proximity of the wake, the standard deviation when expressed as a percentage of the mean is less than 2 %. There is no fluctuation in the RANS model. The SBES case has a TI value of 1.35 %, whereas the RANS model, as expected, was less than 0.01 %. This is one of the limitations of using a hybrid turbulence model. Despite the monitor point only being a small distance from the wake, an inherently unsteady and turbulent region, the CFD model does not capture the velocity fluctuations. This is unsurprising as the monitor point for both CFD models in located in the RANS region of the flow. Upstream turbulence is not induced by a grid or device and so no transition is present.

A summary of the flow velocity, turbulence intensity and sample time for the CFD and experimental tests is given in Table 6.5. The flow velocity shows good agreement and are within 5 % of each other. The resolved turbulence is again a problem for the CFD model and it is heavily under predicted.

Table 6.5: Summary of the flow conditions 1 m upstream of T_{DOWN} for the offset-wake case.

Results	Mean Flow Velocity, $ms^{-}1$	TI, %	Sample Time, s
Experimental	1.08	9.22	200
CFD - RANS	1.03	0.01	20
CFD - SBES	1.03	1.35	50

6.3.3 Measured data

The torque, thrust, bending moment and power measurements for T_{DOWN} were of interest for this chapter. The mean values for thrust, bending moment and power are discussed and compared later. The following section presents a snapshot of the time series for the data measured during the testing. They were captured using a transducer located behind the rotor. The bending moment values for a single blade were measured during the experimental testing and so the comparison is made for only one blade. For all three cases a period of the time series for the torque, thrust and the out-of-plane bending moment have been presented and discussed.

For the experimental results there was less than a 2 % variation in the angular velocity throughout the testing despite using set-point speed control. This is because there is a lag in the speed control loop, causing a discrepancy between the instantaneous rotor angular velocity and the desired angular velocity, hence the variation. The CFD does not have this problem and maintains a fixed angular velocity throughout the entire simulation. For the following data sets the time t=0 corresponds to when the blade is at top-dead centre to facilitate comparisons.

6.3.3.1 Ambient case

The flow analysis of the ambient case showed the lack of fluctuation in the flow upstream of the device. This is also the case for the torque, thrust and out-of-plane bending moment data from the CFD models. Figure 6.19 shows a snapshot of the time series for torque, thrust and bending moment for the experimental testing and the CFD models. Both RANS and SBES have consistent and repeatable profiles throughout the rotation of the device with very small fluctuation. The values themselves are similar for both models, which is expected due to the boundary layer region being treated using RANS in both models. Again it highlights how the introduction of the turbulence throughout the domain needs to be improved for hybrid RANS-LES models.

The experimental results for all three measurements have much larger fluctuations due to the upstream turbulence. The measurements from the torque transducer are shown. Despite the transducer giving readings for all three blades there is a large fluctuation in the readings seen throughout the turbine rotation. The turbulent perturbations in the flow have a large impact on the values.

The out-of-plane bending moments for one blade are shown in Figure 6.20 for both the

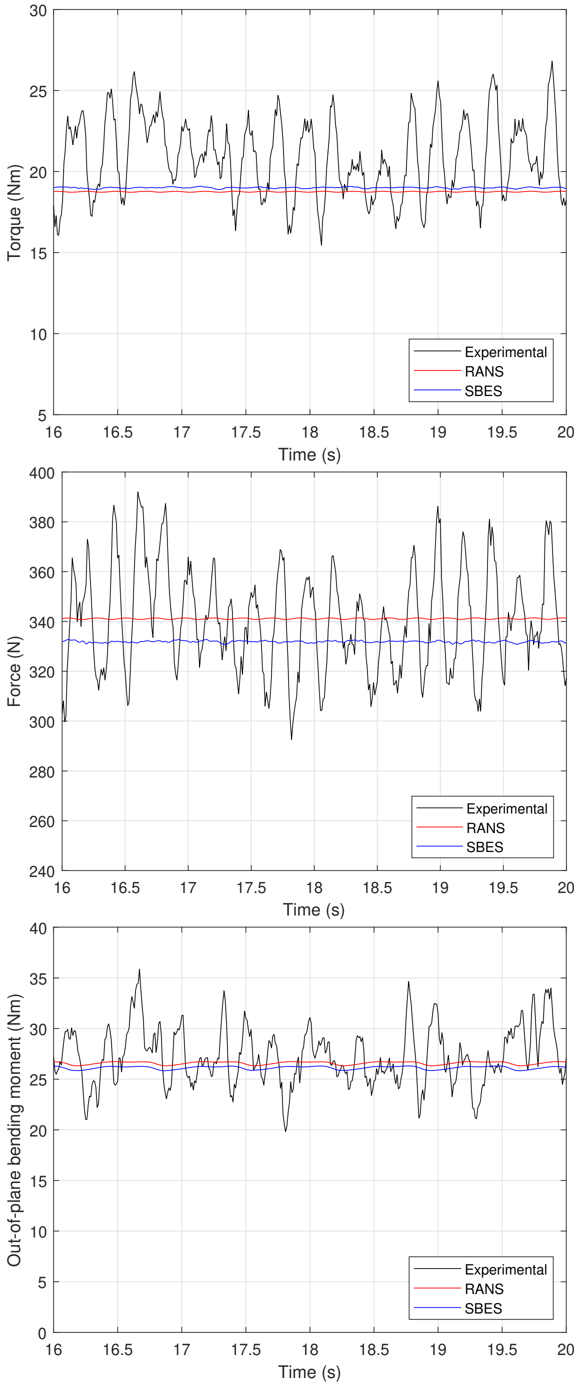

Figure 6.19: Comparison of the time series for the torque, thrust and out-of-plane bending moment for the ambient case.

experimental and CFD models. The SBES time series was plotted to show the variation in the two turbulence models. The same method has been used when presenting the measured data for the in-wake and offset-wake cases. The CFD model has little to no variation in the upstream flow velocity. The outcome of this is that the out-of-plane bending moments of the device for both the RANS and the SBES models are very similar. The predicted instantaneous values do not change throughout the device rotation. There is less than 2 % difference between the two CFD models.

The SBES model uses the RANS formulation in the boundary layer and so the mean performance for both models is expected to be very similar. The values are consistent throughout the entire rotation of the device for both RANS and SBES despite the specified inlet turbulence.

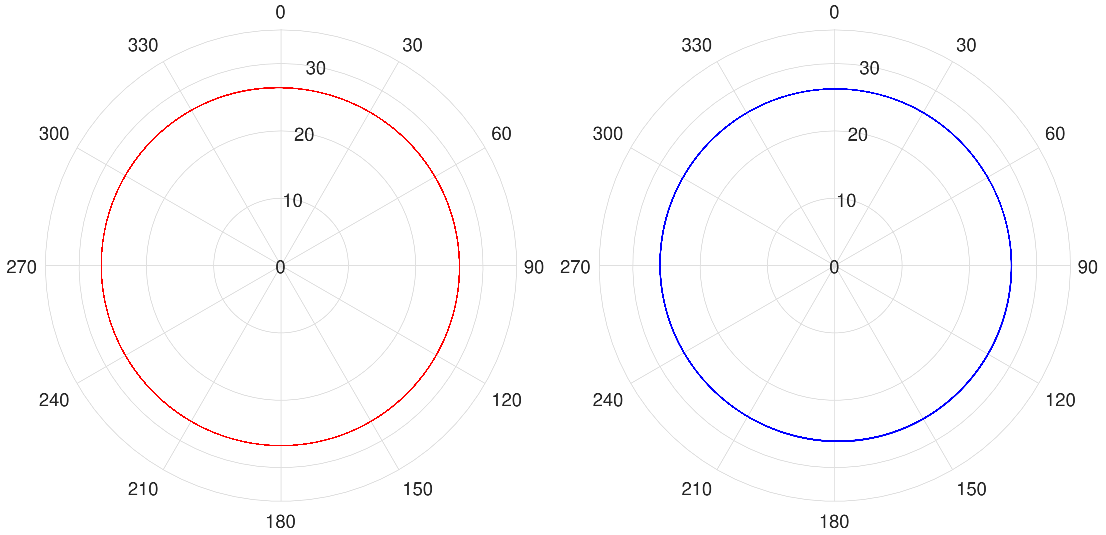

(a) RANS SST k-ω model. **(b)** SBES model.

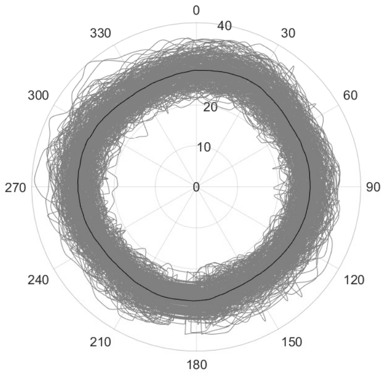

(c) Experimental testing.

Figure 6.20: Out-of-plane bending moment for one blade over the full time series for the ambient case.

6.3.3.2 In-wake case

Figure 6.21 shows a snapshot of the time series for the torque, thrust and bending moment for each of the models. For all three variables measured the CFD data is lower than that of the experimental. As shown in the previous flow analysis the flow velocity that the device was seeing was lower in the CFD than the experimental. Therefore the lower torque and thrust prediction for the device in the CFD modelling would be expected. From Figure 6.16 it is suggested that wake causes flow deficit over a range of +/- 0.4m. This would leave the outer 0.05m of the blades exposed to the ambient flow. The turbulence is under predicted outside of the wake region and so there could be an under prediction of the unsteady loads for the SBES model.

The magnitude of the fluctuations in the measured data is similar for both the experimental and SBES results. As the wake is highly turbulent the LES model is implemented and allows for a better resolution of the flow field. This highlights the suitability of the SBES turbulence model for capturing the fluctuations in the device performance if the LES model is used in the turbulent regions. This could be used to inform developers as to the expected loading a device may experience based on CFD results. The magnitude of the fluctuations of the RANS model is almost unchanged between each of the three cases.

The polar plots displayed in Figure 6.22 show the suitability of the SBES model to capture the fluctuations in the measurements. What is also present in the CFD models is the point at which the blade passes the stanchion. There is a dip in the bending moment values for both CFD models as the blade passes the stanchion before recovering. This was not seen in the results from the CFD models in the ambient case. It is possible that this dip may be associated with the wake of the stanchion from T_{UP} rather than the influence of the stanchion of T_{DOWN}. The upstream stanchion wake may persist further downstream, especially for the SBES case, causing the larger fluctuation in the measured data. This is not as obvious in the experimental results.

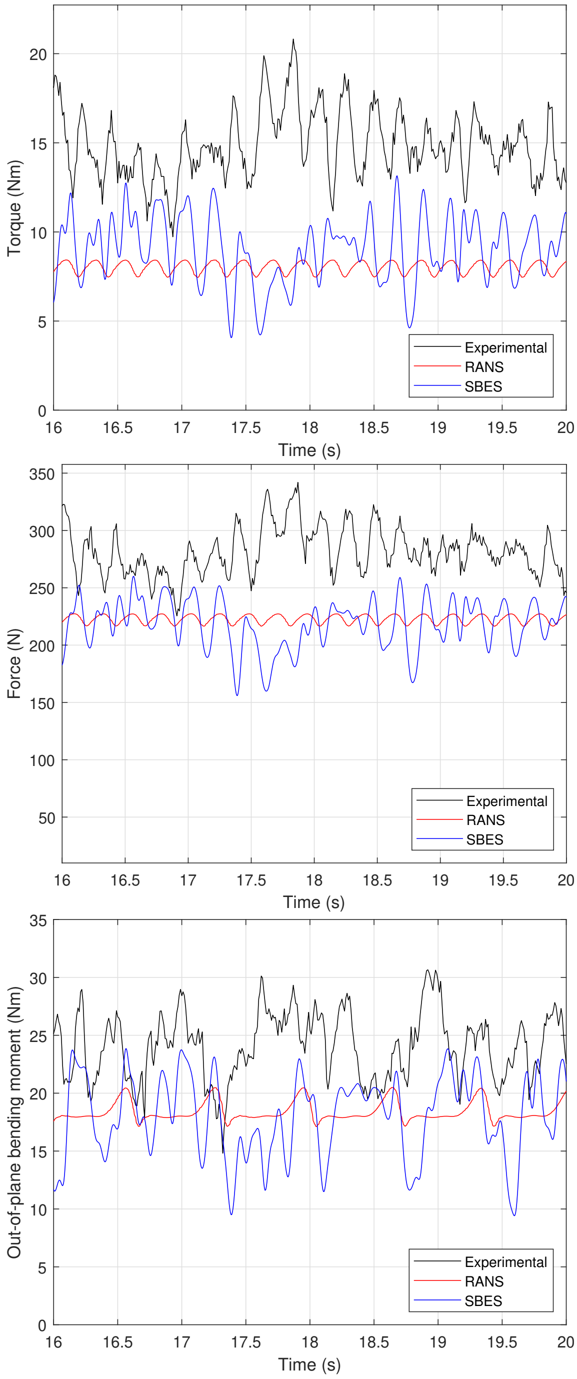

Figure 6.21: Comparison of the time series for the torque, thrust and out-of-plane bending moment for the in-wake case.

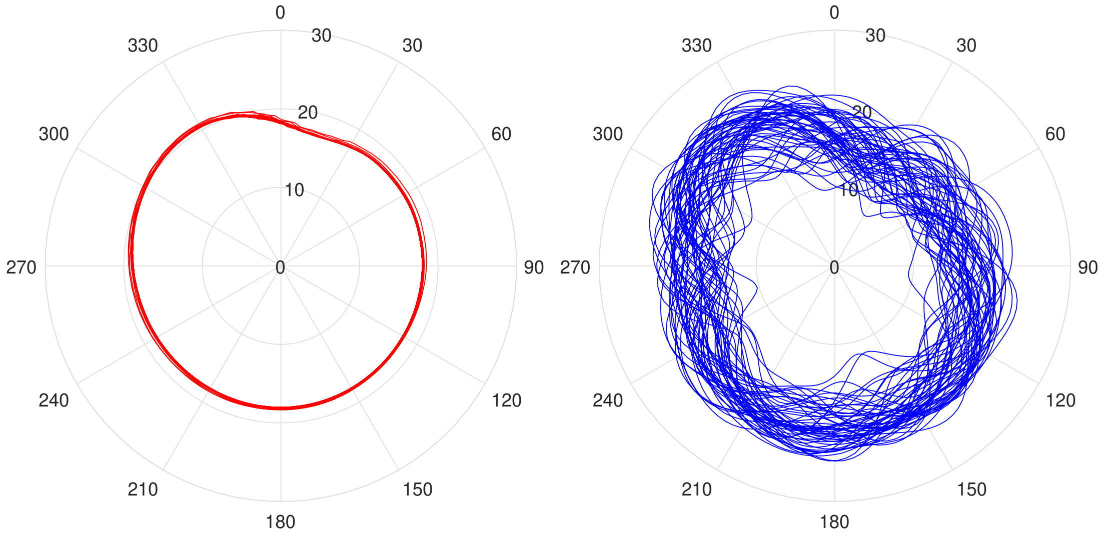

(a) RANS SST-kω model.

(b) SBES model.

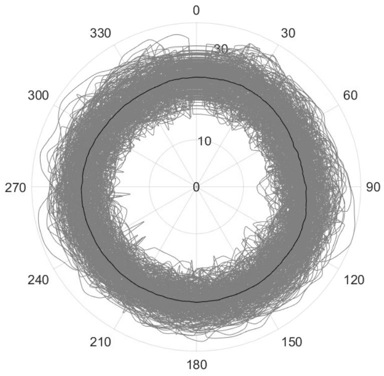

(c) Experimental testing.

Figure 6.22: Out-of-plane bending moment for one blade over the full time series for the in-wake case.

6.3.3.3 Offset-wake case

As with the ambient and in-wake cases, the fluctuations in the experimental values of torque, thrust and bending moment have higher amplitudes as seen in Figure 6.23. The high frequency fluctuations associated with the turbulence are also present in the experimental results and not the CFD. The RANS model shows a continuous uninterrupted sinusoidal wave. The drop in the torque and thrust as the blade passes through the wake is consistent. As the wake of T_{UP} in the SBES model is treated as LES the resolved turbulence in the flow has a greater influence on the blade performance. There is more variation in the predicted torque and thrust generation, however there is still a clear and obvious reduction in the performance as it passes through the wake.

The influence of the wake of T_{UP} is clearly visualised in the polar plots for the out-of-plane bending moment for an individual blade, shown in Figure 6.24. There is $\approx 25\,\%$ drop in the instantaneous bending moment values as the blade passes through the wake. The size of the fluctuations are also increased for the CFD simulation when using SBES.

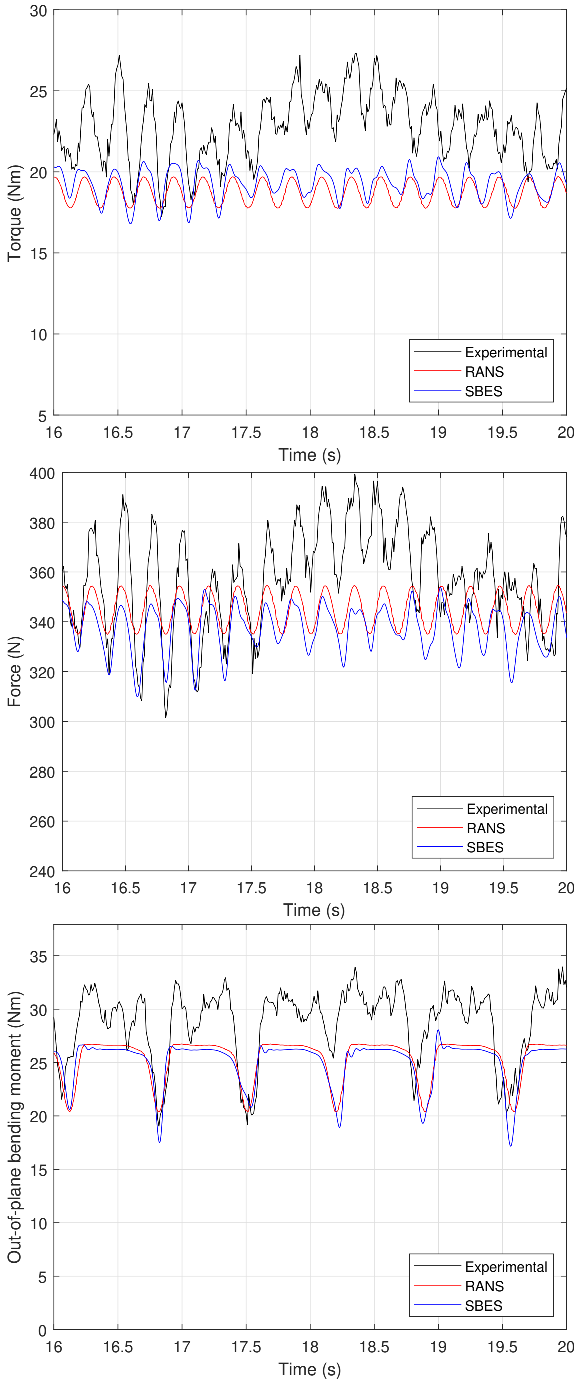

Figure 6.23: Comparison of the time series for the torque, thrust and out-of-plane bending moment for the offset-wake case.

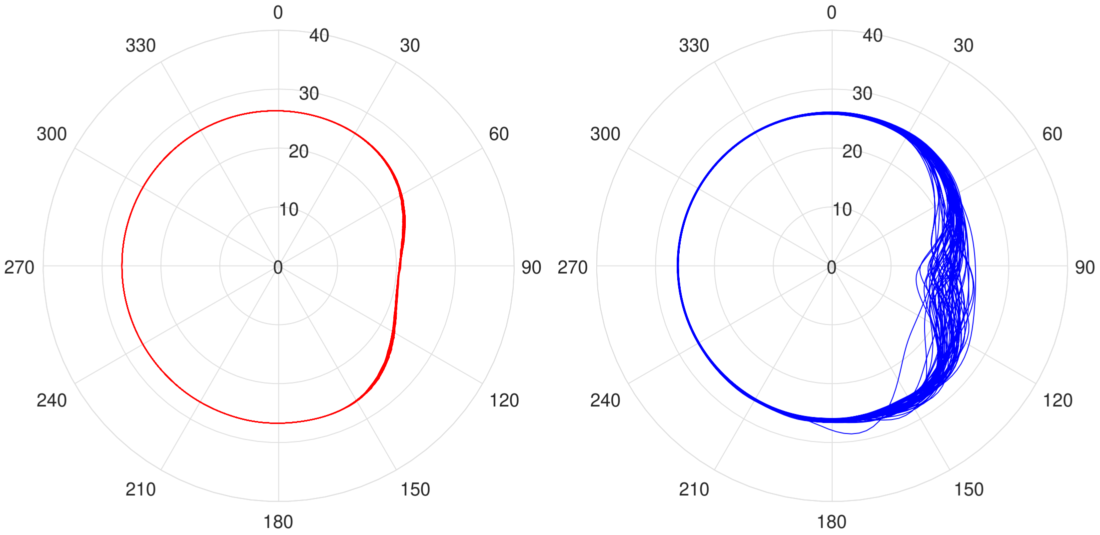

(a) RANS SST k-ω model.

(b) SBES model.

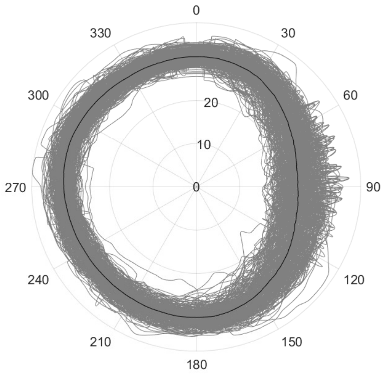

(c) Experimental testing.

Figure 6.24: Out-of-plane bending moment for one blade over the full time series for the offset-wake case.

6.3.4 Power spectral density

The power spectral density for the bending moment on one blade was plotted for each of the three cases. The power spectral density plots are used here to give a better understanding of the dominant frequencies in the results and how these frequencies relate to the turbine rotation and the turbulence.

6.3.4.1 Ambient case

The power spectral density for the ambient case is shown in Figure 6.25. Both the RANS and the SBES model under predict the maximum amplitude of the blade passing frequency compared with the results from the experimental tests. Not only that but the increase in the amplitude of the harmonics of ω_t highlight the lack of resolved turbulence at both the low and high frequencies. There is less energy in the CFD models as there is a lack of resolved ambient turbulence upstream of the device. As the energy is lower throughout the the CFD models there are clear and obvious spikes corresponding to the harmonics of ω_t.

The amplitude of the blade passing frequencies is not much greater than that of the low frequency range and the inertial sub range of the power spectral density of the bending moment for the experimental testing. There is high power in the low frequency range and inertial sub range of the power spectral density of the bending moment.

Rather than seeing a rapid dissipation in the power spectral density of the bending moment at the higher frequencies, it is observed that the power spectral density of the bending moment from the low to high frequencies is generally lower than the experimental. The sudden dissipation that is present and discussed for the in-wake and offset-wake cases is not present.

The amplitude of the low frequency turbulence is certainly smaller in the CFD models than that of the experimental. This points either to an inability to accurately represent the turbulence at the inlet of the domain despite the specification of the turbulence length scale and intensity, or the fact that the resolved turbulent quantities dissipate quickly in RANS regions (ie. the inlet).

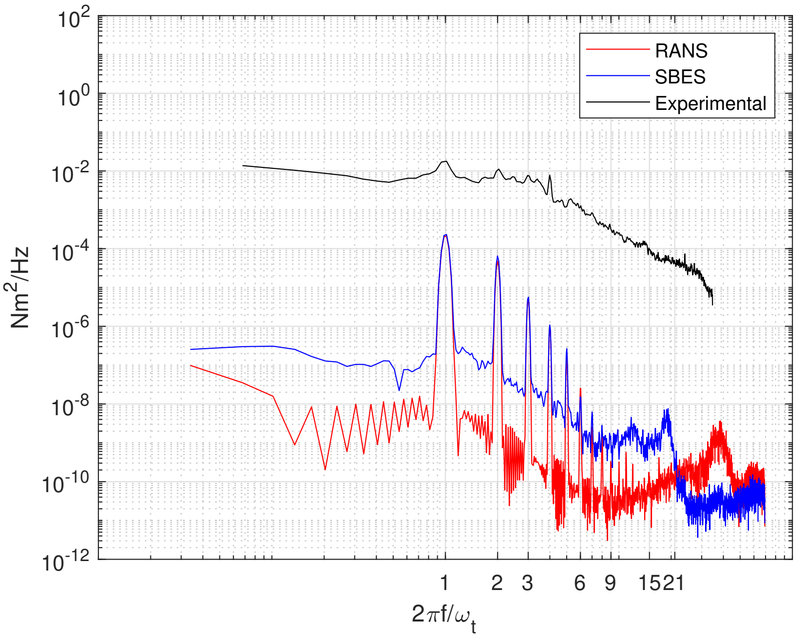

Figure 6.25: Power spectral density bending moment for the ambient case.

6.3.4.2 In-wake case

The power spectral density for the in-wake case is shown in Figure 6.26. As T_{DOWN} is located directly downstream of T_{UP} the onset flow is highly turbulent and the flow velocity is lower than the of the far upstream flow. The RANS model under predicts the amplitude of the harmonics of ω_t. There is good agreement between the amplitude of the blade passing frequency for the SBES and experimental results, however the main levels in the SBES model are much lower. Despite the device being fully within the wake of the T_{UP}, a region of high turbulence, the harmonics of ω_t are dominant when compared with the power spectral density of the bending moment until all but the highest frequencies. Given the turbulence in the wake it would be expected that the inertial sub range would have a higher power. This is seen in both the SBES and experimental models as beyond 3 times the blade passing frequency the power spectral density of the bending moment is more dominant.

As the frequency increases the rate of dissipation in the SBES model increases when compared with the experimental data. One hypothesis for this is that as the boundary layer is treated by RANS the turbulence in the flow is no longer being resolved in the boundary layer. The high frequency fluctuations are no longer being resolved and are instead modelled, giving rise to the rapid dissipation. This can also be seen in the time series of the torque, thrust and bending moment when the curves for the CFD models are smooth. The high frequency fluctuations associated with the smaller scale turbulence are clearly visible in the experimental measurements but not in the CFD.

As the device is in the wake the velocity fluctuates dramatically as seen in the flow analysis. Therefore, there is a much greater variability in the rotational speed of T_{DOWN} in the experimental testing. This is seen by the wider range of frequencies for one and two time the blade passing frequency.

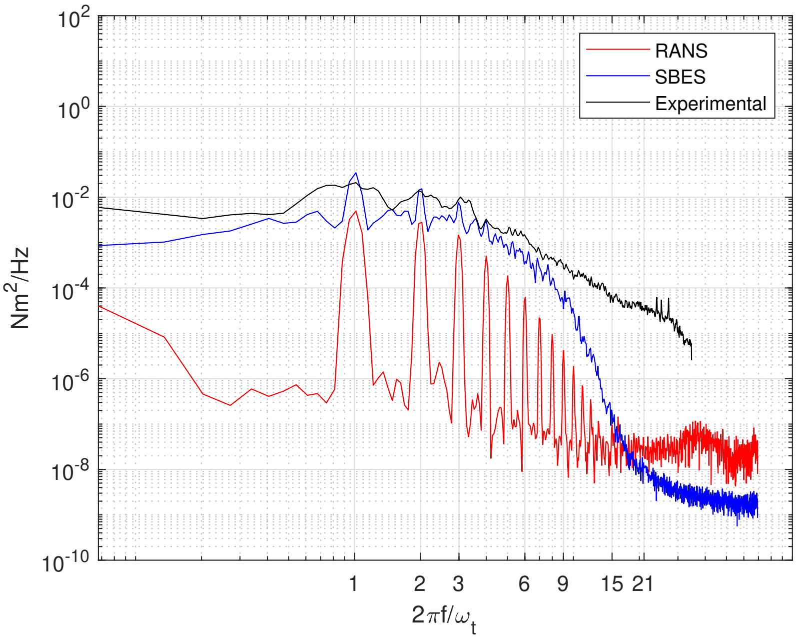

Figure 6.26: Power spectral density bending moment for the in-wake case.

6.3.4.3 Offset-wake case

The power spectral density for the offset-wake case is shown in Figure 6.27. The maximum amplitude of the blade passing frequency is similar for both the CFD models however the experimental case is an order of magnitude higher. It is possible that there was greater wake meander in the experimental testing causing the greater amplitude. The CFD model has a clearly defined wake region with very little wake meander as shown in Section 6.3.1 when looking at the onset flow.

The rate of dissipation seems to dramatically increase in both the CFD models. The higher frequencies in the power spectral density of the bending moment dissipate very quickly. This is very similar to the in-wake case as discussed previously.

Beyond 3 times the blade passing frequency there is still noticeable amplitude at each of the harmonics of ω_t. This is not present in the experimental due to the higher power in the mid to high frequency range, which characterises the inertial sub range of the turbulence spectra.

The amplitude of the low frequency turbulence is certainly smaller in both CFD models, but especially so in the RANS model, compared to the experimental. The SBES model gives a better prediction for low frequency turbulence when compared to the experimental despite the upstream flow region and the boundary layer being treated a RANS. It again shows that while there is a small amount of turbulence dissipation downstream of the inlet, the unresolved turbulence is carried downstream and maintained until it is resolved in the LES regions of the SBES model.

The feedback loop in the control of the turbine means that there is a very slight delay in updating the rotational speed of the turbine. This leads to a small variation in the rotational speed during the experimental testing. The variation in the rotational speed is not present in the CFD models as the angular velocity is a fixed value throughout the simulation. The range of the blade passing frequency is again similar is all cases despite this slight variation in the rotor speed.

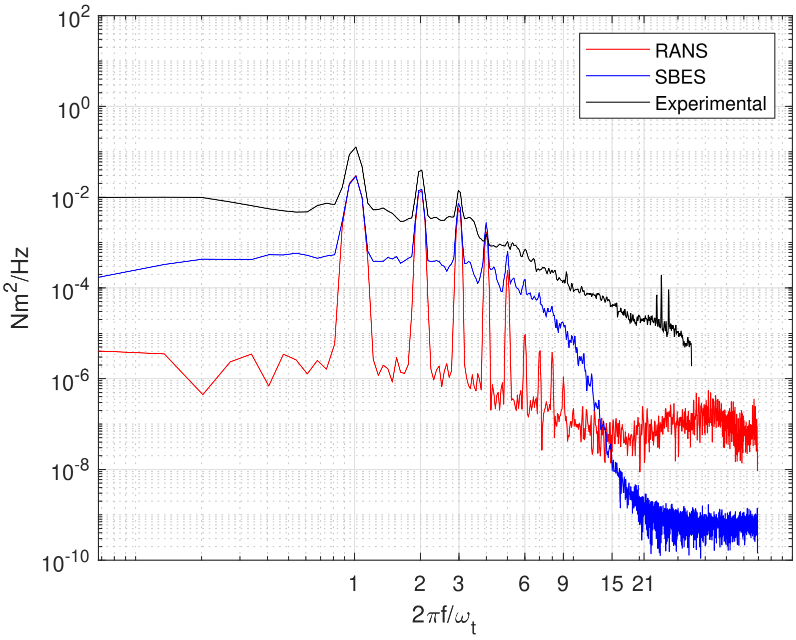

Figure 6.27: Power spectral density bending moment for the offset-wake case.

6.3.5 Non-dimensional performance coefficients

The performance coefficients for each of the three cases are presented below. The methods described in previously when characterising the onset flow in Section 6.3.1 are used here. For all cases the coefficients have been given for each of the methods for the calculation of the velocity. The only exception being that the volumetric average has not been calculated for the ambient case due to a lack of flow measurements and so a single point measurement is assumed to represent a fully uniform velocity. As the CFD model was geometrically similar to the experimental testing no blockage correction has been applied. The results have been calculated using Equations 3.7 - 3.10. The C_{BM} is for a single blade only, as only one blade measurement was available from the experimental testing. The loading is expected to be similar for all three blades, however to avoid giving a false representation of the bending moments, it was only calculated based on a single blade.

The flow velocity found and corresponding TSR has also been included for methods 1, 2 and 5. The flow was cubed and squared in method 3 prior to the averaging and all flow velocities were used in method 4.

Ambient case

The largest difference in the prediction of the performance coefficients for the RANS model is 6 % and that is for the C_P, Table 6.6. It is the only term that uses the cubic velocity and so it is more sensitive to the selection. Due to the steady nature of the flow, as seen previously in the Section 6.3.2, there is no fluctuation in the monitor point 1 m upstream of the device and so methods 1, 3 and 4 all give the same value. Using method 2 the C_P drops. As there is a blockage effect from the device, the flow velocity seen by the device is lower than the value found prior to turbine installation. Method 5 uses a larger number of points across the face of the turbine and catches some of the faster flow region that is accelerated around the turbine due to the blockage hence why the values are lower than a single point measurement.

As the monitor points are in the RANS region of the flow for the SBES model, the trends in the results are the same, see Table 6.7. Again, the maximum percentage difference is found between methods 2 and any of 1, 3 and 4 for the C_P. One obvious difference between the RANS and SBES models is that the values for C_P, C_Q and C_{BM} are higher than the RANS model. This is in keeping with the mean values of the measured data displayed in Section 6.3.3.

The experimental results in Table 6.8 show less continuity between each of the methods due to the increased turbulence in the flow with the greatest percentage difference being 30 % between methods 2 and 4. For methods 1, 3 and 4 the performance coefficients are greater than Betz limit. This is obviously down to the selection of the velocity rather than Betz limit being exceeded. Singular point measurements are obviously not suitable when trying to give the non-dimensional performance of a device in highly turbulent flow, however, single or, at best two, point(s) are likely to be available for full scale deployed devices.

The best match between the CFD and experimental results comes from method 2 which uses the flow measurement found during tank characterisation. As the ambient case is representing a device that is placed in a region where the flow is uninterrupted by an upstream device it gives the most realistic representation of the turbine operation. The other methods used are not such a problem for the CFD models but for the experimental results the performance coefficients seem artificially high. Method 5 was not used as there were not enough measurements taken at the rotor plane prior to turbine installation to provide an accurate estimation for the volumetric average.

Table 6.6: Performance coefficients for the RANS model for the ambient case.

Method	C_P	C_T	C_Q	C_{BM}	U $ms^{-}1$	TSR
1	0.535	1.08	0.131	0.183	1.00	4.1
2	0.505	1.03	0.136	0.177	1.02	4
3	0.535	1.08	0.131	0.183	-	-
4	0.535	1.08	0.131	0.183	-	-
5	0.529	1.07	0.130	0.182	1.01	4.1

Table 6.7: Performance coefficients for the SBES model for the ambient case.

Method	C_P	C_T	C_Q	C_{BM}	U $ms^{-}1$	TSR
1	0.542	1.05	0.133	0.180	1.00	4.1
2	0.512	1.01	0.128	0.173	1.02	4.0
3	0.542	1.05	0.133	0.180	-	-
4	0.542	1.05	0.133	0.180	-	-
5	0.536	1.04	0.132	0.178	1.00	4.1

Table 6.8: Performance coefficients for the experimental testing for the ambient case.

Method	C_P	C_T	C_Q	C_{BM}	U $ms^{-}1$	TSR
1	0.673	1.16	0.131	0.212	0.957	4.3
2	0.555	1.02	0.136	0.187	1.02	4.0
3	0.625	1.14	0.131	0.210	-	-
4	0.790	1.26	0.131	0.230	-	-
5	-	-	-	-	-	-

In-wake case

For the in-wake case using a single measurement does not give a realistic representation of the turbine performance for either the RANS or the SBES model. This can be seen by looking at the values for methods 1, 3 and 4 in Tables 6.9 and 6.10. The C_P values found are considerably greater than one. The flow velocity captured by the monitor point 1 m upstream of T_{DOWN} is clearly not what is being seen by the device. The value used in the calculations is much lower than the flow velocity at the rotor.

This is also a problem for the experimental data, shown in Table 6.11, but the results are not as exaggerated as they are for the CFD model. Clearly using methods 1, 3 and 4 for highly turbulent region is not suitable for the performance prediction of a downstream device.

Method 2 gives an indication as to the device performance in relation to all the other devices in an array as the same flow velocity is used. This would allow a global array performance coefficient to be determined but it wouldn't necessarily be very informative with regards to the performance of the specific device based on the flow it is seeing.

Using the volumetric average allows more of the flow profile to be taking into consideration. The volumetrically average wake recovery study in Chapter 5 showed good agreement between the CFD and the experimental results. This is also the case for the non-dimensional performance coefficients. The best agreement is seen for method 5, however there is still a maximum percentage difference of 33 % between the SBES and experimental values shown in Tables 6.10 and 6.11.

The experimental flow velocity was found using the measurements taken at the rotor plane prior to the turbine installation rather than 1 m upstream. The flow velocity would further recover between the location of the monitor points (5D) and the turbine rotor (7D). The RANS model drastically under predicts the wake recovery and so there would be minimal change in the flow velocity between 5D and 7D hence why the performance coefficients are in better agreement with the experimental values.

Table 6.9: Performance coefficients for the RANS model for the in-wake case.

Velocity method	C_P	C_T	C_Q	C_{BM}	U ms^-1	TSR
1	11.9	9.77	0.783	1.79	0.269	15.2
2	0.217	0.677	0.054	0.124	1.02	4.0
3	11.9	9.77	0.783	1.79	-	-
4	11.9	9.77	0.784	1.79	-	-
5	0.465	1.12	0.090	0.206	0.791	5.16

Table 6.10: Performance coefficients for the SBES model for the in-wake case.

Velocity method	C_P	C_T	C_Q	C_{BM}	U ms^-1	TSR
1	17.1	11.27	1.04	2.08	0.249	16.4
2	0.247	0.669	0.062	0.123	1.02	4.0
3	12.8	10.18	0.939	1.88	-	-
4	40.1	16.77	1.55	3.09	-	-
5	0.624	1.242	0.114	0.229	0.749	5.45

Table 6.11: Performance coefficients for the experimental testing for the in-wake case.

Velocity method	C_P	C_T	C_Q	C_{BM}	U $ms^{-}1$	TSR
1	1.46	2.03	0.137	0.383	0.66	6.18
2	0.397	0.85	0.099	0.161	1.02	4.0
3	1.32	1.96	0.229	0.370	-	-
4	1.84	2.27	0.265	0.429	-	-
5	0.418	0.879	0.103	0.166	0.951	4.29

Offset-wake case

As with the ambient case the monitor point 1 m stream was in the RANS region for both the CFD models. Therefore, there is almost no variation in the non-dimensional coefficients for methods 1, 3 and 4, as shown by the results in Tables 6.12 and 6.13. Due to the flow acceleration around T_{UP} using the method 2 gives a higher performance value as the flow velocity is greater than that measured prior to turbine installation for both the CFD and experimental values.

Throughout the rotation of T_{DOWN} each blade passes through the wake of T_{UP}. Method 5 used an estimation of the wake diameter to determine the angle that the blade passed through. The total area of the wake that the blade passed though was then found. The volumetric average was done for the region where the turbine passed through the wake and did not pass through the wake. While this was considered when finding the experimental volumetrically averaged flow, the measurement prior to turbine installation were again used.

The CFD results for method 5 are higher that any of the other methods used for the CFD results by up to 25 %. This may mean that the estimation of the wake width, and therefore the area the blade passed through was over estimated, causing the volumetrically averaged flow velocity to be lower than was seen by the device.

The experimental results in Table 6.14 for methods 1, 3 and 4 are lower than the values for the ambient case using the same method. The flow measurement is taken further downstream and the velocity profile may be more uniform at this location, rather than directly downstream of the grid. This is backed up by the reduced TI value for the offset-wake case compared to the ambient case calculated in Section 6.3.2.

Table 6.12: Performance coefficients for the RANS model for the offset-wake case.

Velocity method	C_P	C_T	C_Q	C_{BM}	U ms^-1	TSR
1	0.496	1.03	0.125	0.172	1.03	4.0
2	0.505	1.05	0.126	0.174	1.02	4.0
3	0.496	1.03	0.125	0.172	-	-
4	0.496	1.03	0.125	0.172	-	-
5	0.654	1.24	0.150	0.204	0.936	4.4

Table 6.13: Performance coefficients for the SBES model for the offset-wake case.

Velocity method	C_P	C_T	C_Q	C_{BM}	U ms^-1	TSR
1	0.499	0.996	0.126	0.167	1.03	3.9
2	0.518	1.02	0.129	0.171	1.02	4.0
3	0.499	0.996	0.126	0.167	-	-
4	0.500	0.996	0.126	0.167	-	-
5	0.700	1.24	0.158	0.204	0.922	4.4

Table 6.14: Performance coefficients for the experimental testing for the offset-wake case.

Velocity method	C_P	C_T	C_Q	C_{BM}	U ms^-1	TSR
1	0.551	0.960	0.135	0.172	1.03	3.9
2	0.600	1.07	0.150	0.192	1.02	4.0
3	0.498	0.952	0.134	0.171	-	-
4	0.540	0.988	0.139	0.177	-	-
5	0.500	0.947	0.133	0.170	1.08	3.8

Comparison with experimental testing from Acre Road

A final comparison for C_P and C_T found using method 5 and the experimental data recorded during the Acre Road testing is made and can be seen in Figures 6.28 and 6.29. The TSR for each case has been found based on the flow velocity used to calculate the non-dimensional performance coefficients. For the ambient flow case method 5 was not used for the experimental results due to a lack of suitable flow measurements and so no value is given.

The CFD modelling for all three cases both over predicts the performance coefficients and the TSR when compared with the data from Acre Road. The experimental testing from the three cases shows better agreement with the Acre Road data than the CFD. As has already been shown the flow velocity being used to calculate the C_P, C_T, and TSR for the CFD is lower than that of the experimental results hence why there is a greater discrepancy. Based on the differences in the results it is clear that for the CFD method 5 does not give comparable results to a turbine in a well-defined uniform onset flow such as that at Acre Road. As the agreement is better for the experimental the CFD error is due to the inability of the CFD to accurately model the onset flow, specifically for the in-wake and offset-wake cases.

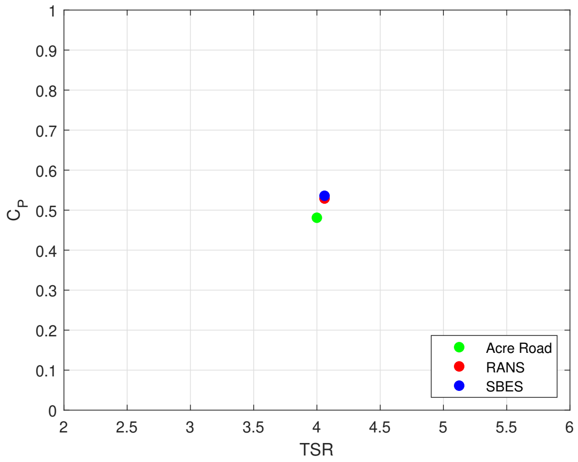

(a) Ambient case.

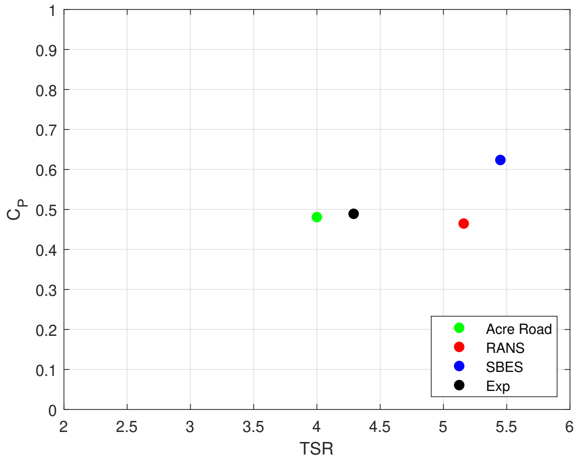

(b) In-wake case.

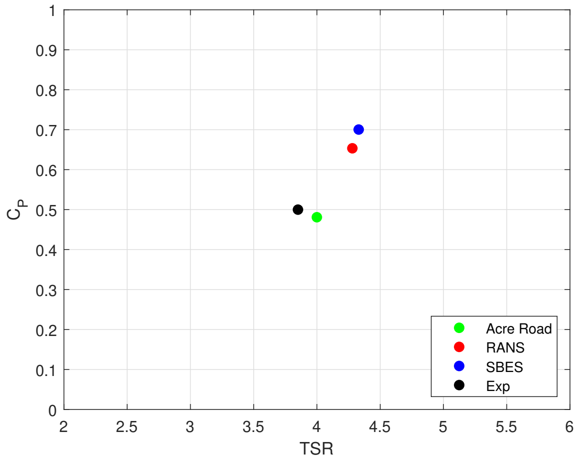

(c) Offset-wake case.

Figure 6.28: Comparison of C_P for the Acre Road test results and the performance coefficients found using method 5. TSR is calculated based on the flow velocity used for the non-dimensional performance coefficients.

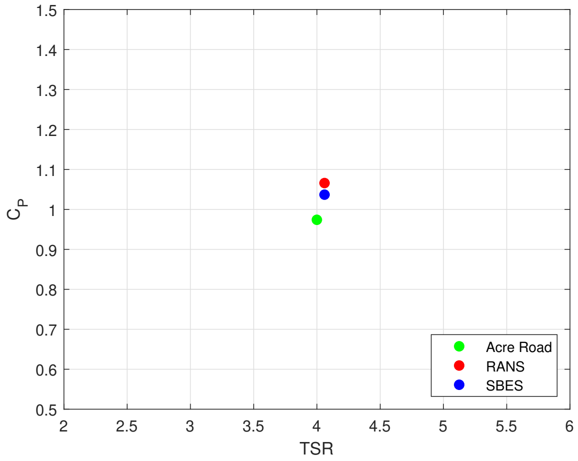

(a) Ambient case.

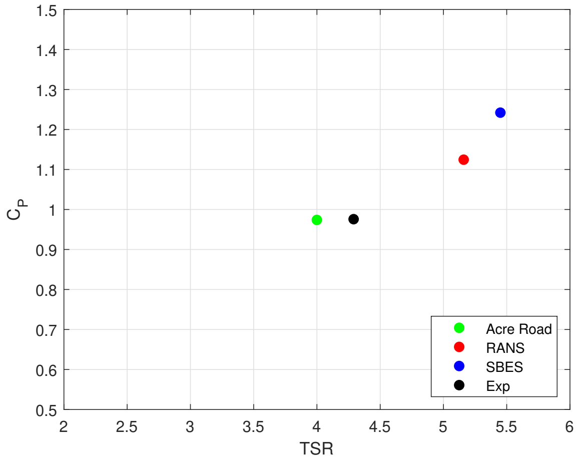

(b) In-wake case.

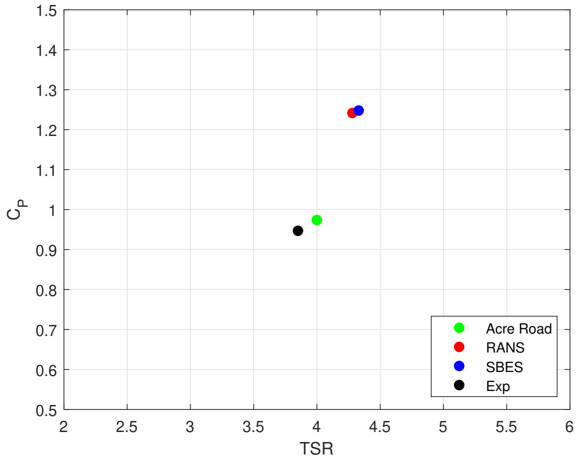

(c) Offset-wake case.

Figure 6.29: Comparison of C_T for the Acre Road test results and the performance coefficients found using method 5. TSR is calculated based on the flow velocity used for the non-dimensional performance coefficients.

6.3.6 Power comparison

In reality a single or, at best two, point(s) are likely to be available for full scale deployed devices and therefore calculating the volumetrically averaged flow is not possible. Even when looking at lab-scale devices the time available for testing is finite, ultimately limiting either the number of measurements that can be taken or the time over which they are taken.

Method 2, using the global flow velocity, provides a useful way to understand the performance of multiple devices relative to the far upstream flow speed and therefore the first row of devices. A singular array power coefficient could be generated using the far upstream velocity however, it gives little information on the performance of a specific device based on the flow it is seeing.

The in-wake case showed the problem when using a singular point measurement to determine the device performance, methods 1, 3 and 4, for turbulent flows. The performance coefficients were highly unrealistic. This means that for this specific case a single point upstream was not informative enough to provide detail about the flow regime over the swept area of the rotor for a turbulent flow, when looking at the non-dimensional performance coefficients. Given most flows will have a velocity profile and be turbulent in nature a more complete characterisation of the flow seems prudent.

The defining factor for the accurate calculation of the non-dimensional performance coefficients is the understanding of the flow regime upstream of the rotor. Using a single flow velocity, as used in Chapter 4, is viable when the there is no velocity profile or turbulence. This is one of the benefits of using a tow tank to characterise device performance.

Based on the results from all of the methods used to calculate the flow velocity for all three cases using the non-dimensional performance coefficients for a downstream device or device within an array may not be suitable. Instead, using the power generated by the device removes the dependency of the turbine performance characteristics on the flow velocity.

For the characterisation of lab-scale devices the power generated can then be compared back to the power generated by the same device in a clean flow, ie. one without turbulence or velocity profile. This will give an indication as to the how the location of the device influences its performance based on a change in the power, thrust, torque and bending moment. In using the power the performance of downstream devices, or devices within an array can all be compared to one another without the flow velocity artificially increasing or decreasing the performance coefficients as was seen previously.

Figure 6.30 shows the mean power and the associated standard deviation for each of the three cases for both experimental and CFD models.

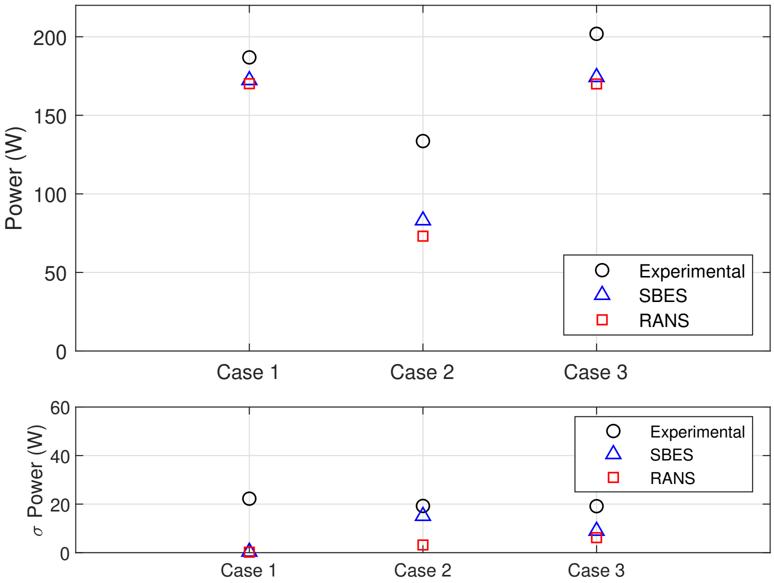

Figure 6.30: Comparisons of the mean power and the standard deviations for the ambient, in-wake and offset wake cases.

The highest power from the experimental testing was when T_{DOWN} was placed in the accelerated flow region for the offset-wake case. Interestingly, it also has the smallest standard deviation despite the interaction of the wake of T_{UP}. The fluctuation in the mean power as characterised by the standard deviation is less than 10 % for the offset-wake case and is ≈ 12 % for the ambient case. There is a reduction in the magnitude of the fluctuations around the mean power seen for T_{DOWN} compared to when T_{DOWN} is placed directly downstream of the turbulence generating grid in the ambient case.

For both the SBES and the RANS models the power from the ambient and offset-wake cases are within 2 % of each other. This is not surprising based on what has been seen in the flow analysis and the values for the mean torque. The fluctuation in the mean power as characterised by the standard deviation is greater for the offset-wake case than the ambient case at 5 % and 3 % for the SBES and RANS models respectively. DES modelling relies on the introduction of turbulence into the flow field due to flow interaction with a physical object. In the ambient case both the CFD models there is no physical body generating turbulence upstream of the device and so the standard deviation is 0. Despite the downstream device being largely out of the wake of T_{UP} in the offset-wake case there is enough overlap to cause a greater fluctuation in the measurements, hence the larger standard deviations.

For the SBES model the normalised power from the offset-wake case is higher than the ambient case. This is in agreement with the experimental results showing that the flow acceleration around T_{UP} has a positive affect on the performance of T_{DOWN}.

As expected the in-wake case has both the lowest normalised power and the highest standard deviation for both the experimental and the SBES model. The fluctuation in the mean power as characterised by the standard deviation is 15 % and 18 % for the experimental and CFD models respectively. Placing a device directly downstream of another leads to a reduced power output and increased fluctuations. It is obvious from this work that having two devices aligned by the rotational axis at a longitudinal spacing of 7D is not beneficial to the global array output or life expectancy. With an increased longitudinal spacing then the power may increase and the standard deviation decrease, however the spatial requirements of the array are then increased.

The mean values of the torque, thrust and bending moment have also been included for completeness when discussing the performance of a downstream device. The trend for the mean torque values shown in Figure 6.31 is the same as the power as the mean angular velocity for the CFD and experimental results was the same in all cases.

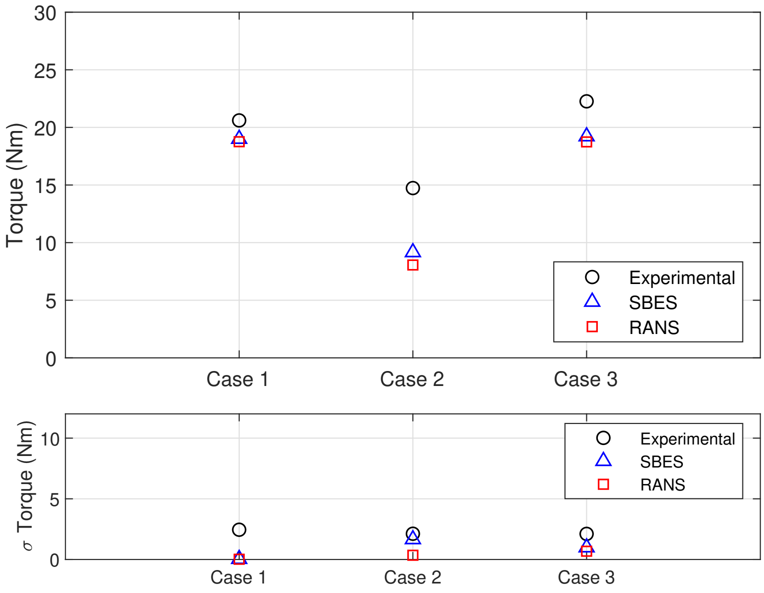

Figure 6.31: Comparisons of the mean torque and the standard deviations for the ambient, in-wake and offset wake cases.

The thrust comparison shown in Figure 6.32, is within 5 % of the experimental results for the ambient and offset-wake cases showing good prediction for the thrust loading by both RANS and SBES for those cases. The standard deviation in both CFD models for the ambient and offset-wake cases is under predicted due to the lack of turbulence resolution in that flow region. For the in-wake case the thrust predictions are within 22 % of the experimental results. The SBES model gives a good prediction for the standard deviation in the in-wake case despite under predicting the mean value.

While the percentage difference in the thrust for the in-wake case is greater than desired it highlights how greatly the prediction of the torque and thrust in the CFD model differs when modelling a turbine in turbulent flow. This could be to do with the mesh quality around the blade and the mesh may need further refinement to capture the flow around the blade as the complexity of the flow regime increases. This results in a reduced prediction for the lift force on the blade.

Figure 6.33 shows the mean values of for the blending moment for a single blade. For the ambient case the bending moment falls within 8 % of the experimental results. The in-wake and offset-wake cases under predict the bending moment and the difference is greater than 20 % for both cases. The torque, thrust and bending moment comparisons confirm what was found during the power comparison.

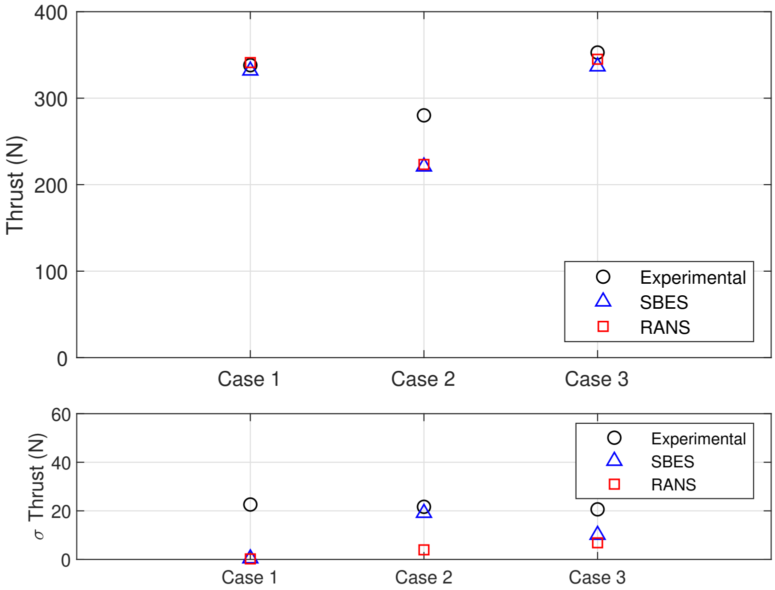

Figure 6.32: Comparisons of the mean thrust and the standard deviations for the ambient, in-wake and offset wake cases.

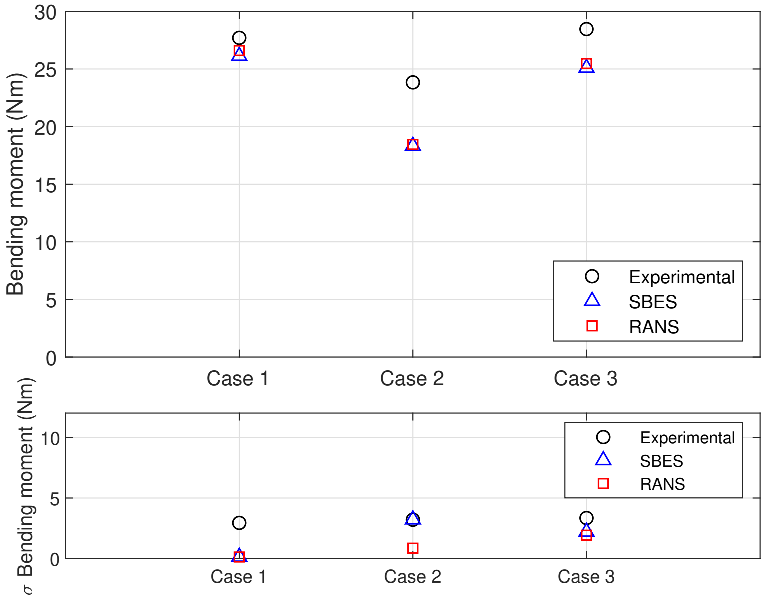

Figure 6.33: Comparisons of the mean bending moment and the standard deviations for the ambient, in-wake and offset wake cases.

6.4 Summary

To study the performance of a downstream device three cases were tested at the IFREMER flume tank and subsequently modelled using ANSYS CFX. The CFD methodology was based on the findings from Chapters 4 and 5. Both the devices modelled in Chapters 4 and 5 were used in the testing. T_{UP} was used purely to generate the wake, the performance of this device was not of interest. T_{DOWN} was operating at peak power, TSR 4. The inlet flow velocity was $1.02\,\mathrm{m\,s^{-1}}$ and the inlet turbulent length scale was $0.27\,\mathrm{m}$. These values were based on the flume characterisation prior to turbine installation.

The flow measurements and the rotor data were compared for each of the three cases between the experimental and CFD models. For the ambient and offset-wake cases the CFD models showed good agreement with the experimental results for the mean flow velocity. The resolved turbulence intensity was under predicted as the monitor points were in the RANS region of the flow even for the SBES model. In the in-wake case the CFD models under predicted all measured variables, except the TI for the SBES model, compared to the experimental.

The power spectral density plots were used to determine the dominant frequencies in each of the Cases. The CFD had a higher rate of dissipation in the turbulence spectra in the high frequency region.

A comparison of the non-dimensional performance coefficients was made. The flow velocity was found using five methods. The influence that the flow velocity had on the performance coefficients was clear, especially for the in-wake case. The values were artificially high or low depending on how far the value used was from the actual flow velocity seen by the device. Finally a comparison of the mean characteristic values for each case was compared to see how the device performance changed based on its location in the flume.

One of the fundamental issues for the in-wake and offset-wake case is the modelling of the wake upstream of T_{DOWN}. The modelling in Chapter 5 showed that at the same location downstream the wake deficit was not directly comparable. At 7D downstream the wake recovery was within $10\,\%$ for the SBES and experimental results. The SBES model showed good agreement with the experimental results for the in-wake case when predicting the standard deviation of the the torque, thrust and bending moment. This shows the suitability of a hybrid RANS-LES model when trying to capture the fluctuation in measured values when the device is located in the LES region. The same was not seen for the ambient and offset-wake cases.

It might be necessary to use full LES simulations to fully capture device interaction if more than the mean values are of interest, however this falls outside the scope of this work and so was not looked at.

Chapter 7

Conclusions

The work undertaken throughout this thesis was done with the purpose of fulfilling the aims and objectives of this thesis outlined in Chapter 1.5. This Chapter provides a summary of the outcomes of the thesis as well as recommendations for further work.

7.1 Blade design and turbine performance

The first objective was to design a new HATT blade using a combination of two numerical methods, that could be used for lab-scale testing. This was done through the use of the BEMT and CFD. The design was selected from a number of alternative geometries each defined by the radial variation of pitch and the chord length. There was good agreement between the CFD and steady BEMT, especially over the desired operating region, highlighting the suitability of such numerical methods for the design of HATT blades.

The validation of the CFD model was based on the ability to predict the three performance coefficients; C_P, C_T and C_Q. Three flow velocities were considered to study the influence of Reynolds number. It was found that for this device at flow speeds greater than $0.8\,\mathrm{m\,s^{-1}}$ the performance of the device was independent of Reynolds number in both the experimental and CFD results. No flow velocities below $0.8\,\mathrm{m\,s^{-1}}$ were tested.

There was good agreement between the CFD and the experimental predictions for the performance coefficients at the proposed operating region of the curve, TSR 3-5. The CFD C_P and C_T results were within 4 % and 6 % respectively of the experimental data at peak power. The ability of the CFD model to capture the high TSR region close to freewheeling was limited, and the lift was under predicted over the blade, leading to a lower

C_P value. This shows the suitability of the RANS SST k-ω for modelling the performance of the proposed operating region of a HATT.

7.2 Influence of discretisation scheme on turbine modelling

7.2.1 Rotor performance

When using a hybrid turbulence model the choice of discretisation scheme had negligible effect on the performance prediction of a HATT. The values for C_P, C_T and C_Q were all within 3 % of each other. The use of the SST k-ω turbulence model in the boundary layer gives similar predictions for all CFD models despite the use of either a first- or second-order upwind scheme.

7.2.2 Wake modelling

The influence of the discretisation scheme and turbulence model on the modelling of a turbine wake for high and low inlet turbulence was studied. The methodology was based on previous work. Experimental testing was used to provide validation. When it comes to the modelling of turbulence the SBES model gave a better prediction for the recovery of the wake compared to either the DES or SST k-ω turbulence models. The switch from RANS to pure LES was improved and was the preferred model for modelling the wake.

The RANS SST k-ω model does not resolve the turbulence in the flow directly. This leads to an under estimation of the magnitude of the fluctuations in a turbulent flow. The SBES turbulence model is a more suitable tool to model turbulent flows based on comparisons with experimental data for the wake. The RANS SST k-ω model was found to give good prediction for rotor performance, in keeping with previous studies.

The selection of the discretisation scheme had a large influence on the centreline velocity recovery. The bounded central difference scheme gave the best prediction of a turbine wake based on the flow recovery when compared to experimental data.

There was a noticeable improvement in the recovery of the wake for the higher inlet turbulence however the rate of wake recovery was very similar for both turbulence intensities tested beyond 5D, as discussed Section 5.3.3. This is in keeping with previous works that have studied wake recovery. Volumetrically averaged velocity recovery is a better metric for wake recovery over centreline recovery as it uses information from a greater number of measurements. There was good agreement between the SBES and experimental results for both high and low inlet turbulence intensities using this approach.

7.3 The performance of a downstream device

RANS modelling is not good where instantaneous fluctuation in the flow are present. The lack of turbulence resolution is a problem. The full effect of the turbulence is not captured however the mean values of the turbine performance are similar for the both RANS and SBES. However, the computational time may mean that using SBES or full LES is not practical and so for the modelling of arrays RANS may be a suitable tool to determine the mean performance of the devices.

The use of non-dimensional performance coefficients gives limited information into device performance within an array unless the flow regime has been fully and comprehensively characterised.

Based on the swept area of T_{DOWN} the volumetrically averaged flow shows nearly 100 % recovery at 7D downstream of T_{UP} when only T_{UP} was placed in the flume. However, despite seeing good wake recovery for a single turbine, the power output was reduced for a second device placed directly in the wake of an upstream device by almost 30 %. The standard deviation is also increased by a factor of ≈ 1.2 compared to when in a turbulent flow based on the experimental results.

When the downstream turbine was moved laterally and placed in the accelerated flow region the characteristic values were increased for both the experimental and the CFD results. The power output was increased by 8 % while the magnitude of the fluctuation was reduced by 20 % for the experimental results compared to a solitary device in the flow. The SBES model shows the same trend however the power increase was not as high. This acceleration of flow between devices can be exploited to inform array layout and maximise potential power extraction from arrays.

The C_P-TSR and C_T-TSR curves showed that the CFD gave results for both both C_P and C_T and the respective TSR than the experimental and for the same device placed in a uniform flow as discussed in Section 6.3.5.

7.4 Recommendations for further work

Throughout the work in this thesis possible opportunities for further work were highlighted. The mesh used for the CFD model when characterising the turbine captured the operating region well however work is required to improve the boundary layer mesh when trying to capture the high TSR region and peak torque region. Also for full characterisation of the device flow speeds lower than $0.8\,\mathrm{m\,s^{-1}}$ could be studied.

Further work must be done to study the CFD modelling of the near wake region behind a turbine. Due to both computational and time constraints the ability to run further tests on this region was limited. A comparison between a hybrid RANS-LES and full LES model should be run to see the influence of resolving the turbulence throughout the entire domain. Other methods for introducing more coherent turbulence structures at the inlet such as zonal LES or the use if a downstream plane from a previous simulation at the inlet should be tested.

To fully understand the influence of the accelerated flow region a greater number of downstream locations needs to be looked at to see if the power of second device can be improved further. Adding a third device into the CFD model is required to see how the performance of a downstream device changes. At the moment the flume wall provides blockage without added turbulence, a second upstream device may affect the performance of the downstream device. Finally the number of TSR values that were modelled for the device interaction need to be increased to get a better understanding of device performance over the full operating region.

The CFD studies using ANSYS CFX can help improve the modelling of a tidal turbine performance and wake for researchers going forward. The findings from the work conducted throughout this thesis could be used by developers to improve array power output of downstream devices while managing the loading of each of these devices.

References

[1] Valérie Masson-Delmotte, Panmao Zhai, H.O. Pörtner, Debra Roberts, Jim Skea, P.R. Shukla, Anna Pirani, Wilfran Moufouma-Okia, Clotilde Péan, Roz Pidcock, Sarah Connors, J.B.R Matthews, Yang Chen, Xiao Zhou, M.I. Gomis, Elisabeth Lonnoy, Tom Maycock, Melinda Tignor, and T. Waterfield (eds). *Global Warming of 1.5°C. An IPCC Special Report on the impacts of global warming of 1.5°C above pre-industrial levels and related global greenhouse gas emission pathways, in the context of strengthening the global response to the threat of climate change.* Tech. rep. 2018, 32 pp. DOI: `10.1017/CBO9781107415324`. arXiv: `arXiv:1011.1669v3`. URL: `http://www.ipcc.ch/report/sr15/`.

[2] United Nations. *The Paris Agreement — UNFCCC.* 2018. URL: `https://unfccc.int/process-and-meetings/the-paris-agreement/the-paris-agreement%20https://unfccc.int/process/the-paris-agreement/what-is-the-paris-agreement` (visited on 11/06/2019).

[3] DECC (Department of Energy and Climate Change). “UK Renewable Energy Roadmap Update 2013”. In: November (2013), p. 76. URL: `https://www.gov.uk/government/uploads/system/uploads/attachment%7B%5C_%7Ddata/file/255182/UK%7B%5C_%7DRenewable%7B%5C_%7DEnergy%7B%5C_%7DRoadmap%7B%5C_%7D-%7B%5C_%7D5%7B%5C_%7DNovember%7B%5C_%7D-%7B%5C_%7DFINAL%7B%5C_%7DDOCUMENT%7B%5C_%7DFOR%7B%5C_%7DPUBLICATIO%7B%5C_%7D%7B%5C_%7D%7B%5C_%7D.pdf`.

[4] UK Government. *PRESS NOTICE STATISTICAL PRESS RELEASE.* Tech. rep. 2019. URL: `www.gov.uk/government/statistical-data-sets/total-final-energy-consumption-at-regional-and-%20www.gov.uk/government/organisations/department-of-energy-climate-change/about/statistics`.

[5] renewable UK. *Wind Energy - RenewableUK.* 2017. URL: `https://www.renewableuk.com/page/WindEnergy` (visited on 10/29/2019).

[6] *Final turbine installed at ‘world’s largest’ offshore wind farm - Energy Live News.* URL: `https://www.energylivenews.com/2019/10/03/final-turbine-installed-at-worlds-largest-offshore-wind-farm/` (visited on 10/29/2019).

[7] The Crown Estate. *UK Wave and Tidal Key Resource Areas Project - Summary Report.* Tech. rep. October. 2012, pp. 1–10. URL: `https://www.thecrownestate.co.uk/media/5478/uk-wave-and-tidal-key-resource-areas-technological-report.pdf`.

[8] Peter Davies. “Turning the Tide: Tidal Power in the UK”. In: *The Severn Barrage and renewable energy in the estuary.* 2008. DOI: `10.1680/tsbareite.42100.0001`. URL: `www.sd-commission.org.uk/wales`.

[9] DECC (Department of Energy and Climate Change). “Severn tidal power - Feasibility Study Conclusions and Summary Report”. In: *October* October (2010), pp. 1–75.

[10] *La Rance Tidal Barrage — Tethys.* URL: `https://tethys.pnnl.gov/annex-iv-sites/la-rance-tidal-barrage` (visited on 11/13/2019).

[11] *Sihwa Tidal Power Plant — Tethys.* URL: `https://tethys.pnnl.gov/annex-iv-sites/sihwa-tidal-power-plant` (visited on 11/15/2019).

[12] Reza Ahmadian, Roger Falconer, and Bettina Bockelmann-Evans. “Far-field modelling of the hydro-environmental impact of tidal stream turbines”. In: *Renewable Energy* 38.1 (Feb. 2012), pp. 107–116. ISSN: 09601481. DOI: `10.1016/j.renene.2011.07.005`.

[13] *Interreg's biggest ever project approved — Interreg.* URL: `https://www.channelmanche.com/en/news-and-media/latest-news/interregs-biggest-ever-project-approved/` (visited on 10/29/2019).

[14] Timothy Ebdon. “The Impact of Turbulence and Turbine Operating Condition on the Wakes of Tidal Turbines”. In: (2019).

[15] SIMEC. *MeyGen — Tidal Projects — SIMEC Atlantis Energy.* 2018. URL: `https://simecatlantis.com/projects/meygen/` (visited on 10/18/2019).

[16] ORBITAL MARINE POWER. *Orbital Marine Power - the world leader in the development of floating tidal stream and run-of-river turbines.* 2018. URL: `https://orbitalmarine.com/technology-development/orbital-o2` (visited on 10/18/2019).

[17] *SABELLA's tidal turbines: tidal stream power to trigger the energy transition.* URL: `https://www.sabella.bzh/en` (visited on 02/11/2020).

[18] *PLAT-I Operational in Nova Scotia.* URL: `https://sustainablemarine.com/news/platipower` (visited on 10/18/2019).

[19] Minesto AB. *The future of renewable energy — Minesto.* 2017. URL: `https://minesto.com/our-technology` (visited on 10/18/2019).

[20] *How CoRMaT works - Nautricity.* URL: `http://www.nautricity.com/cormat/cormat-efficiency/` (visited on 10/23/2019).

[21] *The EEL Tidal Energy Converter and promising performance : Eel energy presentation.* URL: `https://www.eel-energy.fr/en/eel-tidal-energy-convertor/` (visited on 10/18/2019).

[22] *Verdant Power.* URL: `https://www.verdantpower.com/` (visited on 02/11/2020).

[23] *Tidal Turbines – ANDRITZ HYDRO Hammerfest.* URL: `http://www.andritzhydrohammerfest.co.uk/tidal-turbines/` (visited on 02/11/2020).

[24] *Proyecto Magallanes.* URL: `http://www.magallanesrenovables.com/en/proyecto` (visited on 02/03/2020).

[25] C. A. Douglas, G. P. Harrison, and J. P. Chick. “Life cycle assessment of the Seagen marine current turbine”. In: *Proceedings of the Institution of Mechanical Engineers Part M: Journal of Engineering for the Maritime Environment* 222.1 (2008), pp. 1–12. ISSN: 14750902. DOI: `10.1243/14750902JEME94`.

[26] Jessica M. Walker, Karen A. Flack, Ethan E. Lust, Michael P. Schultz, and Luksa Luznik. “Experimental and numerical studies of blade roughness and fouling on marine current turbine performance”. In: *Renewable Energy* 66 (June 2014), pp. 257–267. ISSN: 09601481. DOI: 10.1016/j.renene.2013.12.012.

[27] SIMEC Atlantis Energy. *Atlantis Successfully Decommissions 1.2 MW SeaGen Tidal System in Industry First.* 2019. URL: https://simecatlantis.com/2019/07/26/meygen-operational-update-3-2/ (visited on 10/18/2019).

[28] *Marine Current Turbines & SeaGen in the news - SMRU Consulting.* URL: http://www.smruconsulting.com/marine-current-turbines-seagen-in-the-news/ (visited on 10/18/2019).

[29] Daniel S Coles and Tom Walsh. “Mechanisms for reducing the cost of tidal stream energy”. In: *Proceedings of the 13th European Wave and Tidal Energy Conference (EWTEC2019)* (2019), pp. 1–8.

[30] Carwyn Frost. “Flow Direction Effects On Tidal Stream Turbines”. PhD thesis. 2016.

[31] *Atlantis Resources sets-up first tidal energy turbine near Scotland - Power Technology.* URL: https://www.power-technology.com/news/newsatlantis-resources-deploys-first-tidal-energy-ar1500-turbine-off-scotland-5749736/ (visited on 10/18/2019).

[32] *SIT Instream Turbine - SCHOTTEL.* URL: https://www.schottel.de/schottel-hydro/sit-instream-turbine/ (visited on 10/18/2019).

[33] *PLAT-I.* URL: https://sustainablemarine.com/plat-i (visited on 10/18/2019).

[34] *PLAT-O.* URL: https://sustainablemarine.com/plat-o (visited on 02/11/2020).

[35] *EMEC: European Marine Energy Centre - Orkney.* URL: http://www.emec.org.uk/about-us/our-tidal-clients/nautricity/%20http://www.emec.org.uk/index.asp%7B%5C%%7D5Cnhttp://www.emec.org.uk/downloads.asp%7B%5C%%7D5Cnhttp://www.emec.org.uk/national%7B%5C_%7Dstandards%7B%5C_%7Dabstracts.asp%7B%5C%%7D5Cnhttp://www.emec.org.uk/people.asp (visited on 10/23/2019).

[36] *CoRMaT - Nautricity.* URL: http://www.nautricity.com/cormat/ (visited on 10/23/2019).

[37] Sang Hun Han, Jin Soon Park, Kwang Soo Lee, Woo Sun Park, and Jin Hak Yi. “Evaluation of vertical axis turbine characteristics for tidal current power plant based on in situ experiment”. In: *Ocean Engineering* 65 (2013), pp. 83–89. ISSN: 00298018. DOI: 10.1016/j.oceaneng.2013.03.005.

[38] Sandra Eriksson, Hans Bernhoff, and Mats Leijon. *Evaluation of different turbine concepts for wind power.* June 2008. DOI: 10.1016/j.rser.2006.05.017.

[39] *EMEC: European Marine Energy Centre - Orkney.* URL: http://www.emec.org.uk/marine-energy/tidal-developers/%20http://www.emec.org.uk/index.asp%7B%5C%%7D5Cnhttp://www.emec.org.uk/downloads.asp%7B%5C%%7D5Cnhttp://www.emec.org.uk/national%7B%5C_%7Dstandards%7B%5C_%7Dabstracts.asp%7B%5C%%7D5Cnhttp://www.emec.org.uk/people.asp (visited on 02/11/2020).

[40] M. J. Khan, G. Bhuyan, M. T. Iqbal, and J. E. Quaicoe. *Hydrokinetic energy conversion systems and assessment of horizontal and vertical axis turbines for river and tidal applications: A technology status review.* 2009. DOI: `10.1016/j.apenergy.2009.02.017`.

[41] *Tidal devices : EMEC: European Marine Energy Centre.* 2017. URL: `http://www.emec.org.uk/marine-energy/tidal-devices/`.

[42] *EEL Energy Granted Funding for Development of Tidal Power Machine — Energy — News.* URL: `https://www.oceannews.com/news/energy/eel-energy-granted-funding-for-development-of-tidal-power-machine` (visited on 10/23/2019).

[43] *'Promising' trial prompts EEL Energy's investment search — Marine Energy.* URL: `https://marineenergy.biz/2018/06/04/promising-trial-prompts-eel-energys-investment-search/` (visited on 10/18/2019).

[44] Minesto. *Holyhead Deep – the world's first low-flow tidal stream project — Minesto.* 2014. URL: `https://minesto.com/projects/holyhead-deep` (visited on 10/18/2019).

[45] A. S. Iyer, S. J. Couch, G. P. Harrison, and A. R. Wallace. "Variability and phasing of tidal current energy around the United Kingdom". In: *Renewable Energy* 51 (Mar. 2013), pp. 343–357. ISSN: 09601481. DOI: `10.1016/j.renene.2012.09.017`.

[46] Ian G. Bryden, S. J. Couch, A Owen, and G Melville. "Tidal current resource assessment". In: *Proceedings of the Institution of Mechanical Engineers, Part A: Journal of Power and Energy* 221.2 (Mar. 2007), pp. 125–135. ISSN: 09576509. DOI: `10.1243/09576509JPE238`. URL: `http://journals.sagepub.com/doi/10.1243/09576509JPE238`.

[47] M Lewis, S P Neill, P E Robins, and M R Hashemi. "Resource assessment for future generations of tidal-stream energy arrays". In: *Energy* 83 (2015), pp. 403–415. ISSN: 03605442. DOI: `10.1016/j.energy.2015.02.038`. URL: `http://dx.doi.org/10.1016/j.energy.2015.02.038`.

[48] Iain Fairley, Paul Evans, Chris Wooldridge, Miles Willis, and Ian Masters. "Evaluation of tidal stream resource in a potential array area via direct measurements". In: *Renewable Energy* 57 (Sept. 2013), pp. 70–78. ISSN: 09601481. DOI: `10.1016/j.renene.2013.01.024`.

[49] J. McNaughton, Simon Harper, Rognvald Sinclair, and B. Sellar. "Measuring and Modelling the Power Curve of a Commercial-Scale Tidal Turbine". In: *Proceedings of 11th European Wave and Tidal Energy Conference, Nantes, France* September (2015), pp. 1–9. ISSN: 1098-6596. DOI: `10.1017/CBO9781107415324.004`. arXiv: `arXiv:1011.1669v3`.

[50] Tom Blackmore, Luke E. Myers, and Abubakr S. Bahaj. "Effects of turbulence on tidal turbines: Implications to performance, blade loads, and condition monitoring". In: *International Journal of Marine Energy* 14 (2016), pp. 1–26. ISSN: 22141669. DOI: `10.1016/j.ijome.2016.04.017`. URL: `http://dx.doi.org/10.1016/j.ijome.2016.04.017`.

[51] Paul Mycek, Benoît Gaurier, Grégory Germain, Grégory Pinon, and Elie Rivoalen. "Experimental study of the turbulence intensity effects on marine current turbines behaviour. Part I: One single turbine". In: *Renewable Energy* 66 (2014), pp. 729–746. ISSN: 09601481. DOI: `10.1016/j.renene.2013.12.036`.

[52] A. Mason-Jones. "Performance assessment of a horizontal axis tidal turbine in a high velocity shear environment". In: (2010).

[53] Ian A Milne, Rajnish N Sharma, Richard G J Flay, Simon Bickerton, and Phil Trans R Soc A. "Characteristics of the turbulence in the flow at a tidal stream power site". In: *Philosophical Transactions of the Royal Society A: Mathematical, Physical and Engineering Sciences* 371.1985 (2013), p. 20120196. ISSN: 1364-503X. DOI: `10.1098/rsta.2012.0196`. URL: `http://dx.doi.org/10.1098/rsta.2012.0196%20http://www.ncbi.nlm.nih.gov/pubmed/23319707%7B%5C%%7D5Cnhttp://rsta.royalsocietypublishing.org/content/371/1985/20120196.short`.

[54] Jim Thomson, Brian Polagye, Marshall Richmond, and Vibhav Durgesh. "Quantifying turbulence for tidal power applications". In: *MTS/IEEE Seattle, OCEANS 2010*. 2010. ISBN: 9781424443321. DOI: `10.1109/OCEANS.2010.5664600`.

[55] Ye Li, Neil Kelley, Bonnie Jonkman, Jonathan A. Colby, Robert Thresher, and Scott Hughes. "Inflow measurement in a tidal strait for deploying tidal current turbines-lessons, opportunities and challenges". In: *Proceedings of the International Conference on Offshore Mechanics and Arctic Engineering - OMAE*. 2010. ISBN: 9780791849118. DOI: `10.1115/OMAE2010-20911`.

[56] Emmanuel Osalusi, Jonathan Side, and Robert Harris. "Structure of turbulent flow in EMEC's tidal energy test site". In: *International Communications in Heat and Mass Transfer* (2009). ISSN: 07351933. DOI: `10.1016/j.icheatmasstransfer.2009.02.010`.

[57] Emmanuel Osalusi, Jonathan Side, and Robert Harris. "Reynolds stress and turbulence estimates in bottom boundary layer of Fall of Warness". In: *International Communications in Heat and Mass Transfer* (2009). ISSN: 07351933. DOI: `10.1016/j.icheatmasstransfer.2009.02.004`.

[58] Sam Gooch, Jim Thomson, Brian Polagye, and Dallas Meggitt. "Site characterization for tidal power". In: *MTS/IEEE Biloxi - Marine Technology for Our Future: Global and Local Challenges, OCEANS 2009*. 2009. ISBN: 9781424449606.

[59] Ross Vennell, Simon W. Funke, Scott Draper, Craig Stevens, and Tim Divett. *Designing large arrays of tidal turbines: A synthesis and review*. 2015. DOI: `10.1016/j.rser.2014.08.022`.

[60] Rory O'Hara Murray and Alejandro Gallego. "A modelling study of the tidal stream resource of the Pentland Firth, Scotland". In: *Renewable Energy* 102 (2017), pp. 326–340. ISSN: 18790682. DOI: `10.1016/j.renene.2016.10.053`. URL: `http://dx.doi.org/10.1016/j.renene.2016.10.053`.

[61] A. S. Iyer, S. J. Couch, G. P. Harrison, and A. R. Wallace. "Variability and phasing of tidal current energy around the United Kingdom". In: *Renewable Energy* 51 (2013), pp. 343–357. ISSN: 09601481. DOI: `10.1016/j.renene.2012.09.017`. URL: `http://dx.doi.org/10.1016/j.renene.2012.09.017`.

[62] S.C. Tatum, C.H. Frost, M. Allmark, D.M. O'Doherty, A. Mason-Jones, P.W. Prickett, R.I. Grosvenor, C.B. Byrne, and T. O'Doherty. "Wave–current interaction effects on tidal stream turbine performance and loading characteristics". In: *International Journal of Marine Energy* 14 (2016), pp. 161–179. ISSN: 22141669. DOI: `10.1016/j.ijome.2015.09.002`.

[63] David D. Apsley, Tim Stallard, and Peter K. Stansby. “Actuator-line CFD modelling of tidal-stream turbines in arrays”. In: *Journal of Ocean Engineering and Marine Energy* 4.4 (Nov. 2018), pp. 259–271. ISSN: 21986452. DOI: `10.1007/s40722-018-0120-3`.

[64] H K Versteeg and W Malalasekera. *An Introduction to Computational Fluid Dynamics*. Vol. 1. 2007, p. 503. ISBN: 9780131274983. DOI: `10.2514/1.22547`.

[65] Martin O.L Hansen. *Aerodynamics of Wind Turbines*. 2000, pp. 1–189. ISBN: 978-1-138-77507-7 (hbk). DOI: `10.1002/0470846127`. arXiv: `arXiv:1011.1669v3`.

[66] Ross Vennell. “Exceeding the Betz limit with tidal turbines”. In: *Renewable Energy* 55 (July 2013), pp. 277–285. ISSN: 09601481. DOI: `10.1016/j.renene.2012.12.016`.

[67] H Glauert. *The elements of aerofoil and airscrew theory*. Cambridge University Press, 1946.

[68] J. F. Manwell, J. G. McGowan, and A. L. Rogers. *Wind Energy Explained: Theory, Design and Application*. 2010. ISBN: 9780470015001. DOI: `10.1002/9781119994367`.

[69] S Ordonez-Sanchez, K Porter, C Johnstone, M Allmark, T O‘Doherty, R Ellis, C Frost, and T Nevalainen. “Numerical Modelling Techniques to Predict Rotor Imbalance Problems in Tidal Stream Turbines”. In: *Proceedings of the Twelfth European Wave and Tidal Energy Conference* (2017), {752\hyphen 1}—{752\hyphen 9}.

[70] T. M. Nevalainen, C. M. Johnstone, and A. D. Grant. “A sensitivity analysis on tidal stream turbine loads caused by operational, geometric design and inflow parameters”. In: *International Journal of Marine Energy* 16 (2016), pp. 51–64. ISSN: 22141669. DOI: `10.1016/j.ijome.2016.05.005`.

[71] Rami Malki, Ian Masters, Alison J Williams, and T. Nick Croft. “Planning tidal stream turbine array layouts using a coupled blade element momentum - computational fluid dynamics model”. In: *Renewable Energy* 63 (2014), pp. 46–54. ISSN: 09601481. DOI: `10.1016/j.renene.2013.08.039`. URL: `http://dx.doi.org/10.1016/j.renene.2013.08.039`.

[72] Mark Drela. “XFOIL: An Analysis and Design System for Low Reynolds Number Airfoils”. In: *Lecture Notes in Engineering* 54.October (1989), pp. 1–12. DOI: `10.1007/978-3-642-84010-4`. URL: `http://www.springerlink.com/index/10.1007/978-3-642-84010-4`.

[73] A. F. Molland, A. S. Bahaj, J. R. Chaplin, and W. M. J. Batten. “Measurements and predictions of forces, pressures and cavitation on 2-D sections suitable for marine current turbines”. In: *Proceedings of the Institution of Mechanical Engineers, Part M: Journal of Engineering for the Maritime Environment* 218.2 (2004), pp. 127–138. ISSN: 1475-0902. DOI: `10.1243/1475090041651412`. URL: `http://pim.sagepub.com/content/218/2/127.full.pdf`.

[74] W M J Batten, A S Bahaj, A F Molland, and J R Chaplin. “Hydrodynamics of marine current turbines”. In: *Renewable Energy* 31.2 (2006), pp. 249–256. ISSN: 09601481. DOI: `10.1016/j.renene.2005.08.020`. URL: `www.energy.soton.ac.uk`.

[75] Jai N. Goundar and M. Rafiuddin Ahmed. “Design of a horizontal axis tidal current turbine”. In: *Applied Energy* 111 (2013), pp. 161–174. ISSN: 03062619. DOI: `10.1016/j.apenergy.2013.04.064`.

[76] Chul-hee Jo and Kang-hee Lee. "Application of an Airfoil to the Tidal Turbine Design by Analyzing Two-dimensional Performance in the Water". In: Eesd (2017), pp. 123–138.

[77] J. Morgado, R. Vizinho, M. A.R. Silvestre, and J. C. Páscoa. "XFOIL vs CFD performance predictions for high lift low Reynolds number airfoils". In: *Aerospace Science and Technology* 52 (2016), pp. 207–214. ISSN: 12709638. DOI: `10.1016/j.ast.2016.02.031`. URL: `http://dx.doi.org/10.1016/j.ast.2016.02.031`.

[78] Ju Hyun Lee, Sunho Park, Dong Hwan Kim, Shin Hyung Rhee, and Moon Chan Kim. "Computational methods for performance analysis of horizontal axis tidal stream turbines". In: *Applied Energy* 98 (2012), pp. 512–523. ISSN: 03062619. DOI: `10.1016/j.apenergy.2012.04.018`. arXiv: `arXiv:1011.1669v3`. URL: `http://dx.doi.org/10.1016/j.apenergy.2012.04.018`.

[79] Michael J. Lawson, Ye Li, and Danny C. Sale. "Development and Verification of a Computational Fluid Dynamics Model of a Horizontal-Axis Tidal Current Turbine". In: *Volume 5: Ocean Space Utilization; Ocean Renewable Energy* January (2011), pp. 711–720. ISSN: 01266039. DOI: `10.1115/OMAE2011-49863`. URL: `http://proceedings.asmedigitalcollection.asme.org/proceeding.aspx?articleid=1624988`.

[80] *HARP_Opt — NWTC Information Portal.* URL: `https://nwtc.nrel.gov/HARP%7B%5C_%7DOpt` (visited on 11/08/2019).

[81] W. M.J. Batten, A. S. Bahaj, A. F. Molland, and J. R. Chaplin. "Experimentally validated numerical method for the hydrodynamic design of horizontal axis tidal turbines". In: *Ocean Engineering* (2007). ISSN: 00298018. DOI: `10.1016/j.oceaneng.2006.04.008`.

[82] A. S. Bahaj, A. F. Molland, J. R. Chaplin, and W. M J Batten. "Power and thrust measurements of marine current turbines under various hydrodynamic flow conditions in a cavitation tunnel and a towing tank". In: *Renewable Energy* 32.3 (2007), pp. 407–426. ISSN: 09601481. DOI: `10.1016/j.renene.2006.01.012`.

[83] Andreas Gross, Hermann Fasel, Tillmann Friederich, and Markus Kloker. "Numerical Investigation of S822 Wind Turbine Airfoil". In: *40th Fluid Dynamics Conference and Exhibit* November (2010), pp. 1–25. DOI: `10.2514/6.2010-4478`. URL: `http://arc.aiaa.org/doi/abs/10.2514/6.2010-4478`.

[84] T O 'Doherty, A Mason-Jones, D M O 'Doherty, C B Byrne, I Owen, and Y X Wang. "Experimental and Computational Analysis of a Model Horizontal Axis Tidal Turbine". In: *8th European wave and tidal energy conference* m (2009), pp. 833–841. URL: `http://www.homepages.ed.ac.uk/shs/Wave%20Energy/EWTEC%202009/EWTEC%202009%20(D)/papers/263.pdf`.

[85] Stephanie Ordonez-Sanchez, Kate Porter, Carwyn Frost, Matthew Allmark, and Cameron Johnstone. "Effects of Wave-Current Interactions on the Performance of Tidal Stream Turbines". In: *Proceedings of the 3rd Asian Wave & Tidal Energy Conference* (2016), pp. 394–403. DOI: `10.3850/978-981-11-0782-5`. URL: `https://pure.strath.ac.uk/portal/files/56374602/Ordonez%7B%5C_%7DSanchez%7B%5C_%7Detal%7B%5C_%7DAWTEC2016%7B%5C_%7DEffects%7B%5C_%7Dof%7B%5C_%7Dextreme%7B%5C_%7Dwave%7B%5C_%7Dcurrent%7B%5C_%7Dinteractions.pdf`.

[86] S. Ordonez-Sanchez, M. Allmark, K. Porter, R. Ellis, C. Lloyd, T. O'Doherty, and C. Johnstone. "Analysis of a Horizontal Axis Tidal Turbine Performance in the Presence of Regular and Irregular Waves using Two Control Strategies". In: *Journal of Marine Science and Engineering* Under Revi (2019). ISSN: 1996-1073. DOI: `10.3390/en12030367`.

[87] Matthew Allmark, Robert Ellis, Kate Porter, Tim O Doherty, and Cameron Johnstone. "The Development and Testing of a Lab-Scale Tidal Stream Turbine for the Study of Dynamic Device Loading". In: *Proceedings of the 4th Asian Wave and Tidal Energy Conference* (2018).

[88] Luke Myers and A. S. Bahaj. "Wake studies of a 1/30th scale horizontal axis marine current turbine". In: *Ocean Engineering* 34.5-6 (Apr. 2007), pp. 758–762. ISSN: 00298018. DOI: `10.1016/j.oceaneng.2006.04.013`.

[89] A. S. Bahaj, W. M.J. Batten, and G. McCann. "Experimental verifications of numerical predictions for the hydrodynamic performance of horizontal axis marine current turbines". In: *Renewable Energy* 32.15 (2007), pp. 2479–2490. ISSN: 09601481. DOI: `10.1016/j.renene.2007.10.001`.

[90] Richard McSherry, Jamie Grimwade, Ian Jones, Simon Mathias, Andrew Wells, and Andre Mateus. "3D CFD modelling of tidal turbine performance with validation against laboratory experiments". In: *EWTEC 2011 Proceedings* (2011).

[91] A Mason-Jones, D. M. O'Doherty, C E Morris, T. O'Doherty, C B Byrne, P W Prickett, R I Grosvenor, I Owen, S Tedds, and R J Poole. "Non-dimensional scaling of tidal stream turbines". In: *Energy* 44.1 (2012), pp. 820–829. ISSN: 03605442. DOI: `10.1016/j.energy.2012.05.010`. URL: `https://ac.els-cdn.com/S0360544212003891/1-s2.0-S0360544212003891-main.pdf?%7B%5C_%7Dtid=509d02f4-8da1-4b1d-8fc1-5646d8ec005a%7B%5C&%7Dacdnat=1543326520%7B%5C_%7Db290d1a8d435974f856d81ecddca6fbd`.

[92] Darrel A Doman, Robynne E Murray, Michael J Pegg, Katie Gracie, Cameron M Johnstone, and Thomas Nevalainen. "Tow-tank testing of a 1/20th scale horizontal axis tidal turbine with uncertainty analysis". In: *International Journal of Marine Energy* 11 (2015), pp. 105–119. ISSN: 22141669. DOI: `10.1016/j.ijome.2015.06.003`. URL: `http://dx.doi.org/10.1016/j.ijome.2015.06.003`.

[93] Ceri Morris. "Influence of Solidity on the Performance, Swirl Characteristics, Wake Recovery and Blade Deflection of a Horizontal Axis Tidal Turbine". In: (2014).

[94] Darrell Egarr, Tim O'Doherty, S Morris, N Syred, and RG Ayre. "Computational study of tidal turbines for extracting energy from the tides". In: July (2005). DOI: `10.13140/2.1.1116.7524`.

[95] Luolin Bai, Roy R G Spence, and Grégory Dudziak. "Investigation of the Influence of Array Arrangement and Spacing on Tidal Energy Converter (TEC) Performance using a 3-Dimensional CFD Model". In: *Proceedings of the 8th European Wave and Tidal Energy Conference, Uppsala, Sweeden* (2009), pp. 654–660. ISSN: 18711413. DOI: `10.1016/j.livsci.2011.12.021`. URL: `http://www.homepages.ed.ac.uk/shs/Wave%20Energy/EWTEC%202009/EWTEC%202009%20(D)/papers/167.pdf`.

[96] F. Maganga, G. Germain, J. King, G. Pinon, and E. Rivoalen. "Experimental characterisation of flow effects on marine current turbine behaviour and on its wake properties". In: *IET Renewable Power Generation* 4.6 (2010), pp. 498–509. ISSN: 17521416. DOI: `10.1049/iet-rpg.2009.0205`.

[97] DNV GL. *OFFSHORE STANDARD DNV GL AS Position mooring.* 2015. URL: `http://www.dnvgl.com`.

[98] N. Jarrin, S. Benhamadouche, D. Laurence, and R. Prosser. “A synthetic-eddy-method for generating inflow conditions for large-eddy simulations”. In: *International Journal of Heat and Fluid Flow* 27.4 (Aug. 2006), pp. 585–593. ISSN: 0142727X. DOI: `10.1016/j.ijheatfluidflow.2006.02.006`.

[99] F. Menter. “Best Practice: Scale-Resolving Simulations in ANSYS CFD”. In: *ANSYS Inc* April (2012), pp. 1–70. ISSN: 0889504X. DOI: `10.1155/2013/859465`. URL: `http://ainastran.org/staticassets/ANSYS/staticassets/resourcelibrary/techbrief/tb-best-practices-scale-resolving-models.pdf`.

[100] J. E. Bardina, P. G. Huang, and T. J. Coakley. “Turbulence Modeling Validation, Testing, and Development”. In: *Nasa Technical Memorandum* 110446 (1997), pp. 8–20. DOI: `10.2514/6.1997-2121`. URL: `http://www.ewp.rpi.edu/hartford/%7B~%7Djongel/EP/4.%20Supporting%20Materials/References/19970017828%7B%5C_%7D1997026179.pdf`.

[101] P. R. Spalart and S. R. Allmaras. “One-equation turbulence model for aerodynamic flows”. In: *Recherche aerospatiale* (1994). ISSN: 00341223. DOI: `10.2514/6.1992-439`.

[102] W. P. Jones and B. E. Launder. “The prediction of laminarization with a two-equation model of turbulence”. In: *International Journal of Heat and Mass Transfer* (1972). ISSN: 00179310. DOI: `10.1016/0017-9310(72)90076-2`.

[103] David C. Wilcox. “Turbulence Modeling for CFD (Third Edition)”. In: *DCW Industries* (2006).

[104] F. R. Menter. “Two-equation eddy-viscosity turbulence models for engineering applications”. In: *AIAA Journal* 32.8 (1994), pp. 1598–1605. ISSN: 0001-1452. DOI: `10.2514/3.12149`. URL: `http://arc.aiaa.org/doi/10.2514/3.12149`.

[105] I. Afgan, J. McNaughton, S. Rolfo, D.D. Apsley, T. Stallard, and P. Stansby. “Turbulent flow and loading on a tidal stream turbine by LES and RANS”. In: *International Journal of Heat and Fluid Flow* 43.1 (Oct. 2013), pp. 96–108. ISSN: 0142727X. DOI: `10.1016/j.ijheatfluidflow.2013.03.010`. URL: `http://dx.doi.org/10.1016/j.ijheatfluidflow.2013.03.010%20https://linkinghub.elsevier.com/retrieve/pii/S0142727X13000672`.

[106] T Ebdon, D M O Doherty, and T O Doherty. “Simulating Marine Current Turbine Wakes Using Advanced Turbulence Models”. In: ().

[107] L. E. Myers and A. S. Bahaj. “Experimental analysis of the flow field around horizontal axis tidal turbines by use of scale mesh disk rotor simulators”. In: *Ocean Engineering* 37.2-3 (2010), pp. 218–227. ISSN: 00298018. DOI: `10.1016/j.oceaneng.2009.11.004`. URL: `http://dx.doi.org/10.1016/j.oceaneng.2009.11.004`.

[108] L Myers and A.S. Bahaj. “Near wake properties of horizontal axis marine current turbines”. In: *8th European Wave and Tidal Energy Conference* (2009), pp. 558–565.

[109] A Mason-Jones, D. M. O’Doherty, C E Morris, and T. O’Doherty. “Influence of a velocity profile & support structure on tidal stream turbine performance”. In: *Renewable Energy* 52 (2013), pp. 23–30. ISSN: 09601481. DOI: `10.1016/j.renene.2012.10.022`. URL: `http://dx.doi.org/10.1016/j.renene.2012.10.022`.

[110] W. M. J. Batten, M. E. Harrison, and A. S. Bahaj. "Accuracy of the actuator disc-RANS approach for predicting the performance and wake of tidal turbines". In: *Philosophical Transactions of the Royal Society A: Mathematical, Physical and Engineering Sciences* 371.1985 (2013), pp. 20120293–20120293. ISSN: 1364-503X. DOI: `10.1098/rsta.2012.0293`. URL: `http://rsta.royalsocietypublishing.org/cgi/doi/10.1098/rsta.2012.0293`.

[111] M E Harrison, W M J Batten, L E Myers, and A S Bahaj. "A comparison between CFD simulations and experiments for predicting the far wake of horizontal axis tidal turbines". In: *Renewable Power Generation* 4.6 (2010), pp. 613–627. ISSN: 17521416. DOI: `10.1049/iet-rpg.2009.0193`.

[112] Grégory Pinon, Paul Mycek, Grégory Germain, and Elie Rivoalen. "Numerical simulation of the wake of marine current turbines with a particle method". In: *Renewable Energy* 46 (2012), pp. 111–126. ISSN: 09601481. DOI: `10.1016/j.renene.2012.03.037`. URL: `http://dx.doi.org/10.1016/j.renene.2012.03.037`.

[113] S W Funke, P E Farrell, and M D Piggott. "Tidal turbine array optimisation using the adjoint approach". In: *Renewable Energy* 63 (2014), pp. 658–673. ISSN: 09601481. DOI: `10.1016/j.renene.2013.09.031`. arXiv: `1304.1768`. URL: `http://dx.doi.org/10.1016/j.renene.2013.09.031`.

[114] Martin Nuernberg and Longbin Tao. "Three dimensional tidal turbine array simulations using OpenFOAM with dynamic mesh". In: *Ocean Engineering* 147 (2018), pp. 629–646. ISSN: 00298018. DOI: `10.1016/j.oceaneng.2017.10.053`. URL: `https://doi.org/10.1016/j.oceaneng.2017.10.053`.

[115] Guanghui Bai, Jun Li, Pengfei Fan, and Guojun Li. "Numerical investigations of the effects of different arrays on power extractions of horizontal axis tidal current turbines". In: *Renewable Energy* 53 (2013), pp. 180–186. ISSN: 09601481. DOI: `10.1016/j.renene.2012.10.048`. URL: `http://dx.doi.org/10.1016/j.renene.2012.10.048`.

[116] T Stallard, R Collings, T Feng, and J Whelan. "Interactions between tidal turbine wakes: Experimental study of a group of three-bladed rotors". In: *Philosophical Transactions of the Royal Society A: Mathematical, Physical and Engineering Sciences* 371.1985 (2013). ISSN: 1364503X. DOI: `10.1098/rsta.2012.0159`. URL: `http://dx.doi.org/10.1098/rsta.2012.0159http://dx.doi.org/10.1098/rsta.2012.0159orviahttp://rsta.royalsocietypublishing.org.`.

[117] L E Myers and A S Bahaj. "An experimental investigation simulating flow effects in first generation marine current energy converter arrays". In: *Renewable Energy* 37.1 (2012), pp. 28–36. ISSN: 09601481. DOI: `10.1016/j.renene.2011.03.043`. URL: `www.energy.soton.ac.uk.`.

[118] Carwyn H. Frost, Paul Stephen Evans, Ceri E. Morris, Daphne M. O'Doherty, and Tim O'Doherty. "Flow Misalignment and Tidal Stream Turbines". In: *Proceedings of the 11th European Wave and Tidal Energy Conference* November (2015), pp. 5–10. DOI: `10.13140/RG.2.1.3544.7761`.

[119] Jing Liu, Htet Lin, and Srinivasa Rao Purimitla. "Wake field studies of tidal current turbines with different numerical methods". In: *Ocean Engineering* 117 (May 2016), pp. 383–397. ISSN: 00298018. DOI: `10.1016/j.oceaneng.2016.03.061`.

[120] Daphne Maria O'Doherty, Allan Mason-Jones, Timothy O'Doherty, and Carlton Barrie Baylis Byrne. "Considerations of improved tidal stream turbine performance using double rows of contra-rotating blades". In: *EWTEC 2009 Proceedings* (2009). URL: `http://orca.cf.ac.uk/16917/`.

[121] Paul Mycek, Benoît Gaurier, Grégory Germain, Grégory Pinon, and Elie Rivoalen. "Experimental study of the turbulence intensity effects on marine current turbines behaviour. Part II: Two interacting turbines". In: *Renewable Energy* 68 (2014), pp. 876–892. ISSN: 09601481. DOI: `10.1016/j.renene.2013.12.048`.

[122] Benoît Gaurier, Peter Davies, Albert Deuff, and Grégory Germain. "Flume tank characterization of marine current turbine blade behaviour under current and wave loading". In: *Renewable Energy* 59 (Nov. 2013), pp. 1–12. ISSN: 09601481. DOI: `10.1016/j.renene.2013.02.026`. URL: `http://linkinghub.elsevier.com/retrieve/pii/S0960148113001353`.

[123] I. A. Milne, A. H. Day, R. N. Sharma, and R. G.J. Flay. "Blade loading on tidal turbines for uniform unsteady flow". In: *Renewable Energy* 77 (2015), pp. 338–350. ISSN: 18790682. DOI: `10.1016/j.renene.2014.12.028`. URL: `http://dx.doi.org/10.1016/j.renene.2014.12.028`.

[124] I. A. Milne, A. H. Day, R. N. Sharma, and R. G.J. Flay. "Blade loads on tidal turbines in planar oscillatory flow". In: *Ocean Engineering* 60 (2013), pp. 163–174. ISSN: 00298018. DOI: `10.1016/j.oceaneng.2012.12.027`. URL: `http://dx.doi.org/10.1016/j.oceaneng.2012.12.027`.

[125] Grégory S. Payne, Tim Stallard, Rodrigo Martinez, and Tom Bruce. "Variation of loads on a three-bladed horizontal axis tidal turbine with frequency and blade position". In: *Journal of Fluids and Structures* 83 (Nov. 2018), pp. 156–170. ISSN: 10958622. DOI: `10.1016/j.jfluidstructs.2018.08.010`.

[126] Xue Wang. "CFD Analysis of Unsteady Hydrodynamic Loading on Horizontal Axis Tidal Turbine (HATT) Blades". In: November (2015).

[127] U. Ahmed, D. D. Apsley, I. Afgan, T. Stallard, and P. K. Stansby. "Fluctuating loads on a tidal turbine due to velocity shear and turbulence: Comparison of CFD with field data". In: *Renewable Energy* 112 (2017), pp. 235–246. ISSN: 18790682. DOI: `10.1016/j.renene.2017.05.048`.

[128] A. Roberts, B. Thomas, P. Sewell, Z. Khan, S. Balmain, and J. Gillman. "Current tidal power technologies and their suitability for applications in coastal and marine areas". In: *Journal of Ocean Engineering and Marine Energy* 2.2 (May 2016), pp. 227–245. ISSN: 21986452. DOI: `10.1007/s40722-016-0044-8`.

[129] P L Fraenkel. "Power from marine currents". In: *Proceedings of the I MECH E Part A Journal of Power and Energy* 216.1 (2002), pp. 1–14. ISSN: 09576509. DOI: `10.1243/095765002760024791`.

[130] Eva Segura, Rafael Morales, and José A. Somolinos. "Cost assessment methodology and economic viability of tidal energy projects". In: *Energies* 10.11 (2017), pp. 1–27. ISSN: 19961073. DOI: `10.3390/en10111806`.

[131] I Masters, J C Chapman, M R Willis, and J A C Orme. “A robust blade element momentum theory model for tidal stream turbines including tip and hub loss corrections”. In: 4177.June (2016). ISSN: 14761548. DOI: `10.1016/0306-26197890025-9; Badreddine,K.,Ali,H.,David,A.,Optimumprojectforhorizontalaxiswindturbines' OPHWT'(2005)RenewableEnergy,30,pp.2019-2043;Kishinami,K.,Theoreticalandexperimental Energy,30,pp.2089-2100;Mikkelsen,R.,(2003)ActuatorDiscMethodsAppliedtoWindTurbines, ,DissertationforTechnicalUniversityofDenmark;Shen,W.Z.,Mikkelsen,R. ,Sorensen,J.N.,Bak,C.,Tipl`.

[132] Justin Winslow, Hikaru Otsuka, Bharath Govindarajan, and Inderjit Chopra. “Basic understanding of airfoil characteristics at low Reynolds numbers (104–105)”. In: *Journal of Aircraft* (2018). ISSN: 15333868. DOI: `10.2514/1.C034415`.

[133] Thomas J. Mueller and Stephen M. Batill. “Experimental studies of separation on a two-dimensional airfoil at low reynolds numbers”. In: *AIAA Journal* (1982). ISSN: 00011452. DOI: `10.2514/3.51095`.

[134] H Tennekes and J. L Lumley. *A First Course in Turbulence.* 1972. ISBN: 9780262200196.

[135] W. P. Jones and B. E. Launder. “The calculation of low-Reynolds-number phenomena with a two-equation model of turbulence”. In: *International Journal of Heat and Mass Transfer* 16.6 (1973), pp. 1119–1130. ISSN: 00179310. DOI: `10.1016/0017-9310(73)90125-7`.

[136] S J Kline, B J Cantwell, and G M Lilley Stanford. “The 1980-81 AFOSR-HTTM Stanford Conference on Complex Turbulent Flows: A Comparison of Computation and Experiment, Volumes I, II and III. Edited by”. In: *J. Fluid Mech* (2018), p. 125. DOI: `10.1017/S0022112085211367`. URL: `https://doi.org/10.1017/S0022112085211367`.

[137] David C. Wilcox. “Reassessment of the scale-determining equation for advanced turbulence models”. In: *AIAA Journal* 26.11 (1988), pp. 1299–1310. ISSN: 0001-1452. DOI: `10.2514/3.10041`. arXiv: `arXiv:1011.1669v3`. URL: `http://arc.aiaa.org/doi/10.2514/3.10041`.

[138] F. R. Menter. “Influence of freestream values on k-omega turbulence model predictions”. In: *AIAA Journal* 30.6 (1992), pp. 1657–1659. ISSN: 0001-1452. DOI: `10.2514/3.11115`. arXiv: `arXiv:1011.1669v3`. URL: `http://arc.aiaa.org/doi/10.2514/3.11115`.

[139] F. R. Menter. “Zonal Two Equation k-w Turbulence Models For Aerodynamic Flows”. In: *23rd Fluid Dynamics, Plasmadynamics, and Lasers Conference*. 1993. ISBN: 103975. DOI: `10.2514/6.1993-2906`. URL: `http://arc.aiaa.org/doi/10.2514/6.1993-2906`.

[140] F R Menter, M Kuntz, and R Langtry. “Ten Years of Industrial Experience with the SST Turbulence Model”. In: *Turbulence Heat and Mass Transfer 4* 4 (2003), pp. 625–632. ISSN: 1662-8985. DOI: `10.4028/www.scientific.net/AMR.576.60`. URL: `http://aaac.larc.nasa.gov/tsab/cfdlarc/aiaa-dpw/%20http://cfd.mace.manchester.ac.uk/flomania/pds%7B%5C_%7Dpapers/file%7B%5C_%7Dpds-1068134610Menter-SST-paper.pdf`.

[141] Florian R. Menter, Jochen Schütze, and Mikhail Gritskevich. “Global vs. zonal approaches in hybrid RANS-LES turbulence modelling”. In: *Notes on Numerical Fluid Mechanics and Multidisciplinary Design* 117 (2012), pp. 15–28. ISSN: 16122909. DOI: `10.1007/978-3-642-31818-4-2`.

[142] M Strelets. “Detached Eddy Simulation of Massively Separated Flows”. In: January 2001 (2001). DOI: `10.2514/6.2002-1021`.

[143] “ANSYS CFX-Solver Theory Guide”. In: 15317.April (2009), pp. 724–746.

[144] P. R. Spalart, S. Deck, M. L. Shur, K. D. Squires, M. Kh Strelets, and A. Travin. “A new version of detached-eddy simulation, resistant to ambiguous grid densities”. In: *Theoretical and Computational Fluid Dynamics* 20.3 (2006), pp. 181–195. ISSN: 09354964. DOI: `10.1007/s00162-006-0015-0`.

[145] H Jasak. “Error Analysis and Estimation for the Finite Volume Method with Applications to Fluid Flows”. In: *02.02.00_Cfd* M.June (1996), p. 394. ISSN: 00207683. DOI: `10.1016/S0020-7683(02)00168-3`. arXiv: `0911.1613`.

[146] P. H. Gaskell and A. K C Lau. “Curvature-compensated convective transport: SMART, A new boundedness-preserving transport algorithm”. In: *International Journal for Numerical Methods in Fluids* 8.6 (1988), pp. 617–641. ISSN: 10970363. DOI: `10.1002/fld.1650080602`.

[147] H. Jasak, H. G. Weller, and A. D. Gosman. “High resolution NVD differencing scheme for arbitrarily unstructured meshes”. In: *International Journal for Numerical Methods in Fluids* 31.2 (1999), pp. 431–449. ISSN: 02712091. DOI: `10.1002/(SICI)1097-0363(19990930)31:2<431::AID-FLD884>3.0.CO;2-T`.

[148] DA Egarr, T O’doherty, S Morris, and RG Ayre. “Feasibility study using computational fluid dynamics for the use of a turbine for extracting energy from the tide”. In: *... Fluid Mechanics ...* December (2004), pp. 1–4. DOI: `10.13140/2.1.4852.3041`. URL: `http://www.ae.su.oz.au/15afmc/proceedings/papers/AFMC00024.pdf`.

[149] Matthew James Allmark. “Condition monitoring and fault diagnosis of tidal stream turbines subjected to rotor imbalance faults”. PhD thesis. 2016. URL: `https://orca.cf.ac.uk/98633/1/2017AllmarkMPhD.pdf%20http://orca.cf.ac.uk/98633/`.

[150] Michael S. Selig and Bryan D. McGranahan. “Wind Tunnel Aerodynamic Tests of Six Airfoils for Use on Small Wind Turbines”. In: *Journal of Solar Energy Engineering* 126.November (2004), p. 986. ISSN: 01996231. DOI: `10.1115/1.1793208`.

[151] Stephanie Eugenia Ordonez-Sanchez, Kate Porter, Rob Ellis, Carwyn Frost, Matthew Allmark, Thomas Nevalainen, Tim O’Doherty, and Cameron Johnstone. “Numerical modelling techniques to predict rotor imbalance problems in tidal stream turbines”. In: August 2018 (2017). URL: `https://strathprints.strath.ac.uk/61697/`.

[152] “ANSYS Meshing User ’s Guide”. In: vol. 80. November. 2011, pp. 724–746.

[153] “ANSYS CFX-Solver Modeling Guide”. In: vol. 15317. November. 2011, pp. 724–746.

[154] Matthew Allmark, Robert Ellis, Catherine Lloyd, Stephanie Ordonez-Sanchez, Kate Johannesen, Carl Byrne, Cameron Johnstone, Tim O Doherty, and Allan Mason-jones. “The development , design and characterisation of a scale model Horizontal Axis Tidal Turbine for Dynamic Load Quantification .” In: ().

[155] M. Coroneo, G. Montante, A. Paglianti, and F. Magelli. “CFD prediction of fluid flow and mixing in stirred tanks: Numerical issues about the RANS simulations”. In: *Computers and Chemical Engineering* 35.10 (Oct. 2011), pp. 1959–1968. ISSN: 00981354. DOI: `10.1016/j.compchemeng.2010.12.007`.

[156] J. L. Tangler. "Comparison of Wind Turbine Performance Prediction and Measurement". In: *Journal of Solar Energy Engineering* 104.2 (1982), pp. 84–88. ISSN: 0199-6231. DOI: `10.1115/1.3266290`.

[157] Robert Ellis, Matthew Allmark, Tim O Doherty, Allan Mason-jones, Stephanie Ordonez-sanchez, Kate Johannesen, and Cameron Johnstone. "Design Process for a Scale Horizontal Axis Tidal Turbine Blade ." In: *Proceedings of the 4th Asian Wave and Tidal Energy Conference* October (2018).

[158] Jo I Whelan, J. M.R. Graham, and J. Peiró. "A free-surface and blockage correction for tidal turbines". In: *Journal of Fluid Mechanics* 624 (2009), pp. 281–291. ISSN: 00221120. DOI: `10.1017/S0022112009005916`. URL: `https://doi.org/10.1017/S0022112009005916`.

[159] ANSYS Inc. *ANSYS CFX Reference Guide*. 2018. ISBN: 9789747946963. DOI: `10.1186/1756-0381-3-1`.

Appendix A

Appendix Title

A.1 Centreline velocity convergence

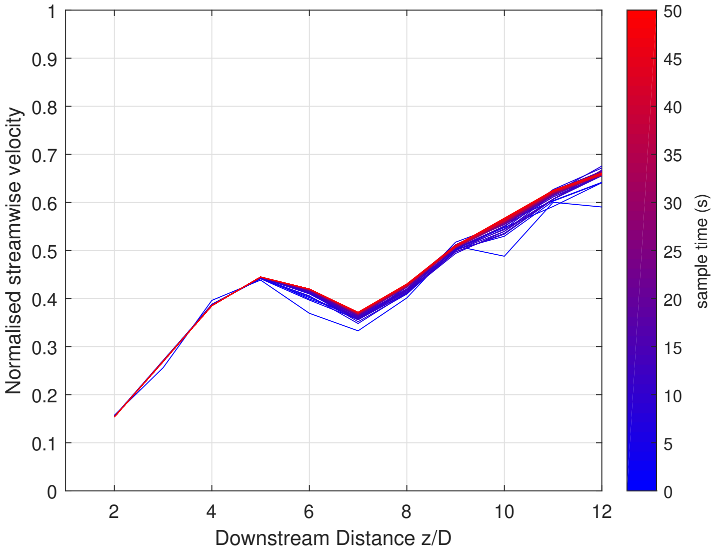

Figure A.1: The effect of sampling time on the centreline velocity recovery downstream of the turbine rotor for Run 1.

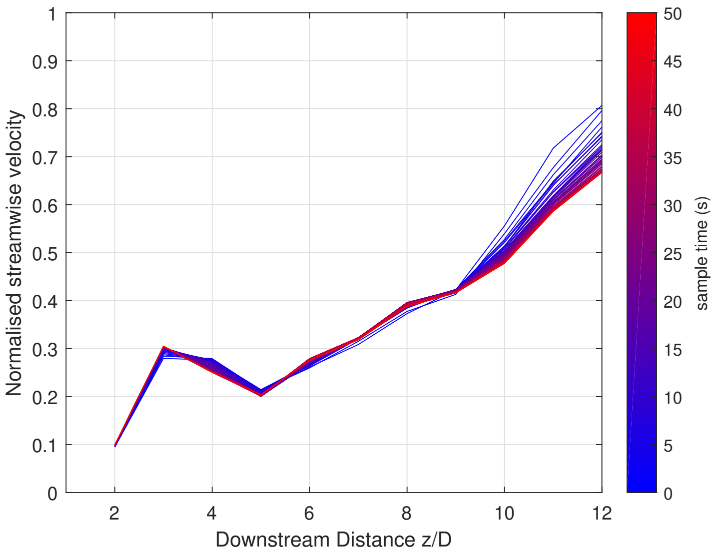

Figure A.2: The effect of sampling time on the centreline velocity recovery downstream of the turbine rotor for Run 2.

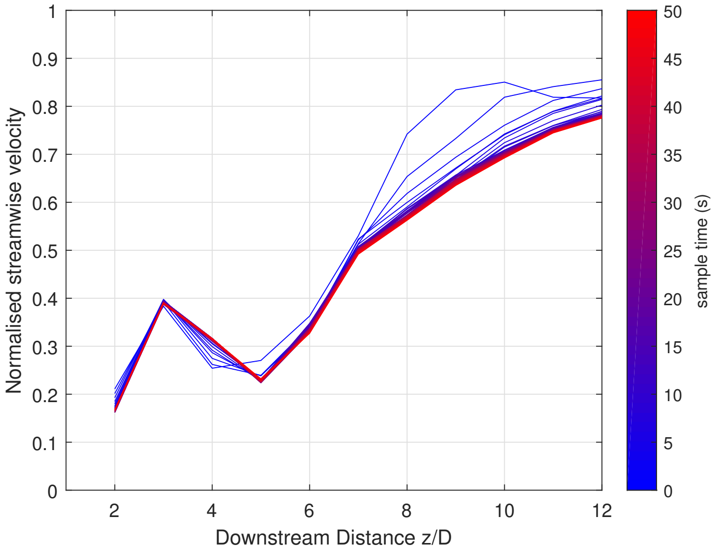

Figure A.3: The effect of sampling time on the centreline velocity recovery downstream of the turbine rotor for Run 3.

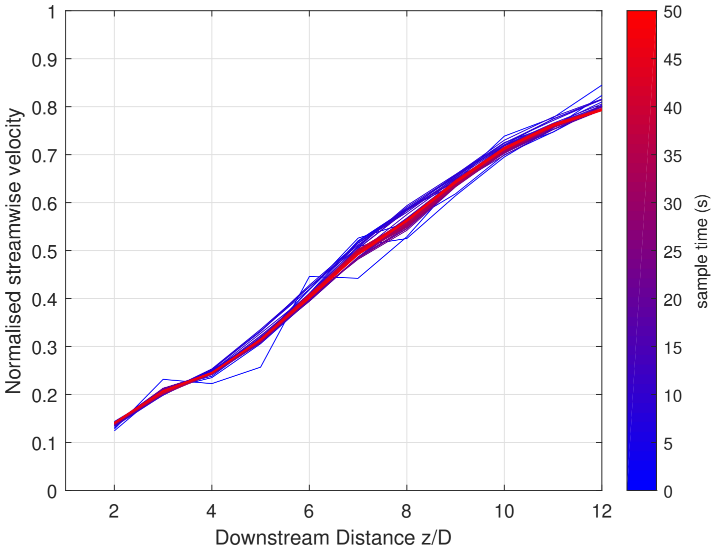

Figure A.4: The effect of sampling time on the centreline velocity recovery downstream of the turbine rotor for Run 4.

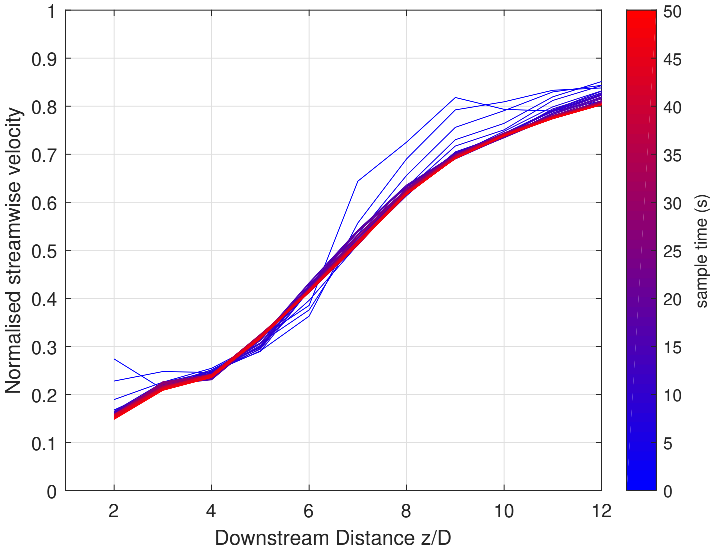

Figure A.5: The effect of sampling time on the centreline velocity recovery downstream of the turbine rotor for Run 5.

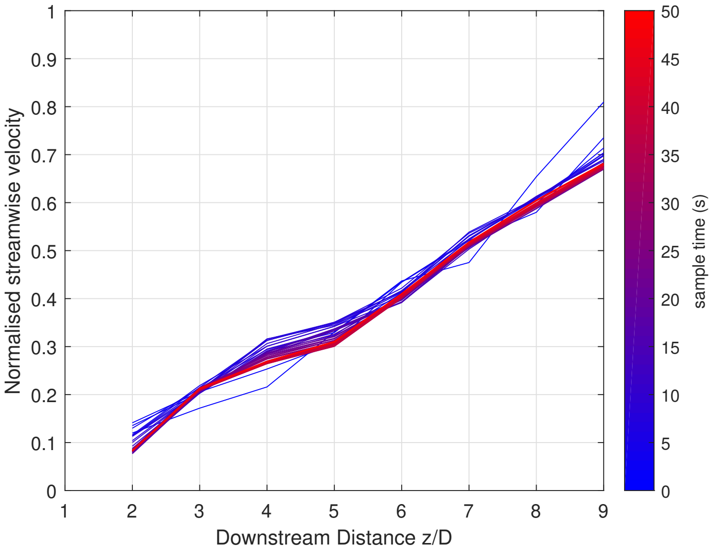

Figure A.6: The effect of sampling time on the centreline velocity recovery downstream of the turbine rotor for Run 7.

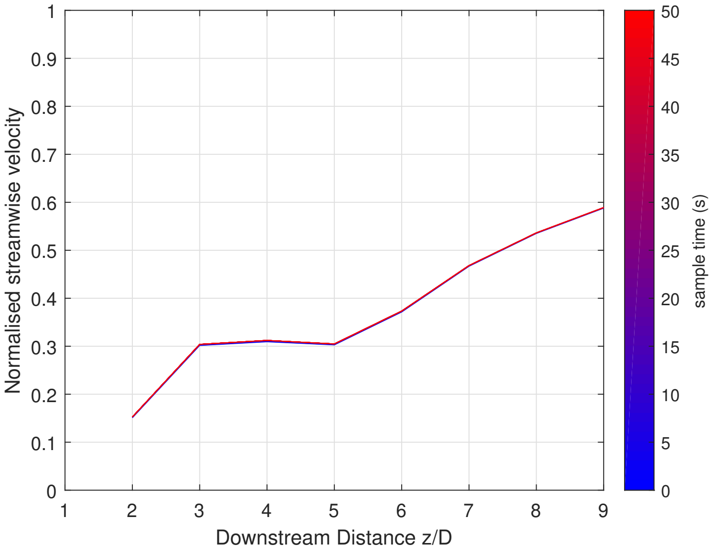

Figure A.7: The effect of sampling time on the centreline velocity recovery downstream of the turbine rotor for Run 8.

A.2 Measured data plots